

# Loughborough University Institutional Repository

---

## *Time-domain simulations for floating structures*

This item was submitted to Loughborough University's Institutional Repository by the/an author.

**Additional Information:**

- A Doctoral Thesis. Submitted in partial fulfilment of the requirements for the award of Doctor of Philosophy of Loughborough University.

**Metadata Record:** <https://dspace.lboro.ac.uk/2134/14475>

**Publisher:** © Colm James Fitzgerald

Please cite the published version.

This item was submitted to Loughborough University as a PhD thesis by the author and is made available in the Institutional Repository (<https://dspace.lboro.ac.uk/>) under the following Creative Commons Licence conditions.



**Attribution-NonCommercial-NoDerivs 2.5**

**You are free:**

- to copy, distribute, display, and perform the work

**Under the following conditions:**

 **Attribution.** You must attribute the work in the manner specified by the author or licensor.

 **Noncommercial.** You may not use this work for commercial purposes.

 **No Derivative Works.** You may not alter, transform, or build upon this work.

- For any reuse or distribution, you must make clear to others the license terms of this work.
- Any of these conditions can be waived if you get permission from the copyright holder.

**Your fair use and other rights are in no way affected by the above.**

This is a human-readable summary of the [Legal Code \(the full license\)](#).

[Disclaimer](#) 

For the full text of this licence, please go to:  
<http://creativecommons.org/licenses/by-nc-nd/2.5/>



## University Library

Author/Filing Title ..... FITZGERALD

Class Mark ..... T

Please note that fines are charged on ALL  
overdue items.

--	--	--

0403820596



# Time-domain simulations for floating structures

Colm James Fitzgerald

## A DOCTORAL THESIS

SUBMITTED IN PARTIAL FULFILMENT OF THE REQUIREMENTS  
FOR THE AWARD OF  
DOCTOR OF PHILOSOPHY OF LOUGHBOROUGH UNIVERSITY  
April 2009

Supervisor: Professor Phil McIver  
Director of Research: Professor Chris Linton

---



Loughborough  
University  
Pilkington Library

Date 9/7/10

Class T

Acc No. 0603820596

## Acknowledgements

There are many people to whom I owe a great deal of thanks and without whom this PhD would not have been possible. First and foremost among these people is my supervisor, Professor Phil McIver. During the past few years he has always been available to answer questions, give advice and lend direction to my research. I cannot but have admiration for his depth of knowledge and diligent approach to research. I have been truly lucky to have such an exemplary supervisor.

I would like also to mention the other senior members of the Waves Group, namely Professor Chris Linton, Dr Maureen McIver and Dr Ian Thompson, who have been very friendly and approachable in all matters. The regular group meetings over the past couple of years have been very helpful in developing my approach to presentations and have kept me up to date with current research. Further thanks to Phil and Chris for agreeing to send me to the waves workshop in far-flung destinations and to Ian and Dr Keith Watling for helping out with my numerous computing issues! The administrative staff of the department have also been of great assistance and very friendly and deserve a warm thanks.

Lastly, without the help of my parents and family none of this would have been possible. They have been unwavering in their support of me and have always been there for me through the good times and the bad. My frequent trips home for all the celebrations over the past few years have been a great source of happiness and joy. I thank you with all my heart.

## Abstract

In this thesis numerical and analytical investigations of wave-structure interactions are conducted within the linearised theory of water waves. The primary objective of the thesis was to develop a numerical time-domain solution method capable of simulating wave-structure interactions in three-dimensions involving axisymmetric structures. Although the solution method was developed for three-dimensional problems, many two-dimensional interactions were also simulated using an existing time-domain solution method.

The numerical method for obtaining the solution of the time-domain water wave problem combines a cubic spline boundary element method (BEM) which yields a solution to the boundary integral equation with a time-stepping algorithm to advance the solution in time. The assumption regarding the axisymmetric nature of the structural geometry results in significant simplifications of the governing boundary integral equation and allows the existing BEM implementation for two-dimensional problems to be used as the basis for the solution method. The time-advancement algorithm was implemented such that radiation, scattering and floating body interactions can be simulated.

Despite the focus on the time-domain investigations, the interactions were also considered in the frequency-domain to complement the time-domain results and for the purposes of verification. The analytical frequency-domain investigations are particularly relevant to highly resonant interactions where the response of the fluid and structure is related to the location of the resonance in the complex frequency plane. The complementary frequency-domain analysis was utilised in the development of a damped harmonic oscillator model to approximate the transient fluid motions in resonant scattering interactions. Passive trapped modes which can be supported by both fixed and floating structures were discovered in frequency-domain uniqueness investigations in the water-wave problem for a floating structure and their existence was confirmed in both two and three dimensions using time-domain excitation simulations. Finally, the time-domain BEM code was utilised to simulate various wave-structure interactions of practical interest.

---

# Contents

<b>1</b>	<b>Introduction</b>	<b>1</b>
1.1	Time-domain simulations - a perspective . . . . .	1
1.2	Motivations and research topics . . . . .	3
1.3	Structure of thesis . . . . .	5
<b>2</b>	<b>Time-domain equations and solution methods</b>	<b>7</b>
2.1	Time domain description of wave-structure interactions . . . . .	7
2.1.1	Small-amplitude approximation . . . . .	12
2.2	Review of time-domain models . . . . .	19
2.2.1	Frequency domain definitions . . . . .	20
2.2.2	Frequency-domain equation of motion . . . . .	22
2.2.3	Integro-differential equation method . . . . .	24
2.2.4	Generalised eigenfunction expansion method . . . . .	25
2.3	BEM and time-marching model . . . . .	28
<b>3</b>	<b>Boundary element method – theory</b>	<b>29</b>
3.1	Introduction . . . . .	29
3.2	Boundary integral equation . . . . .	29
3.2.1	Simplifications due to rotational symmetry . . . . .	32
3.3	Boundary element discretisation . . . . .	35
3.3.1	Discretisation of the BIE . . . . .	35

3.3.2	Evaluation of the influence coefficients . . . . .	44
3.4	Time-stepping algorithm . . . . .	51
3.4.1	Piston boundary condition . . . . .	51
3.4.2	Runge-Kutta method . . . . .	53
3.4.3	Computing the hydrodynamic force . . . . .	57
3.5	Structure of Fortran code . . . . .	58
<b>4</b>	<b>Boundary element method – development</b>	<b>61</b>
4.1	Verification of BEM computations . . . . .	61
4.2	Verification of time-stepping results . . . . .	65
4.2.1	Radiation and diffraction problems . . . . .	66
4.2.2	Cauchy-Poisson problem . . . . .	72
4.2.3	Coupled motion simulations . . . . .	75
4.2.4	Free surge motion of a torus . . . . .	79
4.3	Generalisation of time-domain solver . . . . .	81
4.3.1	Cross coupled modes of motion . . . . .	81
<b>5</b>	<b>Approximation of near-resonant wave motion using a damped harmonic oscillator model</b>	<b>83</b>
5.1	Introduction . . . . .	83
5.2	Oscillator model background . . . . .	85
5.2.1	Resonance location estimate . . . . .	87
5.3	Numerical implementation . . . . .	90
5.3.1	Time-domain computations . . . . .	90
5.3.2	Damped harmonic oscillator model computations . . . . .	92
5.4	Application and results . . . . .	92
5.4.1	Three dimensional scattering interactions . . . . .	98
5.5	Conclusion . . . . .	99

<b>6 Passive trapped modes</b>	<b>102</b>
6.1 Introduction . . . . .	102
6.2 Formulation . . . . .	104
6.3 Conditions for the existence of passive trapped modes . . . . .	106
6.4 Construction of passive trapping structures . . . . .	108
6.4.1 Two dimensional structures . . . . .	108
6.4.2 Three dimensional structures . . . . .	112
6.5 Excitation of passive trapped modes . . . . .	116
6.5.1 Excitation condition in the frequency-domain . . . . .	116
6.5.2 Resonant free-surface pressure forcing . . . . .	118
6.6 Time-domain simulations of transient excitations . . . . .	120
6.6.1 Two-dimensions . . . . .	120
6.6.2 Three dimensions . . . . .	123
6.7 Conclusion . . . . .	124
<b>7 Simulations of wave-structure interactions</b>	<b>126</b>
7.1 Plane-wave propagation . . . . .	126
7.2 Latching control . . . . .	133
7.2.1 Equations of motion for latching . . . . .	135
7.2.2 Time-domain latching simulations . . . . .	137
7.3 Multiple-mode motion of a moored freely floating body . . . . .	142
7.3.1 Cross coupling of modes of motion . . . . .	143
7.3.2 Stability of the cross-coupled motion . . . . .	146
7.3.3 Floating body motion excited by an incident wave . . . . .	152
7.4 Conclusions . . . . .	160
<b>8 Conclusions</b>	<b>162</b>
8.1 Summary . . . . .	162

8.2 Future work . . . . .	165
<b>A Evaluations of the general-order ring-source potentials and its derivatives</b>	<b>166</b>
A.1 Asymptotic form of the Legendre function $Q_{n-\frac{1}{2}}(Z)$ . . . . .	167
A.2 Asymptotic behaviour of $R_n$ . . . . .	168
A.3 Asymptotic form of $\frac{\partial}{\partial n}R_n$ . . . . .	170
<b>B Asymptotic analysis of far-field dipole potential</b>	<b>173</b>

# Chapter 1

## Introduction

### 1.1 Time-domain simulations - a perspective

The study of interactions between water waves and floating structures constitutes a distinct and important area of research in the field of hydrodynamics. An accurate description of such interactions requires the synthesis of water-wave theory with classical mechanics in order to describe the effect of the structural motion on the surrounding fluid and *vice versa*. The distinguishing feature of water-wave problems is the presence of the air-water interface referred to as the free surface which, together with the wetted surface of any surface-piercing structures, defines the upper boundary of the fluid. Any waves propagating in the fluid will be most prominent on the free surface and the dominant restoring force is gravity (assuming the wavelengths are sufficiently large to neglect surface tension) so that these waves are called surface gravity waves. Historically, accounts of the theory of surface gravity waves can be traced back to the treatise by Lamb (1932) on hydrodynamics originally published in the late nineteenth century. An authoritative review by Wehausen & Laitone (1960) of surface waves in the mid-twentieth century was indicative of the continued research in the area and the review contains an important summary of the theory of classical infinitesimal-waves in an inviscid fluid (now referred to as the linearised theory of water waves). This rather mathematical account of the theory of linearised water waves is complemented by the later, more applied works of Newman (1977a) and Mei (1982). Newman (1977a) in particular describes the importance of surface wave theory to naval engineering and presents a detailed exposition of the problem of a floating-body interaction in water-waves under the assumption that all motions are harmonic in time.

In this thesis, the linearised theory of water-waves is chosen as the theoretical framework for the simulations of the floating structure interactions because it provides a suitable basis for analytical and numerical analysis of the interactions. Recently, more complex

formulations of water-wave theory, such as the fully nonlinear description by Ducrozet, Bonnefoy, Le Touzé & Ferrant (2005), have been used to as the basis of numerical simulations of water-wave interactions. However, it is very difficult to make analytical progress having adopted this formulation. Within the linearised theory, two complementary descriptions of interaction problems exist referred to as the time-domain and frequency-domain equations. The frequency domain equations are developed under the assumption that all motions are harmonic in time whereas the time domain equations allow for general time-dependent motions. A Fourier transform relation exists between the two definitions so that results in the frequency domain are relevant and often important in the time domain. In a thorough review of water wave diffraction Eatock Taylor (2007) presents various models of the diffraction of water wave including a description of the linear frequency-domain and time-domain analyses. The complementary nature of the two models is illustrated by examining the time taken for the transient motion to reach steady state by comparison of the time- and frequency-domain results.

In much of the past literature, when developing both analytical and numerical solutions, it was standard to assume that all motions in linearised wave-structure interactions are time harmonic because of the difficulty in describing transient motions of the structure and fluid. Therefore, it was customary for authors such as Newman in his book on marine hydrodynamics to base the description of a floating body interaction within the frequency-domain framework. However, prior to the assumption of time harmonic motions Mei (1982) describes the dynamics of a floating body in terms of the linearised time-domain equations which can account for transient motions. The numerical simulation method developed in this project is based upon this description of wave-structure interactions. Nonetheless, much of the analytical work in this thesis is conducted in the frequency-domain and the corresponding computations for the linearised wave-structure interaction problems are obtained using WAMIT (<http://www.wamit.com>). This frequency-domain code is based on the boundary element method (BEM) and allows the computation of the hydrodynamic force coefficients of a structure which, as will be explained later in the thesis, can be used to obtain important information regarding the motion of the structure and response of the fluid during a wave-structure interaction. Although the time-domain solution can be obtained from an appropriate Fourier transform of the frequency-domain solution, in this project a numerical time-domain simulation method independent of frequency-domain data is employed to describe the transient motions in wave-structure interactions.

The simulation method developed here is a time-domain BEM and comprises two separate components. The first component is the cubic-spline boundary element discretisation (Sen (1995)) of the boundary integral equation describing the water-wave boundary value problem. The second component involves the application of a time-stepping algorithm to advance the solution in time from specified initial conditions using the free-surface evolution equations and the equation of motion of the body. It is in this

manner that the time-domain simulations of water-wave problems are generated. A significant restriction for the time-domain BEM is that the structures involved must possess a vertical axis of symmetry at the origin of the fluid domain – this assumption allows an essentially two-dimensional BEM to be applied to the boundary integral equations describing the problem. Black (1975), Fenton (1978) and more recently Kim & Yue (1989) describe how the boundary integral equation involving an axisymmetric structure can be reduced to a sequence of one-dimensional integral equations. Kim & Yue (1989) uses Green's theorem to give the two-dimensional boundary integral equation and the resultant one-dimensional equations can be solved by application of the BEM described by Sen (1995). Although the structure geometries are required to be axisymmetric the complete time-domain BEM code is capable of describing fully general fluid motions, not just axisymmetric motions. It should also be noted that the time domain BEM is just one of a number of different numerical solution methods – the singularity expansion method employed by Meylan & Eatock Taylor (2008) can be used to describe transient effects in scattering problems and the motion of a floating structure can be described using a Fourier transform method based on the Cummins decomposition as described in chapter 2.

## 1.2 Motivations and research topics

The development of a time-domain BEM for linearised interactions involving axisymmetric structures was motivated primarily by the desire to extend the scope of an existing time-domain code for interactions from two dimensions to three dimensions. The simulations of transient motions in two dimensions have proved valuable in investigations into resonant behaviour (McIver (2005)) and trapped mode excitation (McIver, McIver & Zhang (2003)) and given the wider relevance of three-dimensional interactions it was considered a natural progression to extend the method to include three-dimensional problems. Furthermore, not only does the BEM for two-dimensional problems provide the motivation for developing a time-domain solution algorithm for interaction problems in three dimensions, it also provides the means – the solution algorithm for problems in two dimensions is, apart from some necessary modifications, the same for structures possessing a vertical axis of symmetry. Under this assumption, the two-dimensional boundary integral equation can be reduced to a series of one-dimensional boundary integral equations by expanding the velocity potential and the normal velocity of the fluid as Fourier series in the cylindrical polar coordinate. Each boundary integral equation resultant from the Fourier series expansion possesses the same basic form as the boundary integral equation generated from the two-dimensional problem so that successive application of the previously developed BEM to each boundary integral equation (BIE) yields a three-dimensional solution after implementation of the time-stepping. An extension of the BEM to include fully general three-dimensional

structures is a much more demanding problem and was considered beyond the scope of this research. The extension of the time-domain BEM to three-dimensional problems also presents the possibility of simulating real-world interactions (as opposed to the more artificial case of two-dimensional interactions). So, although specific practical applications form only small part of the thesis the development of a code capable of simulating transient motions in three-dimensions with many possible future applications is desirable.

The time-domain simulations of wave-structure interactions are not solely obtained using the time-domain BEM solution algorithm. For example, the diffraction of a finite incident wave by a structure enclosing a portion of the free-surface is also simulated using a mechanical oscillator model. Resonant motion plays an important role in these scattering interactions and the mechanical oscillator model is used to predict the motion of the fluid enclosed by the structure (in two or three dimensions) provided a single resonant mode only is excited significantly. A considerable part of the thesis is concerned with investigations and simulations of resonant fluid and structure motions and the dynamics of resonant excitation; the application of the mechanical oscillator model is one aspect of these investigations. The model predictions are compared with results of the time-domain BEM code in order to illustrate both the successes and shortcomings of the model. It is shown that, given an accurate estimate of the location of the resonance in the complex frequency plane and *a priori* knowledge of the form of the incident wave, the model can successfully predict the time-dependent behaviour of the motion and in particular the beating phenomenon due to the interaction of two modes of a similar frequency.

The investigations into resonant motions are not limited to scattering interactions. Trapped modes are considered to be a special case of resonant motion where no damping occurs so that the motion persists for all time. Therefore, the discovery of passive trapped modes in the problem of a freely floating structure continues and extends the theme beyond the previously mentioned scattering problems. Passive trapped modes are free oscillations of the fluid which exert no force on the surrounding structure at the trapped mode frequency and can be supported by special fixed or freely floating structures referred to as passive trapping structures. A comprehensive account of how passive trapped modes relate to the sloshing and motion trapped modes discovered by McIver (1996) and McIver & McIver (2006), respectively, is provided later in the thesis. Passive trapping structures are constructed in both two and three dimensions and the three-dimensional structures possess a vertical axis of symmetry. A method for exciting these modes is outlined using frequency-domain analysis and confirmed using the results of time-domain BEM simulations.

The time-domain BEM code for structures with a vertical axis of symmetry has an important role in verifying the theory of resonant and trapped mode excitation. However,

the excitation simulations of the scattering interactions and the passive trapped mode oscillations in three dimensions involve relatively simple motions, that is axisymmetric fluid motion in the resonant scattering interactions and in the case of the passive trapped modes the vertical (heave) motion of the structure. However, as outlined in chapter 4 the time-domain BEM is developed to simulate completely general structural and fluid motions – the only restriction is on the geometry of the structures. To illustrate the full scope of the code a number of practical problems involving complex interactions are solved. The simulations include the propagation of an incident wave packet with a dominant plane wave component, the control of the motion wave-energy device by latching and the motion of a moored floating structure allowing for the cross-coupling of the modes of motion.

### 1.3 Structure of thesis

A particular structure is used in this thesis reflecting the approach taken in the underlying research. Each chapter pertains to a particular aspect of the overall investigation into time-domain simulations and problems. In some cases, such as the mechanical oscillator model of resonant motion in scattering problems and the investigation into passive trapped modes, the chapters are almost self-contained and may stand alone. Thus, separate introduction and conclusion sections are presented and some previously presented equations and ideas are repeated for clarity. This is considered the most intuitive way to describe the topics within the remit of time-domain simulations.

Chapter 2 provides a formulation of the general linearised time-domain water-wave problem for a floating structure. The relationship between the time domain (transient motions) and frequency domain (time harmonic motions) is discussed and a brief review of two alternative solution methods for time-domain water-wave problems is also given.

The BEM solution method utilised in this thesis is explained in chapter 3. This chapter contains a detailed exposition of the BEM implementation in terms of a cubic spline parameterisation of the boundary coordinates and boundary integral equation variables. The particular details of the three-dimensional BEM for a domain with a vertical axis of symmetry are explained in the context of the two-dimensional BEM to form a full, consistent and comprehensive description of the method. An outline of the time-stepping algorithm is also provided along with a brief summary of the structure of the solution code.

Chapter 4 is the final chapter directly related to the development of the BEM time-domain solution method. It contains numerous verifications of the BEM and time-stepping components of the total solution code which require some important relations between the time and frequency domain descriptions. Thereafter, chapter 5 describes

the mechanical oscillator model of resonant scattering interactions and chapter 6 contains the investigation of passive trapped modes. Finally, chapter 7 presents the results of various simulations of wave-structure interaction problems.

## **Chapter 2**

# **Time-domain equations and solution methods**

### **2.1 Time domain description of wave-structure interactions**

This study of the interaction of water waves with structures begins with a mathematical formulation of the standard water wave equations describing the fluid and structural motions. These equations can be derived from the basic fluid-flow equations, known as the Navier-Stokes equations, by a formal mathematical description of the constituent properties of the water and its flow. Thereafter, the equations of inviscid water-wave theory can be extended to include the presence of structures in the fluid domain by applying the necessary boundary conditions on the wetted surface of the structure. The estimated magnitude of the wave-motion and structural-motion amplitudes determine the best method for solving these equations. Under the small-amplitude assumption, a perturbation procedure can be used to solve these equations to an arbitrary order, in theory at least, of the wave amplitude. However, in this thesis only the first order equations are considered, i.e. the wave-structure interactions are described within the framework of the linearised water wave theory. The general theory in this section is primarily based on the comprehensive account of hydrodynamics given by Newman (1977a) while the description of the linear water-wave theory is based on that of Linton & McIver (2001). The derivation of the linearised equations for the general coupled wave-structure interaction problem is a summarised form of the relevant sections on the time-domain equations in chapter 7 of Mei (1982).

The theory of water-waves utilised in this project is based on the assumption that water is an ideal fluid. This implies that the water is assumed to be both inviscid and incompressible. The Reynolds number of the flow is assumed to be sufficiently small for

the flow to remain laminar at all times. Therefore, the assumption of zero viscosity will be accurate in the main body of the fluid. The parameters characterising the waves and structure dimensions are assumed to be such that the viscous losses at the surface of the structures are negligible, i.e. the wave-structure interactions will occur in the inviscid regime. Under all but the most extreme pressures and (variations in) temperatures water is accurately approximated as being incompressible. The approximation of water as an ideal fluid accurately describes its behaviour in many physical situations and flow regimes. By applying these simplifying assumptions concerning the material properties of water to the Navier-Stokes and continuity equation, simpler equations to describe wave motions in water can be derived. These equations will accurately model the behaviour of the fluid in the flow regimes mentioned above.

The continuity equation and the Navier-Stokes equation are given by

$$\frac{D\rho}{Dt} + \rho \nabla \cdot \mathbf{v} = 0 \quad (2.1)$$

and

$$\frac{D\mathbf{v}}{Dt} = -\frac{1}{\rho} \nabla p + \nu \nabla^2 \mathbf{v} - \nabla(gz) \quad (2.2)$$

respectively, where  $\mathbf{v}$  is the fluid velocity,  $p$  is the pressure in the fluid,  $\nu$  is the kinematic viscosity of the fluid,  $\rho$  is the density of the fluid and  $g$  is the acceleration due to gravity.

The operator  $\frac{D}{Dt}$  is the convective derivative and is defined by

$$\frac{D}{Dt} = \frac{\partial}{\partial t} + (\mathbf{v} \cdot \nabla) = \frac{\partial}{\partial t} + u \frac{\partial}{\partial x} + v \frac{\partial}{\partial y} + w \frac{\partial}{\partial z}, \quad (2.3)$$

where the velocity vector has the components  $(u, v, w)$ . In the equations above, a Cartesian coordinate system is adopted to describe positions and the orientation of the coordinate system is such that the  $z$ -axis points vertically upwards. The interface between water and air is called the *free surface*. When the water is in the undisturbed state the free surface is at the *Still Water Level* (SWL) defined as  $z = 0$ . Apart from the pressure of the air above the water at the free surface, which is assumed constant even when the free surface departs from the SWL, the dynamics and kinematics of the air motion are of no concern. This is physically justifiable because the density of air compared to water is quite small and so any waves generated locally by winds have relatively small amplitudes.

For an incompressible fluid  $\rho$  will be constant and uniform so that  $\frac{D\rho}{Dt} = 0$  and the continuity equation then simplifies to

$$\nabla \cdot \mathbf{v} = 0. \quad (2.4)$$

The kinematic viscosity is taken to be zero because of the inviscid assumption regarding the fluid, and therefore, the Navier-Stokes equation for an ideal fluid, known as the

Euler equation, is written

$$\frac{D\mathbf{v}}{Dt} = -\frac{1}{\rho} \nabla p - \nabla(gz) . \quad (2.5)$$

Using the vector identity  $\mathbf{v} \times (\nabla \times \mathbf{v}) \equiv \frac{1}{2} \nabla(v^2) - (\mathbf{v} \cdot \nabla)\mathbf{v}$ , the Euler equation becomes

$$\frac{\partial \mathbf{v}}{\partial t} + \frac{1}{2} \nabla v^2 - \mathbf{v} \times (\nabla \times \mathbf{v}) + \nabla \left( \frac{p}{\rho} + gz \right) = 0 . \quad (2.6)$$

The equations (2.4) and (2.6) can be simplified further by assuming the fluid motion is irrotational. Mathematically this assumption is expressed as

$$\nabla \times \mathbf{v} \equiv 0 \quad (2.7)$$

and this implies that the fluid velocity can be written as the gradient of a velocity potential  $\Phi(x, y, z, t)$ , i.e.  $\mathbf{v} = \nabla\Phi(x, y, z, t)$ . Hence Euler's equation can be re-expressed as

$$\nabla \left( \frac{\partial \Phi}{\partial t} + \frac{1}{2} (\nabla \Phi)^2 + \frac{p}{\rho} + gz \right) = 0 \quad (2.8)$$

or equivalently

$$\frac{\partial \Phi}{\partial t} + \frac{1}{2} (\nabla \Phi)^2 + \frac{p}{\rho} + gz = F(t) \quad (2.9)$$

where  $F(t)$  is an arbitrary function of time. This last equation is known as the non-stationary version of Bernoulli's equation and the arbitrary function of time  $F(t)$  can be removed from the equations by redefining the potential as

$$\tilde{\Phi} = \Phi + \int^t \left( -F(\tau) + \frac{p_a}{\rho} \right) d\tau . \quad (2.10)$$

In this equation  $p_a$  is the (constant) pressure of air at the free-surface. This redefinition of the potential does not alter the physical behaviour of the flow because  $\mathbf{v} = \nabla\Phi$  is invariant under the transformation  $\tilde{\Phi} \rightarrow \Phi$  and so Bernoulli's equation can be reformulated with  $\tilde{\Phi}$  instead of  $\Phi$ . The reformulated Bernoulli equation is

$$\frac{\partial \tilde{\Phi}}{\partial t} + \frac{1}{2} (\nabla \tilde{\Phi})^2 + \frac{p - p_a}{\rho} + gz = 0 \quad (2.11)$$

and henceforth the tilde notation is dropped because of the physical equivalence of the potentials.

By imposing the condition that the fluid motion is irrotational, the continuity equation (2.4) and Navier-Stokes equation (2.2) can be simplified to

$$\begin{aligned} \nabla^2 \Phi &= 0 , \\ \frac{\partial \Phi}{\partial t} + \frac{1}{2} (\nabla \Phi)^2 + \frac{p - p_a}{\rho} + gz &= 0 , \end{aligned} \quad (2.12)$$

which determine the kinematics and dynamics of the fluid motion respectively. Both of these equations hold throughout the fluid domain. The assumption of irrotational motion simplifies the mathematical description of the wave motion in water significantly by allowing the problem to be expressed in terms of a potential function. In many branches of physics waves are described in terms of a potential function and thus a significant number of solution methods and mathematical constructs involving wave-potentials have been developed previously. However, the presence of the free surface adds an additional degree of complexity to the water-wave problem and distinguishes it from other wave theories.

Boundary conditions on the free surface and on the bottom surface are required to complete the formulation. No boundary conditions relating to the tangential flow or tangential stresses are appropriate on either surface because the water is assumed inviscid. In the general case where the bottom surface is described by  $z = -h(x, y)$  for  $h(x, y) > 0$ , the no-flow condition on this surface is written

$$\mathbf{n} \cdot \nabla \Phi = 0 \quad \text{on } z = -h(x, y), \quad (2.13)$$

where  $\mathbf{n}$  is the unit normal to the bottom surface. A normal stress condition is not required on the sea bottom; in contrast, both *kinematic* and *dynamic* (normal) boundary conditions are specified on the free surface. The kinematic boundary condition specifies that the boundary remains intact only if particles on the free surface move with the velocity of the free surface. Mathematically, this is expressed as

$$\frac{D}{Dt} (z - \eta(x, y, t)) = 0 \quad \text{on } z = \eta(x, y, t) \quad (2.14)$$

and using the definition of the convective derivative (2.3), this can be rewritten as

$$\frac{\partial \Phi}{\partial z} = \frac{\partial \eta}{\partial t} + \frac{\partial \Phi}{\partial x} \frac{\partial \eta}{\partial x} + \frac{\partial \Phi}{\partial y} \frac{\partial \eta}{\partial y} \quad \text{on } z = \eta(x, y, t). \quad (2.15)$$

The dynamic free-surface condition specifies the pressure at the free-surface to be equal to the atmospheric pressure ( $p = p_a$ ) and assuming the wavelengths involved are sufficiently large to neglect surface tension, application of Bernoulli's equation on this boundary yields

$$\frac{\partial \Phi}{\partial t} + \frac{1}{2}(\nabla \Phi)^2 + gz = 0 \quad \text{on } z = \eta(x, y, t). \quad (2.16)$$

With the boundary conditions now formulated in addition to the governing equations

of motion, it is possible to present the full set of general water-wave equations:

$$\nabla^2 \Phi = 0 \quad \text{in the fluid,} \quad (2.17)$$

$$\mathbf{n} \cdot \nabla \Phi = 0 \quad \text{on } z = -h(x, y), \quad (2.18)$$

$$\frac{D}{Dt}(z - \eta) = 0 \quad \text{on } z = \eta(x, y, t), \quad (2.19)$$

$$\frac{\partial \Phi}{\partial t} + \frac{1}{2}(\nabla \Phi)^2 + gz = 0 \quad \text{on } z = \eta(x, y, t). \quad (2.20)$$

Solving Laplace's equation for  $\Phi$  and ensuring it satisfies the boundary conditions yields a valid solution to these equations. The pressure in the fluid is determined from Bernoulli's equation (2.11) if required. In the case where structures are present in the fluid, another no-flow boundary condition holds on the surface of the structure. This condition is similar to the boundary condition on the sea-bed, except that in general the structure's surface will not be fixed. Assuming that the velocity of a general point  $r$  on the surface is given by  $\mathbf{V}(r, t)$  then  $\Phi$  satisfies

$$\frac{\partial \Phi}{\partial n} = \mathbf{V} \cdot \mathbf{n} \quad \text{on } \Gamma \quad (2.21)$$

where  $\Gamma$  is the wetted surface of the structure. The velocity of the structure is determined by applying the conservation of linear and angular momentum to the motion of the structure. The resultant equations for the conservation of linear momentum and the conservation of angular momentum  $\mathbf{L} = \mathbf{X} \times (m\omega \times \mathbf{X})$  with respect to the centre of rotation  $\mathbf{X}$  are

$$M\ddot{\mathbf{x}}_c = \iint_{\Gamma} p\mathbf{n} dS - Mge_3 + \mathbf{F} \quad (2.22)$$

and

$$\iiint \rho(\mathbf{x} - \mathbf{X}) \times \ddot{\mathbf{x}} dV = \iint_{\Gamma} (\mathbf{x} - \mathbf{X}) \times p\mathbf{n} dS + (\mathbf{x}_c - \mathbf{X}) \times (-Mge_3) + (\mathbf{T} + \mathbf{F} \times \mathbf{X}) \quad (2.23)$$

where  $M$  is the mass of the body,  $p$  is the fluid pressure,  $e_3$  is a unit vector in the vertical direction,  $\mathbf{x}_c$  is the position of the centre of mass relative to the origin and  $\mathbf{F}$  and  $\mathbf{T}$  are, respectively, the external force and torque due to mooring constraints and applied forces. The density of the body is assumed to be uniform and the total volume of the body is denoted  $V_b$ . A full explanation of these equations is given in Mei (1982); it is more important in the context of this thesis to give a detailed consideration to the linearised form of these equations, as will be done next.

Before simplifying the equations describing the wave-structure interaction so that they are in tractable form, it is useful to describe the domain of the problem. Thus, the surface of the sea-bed and the structure surface should be specified. The water surrounding the structure is assumed here to have constant finite-depth  $h$  in the absence of waves, so that the sea bed is described by  $z = -h$  and the normal derivative to the

boundary is  $\frac{\partial}{\partial z}$ . Thus, the boundary condition on the sea bed becomes

$$\frac{\partial \Phi}{\partial z} = 0 \quad \text{on } z = -h. \quad (2.24)$$

In this thesis the structure is assumed to have a vertical axis of symmetry so that the surface, in a body-fixed coordinate system, is best described in terms of cylindrical coordinates  $(r, \theta, z)$ . Therefore, it will be necessary in later formulations, in particular when recasting the problem in a form suitable for numerical solution, to use a cylindrical coordinate system rather than the Cartesian system. However, the origin in both coordinate systems will be the same, namely the intersection of the structures' axis of symmetry with the undisturbed free surface. Furthermore, the  $z$ -axes in both coordinate systems coincide with the axis of symmetry of the structure. For a given time  $t$ , the boundary surfaces of the domain will be described as

$$\begin{aligned} F : \quad & z = \eta(x, y, t) \quad -\infty < x, y < \infty, \quad (x, y) \notin W_{\Gamma}(t) \\ B : \quad & z = -h \quad -\infty < x, y < \infty, \\ \Gamma : \quad & G((x^2 + y^2)^{1/2}, z, t) = 0 \quad z \leq 0, \end{aligned} \quad (2.25)$$

where  $F$ ,  $B$ ,  $\Gamma$  denote the free-surface, the sea-bed and the wetted surface of the structure respectively. The notation  $W_{\Gamma}(t)$  is used to denote the domain of the free-surface occupied by the structure and  $G(r, z, t) = 0$  implicitly defines the instantaneous position of the surface of the structure. This definition is for non-bulbous and non-wall-sided structures only and for the derivations which follow it is assumed here that the instantaneous position of  $\Gamma$  can be written as  $z = f(x, y, t)$ .

### 2.1.1 Small-amplitude approximation

The general wave-structure interaction problem is a very complex problem, even with the assumptions that water is an ideal fluid and that the motion is irrotational. This complexity derives from the combination of the nonlinearity in the free-surface conditions (2.14) and (2.16), and the application of these conditions, in addition to the body boundary conditions, on boundaries which change in time. In the most general interaction problem the floating structure is free to respond to incident waves and may be subjected to mooring and externally applied forces. Since the reacting forces on the structure depend on the motion of the structure itself, the structure, the constraint and the surrounding water are dynamically coupled in the presence of incident waves. In order to simplify this problem, the amplitudes of any waves generated are assumed to be small in some sense. This assumption must hold throughout the fluid including near any boundaries and hence the motion of the floating structure must be such that any generated waves also have small amplitudes. Therefore, a restriction on the amplitudes of the structural motions also exists. The small-amplitude assumption is implemented

mathematically with a perturbation expansion in the dynamic quantities describing the wave motion, as will be shown next. The conditions on the moving boundaries will be significantly simplified after the application of the perturbation expansion and the linearised water-wave equations will be obtained by considering only the first order equations in  $\varepsilon$ .

If certain physical scales of motion are expected prior to the solution of the wave-structure interaction problem, it is possible to introduce non-dimensional parameters based on these scales to classify the problem. If  $\lambda$  is the wavelength and  $k = \frac{2\pi}{\lambda}$  is the wavenumber then the length of the waves relative to the depth of the water can be expressed via the parameter  $kh$ . Furthermore, if  $A$  is the expected amplitude of the waves (for the problem of a structure free to respond to an incident wave, the amplitude scale will be the incident wave amplitude) then the parameter  $\varepsilon = kA$ , the wave slope, expresses the height of the waves relative to the wavelength. The small-amplitude assumption is then defined by the relation  $\varepsilon \ll 1$  and is equivalent to the assumption that the wave motion is just a small disturbance of the still water state. Thus, the quantities describing the wave motion,  $\Phi$  and  $\eta$ , can be approximated as perturbation series expansions in terms of the wave slope:

$$\begin{aligned}\Phi(x, t) &= \varepsilon\Phi^{(1)}(x, t) + \varepsilon^2\Phi^{(2)}(x, t) + \dots, \\ \eta(x, y, t) &= \varepsilon\eta^{(1)}(x, y, t) + \varepsilon^2\eta^{(2)}(x, y, t) + \dots.\end{aligned}\quad (2.26)$$

Since the free-surface waves  $z = \eta(x, y, t)$  are just small disturbances from the still water plane  $z = 0$ , any quantities evaluated on the boundary can be determined using a Taylor expansion about  $z = 0$ . For example, the evaluation of a general function  $F(x, y, z, t)$  on the time-dependent boundary  $z = \eta(x, y, t)$  can be simplified in the following manner:

$$\begin{aligned}F(x, y, \eta, t) &= F(x, y, 0, t) + \eta \left[ \frac{\partial F}{\partial z} \right]_{z=0} + \dots \\ &= F + \frac{\partial F}{\partial z} (\varepsilon\eta^{(1)} + \varepsilon^2\eta^{(2)} + \dots) + \dots, \quad \text{on } z = 0, \\ &= F + \varepsilon\eta^{(1)} \frac{\partial F}{\partial z} + O(\varepsilon^2), \quad \text{on } z = 0,\end{aligned}\quad (2.27)$$

so that it becomes a power series with coefficients evaluated on the still water free surface  $z = 0$ . Therefore, it is possible to simplify the free-surface conditions (2.15) and (2.16) to conditions on the static boundary  $z = 0$ , although in this case it will also be necessary to expand  $\Phi$  (or one of its derivatives) in powers of  $\varepsilon$ .

The perturbation scheme adopted to solve the coupled motion problem is a powerful method for finding approximate solutions to non-linear differential equations. However, it is not a rigorous method and there are some important intrinsic assumptions that should be recognised. Firstly, the existence of a solution is assumed — it cannot be

guaranteed. Furthermore, the convergence of the perturbation series solution is also not guaranteed *a priori*. Finally, and most importantly for the present problem, it is assumed that the equations requiring solution, after substitution of the perturbation series, will be satisfied at every order of the perturbation parameter. Thus, each order of  $\varepsilon$  can be considered separately. The expansion of the general water-wave equations (2.17) governing the motion of the fluid is considered first. Laplace's equation becomes

$$\varepsilon \nabla^2 \Phi^{(1)} + \varepsilon^2 \nabla^2 \Phi^{(2)} + \dots = 0 \quad (2.28)$$

under the perturbation scheme and must be satisfied at each order of  $\varepsilon$  within the fluid. The boundary condition on the sea-bed becomes

$$\varepsilon \frac{\partial \Phi^{(1)}}{\partial z} + \varepsilon^2 \frac{\partial \Phi^{(2)}}{\partial z} + \dots = 0 \quad \text{on } z = -h \quad (2.29)$$

and the free-surface conditions, following the substitution of the expansions (2.26) and the Taylor expansion about the SWL, become

$$\varepsilon \left( \eta_t^{(1)} - \Phi_z^{(1)} \right) + O(\varepsilon^2) = 0 \quad (2.30)$$

and

$$\varepsilon \left( \Phi_t^{(1)} + g\eta^{(1)} \right) + O(\varepsilon^2) = 0 \quad (2.31)$$

with both equations evaluated on the SWL  $z = 0$ . In order to obtain the linearised description of the interaction problem only the set of first order equations is required.

The small-amplitude assumption also requires the motions of the structure to be small so that any generated waves also satisfy  $\varepsilon \ll 1$ . Therefore we expect body motions to be at most of the same order as the wave slope  $\varepsilon$ . The perturbation expansion method can then be applied to the kinematic (2.21) and dynamic (2.22) body boundary conditions. The kinematic condition can be rewritten as

$$\frac{\partial \Phi}{\partial n} = \mathbf{V} \cdot \mathbf{n} \quad \text{on } z = f(x, y, t), \quad (2.32)$$

assuming the instantaneous position of the structure is described  $z = f(x, y, t) = f^{(0)}(x, y) + \varepsilon f^{(1)}(x, y, t) + O(\varepsilon^2)$ . The structures involved in the wave-interactions are assumed to have a vertical axis of symmetry and to be half-immersed in the water when in static equilibrium. Therefore, when the body is at rest the centre of rotation  $Q$  and the centre of mass  $C$  will coincide at the origin of the coordinate system (at the intersection of the axis of symmetry and the still water level). The coordinate of the centre of rotation can be expanded in a perturbation series as follows

$$\mathbf{X} = \mathbf{X}^{(0)} + \varepsilon \mathbf{X}^{(1)} + O(\varepsilon^2). \quad (2.33)$$

where the rest position  $\mathbf{X}^{(0)}$  is at the origin. The linearised translational and rotational

displacements of the structure are respectively denoted  $\varepsilon \mathbf{X}^{(1)}(t) = (\varepsilon\xi, \varepsilon\chi, \varepsilon\zeta)$  and  $\varepsilon\Theta(t) = (\varepsilon\alpha, \varepsilon\beta, \varepsilon\gamma)$ , with the angular displacements measured relative to the  $x$ ,  $y$  and  $z$  axes. Since the displacement amplitude is small, it is possible to expand the body boundary condition about the undisturbed body surface  $\Gamma^{(0)}$ , that is,  $z = f^{(0)}(x, y)$ . Therefore, to express the boundary condition (2.32) in terms of a power series expansion in  $\varepsilon$ , the substitution of the perturbation series expansions for the velocity potential, the prescribed velocity and the surface equation of the body is necessary.

The linearised body motions, described by  $\mathbf{X}^{(1)}$  and  $\Theta$ , are obtained by simplifying the equations of motion (2.22) and (2.23) using similar perturbation expansions methods. A detailed description of this method for general structures is provided in Mei (1982) § 7.2.2 and § 7.2.3. Nonetheless, a more specific description is included here also because the symmetry of the structure and the assumption of the coincidence of the centres of rotation and mass significantly simplifies the derivation of these equations of motion. The kinematic condition on the boundary of the structure simplifies to

$$\begin{aligned}\varepsilon \mathbf{n} \cdot \nabla \Phi^{(1)} + O(\varepsilon^2) &= \varepsilon \dot{\mathbf{X}}^{(1)}(t) \cdot \mathbf{n} + \varepsilon((\mathbf{x} - \mathbf{X}^{(0)}) \times \mathbf{n}) \cdot \Theta(t) + O(\varepsilon^2) \\ &= \varepsilon(\xi(t) \cdot \mathbf{n} + \mathbf{x} \times \mathbf{n} \cdot \Theta(t)) + \varepsilon^2\end{aligned}\quad (2.34)$$

where  $\mathbf{x}$  is a position measured relative to the origin of the fixed coordinates and  $\mathbf{X}^{(0)} = \mathbf{0}$ . The right hand-side of this equation can be expressed using generalised vectors containing six terms corresponding to the translational and rotational modes. The generalised displacement and normal vectors are

$$\begin{aligned}\{X_\nu\}^T &= \{\xi, \chi, \zeta, \alpha, \beta, \gamma\} \\ \{n_\nu\}^T &= \{n_1, n_2, n_3, n_3y - n_2z, n_1z - n_3x, n_2x - n_1y\}\end{aligned}\quad (2.35)$$

where the last three elements of  $\{n_\nu\}$  are the elements of  $\mathbf{x} \times \mathbf{n}$ . Therefore, the linearised kinematic boundary condition on the structure surface can be expressed in the following compact form

$$\frac{\partial \Phi^{(1)}}{\partial \mathbf{n}} = \sum_{\nu=1}^6 \dot{X}_\nu n_\nu. \quad (2.36)$$

Thus, the kinematic condition on the structure surface has been linearised.

Linearising the dynamic structure conditions (2.22) requires the substitution of a number of different expansions. These include the position (2.33) of the centre of rotation, the pressure  $p$  consisting of a hydrostatic part  $-\rho g z$  and a hydrodynamic part  $-\varepsilon p \Phi_t^{(1)} + O(\varepsilon^2)$  and the external force (or torque) which will be composed of a static part  $\mathbf{F}^{(0)}$  and a dynamic part  $\varepsilon \mathbf{F}^{(1)} + O(\varepsilon^2)$ . The position of the centre of mass  $\mathbf{x}_c$  must also be expressed in terms of the position of the centre of rotation  $\mathbf{X}$  and is given by

$$\mathbf{x}_c = \varepsilon(\mathbf{X}^{(1)} + \Theta \times (\bar{\mathbf{x}}_c - \mathbf{X}^{(0)})) \quad (2.37)$$

where positions in the body coordinate system are denoted by  $\bar{\mathbf{x}} = (\bar{x}, \bar{y}, \bar{z})$ . However, the centres of mass and rotation coincide at the origin when the body is at rest so the expression for the centre of mass  $\mathbf{x}_c$  is simply  $\varepsilon \mathbf{X}^{(1)}$ . Therefore, it is straightforward to show that the translational equation of motion for the body in the first order of  $\varepsilon$  is

$$M\ddot{\mathbf{X}}^{(1)} = -\rho \iint_{S_B^{(0)}} \frac{\partial \Phi^{(1)}}{\partial t} \mathbf{n} dS - Mge_3 + \mathbf{F}^{(1)}. \quad (2.38)$$

The zero-order equation in the absence of a constant applied force is  $Mg = \rho g V^{(0)}$  which is just Archimedes principle, where  $V^{(0)}$  is the static submerged volume.

The derivation of the linearised equation of motion for the rotational displacements requires more investigation. In particular, it is important to account for the difference between the body and fixed coordinate systems as the angular momentum is conserved relative to the centre of rotation of the body. As mentioned above, positions in the body coordinate system will be denoted  $\bar{\mathbf{x}}$  and the moments of inertia will be calculated in terms of these coordinates. Positions measured in the fixed coordinate system are related to the body coordinate system by

$$\mathbf{x} = \bar{\mathbf{x}} + \varepsilon \left[ \mathbf{X}^{(1)} + \Theta \times (\bar{\mathbf{x}} - \mathbf{X}^{(0)}) \right] + O(\varepsilon^2). \quad (2.39)$$

as was assumed in equation (2.37). To obtain the inertial term in the equation of motion, the following relations obtained using (2.33) and (2.39):

$$\ddot{\mathbf{x}} = \varepsilon \left[ \ddot{\mathbf{X}}^{(1)} + \ddot{\Theta} \times (\bar{\mathbf{x}} - \mathbf{X}^{(0)}) \right] + O(\varepsilon^2), \quad (2.40)$$

where  $\bar{\mathbf{x}}$  is fixed in time, and

$$\mathbf{x} - \mathbf{X} = \bar{\mathbf{x}} - \mathbf{X}^{(0)} + \varepsilon \left[ \Theta \times (\bar{\mathbf{x}} - \mathbf{X}^{(0)}) \right] + O(\varepsilon^2). \quad (2.41)$$

are substituted into equation (2.23). Given that  $\mathbf{X}^{(0)} = \mathbf{0}$  the inertial term in the equation of motion then becomes

$$\epsilon \left\{ \iiint_{V_b} \bar{\mathbf{x}} \times \ddot{\mathbf{X}}^{(1)} \rho dV + \ddot{\Theta} \rho \iiint_{V_b} \bar{\mathbf{x}}^2 dV - \left[ \ddot{\Theta}^{(1)} \cdot \rho \iiint_{V_b} \bar{\mathbf{x}} \right] \bar{\mathbf{x}} dV + O(\varepsilon^2) \right\}. \quad (2.42)$$

The first term on the right hand side of (2.23) vanishes under the assumption that the structure has rotational symmetry about the vertical axis. The combination of the second and third terms equals the diagonal component of the moment of inertia tensor, denoted  $\{I_{11}, I_{22}, I_{33}\}$ . The rotational equation of motion (2.23) also has three other terms to consider: the hydrodynamic torque; the buoyancy torque; the gravitational torque and the external/applied torque. Both the hydrodynamic and buoyancy torque arise from the expansion of the pressure in terms of  $\varepsilon$ . Considering the first order term in  $\varepsilon$  and utilising the generalised normal, the components of the hydrodynamic torque

are

$$-\varepsilon \iint_{S_B^{(0)}} \rho \Phi_t^{(1)} n_\alpha dS + O(\varepsilon^2), \quad \alpha = 4, 5, 6 \quad (2.43)$$

where  $S_B^{(0)}$  is the waterplane area of the static body. The torque due to applied forces and constraints is expanded as  $\varepsilon(\mathbf{T}^{(1)} + \mathbf{F}^{(0)} \times \mathbf{X}^{(1)}) + O(\varepsilon^2)$ . The gravitational torque is zero due to the coincidence of the centre of mass and the centre of rotation when the body is at rest. Each component of the buoyancy term must be considered separately and it is shown in Mei (1982) that the  $x$  and  $y$  components of the buoyancy term are

$$-\varepsilon \rho g [\alpha(I_{22}^A + I_3^V)] \quad (2.44)$$

and

$$-\varepsilon \rho g [-\beta(I_{11}^A - I_3^V)] \quad (2.45)$$

where  $I_3^V = \iiint_{V^{(0)}} z dV$  is  $z$ -component of the centre of buoyancy and  $I_{11}^A = \iint_{S_A^{(0)}} x^2 dS$  with a similar definition for  $I_{22}^A$ . The integration for the centre of buoyancy occurs over the static submerged volume of the body and for the moments of the waterplane area the integration occurs over the static waterplane area. It is interesting to note that some structures may not be *statically stable*, i.e. the waterplane moment and the centre of buoyancy are such that the buoyancy torque does not oppose small angular displacements of the body. The  $z$ -component of the buoyancy term is zero.

It is now possible to quote the first order equations of motion for the rotational modes of the floating structure. Rather than quoting them all, only the equation corresponding to pitch (the  $y$ -component of  $\Theta$ ) will be presented. For a body with a rotational symmetry about a vertical axis in the presence of incident waves, the pitch motion will describe completely the rotational motion of the body. The roll term is essentially symmetric and the yaw term does not contribute as it involves rotation about the axis of symmetry. Therefore, the rotation of the body is described by the equation

$$I_{22} \ddot{\beta} = -\rho \iint_{S_B^{(0)}} \Phi_t^{(1)} n_5 dS - \rho g \beta (I_{11}^A - I_3^V) + T_2^{(1)} + F_3^{(0)} \xi - F_1^{(0)} \zeta. \quad (2.46)$$

Thus, the equations of motion have now all been considered in terms of the perturbation expansion of the dynamic quantities and the exact form of the equations have been determined to  $O(\varepsilon)$ , i.e. the interaction has been linearised.

The linearised theory of wave-structure interactions is a very simple and effective description of many wave-phenomena. It has been widely experimentally verified for

interactions involving waves of small amplitudes. The linearised equations are

$$\begin{aligned}
 \nabla^2 \Phi &= 0 && \text{in the fluid,} \\
 \frac{\partial \Phi}{\partial n} &= 0 && \text{on } z = -h, \\
 \frac{\partial \Phi}{\partial t} + g\eta &= 0 && \text{on } z = 0, \\
 \frac{\partial \Phi}{\partial z} - \frac{\partial \eta}{\partial t} &= 0 && \text{on } z = 0, \\
 \frac{\partial \Phi}{\partial n} &= \sum_{\nu=1}^6 \dot{X}_\nu n_\nu && \text{on } \Gamma,
 \end{aligned} \tag{2.47}$$

where the superscripts have been dropped from  $\Phi^{(1)}$ ,  $\eta^{(1)}$  etc., in the interests of brevity and where  $\Gamma$  refers to the still water position of the wetted body surface. To fully formulate the initial value problem, it is necessary to assign initial conditions to the velocity potential. Furthermore, a far-field condition is also required in order to ensure that the solution has finite energy. Assuming the motion starts from rest, the two initial conditions for  $\Phi$  are

$$\Phi(\mathbf{x}, 0) = \frac{\partial \Phi}{\partial t}(\mathbf{x}, 0) = 0 \tag{2.48}$$

and the finite energy condition is

$$\nabla \Phi \rightarrow 0 \quad \text{as} \quad (x^2 + y^2)^{1/2} \rightarrow 0 \tag{2.49}$$

for any fixed time. It is clear that the domain of the linearised problem is much simpler than for the general water-wave problem. For future reference, it is useful to redefine the boundaries as

$$\begin{aligned}
 F: \quad &z = 0, \quad -\infty < x, y < \infty, \quad (x, y) \notin W \\
 B: \quad &z = -h, \quad -\infty < x, y < \infty, \\
 \Gamma: \quad &G((x^2 + y^2)^{1/2}, z) = 0 \quad z \leq 0,
 \end{aligned} \tag{2.50}$$

where the equation  $G((x^2 + y^2)^{1/2}, z) = 0$  defines the static position of the structure and  $W$  the static waterplane area.

The coupled problem is completed by the inclusion of the linearised equations of motion for the structures translational and rotational displacements. An exact specification of the external forces and torques will result in a fully specified problem. In this project, the structure is assumed to be free to respond to waves subject to a mooring constraint and may also be subject to a possibly non-linear applied force or torque. The mooring constraint is envisaged as a system of springs and dampers, described respectively by the constant coefficient matrices  $k_{\mu\nu}$  and  $\gamma_{\mu\nu}$ . The time-varying applied force is generalised to include the rotational modes and is denoted  $F_\mu$ . Therefore, the generalised equation

of motion is

$$M_{\mu\mu} \ddot{X}_\mu = -\rho \iint_{\Gamma} \frac{\partial \Phi}{\partial t} n_\mu dS - \sum_{\nu=1}^6 [c_{\mu\nu} X_\nu(t) + \gamma_{\mu\nu} \dot{X}_\nu] + F_\mu(t), \quad \mu = 1, \dots, 6 \quad (2.51)$$

where  $M_{\mu\mu}$  are the diagonal elements of mass matrix for the structure, i.e.  $M_{\mu\mu} = M$  for  $\mu = 1, 2, 3$  and  $M_{\mu\mu} = I_{\mu-3,\mu-3}$  for  $\mu = 4, 5, 6$ . The initial generalised displacements  $X_\mu$  and velocities  $\dot{X}_\mu$  of the body must be specified for all modes  $\mu = 1, \dots, 6$  in order to solve the equation. The effect of the buoyancy and the mooring springs are included in the term  $c_{\mu\nu} = \rho g b_\mu \delta_{\mu\nu} + k_{\mu\nu}$  with the term  $b_\mu$  accounting for the buoyancy effect. It is non-zero for the heave, roll and pitch modes only and these terms are  $b_3 = W$ ,  $b_4 = I_{22}^A + I_3^V$  and  $b_5 = I_{11}^A + I_3^V$  respectively. Thus, the coupled equations of motion for a floating structure subjected to some constraint forces have been derived. Different computational methods have been developed to solve these equations numerically and it is useful to review these methods before describing the particular one chosen for this project.

## 2.2 Review of time-domain models

Analytical solutions of the linearised time-domain equations for a coupled-motion or forced-motion problems are very rare. In fact, only a small number of analytic time-domain solutions have been obtained (see the papers by Kennard (1949), McIver (1994)) for structures with simple geometries. Therefore, a variety of numerical methods have been developed to solve initial-value time-domain wave-structure interaction problems. It is important to consider the method used in this project, referred to as the boundary element method, in the context of alternative approaches and these will be examined next. Before discussing these time-domain solution methods the frequency domain description of wave-structure interactions must be examined as it forms an integral part of the time-domain methods. The Fourier transform enables the time and frequency domain quantities to be related and the frequency domain forces and potentials have important roles in the development of the numerical time-domain solution methods. This can be partly attributed to the fact that, in the past, analytical or semi-analytical solutions to linearised water-wave problems were more easily obtained in the frequency domain given that the assumption of time-harmonic motion results in a significant simplification of the interaction equations. Therefore, it was natural to develop time-domain solutions based on frequency domain results and the Fourier transform relation between the domains.

### 2.2.1 Frequency domain definitions

Linearised water-wave problems were first investigated in the frequency domain wherein all motions are assumed to be time-harmonic and to have begun from  $t = -\infty$ . The time-dependence can be removed in a straightforward manner by substituting for the potential and any structural motions using

$$\begin{aligned}\Phi(\mathbf{x}, t) &= \operatorname{Re}\{\phi(\mathbf{x}, \omega)e^{-i\omega t}\} \\ V(\mathbf{x}, t) &= \operatorname{Re}\{v(\mathbf{x}, \omega)e^{-i\omega t}\}\end{aligned}\quad (2.52)$$

and this results in a considerable simplification of the problem. The complex amplitudes of the dynamic quantities vary with frequency and by removing the time-dependence the governing equations and boundary conditions will feature these terms only. However, McIver et al. (2003) have shown that the frequency-domain potential can also be defined using the following operations on the time-domain solution:

- take a Laplace transform of the time-domain potential

$$\hat{\phi}(\mathbf{x}, s) = \int_0^\infty \Phi(\mathbf{x}, t)e^{-st} dt, \quad \operatorname{Re} s > 0; \quad (2.53)$$

- apply the change of variables  $s = -i\omega$  so that

$$\phi(\mathbf{x}, \omega) = \hat{\phi}(\mathbf{x}, -i\omega). \quad (2.54)$$

- noting that  $\phi(\mathbf{x}, -\omega) = \bar{\phi}(\mathbf{x}, \omega)$ , the inverse Fourier transform is given by

$$\Phi(\mathbf{x}, t) = \frac{1}{2\pi} \int_{-\infty}^{\infty} \phi(\mathbf{x}, \omega)e^{-i\omega t} d\omega = \frac{1}{\pi} \operatorname{Re} \int_0^\infty \phi(\mathbf{x}, \omega)e^{-i\omega t} d\omega \quad (2.55)$$

where the path of integration must pass over any singularities of  $\phi$  that lie on the real axis and it has been assumed that there is no motion prior to  $t = 0$ , i.e.  $\Phi(\mathbf{x}, t) = 0$  for  $t < 0$ .

If  $\omega$  is real then  $\phi(\mathbf{x}, \omega)$  is just the frequency domain potential. By the principle of causality, which precludes the existence of the response before the cause so that  $\Phi(\mathbf{x}, t) = 0$  for  $t < 0$ , no singularities can exist in  $\operatorname{Im} \omega > 0$ . Therefore, if it is assumed that no singularities exist on the real axis the inverse transform will integrate the frequency-domain potential over the full range of  $\omega$ . With this approach, the frequency-domain equations are obtained by applying the Fourier transform to the time-dependent equations. However, unlike the equations resulting from the assumptions (2.52) of time-harmonic motion from  $t = -\infty$ , the initial conditions will be present in the frequency-domain equations arising from the Fourier transformation. Although, the latter equations are more mathematically consistent it is usual to set all

initial conditions to zero before attempting to solve the equations even if this is not the case. Nevertheless, in the frequency-domain analysis of resonances in coupled motion problems McIver (2005) retains the initial condition terms in the equation of motion for the structure and obtains some important results regarding the resonant behaviour of the motion. Therefore, the retention of the initial condition terms depends on the application of the subsequent equations.

Many analytical and approximate solutions exist for frequency-domain problems involving structures with simple geometries. Thus, in the simplest frequency-domain radiation and diffraction problems it is possible to completely determine the velocity potential analytically. The hydrodynamic forces, which are crucial in the context of marine engineering, can then be calculated directly from the potential. For more general geometries this is not possible and the hydrodynamic forces must be computed using numerical methods. Nevertheless, it is useful to consider the analytical expressions for the various potentials and forces in the frequency-domain problem. In a linearised coupled motion problem, it is customary to decompose the total velocity potential into a scattering potential  $\phi^S$  and a radiation potential  $\phi^R$ . Thus, the coupled motion problem will require the solution of the radiation problem and the scattering problem. The radiation potential can be further decomposed into a sum over the six modes of motion so that the total frequency domain potential is

$$\phi = \phi^S + \sum_{\mu} v_{\mu} \phi_{\mu} \quad (2.56)$$

where  $v_{\mu}$  is the complex amplitude of the generalised velocity in the  $\mu$  direction and  $\phi_{\mu}$  describes the fluid response due to the forced oscillations in mode  $\mu$  with unit velocity amplitude. The velocities in each mode will be determined from the frequency domain equation of motion for the body. However, this requires the computation of the radiation and exciting forces on the structure. Therefore, it is necessary to consider the radiation problem prior to the coupled motion equation. It is first important to note that, for a given mode  $\mu$  the boundary condition on the structure will be

$$\frac{\partial \phi_{\mu}}{\partial n} = n_{\mu}, \quad (2.57)$$

because the total velocity is

$$v(\omega) = \sum_{\mu} v_{\mu} n_{\mu} \quad (2.58)$$

where  $n_{\mu}$  is the  $\mu$  component of the generalised normal and  $v_{\mu}$  is the component of the generalised complex velocity amplitude in this direction. The hydrodynamic force on the structure in the  $\mu$  direction due to the fluid response to the forced oscillations is

$$F_{\mu}^R = i\omega\rho \iint_{S_B} \phi^R n_{\mu} dS \quad (2.59)$$

and the force due to the diffraction of an incident wave by the fixed structure is

$$F_\mu^S = i\omega\rho \iint_{S_B} \phi^S n_\mu dS \quad (2.60)$$

where the time-dependence has been removed in both cases. By expressing the radiation potential as a sum over the individual modes, the radiation force can be written as  $\sum_\nu v_\nu f_{\nu\mu}$  where

$$f_{\nu\mu} = i\omega\rho \iint_{\Gamma} \phi_\nu n_\mu dS. \quad (2.61)$$

It is conventional to decompose the radiation force into a term featuring the added mass matrix  $a_{\alpha\beta}$  and a term featuring the damping matrix  $b_{\alpha\beta}$  as follows

$$f_{\beta\alpha} = i\omega(a_{\beta\alpha} + \frac{ib_{\beta\alpha}}{\omega}) \quad (2.62)$$

where the added mass and damping coefficients are in phase with the acceleration and velocity respectively. These real quantities depend only on the geometry of the structure and the oscillation frequency  $\omega$  and describe many of the properties of the structure. In particular, (as will be shown later) if the variation of these coefficients with frequency is known then we can predict the resonant behaviour of the structure in the time-domain as well as the frequency domain. The computation of these quantities was considered to be very important in marine engineering and naval architecture and so a variety of different computer codes were developed to compute the coefficients efficiently. The boundary element method forms the basis of most of the computer code algorithms, the most widely-used example being WAMIT (see <http://www.wamit.com>) which determines frequency domain solutions for prescribed structures and structure motions.

### 2.2.2 Frequency-domain equation of motion

The radiation force coefficients also play a significant role in determining the motion of a floating structure possibly subject to mooring and applied forces. To obtain the correct equation of motion in the frequency domain it is important to adopt the approach similar to that taken by McIver (2005), i.e. keep the initial condition terms in the Fourier transform operations. Therefore, if the Fourier transform of the velocity is  $v_\mu(\omega)$  then the Fourier transform of the acceleration is given by

$$\int_0^\infty \ddot{X}_\mu(t) e^{i\omega t} dt = -i\omega v_\mu(\omega) - V_\mu(0) \quad (2.63)$$

the time-derivative of the potential obeys a similar relation

$$\int_0^\infty \frac{\partial \Phi}{\partial t} e^{i\omega t} dt = -i\omega \phi_\mu(\omega) - \Phi(x, 0). \quad (2.64)$$

Therefore, the initial conditions of the structure ( $X_\mu(0)$ ,  $V_\mu(0)$ ) and of the potential  $\Phi(\mathbf{x}, 0)$  will be present in the Fourier transform of the equation motion which will be referred to as the frequency-domain equation of motion. If the frequency domain potential is decomposed in the same manner as before (2.56) then the Fourier transform of the equation of motion (2.51) for the structure is

$$M[-V_\mu(0) - i\omega v_\mu(\omega)] = -\rho \iint_{\Gamma} (-\Phi(\mathbf{x}, 0)) n_\mu dS + F_\mu^S(\omega) + i\omega \sum_{\nu} (f_{\mu\nu}(\omega) + i\gamma_{\mu\nu}/\omega) v_\nu(\omega) - \sum_{\nu} c_{\mu\nu} \frac{v(\omega) + X(0)}{-i\omega} + f_\mu^A(\omega) \quad (2.65)$$

for  $\mu = 1, \dots, 6$ , where  $f_\mu^A(\omega)$  is the Fourier transform of the applied force  $F_\mu(t)$  in equation (2.51). Although it is assumed that  $\Phi(\mathbf{x}, t) = 0$  for  $t < 0$ , for a non-zero initial velocity  $\lim_{t \rightarrow 0^-} \Phi(\mathbf{x}, t) \neq 0$  because of the impulsive pressure on the free-surface resulting from the initial motion of the pressure. Therefore, the first term on the right-hand side of the above equation is not identically zero, rather is given by

$$\rho \iint_{\Gamma} (-\Phi(\mathbf{x}, 0)) n_\mu dS = a(\infty) V(0) \quad (2.66)$$

(see Mei, Stiassnie & Yue (2005), § 8.12.1) where  $a(\infty) = \lim_{\omega \rightarrow \infty} a(\omega)$  is the infinite frequency added mass.

The frequency-domain equation is usually re-expressed in the following form

$$\begin{aligned} & \sum_{\nu} \{c_{\mu\nu} - \omega^2 [M_{\mu\mu}\delta_{\mu\nu} + a_{\mu\nu}(\omega) + i(b_{\mu\nu} + \gamma_{\mu\nu})/\omega]\} v_\nu(\omega) \\ &= -i\omega [F_\mu^S(\omega) + f_\mu^A(\omega) + (M_{\mu\mu} + a_{\mu\mu}(\infty)) V_\mu(0)] - \sum_{\nu} c_{\mu\nu} X_\nu(0) \end{aligned} \quad (2.67)$$

for  $\mu = 1, \dots, 6$ . If it is assumed that the structure can only move in one mode of motion and that there is no incident wave or applied force then the complex velocity will be given by

$$v_\mu(\omega) = \frac{-i\omega(M_{\mu\mu} + a_{\mu\mu}(\infty)) V_\mu(0) - c_{\mu\mu} X_\mu(0)}{c_{\mu\mu} - \omega^2 [M_{\mu\mu} + a_{\mu\mu}(\omega) + i(b_{\mu\mu} + \gamma_{\mu\mu})/\omega]}. \quad (2.68)$$

As described by McIver & McIver (2006), the zero of the denominator gives the location of the pole referred to as the motion resonance. The complex force coefficient  $f_{\mu\nu}(\omega)$  will also possess a pole, however this resonance is annulled by the frequency-dependence of the complex velocity (see § 6 of McIver & McIver (2006)) and so the motion, in the absence of incident waves, is dominated by the motion resonance term. Solving equation (2.68) for  $v(\omega)$  then the time-domain velocity can be recovered using the inverse transform

$$V(t) = \frac{1}{\pi} \operatorname{Re} \int_0^\infty v(\omega) e^{-i\omega t} dt. \quad (2.69)$$

### 2.2.3 Integro-differential equation method

The widespread availability of numerical and analytical methods for determining hydrodynamic coefficients in the frequency domain facilitated the development of a solution method for the motion of a floating body in the time domain. The principles of this method are described by Mei (1982) in §7.11 based on work by Cummins (1962) and Wehausen (1971) among others. The method requires the consideration of the fluid response to a displacement given impulsively to a structure denoted by  $\delta(t - \tau)V_\alpha(\tau)$  where  $\dot{X}_\alpha = V_\alpha$ . The resultant impulse response functions for the velocity potential and the hydrodynamic force are written as the sum of an infinite frequency component and a time-dependent component using the Cummins' decomposition. To obtain the fluid response to a general continuous velocity function  $V_\alpha(t)$  an integral of the impulse response over the range  $-\infty < \tau < \infty$  must be calculated. The hydrodynamic force on the structure due to the forced motion of the structure is then shown to be

$$\mathcal{F}_\beta^R(t) = -m_{\beta\alpha}(\infty)\ddot{X}_\alpha - \int_{-\infty}^t L_{\beta\alpha}(t - \tau)\ddot{X}_\alpha(\tau) d\tau \quad (2.70)$$

where  $m_{\beta\alpha}(\infty)$  is an infinite frequency added mass coefficient and  $L_{\beta\alpha}(t - \tau)$  is referred to as the impulse response function. By considering the velocity of the body to be time-harmonic, i.e.  $V_\alpha(t) = \text{Re}\{v_\alpha e^{-i\omega t}\}$ , the impulse response function  $L_{\beta\alpha}$  can be related to the added mass and damping coefficients by comparing the force expression (2.70) to (2.59). The comparison yields the following relations

$$\begin{aligned} a_{\alpha\beta} - m_{\alpha\beta}(\infty) &= \int_0^\infty L_{\alpha\beta}(\tau) \cos \omega \tau d\tau \\ b_{\alpha\beta} &= \omega \int_0^\infty L_{\alpha\beta}(\tau) \sin \omega \tau d\tau \end{aligned} \quad (2.71)$$

and so if the added mass or damping coefficients are known for all frequencies  $0 \leq \omega \leq \infty$ , the impulse response or memory function  $L_{\alpha\beta}(t)$  can be found by inverse cosine or sine transform. Therefore, it is possible to determine the radiation force due to a non-harmonic forcing by using frequency-domain information. The exciting force can also be determined in a similar manner; to obtain it the incident wave-form and the radiation impulse response function are required.

By expressing the total hydrodynamic force in terms of the radiation force (2.70) and the exciting force, the equation of motion (2.51) for transient motions of a floating structure becomes

$$[M_{\alpha\beta} + m_{\alpha\beta}(\infty)]\ddot{X}_\beta + \int_{-\infty}^t L_{\beta\alpha}(t - \tau)\ddot{X}_\alpha(\tau) d\tau + c_{\alpha\beta}X_\beta = \mathcal{F}_\alpha^D + F_\mu(t), \quad (2.72)$$

for  $\alpha = 1, \dots, 6$ , where repeated indices implies summation. This set of integro-differential equations is to be solved given the position and velocity of the body. It

is assumed that the impulse response function and infinite frequency added mass are known from Fourier transforms of the frequency domain hydrodynamic coefficients. Thus, it is possible, in principle, to calculate the transient response of a floating structure from the frequency-domain responses. Numerically, an accurate calculation of transient response requires that the hydrodynamic coefficients be computed at a large number of discrete values of the frequency  $\omega$  on the interval  $[0, \infty)$ . This time-domain solution method has been in use since the work by Cummins and Wehausen. As numerical methods and computing power have improved, more complex problems can be solved to a higher degree of accuracy. A recent application of the method can be found in the investigations into latching control by Babarit & Clément (2006). The principal drawback of the application of this method is that the motion of the fluid cannot be determined from the computational results. Therefore, if the fluid response is required, for example in the investigation of trapped modes, further computations are necessary.

#### 2.2.4 Generalised eigenfunction expansion method

The singularity expansion method (SEM) is based on a general scattering theory for general wave problems and has been adapted by Hazard (2000) and Meylan & Eatock Taylor (2008) to problems in hydrodynamics and hydro-elasticity. The central concept in the theory is to express the governing equations for the scattering problem in terms of an evolution equation involving a unitary operator and to use the generalised eigenfunctions and eigenfrequencies of this operator to give an approximation to the time-domain solution of the scattering problem. To give a brief overview of the method the scattering equations must be re-expressed using a harmonic lifting operator  $\mathbf{B}$  which maps a function defined on the free-surface onto the total fluid domain. This harmonic lifting operator is denoted by  $\mathbf{B}$  so that  $\mathbf{B}\Psi = \Phi$  where  $\Psi = \Phi$  on the free-surface  $F$ . If  $D$  denotes the total fluid domain, then potential  $\Phi$  satisfies

$$\nabla^2\Phi = 0 \quad \text{in } D, \tag{2.73}$$

$$\frac{\partial\Phi}{\partial n} = 0 \quad \text{on } \partial D, \tag{2.74}$$

$$\Phi = \Psi \quad \text{on } F \tag{2.75}$$

where  $\partial D$  includes the bed and the structure surface. The Dirichlet to Neumann map  $\partial_n \mathbf{B}$  defined by

$$\partial_n \mathbf{B}\Psi = \frac{\partial\Phi}{\partial z}, \quad x \in F, \tag{2.76}$$

then recovers the corresponding normal derivative to  $\Psi$  on the free surface.

The evolution equation

$$i\frac{\partial U}{\partial t} = \mathcal{A}U \tag{2.77}$$

accounts for the linear time-dependent free-surface equations using the vector

$$\mathbf{U} = \begin{pmatrix} \Psi \\ -i\eta \end{pmatrix}, \quad (2.78)$$

with  $\eta$  denoting the time-dependent free-surface elevation, and the operator  $\mathcal{A}$  which is both unitary and self-adjoint given by

$$\mathcal{A} = \begin{pmatrix} 0 & g \\ \partial_n \mathbf{B} & 0 \end{pmatrix} \quad (2.79)$$

A self-adjoint operator will possess an entirely real spectrum and the generalised eigenfunctions  $\mathbf{u} = (\psi, -i\zeta)^T$ , which are non-trivial solutions of

$$\mathcal{A}\mathbf{u} = \omega\mathbf{u}, \quad (2.80)$$

are just frequency-domain scattering solutions. (On a technical note, the word ‘generalised’ precedes eigenfunction because the energy is unbounded.) This can be shown easily by combining the scalar equations resulting from (2.80) so as to give the frequency-domain free-surface condition. For a given frequency  $\omega$ , the free-surface condition in three-dimensions is satisfied by waves from an infinite number of directions and so for each  $\omega$  there is an infinite set of eigenfunctions  $\mathbf{u}_n = (1, \omega/g)^T \psi_n(\mathbf{x}, \omega)$ , with the  $n^{th}$  eigenfunction corresponding to incident waves of the form  $J_n(kr)e^{in\theta}$ . The general solution of the time-evolution equation is, from spectral theory,

$$\mathbf{U}(\mathbf{x}, t) = \int_{-\infty}^{\infty} \left[ \sum_n f_n(\omega) \mathbf{u}_n(\mathbf{x}, \omega) \right] e^{-i\omega t} d\omega \quad (2.81)$$

where  $f_n(\omega)$  is determined by the initial conditions now expressed as  $\mathbf{U}(\mathbf{x}, 0)$ . To obtain this expression for  $f_n(\omega)$ , apply the energy inner product to (2.81) evaluated at  $t = 0$ . The eigenfunctions satisfy the orthogonality condition

$$\langle \mathbf{u}_m(\mathbf{x}, \omega), \mathbf{u}_n(\mathbf{x}, \omega') \rangle_E = \Lambda_m(\omega) \delta_{mn} \delta(\omega - \omega') \quad (2.82)$$

where  $\langle \cdot \rangle_E$  denotes a special energy inner product (defined with a  $\mathcal{H}$  subscript by Meylan & Eatock Taylor (2008)) and it can be shown that

$$\Lambda_m(\omega) = \frac{4\pi\omega^2}{gk} \frac{d\omega}{dk}. \quad (2.83)$$

Therefore, it is straightforward to show that

$$f_n(\omega) = \frac{1}{\Lambda_n(\omega)} \langle \mathbf{U}(\mathbf{x}, 0), \mathbf{u}_n(\mathbf{x}, \omega) \rangle_E. \quad (2.84)$$

by evaluating the energy inner product  $\langle \mathbf{U}(\mathbf{x}, 0), \mathbf{u}_n(\mathbf{x}, \omega) \rangle_E$  using the orthogonality

relation (2.82) and the definition (2.81). This expression can be further simplified using the definition of the energy product but details will not be provided here. Instead, it should be noted that an analytic expression for the general solution has been obtained. Thus, for a given scattering problem it is in theory possible to obtain the motion of the free-surface and the potential on the free-surface.

The singularity expansion method involves moving the path of integration in (2.81) in the  $\omega$ -plane across the singularities in the lower half plane  $\text{Im } \omega \leq 0$  using the method of contour integration. Thus, the general solution will consist of contributions from the poles, any branch cuts, the path at infinity and the remainder of the path located below the poles in the  $\omega$ -plane. As explained by Hazard (2000), the contributions from infinity are assumed to be identically zero and the contribution from the remainder of the path decays faster than the pole contributions. Given that the contribution from the branch cuts are thought to be significant only for very large times an approximation to the general solution can be obtained for medium and large  $t$  because the contributions from the poles dominate for this range of times. Therefore, the SEM requires a knowledge of the pole structure of the integrand to approximate the complete integral. Furthermore, the behaviour of the eigenfunctions in the vicinity of the poles must be known in order to compute the residue of each pole. The scattering potential will satisfy

$$(I + T(\omega))\phi^S = g_I \quad (2.85)$$

where the form of the operator  $T(\omega)$  depends on the solution method chosen and  $g_I$  is determined by the incident wave. Given  $g_I$ , the scattered field is

$$\phi^S = (I + T(\omega))^{-1}g_I \quad (2.86)$$

and the pole structure of  $\phi_S$  will be inherited from the operator  $(I + T(\omega))^{-1}$ , referred to as the resolvent. In the case where the resolvent operator is approximated by a matrix, it can be shown that the potential has the form

$$\phi_n(x, \omega) \sim \frac{a_{nj}v_j(x)}{\omega - \omega_j} \text{ as } \omega \rightarrow \omega_j \quad (2.87)$$

in the vicinity of the pole. The poles themselves are determined by locating values of  $\omega$  in the lower complex plane where the resolvent is not invertible. Thus,  $v_j$  is a generalised eigenfunction of  $A_{j0} = I + T(\omega_j)$ . The integral in equation (2.81) can be approximated by closing the integration path in the lower half plane and then moving the integration path across a finite number of  $P$  poles and summing over the contributions of these poles. As described by Hazard (2000), any branch cuts in the complex  $\omega$ -plane will only be significant at very large times and the integrals at infinity are expected to be zero. Therefore, the contribution of the  $P$  poles closest to the real- $\omega$  axis (and hence with the smallest decay rates  $e^{-Im(\omega_j)}$ ) will dominate in the medium term. So, after

neglecting other contributions to the integral and using (2.87) to determine the residues of the poles, the potential on the free-surface will be given by

$$\Psi(\mathbf{x}, t) \approx -2\pi \sum_j \left[ \sum_n f_n(\omega_j) \alpha_{nj} \right] v_j(\mathbf{x}, 0) e^{-i\omega_j t}. \quad (2.88)$$

Although full details of how this expression can be evaluated are not given here, examples of applications of this method are given by Eatock-Taylor & Meylan (2007), Meylan & Eatock Taylor (2008) and Meylan (2002). Each of these papers also contain more detailed instructions regarding the computational aspects of the method, such as determining the locations of the poles. Hazard (2000) notes that the SEM is a non-rigorous method and requires some heuristic arguments to justify its use. However, in the specific cases considered the results are generally accurate for a large range of times and much frequency-domain information regarding resonances is inherent in the time-domain solution. At present, the method only applies to scattering problems; however, it is hoped that it can be extended to radiation and coupled motion problems. It is not clear how the forces on the structure will be determined.

### 2.3 BEM and time-marching model

In the next chapter a full description of the boundary element method coupled with a time-advancement algorithm will be provided. It suffices to say that this method is quite different to the previous time-domain models given that it does not require the frequency-domain solutions in order to obtain the time-dependent behaviour of the solution. It is also based on principles that can be applied to non-linear water wave equations. The outline of the method is as follows:

- simplify the boundary integral equation;
- apply the boundary element discretisation using cubic splines;
- implement the time-advancement algorithm.

Each of these steps will be considered in detail in the next chapter.

## **Chapter 3**

# **Boundary element method – theory**

### **3.1 Introduction**

In this chapter, the numerical solution algorithm for the linearised floating body interaction in three dimensions is described. The first part of the algorithm requires the formulation of the linearised water-wave equations describing the motion of the structure and fluid in terms of a boundary integral equation (BIE). Thereafter, this two-dimensional BIE is transformed into a series of one-dimensional BIEs. Both the derivation of the BIE and its subsequent transformation are presented here. The discretisation of the transformed BIE is achieved by a boundary element method (BEM) and the main facets of the computer implementation of this method are described later in the chapter. In addition, the time-stepping algorithm used, in conjunction with the BEM, to simulate the evolution of the wave motion is outlined. Some of the details of the Fortran implementation will also be described, with emphasis placed on some of the difficulties that were encountered.

### **3.2 Boundary integral equation**

The fluid response to the motion of a structure is described, within the linear theory, by the boundary-value problem (2.47). This problem can also be formulated as a boundary integral equation where the integrals are computed over the boundary surfaces. In two-dimensional problems, the BIE can be discretised using a BEM like that described by Sen (1995). In general three-dimensional problems, the BEM becomes significantly more complex. Among the problems posed by the BEM in three-dimensions is the difficulty in approximating the boundary geometries and the increase in computational

power necessary to solve the resultant system of linear equations. However, for axisymmetric structures it is possible to reduce the boundary integral equation to an infinite series of integral equations each of which involves only line integrals. These integral equations can then be solved using the BEM in two-dimensions.

The fundamental equation of the boundary integral equation method (BIEM) is derived from Green's second identity which is a powerful relation from vector calculus with many useful applications in water wave theory. For a closed domain  $\Omega$  bounded by a surface  $\partial\Omega$ , the identity is

$$\iiint_{\Omega} (\psi \nabla^2 \phi - \phi \nabla^2 \psi) dV = \iint_{\partial\Omega} \left( \psi \frac{\partial \phi}{\partial n} - \phi \frac{\partial \psi}{\partial n} \right) dS, \quad (3.1)$$

where  $\phi$  and  $\psi$  are twice continuously-differentiable functions on  $\Omega$ . If  $\psi$  and  $\phi$  are harmonic, i.e. satisfy Laplace's equation, on  $\Omega$  then the relation

$$\iint_{\partial\Omega} \left( \psi \frac{\partial \phi}{\partial n} - \phi \frac{\partial \psi}{\partial n} \right) dS = 0 \quad (3.2)$$

is obtained. It is customary for  $\psi$  to be replaced by the free-space Green's function, which in three-dimensional space is

$$G(\mathbf{x}; \mathbf{x}') = -\frac{1}{4\pi|\mathbf{x} - \mathbf{x}'|} \quad (3.3)$$

where  $\mathbf{x}$  is the field point and  $\mathbf{x}'$  the source point over which the integrals are taken. In this case, it is necessary to introduce another boundary surface excluding the singularity at  $\mathbf{x}' = \mathbf{x}$  to ensure the assumptions regarding the harmonic nature of  $\psi$  and  $\phi$  still hold. The integral excluding the singularity contributes a single additional term to the Green's theorem equation (3.2) in the limit as the radius of this surface approaches zero. (Details of this method are described in § 4.11 of the book by Newman (1977a).)

The fundamental equation of the BIEM

$$\alpha(\mathbf{x})\Phi(\mathbf{x}, t) - \int_{\partial\Omega} \Phi(\mathbf{x}', t) \frac{\partial G}{\partial n}(\mathbf{x}, \mathbf{x}') dS + \int_{\partial\Omega} G(\mathbf{x}, \mathbf{x}') \frac{\partial \Phi}{\partial n}(\mathbf{x}', t) dS = 0 \quad (3.4)$$

is then obtained by substituting the time-domain (three-dimensional) velocity potential  $\Phi(\mathbf{x}, t)$  for the function  $\phi$ . The term  $\alpha(\mathbf{x})\Phi(\mathbf{x}, t)$  is due to the singularity in the Green's function and the value of  $\alpha(\mathbf{x})$  depends on the position of the field point  $\mathbf{x}$  as follows

$$\alpha(\mathbf{x}) = \begin{cases} \frac{\beta(\mathbf{x})}{4\pi} & \mathbf{x} \in \partial\Omega, \\ 0 & \mathbf{x} \notin \Omega, \\ 1 & \mathbf{x} \in \Omega, \end{cases} \quad (3.5)$$

where  $\beta(\mathbf{x})$  is the solid angle subtended by the tangent to the surface at  $\mathbf{x}$ . The evaluation of  $\alpha(\mathbf{x})$  is straightforward at points where the surface is continuous as  $\beta(\mathbf{x}) = 2\pi$ ;

however, care must be taken where the various continuous surface segments intersect.

In the linearised wave-structure interaction boundary-value problem described in § 2.1.1, the fluid domain  $\Omega$  is bounded by the surfaces (2.50) and is of infinite horizontal extent. In order to obtain a numerical solution of the boundary-value problem it is convenient to truncate the fluid domain because the discretisation of the boundary and the subsequent collocation of the integral equation on the discretised boundary will yield a finite system of linear equations. Obtaining a solution is then a straightforward numerical problem. Thus, finite bounds are imposed on the fluid domain and the necessary truncation is achieved by enclosing the structure and surrounding fluid in a vertical circular cylindrical, whose axis coincides with the axis of symmetry of the structure. The curved surface of this cylinder between the sea-bed and undisturbed free-surface defines the last boundary surface of the closed domain  $\Omega$ . Mathematically, the control surface is defined by  $P = \{(r, \theta, z) : r = L, -h < z < 0\}$  and the boundary of the fluid domain  $\partial\Omega$  is now  $F \cup \Gamma \cup P \cup B$ . Appropriate boundary conditions must be placed on this control surface to ensure the numerical solution returns physically consistent results. For example, if the control surface is envisaged as a rigid wall then unphysical reflections will occur at this artificial boundary thus invalidating the computational results. A typical method to prevent these reflection involves introducing an “absorption beach” or damping zone in the vicinity of the control surface and applying piston absorption boundary conditions on the control surface. These methods are discussed by McIver et al. (2003) and the numerical implementation will be described later.

Before using the axisymmetric nature of the fluid domain to reduce the BIE (3.4) to a more tractable form, one immediate simplification is possible. It was noted previously that simplifying the BIE for the time-domain water-wave problem by altering the Green's function so as to satisfy the time dependent boundary conditions is difficult. Nevertheless, for a domain of constant finite depth, the bottom boundary is described by  $z = -h$  and the no-flow condition on this boundary (2.24) is not explicitly time-dependent. Therefore, by augmenting the free-space Green's function (3.3) with an image source term the normal derivative of the Green's function is also zero on the sea-bed. Thus, the integral over that same surface in (3.4) will vanish. Henceforth, the Green's function notation  $G(\mathbf{x}, \mathbf{x}')$  will refer to source and image-source Green's function

$$G(\mathbf{x}, \mathbf{x}') = -\frac{1}{4\pi} \left( \frac{1}{|\mathbf{x} - \mathbf{x}'|} + \frac{1}{|\mathbf{x} - \tilde{\mathbf{x}}'|} \right), \quad (3.6)$$

where  $\tilde{\mathbf{x}}' = (\mathbf{x}', \mathbf{y}', z - 2h)$ , rather than the free-space function on its own. Thus, the bottom boundary will not feature in the BIEM and the notation for the domain boundary  $\partial\Omega$  will refer to the surfaces  $F$ ,  $\Gamma$  and  $P$  only.

### 3.2.1 Simplifications due to rotational symmetry

All the boundary surfaces of the fluid domain  $\Omega$  are axisymmetric, i.e. they are surfaces of revolution about the  $z$ -axis. Therefore, these surfaces and also the velocity potential and Green's function in the BIE are most naturally expressed in terms of cylindrical polar coordinates  $(r, \theta, z)$ . The expansion of the velocity potential and Green's function as Fourier series in  $\theta$  and the subsequent evaluation of the  $\theta$  component of the surface integrals reduces the two-dimensional boundary integral equation to a series of integral equations involving one-dimensional integrals. This method was first adopted by Black (1975) to obtain the frequency-domain wave forces on a body that is scattering an incident wave and developed further by both Fenton (1978) and Kim & Yue (1989) with the latter authors considering second order diffraction. The approach outlined by Kim & Yue (1989) is adopted here for the case of linear time-domain water-wave problems because they use Green's theorem to generate the boundary integral equation rather than the source distribution method which is used by the other authors mentioned above. Also, the computations for a general Fourier mode are considered by Kim & Yue (1989) whereas the previous authors limit numerical examples to the first two modes which relate to wave forces only. Before demonstrating the method of simplification, a general integral over an axisymmetric surface is considered. If the surface  $S$  can be described by rotating the contour  $C$  in the  $(r, z)$  plane around the  $z$ -axis then

$$\iint_S f(r, \theta, z) dS = \int_C \int_0^{2\pi} r f(r, \theta, z) d\theta dl. \quad (3.7)$$

Assuming that separation of variables can be applied to the integrand so that  $f(r, \theta, z) = \tilde{f}(r, z)g(\theta)$ , then the double integral in (3.7) can be reduced to

$$\int_0^{2\pi} g(\theta) d\theta \int_C r \tilde{f}(r, z) dl \quad (3.8)$$

which can be further simplified provided  $g(\theta)$  is known. This is the basic method used to separate the  $\theta$  integral from the integrals along the  $(r, z)$  contours in the reduction procedure for the BIE (3.4).

To simplify equation (3.4), the velocity potential and Green's function are first expanded as Fourier cosine series in the azimuthal angles  $\theta$  and  $\theta - \theta'$  respectively,

$$\Phi(r, \theta, z, t) = \sum_{m=0}^{\infty} \phi_m(r, z, t) \cos m\theta \quad (3.9)$$

$$G(r, \theta, z; r', \theta', z') = \sum_{m=0}^{\infty} \frac{\varepsilon_m}{2\pi} G_m(r, z; r', z') \cos m(\theta - \theta'), \quad (3.10)$$

where  $\Phi$  is the total velocity potential and  $\varepsilon_0 = 2$  and  $\varepsilon_m = 1$  otherwise. Implicit in

the expansion of  $\Phi$  in terms of even functions of  $\theta$  is the assumption that the motion of the structure or the diffraction of the incident waves will be such that the total fluid velocity will be symmetric about  $\theta = 0$ . This assumption requires the alignment of the  $x$ -axis along the direction of the incident wave in the diffraction problem. A similar argument can be applied to the Green's function regarding symmetry about  $\theta = \theta'$  after observing that it can be rewritten in the form

$$G(\mathbf{x}, \mathbf{x}') = -\frac{1}{4\pi} \left( \frac{1}{(R^2 + (z - z')^2)^{\frac{1}{2}}} + \frac{1}{(R^2 + (z + z' + 2h)^2)^{\frac{1}{2}}} \right) \quad (3.11)$$

where  $R^2 = (r \cos \theta - r' \cos \theta')^2 + (r \sin \theta - r' \sin \theta')^2 = r^2 + r'^2 - 2rr' \cos(\theta - \theta')$ . Furthermore, on the axisymmetric surfaces where

$$\frac{\partial}{\partial n} = n_r \frac{\partial}{\partial r} + n_z \frac{\partial}{\partial z}, \quad (3.12)$$

both  $\frac{\partial \Phi}{\partial n}$  and  $\Phi$  (or  $G$  and  $\frac{\partial G}{\partial n}$ ) will have the same symmetry with respect to  $\theta = 0$  (or  $\theta = \theta'$ ). This enables the integrals over  $\theta'$  and over the contours in the  $(r, z)$  planes to be evaluated independently, as outlined above.

To illustrate the method by which the complete integral equation (3.4) is simplified, the term  $\iint_S \Phi(\mathbf{x}', t) \frac{\partial G}{\partial n}(\mathbf{x}, \mathbf{x}') dS$  will be evaluated by substituting the equations (3.9) and (3.10) into the integrand. In this integral, the surface  $S$  can be any portion of the total axisymmetric surface  $\partial\Omega$ . The integral is calculated as follows:

$$\begin{aligned} & \iint_S \Phi(\xi, t) \frac{\partial G}{\partial n}(\mathbf{x}, \xi) dS = \\ & \int_C \int_0^{2\pi} \left[ \sum_{k=0}^{\infty} \phi_k(r', z', t) \cos k\theta' \sum_{m=0}^{\infty} \frac{\varepsilon_m}{2\pi} \frac{\partial G_m}{\partial n}(r, z; r', z') \cos m(\theta - \theta') r' d\theta' \right] dl' \\ & = \sum_{k=0}^{\infty} \sum_{m=0}^{\infty} \frac{\varepsilon_m}{2\pi} \int_C r' \frac{\partial G_m}{\partial n}(r, z; r', z') \phi_k(r', z', t) dl' \int_0^{2\pi} \cos m(\theta - \theta') \cos k\theta' d\theta'. \end{aligned} \quad (3.13)$$

Therefore, the particular integral term under consideration satisfies the following equation

$$\iint_S \Phi(\mathbf{x}', t) \frac{\partial G}{\partial n}(\mathbf{x}, \mathbf{x}') dS = \sum_{m=0}^{\infty} \cos m\theta \int_C r' \left\{ \phi_m(r', z', t) \frac{\partial G_m}{\partial n}(r, z; r', z') \right\} dl' \quad (3.14)$$

given that the integral over the polar coordinate can be simplified to give

$$\int_0^{2\pi} \cos m(\theta - \theta') \cos k\theta' d\theta' = \frac{2\pi}{\varepsilon_k} \delta_{mk} \cos k\theta \quad (3.15)$$

where  $\delta_{mk}$  is the Kronecker delta symbol.

Applying a similar method to the other integral terms, equation (3.4) can be rewritten as:

$$\Phi(r, \theta, z, t)\alpha(\mathbf{x}) = \sum_{m=0}^{\infty} \cos m\theta \int_C r' \left\{ \phi_m(r', z', t) \frac{\partial G_m}{\partial n}(r, z; r', z') - \frac{\partial \phi_m}{\partial n}(r', z', t) G_m(r, z; r', z') \right\} dl' \quad (3.16)$$

and hence the  $m^{th}$  azimuthal mode of the total potential satisfies the equation

$$\phi_m(r, z, t)\alpha(\mathbf{x}) = \int_C r' \left\{ \phi_m(r', z', t) \frac{\partial G_m}{\partial n}(r, z; r', z') - \frac{\partial \phi_m}{\partial n}(r', z', t) G_m(r, z; r', z') \right\} dl', \quad m = 0, 1, 2, \dots \quad (3.17)$$

Given the axisymmetric nature of the domain,  $\alpha(\mathbf{x}) = \frac{\beta(\mathbf{x})}{4\pi}$  evaluates to  $\frac{1}{2}$  at points where the boundary surface is continuous and at points of discontinuity it evaluates to the interior angle between the tangents to the cross-sectional boundary  $C$  at  $\mathbf{x}$ , analogous to the BEM applied on a two-dimensional fluid domain. Furthermore, in this context  $C$  denotes the piecewise contour in the  $(r, z)$  plane which when rotated once around the axis of symmetry would generate the axisymmetric surface  $F \cup \Gamma \cup P$ . The continuous pieces of this contour line are denoted as  $C_F$ ,  $C_\Gamma$  and  $C_P$  to distinguish them from the associated *surface* boundaries which occur in the two-dimensional integral equation. Thus, the problem has been reduced to finding a set of velocity potentials  $\{\phi_m\}$  which satisfy integral equations involving only line integrals.

In order to reduce the integral equation (3.4) to the simpler form (3.16) it was necessary to expand the Green's function and velocity potential in Fourier cosine series as shown in equations (3.9) and (3.10). To solve (3.16), the  $n^{th}$  order ring source

$$G_n(r, z; r', z') = \int_0^{2\pi} G(r, z; r', z'; \cos(\theta - \theta')) \cos n(\theta - \theta') d(\theta - \theta'), \quad (3.18)$$

must be evaluated, where it has been noted from (3.11) that the Green's function has an angular dependence of the form  $G(r, z; r', z'; \cos(\theta - \theta'))$ . Furthermore the quantity  $\frac{\partial}{\partial n} G_n$  must also be evaluated on the boundaries to allow the solution of the boundary integral equation to be found. In appendix A the various representations of the ring-source potential  $G_n$  and its normal derivative are investigated with a particular focus on the asymptotics of the potential near the ring-source. These results were derived previously by Kim & Yue (1989) but it is expedient to reiterate the derivations for completeness as some of the representations are needed in the numerical evaluation of the boundary integrals.

### 3.3 Boundary element discretisation

The boundary integral equation series (3.16) can be solved numerically using a BEM suitable for two dimensional water-wave problems. The basic approach is to discretise the boundaries using a distribution of nodes and to approximate the geometry and the variation of  $\Phi$  and  $\frac{\partial\Phi}{\partial n}$  with cubic splines. By collocating the equations (3.16) on the nodes, the integral equations can be transformed into finite systems of linear algebraic equations. It is assumed that the values of potential  $\Phi$  are known on the free-surface nodes and that the normal velocity  $u = \partial\Phi/\partial n$  nodal values are known on the body and control surface boundaries. Provided some auxiliary conditions at the intersections between the boundaries are imposed, a system of linear algebraic equations with a unique solution is generated. Solving this system will yield the unknown values of  $\Phi$  and  $u = \frac{\partial\Phi}{\partial n}$  on the nodes.

Utilising cubic-splines to describe the variation of the boundary coordinates and data ( $\Phi$  and  $u$ ) enables the imposition of the continuity of velocity and potential at all boundary intersections. Consequently, the accuracy of the solution at the corners is improved relative to lower-order boundary element methods. This improves the stability and robustness of the time-stepping algorithm as the error throughout the domain will be largely uniform. Sen (1995) provides an in-depth discussion on the improvement in solution accuracy at the corners due to the implementation of a cubic-spline BEM instead of lower-order BEM. Also provided in this paper is a full description of the cubic spline representation and the resultant discretisation and collocation of the BIE. In this section a brief summary of the discretisation procedure is presented for a general mode of the reduced BIE series with particular emphasis on how the extra continuity conditions affect the number of equations compared to the number of unknowns. Any differences in the BEM used here compared to the algorithm described by Sen (1995) will be noted, in particular the treatment of the control surface and the introduction of ‘double nodes’ at the intersections will be described.

#### 3.3.1 Discretisation of the BIE

To describe the discretisation of the boundary integral equations (3.17), it is useful to re-state the general form of the equations and to illustrate the boundaries involved. It is assumed here that the structure is toroidal, i.e. it encloses a portion of the free-surface, although it is straightforward to modify the analysis for structures that do not enclose any free-surface. For such structures it is necessary to ensure the parameterisation of the structural boundary at the axis of symmetry describes a continuous boundary. More details are provided during the description of the cubic-spline representation. The  $n^{th}$  mode of the Fourier cosine expansion of  $\Phi$  in the azimuthal angle  $\theta$  at a particular

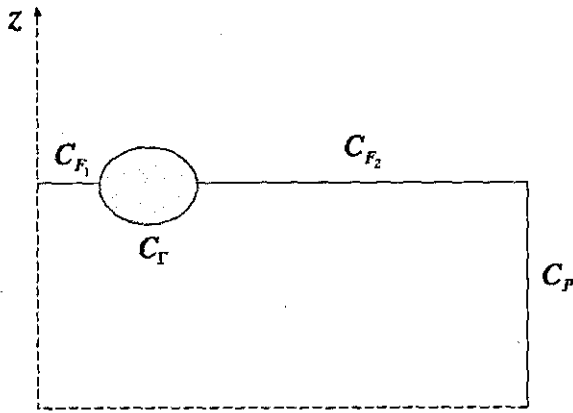


Figure 3.1: Linearised equations domain boundary in the  $r$ - $z$  plane.

time  $\tau$ :

$$\phi_n(r, z, \tau) \alpha(x) = \int_C \left( \phi_n(r', z', \tau) r' \frac{\partial G_n}{\partial n}(r, z; r', z') - \frac{\partial \phi_n}{\partial n}(r', z', \tau) r' G_n(r, z; r', z') \right) dl'. \quad (3.19)$$

The boundary contour  $C$  corresponds to the total surface of a toroidal structure in the  $r$ - $z$  plane and consists of four contiguous sections/sections each of which is geometrically continuous. These are illustrated in figure 3.1 and consist of two free-surface sections  $C_{F_1}$  and  $C_{F_2}$  and the structure and piston boundary sections  $C_T$  and  $C_P$ . For ease of reference the contours  $(C_{F_1}, C_T, C_{F_2}, C_P)$  will be referred to as  $(C_1, C_2, C_3, C_4)$ . The discretisation of the boundary is achieved by distributing a set of  $M_i$  nodal points, with a cosine spacing, on each of the continuous boundary portions so as to subdivide the portions into smaller elements. The cosine spacing ensures the nodes are concentrated near the intersection points – this improves the solution accuracy which is significantly impaired by boundary discontinuities as discussed by Sen (1995). The total number of nodes dividing the boundary into discrete elements is  $N = \sum_{i=1}^4 M_i - 3$  because of the presence of three intersection points on the boundary. The positions of the nodes are denoted  $x_j$  for  $j = 1, \dots, N$  and the  $j^{th}$  element is denoted by  $\Delta C_j$ . This nodal distribution is illustrated in figure 3.2 where the number of nodes  $M_i$  on each the boundary sections indexed  $i = 1, \dots, 4$  are also indicated. For  $N$  nodes there are  $N - 1$  elements and on each of these elements the boundary geometry and the

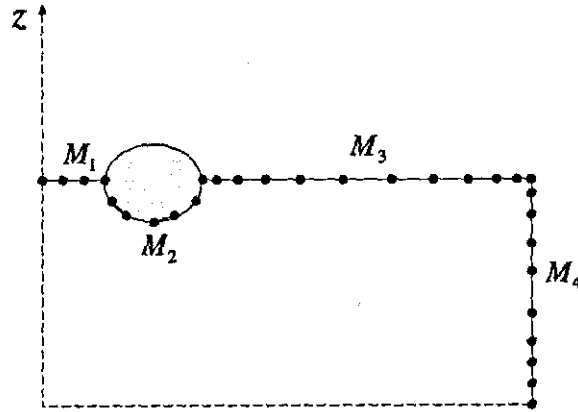


Figure 3.2: Nodal distribution on the domain boundary for a toroidal structure.

variation in  $\phi$  and  $u$  are approximated using cubic splines. Thus, for example,  $\phi$  can be represented in terms of its nodal values  $\phi_j$  and  $\phi'_j$  which is the derivative of  $\phi$  with respect to the spline parameter  $t$  calculated at node  $j$ . This representation permits the implementation of the continuity conditions for the velocity because  $\phi'_j$  is not specified *a priori* at the intersections of the boundary portions. The cubic spline approximation and the conditions necessary for a consistent representation are considered next.

On a general boundary element  $\Delta C_j$  such as that illustrated in figure 3.3, both the boundary coordinates  $(r, z)$  and the boundary variables  $(\phi, \frac{\partial \phi}{\partial n})$  are expressed in the form

$$f^j(t) = \sum_{k=0}^3 c_{kj} t^k \quad 0 \leq t \leq t_{j+1}.$$

where  $t$  is the cubic spline parameter and  $t = 0$  and  $t = t_{j+1}$  correspond to the  $j^{th}$  and  $(j+1)^{th}$  nodes respectively. The coefficients  $\{c_{kj}\}$ , for  $k = 1, \dots, 4$ , are defined from cubic spline theory (see Rogers & Adams (1989)) as

$$\begin{aligned} c_{0j} &= f_j, & c_{1j} &= f'_j \\ c_{2j} &= \frac{3}{t_{j+1}^2} (f_{j+1} - f_j) - \frac{1}{t_{j+1}} (2f'_j + f'_{j+1}) \\ c_{3j} &= \frac{2}{t_{j+1}^2} (f_j - f_{j+1}) + \frac{1}{t_{j+1}^2} (f'_j + f'_{j+1}) \end{aligned} \quad (3.20)$$

where  $f_j$  and  $f'_j$  are the values of  $f$  and its derivative with respect to  $t$  at the  $j^{th}$  node.

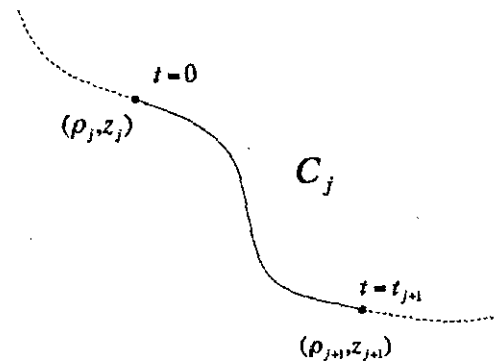


Figure 3.3: A schematic of the general element  $C_j$  with the cubic-spline parameters indicated.

The nodal values of the function  $f$  are related to the nodal values of the derivative (or slope)  $f'$  by applying continuity of curvature at each of the interior nodes in addition to some special conditions at the end nodes on a given boundary portion. Continuity of curvature condition requires that

$$\frac{d^2 f^j}{dt^2}(t_{j+1}) = \frac{d^2 f^{j+1}}{dt^2}(0), \quad j = 1, \dots, M-1, \quad (3.21)$$

i.e. the curvature of adjoining elements must match at the common node. The end conditions are necessary to determine the derivative  $f'$  with respect to the cubic spline parameter at the first and last nodes, that is the ‘end slopes’, on a given boundary portion. The conditions can be as follows:

- ‘natural/free boundary conditions’ – the function has zero curvature  $f'' = 0$  at the boundary portion ends;
- ‘clamped conditions’ – the slope of the function is specified at the ends;
- ‘mixed conditions’ – the slope has one specified end slope and one free end slope.

In the cubic-spline representation of  $\phi$  the end-slopes are assumed specified by the continuity of velocity condition. This condition does not apply at the axis of symmetry  $r = 0$  where the end-slope of  $\phi$  depends on the Fourier mode under consideration. In all modes except the surge mode,  $n = 1$ , the tangential velocity (and hence the end-slope) is zero and so the specification is straightforward. However, for  $n = 1$  the end slope is not generally zero and a free end condition is used. Therefore, a mixed end slope

condition exists for  $\phi$  on the first boundary portion in mode  $n = 1$ . No particular conditions need be applied on the slope of the normal velocity at the intersections so in all cases natural end conditions are applied. Similarly, the boundary coordinates are assumed to have natural end conditions except in the case of a cylindrical structure where the derivative  $dz/dt$  with respect to the spline parameter must be zero to preclude the existence of a cusp in the structure geometry.

The combination of the continuity of curvature and the relevant end conditions on a given boundary portion  $C_p$  yields matrix equations relating the derivative nodal values to the function nodal values. The potential and the normal derivative evaluated on the  $j^{th}$  node of the boundary portion  $C_p$  are denoted  $\phi_{p,j}$  and  $u_{p,j}$ . The general relation between the nodal values of  $\phi'$  and  $\phi$  for specified end conditions is

$$A_4^{(p)} \mathbf{a}_2^{(p)} = A_5^{(p)} \mathbf{a}_1^{(p)} - A_6^{(p)} \mathbf{a}_3^{(p)} \quad (3.22)$$

where  $A$  denotes a matrix and  $a$  a vector. The vectors of nodal values are

$$\begin{aligned} \mathbf{a}_1^{(p)} &= (\phi_{p,1} \ \phi_{p,2} \ \dots \ \phi_{p,M_p-1} \ \phi_{p,M_p})^T, \\ \mathbf{a}_2^{(p)} &= (\phi'_{p,2} \ \phi'_{p,3} \ \dots \ \phi'_{p,M_p-2} \ \phi'_{p,M_p-1})^T, \\ \mathbf{a}_3^{(p)} &= (\phi'_{p,1} \ \phi'_{p,M_p})^T, \end{aligned} \quad (3.23)$$

and the matrices are

$$\begin{aligned} A_4 &= \begin{pmatrix} 2(t_2 + t_3) & t_2 & 0 & 0 & \dots & 0 & 0 & 0 \\ t_4 & 2(t_3 + t_4) & t_3 & 0 & \dots & 0 & 0 & 0 \\ 0 & t_4 & 2(t_3 + t_4) & t_3 & \dots & 0 & 0 & 0 \\ \vdots & \vdots & \vdots & \vdots & \ddots & \vdots & \vdots & \vdots \\ 0 & 0 & 0 & 0 & \dots & t_{M-1} & 2(t_{M-2} + t_{M-1}) & t_{M-2} \\ 0 & 0 & 0 & 0 & \dots & 0 & t_M & 2(t_{M-1} + t_M) \end{pmatrix}, \\ A_5 &= \begin{pmatrix} -3\frac{t_3}{t_2} & \left(3\frac{t_3}{t_2} - \frac{t_2}{t_3}\right) & 3\frac{t_2}{t_3} & 0 & \dots & 0 & 0 & 0 \\ 0 & -3\frac{t_4}{t_3} & \left(3\frac{t_4}{t_3} - \frac{t_3}{t_4}\right) & 3\frac{t_3}{t_4} & 0 & \dots & 0 & 0 \\ \vdots & \vdots & \vdots & \vdots & \ddots & \vdots & \vdots & \vdots \\ 0 & 0 & 0 & 0 & \dots & -3\frac{t_M}{t_{M-1}} & 3\left(\frac{t_M}{t_{M-1}} - \frac{t_{M-1}}{t_M}\right) & 3\frac{t_{M-1}}{t_M} \\ 0 & 0 & 0 & 0 & \dots & 0 & -3 & 3 \end{pmatrix}, \\ A_6 &= \begin{pmatrix} t_3 & 0 \\ 0 & 0 \\ \vdots & \vdots \\ 0 & t_{M-1} \end{pmatrix}, \end{aligned}$$

where the  $p$  superscript has been dropped here for brevity. In equation (3.22),  $A_4^{(p)}$ ,  $A_5^{(p)}$  and  $A_6^{(p)}$  are  $M_p \times (M_p - 2)$ ,  $M_p \times M_p$  and  $M_p \times 2$  matrices, respectively. The

mixed end condition relation for the surge mode on the boundary portion with the first node at  $r = 0$  is

$$\tilde{\mathbf{A}}_4 \tilde{\mathbf{a}}_2 = \tilde{\mathbf{A}}_5 \mathbf{a}_1^{(1)} - \tilde{\mathbf{A}}_6 \tilde{\mathbf{a}}_3 \quad (3.24)$$

where the vectors are

$$\begin{aligned} \tilde{\mathbf{a}}_2 &= (\phi'_{1,1}, \phi'_{1,2}, \phi'_{1,3} \dots \phi'_{1,M_1-2}, \phi'_{1,M_1-1})^T, \\ \tilde{\mathbf{a}}_3 &= (\phi'_{1,M_1})^T \end{aligned} \quad (3.25)$$

and  $\tilde{\mathbf{A}}_4$ ,  $\tilde{\mathbf{A}}_5$  and  $\tilde{\mathbf{A}}_6$  are, respectively,  $M_p - 1 \times M_p - 1$ ,  $M_p - 1 \times M_p$  and  $M_p - 1 \times 1$  matrices. The matrix  $\tilde{\mathbf{A}}_6$  is simply the right-hand column of  $\mathbf{A}_6^{(p)}$  and  $\tilde{\mathbf{A}}_5$  is the matrix  $\mathbf{A}_5^{(p)}$  with the additional row of length  $M_p$

$$\begin{pmatrix} -3 & -3 & 0 & \dots & 0 \end{pmatrix} \quad (3.26)$$

prepended. Finally,  $\tilde{\mathbf{A}}_4$  is similar to  $\mathbf{A}_4^{(p)}$  with an extra row and column prepended. The row of length  $M_p - 1$  is given by

$$\begin{pmatrix} 2t_2 & t_2 & 0 & \dots & 0 \end{pmatrix} \quad (3.27)$$

and the column is

$$\begin{pmatrix} 2t_2 & t_3 & 0 & \dots & 0 \end{pmatrix}^T \quad (3.28)$$

where the first element in both must be identical. The addition of these rows and columns corresponds to the free condition on the first node of the  $p = 1$  surface portion. This special treatment is necessary to ensure the  $n = 1$  mode can be described properly because the slope  $\phi'$  related to the horizontal velocity is non-zero at the axis of symmetry  $r = 0$  only for this mode. For the other modes, the slope is known to be zero. Note that the mixed conditions only apply on the  $p = 1$  boundary (which has the axis of symmetry as one endpoint) hence no superscript is necessary for the matrices involved.

The relation for the  $u$  values is

$$\mathbf{B}_2^{(p)} \mathbf{b}_4^{(p)} = \mathbf{B}_5^{(p)} \mathbf{b}_1^{(p)} \quad (3.29)$$

and this applies on all boundary portions. In this equation and the previous  $\phi$ -related equations, the elements of the matrices are functions of the spline parameter  $t_{p,j+1}$  for  $j = 1, \dots, M_p - 1$  where  $t_{p,j}$  is the maximum value of the cubic spline parameter on the  $j^{\text{th}}$  element of the surface portion of index  $p$ . The vectors featured in (3.29) are

$$\begin{aligned} \mathbf{b}_1^{(p)} &= (u_{p,1} u_{p,2} \dots u_{p,M-1} u_{p,M})^T, \\ \mathbf{b}_4^{(p)} &= (u'_{p,2} u'_{p,3} \dots u'_{p,M-2} u'_{p,M-1})^T \end{aligned} \quad (3.30)$$

and the matrices (without the superscripts) are

$$B_4 = \begin{pmatrix} 2t_2 & t_2 & 0 & 0 & \dots & 0 & 0 & 0 \\ t_3 & 2(t_2 + t_3) & t_2 & 0 & \dots & 0 & 0 & 0 \\ 0 & t_4 & 2(t_3 + t_4) & t_3 & \dots & 0 & 0 & 0 \\ \vdots & \vdots & \vdots & \vdots & \ddots & \vdots & \vdots & \vdots \\ 0 & 0 & 0 & 0 & \dots & t_M & 2(t_{M-1} + t_M) & t_{M-1} \\ 0 & 0 & 0 & 0 & \dots & 0 & t_M & 2t_M \end{pmatrix}$$

and

$$B_5 = \begin{pmatrix} -3 & -3 & 0 & 0 & \dots & 0 & 0 & 0 \\ 3\frac{t_3}{t_2} & \left(3\frac{t_3}{t_2} - \frac{t_2}{t_3}\right) & 3\frac{t_2}{t_3} & 0 & \dots & 0 & 0 & 0 \\ \vdots & \vdots & \vdots & \vdots & \ddots & \vdots & \vdots & \vdots \\ 0 & 0 & 0 & 0 & \dots & -3\frac{t_M}{t_{M-1}} & 3\left(\frac{t_M}{t_{M-1}} - \frac{t_{M-1}}{t_M}\right) & 3\frac{t_{M-1}}{t_M} \\ 0 & 0 & 0 & 0 & \dots & 0 & -3 & 3 \end{pmatrix}.$$

In addition to representing the BIE variables  $\phi$  and  $u$ , the cubic splines are also used to represent the boundary coordinates. Thus,  $(r, z)$  are parameterised on each boundary portion with the natural end conditions described by (3.29) assumed except for the case of structure that does not enclose a portion of the free-surface. In this case  $dz/dt = 0$  at the axis of symmetry and this is incorporated into equation (3.29) by changing the elements of the first row in both  $B_4^{(1)}$  and  $B_5^{(1)}$  so that the only non-zero element is that corresponding to  $z'_1$  thus yielding  $z' = 0$  at  $r = 0$ .

Once the cubic spline parameterisation is complete, the BIE (3.19) can be discretised. Consider the first integral term  $\int_{C_3} \phi_n(r', z', \tau) r' \frac{\partial G_n}{\partial n}(r, z; r', z') dl'$  over the free-surface section external to the structure in equation (3.19). By substituting for the cubic spline representations of the boundary coordinates and the potential, the following finite sum approximation is obtained

$$\begin{aligned} & \int_{C_3} \phi_n(r', z', \tau) r' \frac{\partial G_n}{\partial n}(r, z; r', z') dl' = \\ & \sum_{j=1}^{M_3-1} \int_{\Delta C_j} \sum_{k=0}^3 c_{kj} t^k r'_j(t) G_n(\mathbf{x}, \mathbf{x}'_j(t)) \frac{dl'}{dt} dt. \end{aligned} \quad (3.31)$$

The derivative of the differential length term is  $dl'/dt = ((dx'_j/dt)^2 + (dz'_j/dt)^2)^{1/2}$  which equals unity on straight-line boundaries. By collocating this equation on the  $M_3$  nodes  $\mathbf{x} = \mathbf{x}_i$ ,  $i = 1, \dots, M_3$  of the boundary in question the equation (3.31) can be written in matrix form as

$$\mathbf{e} = A_1^{(3)} \mathbf{a}_1^{(3)} + B_2^{(3)} \mathbf{a}_4^{(3)} \quad (3.32)$$

where  $\mathbf{e}$  is a vector of the  $M_3$  evaluations on  $\mathbf{x}_i$  of  $\int_{C_3} \phi_n(r', z', \tau) r' \frac{\partial G_n}{\partial n}(r, z; r', z') dl'$ .

The matrices  $\mathbf{A}_1$  and  $\mathbf{B}_2$  are populated by terms involving the so-called influence coefficients which will be investigated in more detail later. Replacing the vector of derivatives term  $\mathbf{a}_4$  in (3.32) using the relation (3.22) (valid for the boundary portion  $C_3$ ) yields a new expression for  $\mathbf{e}$

$$\mathbf{e} = (\mathbf{A}_1^{(3)} + \mathbf{A}_2^{(3)}(\mathbf{A}_4^{(3)})^{-1}\mathbf{A}_5^{(3)})\mathbf{a}_1^{(3)} - (\mathbf{A}_2^{(3)}(\mathbf{A}_4^{(3)})^{-1}\mathbf{A}_6^{(3)} - \mathbf{A}_3^{(3)})\mathbf{a}_3^{(3)} \quad (3.33)$$

which includes the end-slope values only and no other derivative terms. These end-slope terms can be replaced using the continuity of velocity conditions.

The system of linear algebraic equations is constructed by applying the necessary cubic-spline relations to the finite-sum approximations of the boundary integrals and combining the resultant expressions to approximate (3.19). Thereafter, the expressions should be grouped with reference to domain sections, whereby  $\phi$  is known on the free-surface and the control surface and  $u$  on the structure surface, so that all unknowns are on the left hand side of the equation. The domain sections are referred to by the index  $p$  with  $R_1 = \{C_1, C_3, C_4\}$  and  $R_2 = C_2$ . The resultant discretised BIE for the mode  $n = 1$  is

$$\begin{aligned} & \alpha(\mathbf{x}_i)\phi_i + \sum_{p \in R_1} (\mathbf{C}_1^{(p)} + \mathbf{D}_2^{(p)}(\mathbf{B}_4^{(p)})^{-1}\mathbf{B}_5^{(p)})\mathbf{b}_1^{(p)} \\ & - \sum_{p \in R_2} \left[ (\mathbf{A}_1^{(p)} + \mathbf{A}_2^{(p)}(\mathbf{A}_4^{(p)})^{-1}\mathbf{A}_5^{(p)})\mathbf{a}_1^{(p)}(\mathbf{A}_2^{(p)}(\mathbf{A}_4^{(p)})^{-1}\mathbf{A}_6^{(p)} - \mathbf{A}_3^{(p)})\mathbf{a}_3^{(p)} \right] \\ & = (\mathbf{A}_1^{(1)} + \tilde{\mathbf{A}}_2(\tilde{\mathbf{A}}_4)^{-1}\tilde{\mathbf{A}}_5)\mathbf{a}_1^{(1)} + (\tilde{\mathbf{A}}_3 - \tilde{\mathbf{A}}_2(\tilde{\mathbf{A}}_4)^{-1}\tilde{\mathbf{A}}_6)\mathbf{a}_3 \\ & + \sum_{p \in R_1, p \neq 1} \left[ (\mathbf{A}_1^{(p)} + \mathbf{A}_2^{(p)}(\mathbf{A}_4^{(p)})^{-1}\mathbf{A}_5^{(p)})\mathbf{a}_1^{(p)} - (\mathbf{A}_2^{(p)}(\mathbf{A}_4^{(p)})^{-1}\mathbf{A}_6^{(p)} - \mathbf{A}_3^{(p)})\mathbf{a}_3^{(p)} \right] \\ & - \sum_{p \in R_2} (\mathbf{C}_1^{(p)} + \mathbf{D}_2^{(p)}(\mathbf{B}_4^{(p)})^{-1}\mathbf{B}_5^{(p)})\mathbf{b}_1^{(p)} \end{aligned} \quad (3.34)$$

where the first term on the right-hand side of the equation corresponds to the mixed end conditions on the the first ( $p = 1$ ) boundary portion. For all other modes this special term is not present, it is replaced by the  $p = 1$  term in the subsequent sum. This equation includes the end-slopes of  $\phi$  in the  $\mathbf{a}_3^{(p)}$  vectors which must be replaced using the continuity of velocity conditions. In this way, the continuity of velocity will be inherently satisfied in the governing BEM equations. The continuity conditions are obtained by ensuring the equality of the normal and tangential components of the velocity across the intersections. By manipulating the resultant equations so that only one  $\phi'$  term exists in both equations and by grouping the conditions according to the

boundary portion  $p$ , the relations

$$\begin{pmatrix} \phi'_{p,1} \\ \phi'_{p,M} \end{pmatrix} = \begin{pmatrix} -J_{p,1}/\sin(\alpha_p\pi) \\ 0 \end{pmatrix} u_{p-1,M} + \begin{pmatrix} -J_{p,1}\cot(\alpha_p\pi) \\ 0 \end{pmatrix} u_{p,1} + \begin{pmatrix} 0 \\ J_{p,M}\cot(\alpha_{p+1}\pi) \end{pmatrix} u_{p,M} + \begin{pmatrix} 0 \\ J_{p,M}/\sin(\alpha_{p+1}\pi) \end{pmatrix} u_{p+1,1} \quad (3.35)$$

are obtained for  $p = 1, \dots, 3$ . The upper equation corresponds to the continuity condition on the intersection between the boundaries portions  $p-1$  and  $p$ . On the other hand, the lower equation corresponds to the continuity condition on the intersection between the portions  $p$  and  $p+1$ . The term  $\alpha_p\pi$  is the interior angle between the boundary portions  $p-1$  and  $p$  and  $J_{p,j}$  is the derivative term  $dl/dt = ((dx'_j/dt)^2 + (dz'_j/dt)^2)^{1/2}$  on the boundary  $p$ . On the boundary  $r = 1$ ,  $\phi'_{1,1} = 0$  for all modes apart from the  $n = 1$  mode. Therefore, only the equation

$$\phi'_{p,M} = J_{p,M}\cot(\alpha_{p+1}\pi)u_{p,M} + J_{p,M}/\sin(\alpha_{p+1}\pi)u_{p+1,1} \quad (3.36)$$

is implemented for  $p = 1$ . In the BIE for  $n = 1$ , no continuity equation is permitted as  $\phi'_1$  is not assumed specified. Therefore, in equation (3.34) the  $a_3$  vectors may be replaced with expressions containing the known and unknown  $u$  terms.

The  $n^{th}$  boundary integral equation (3.19) can thus be discretised into a system of  $\sum_{p=1}^4 M_p = N + 3$  linear algebraic equations of the form

$$[\mathbf{H}_Y]\mathbf{y} = [\mathbf{H}_X]\mathbf{x} \quad (3.37)$$

where

$$\begin{aligned} \mathbf{x} &= (\phi_{1,1}, \dots, \phi_{1,M_1}, u_{2,1}, \dots, u_{2,M_2}, \phi_{3,1}, \dots, \phi_{3,M_3}, \phi_{4,1}, \dots, \phi_{4,M_4})^T \\ \mathbf{y} &= (u_{1,1}, \dots, u_{1,M_1}, \phi_{2,1}, \dots, \phi_{2,M_2}, u_{3,1}, \dots, u_{3,M_3}, u_{4,1}, \dots, u_{4,M_4})^T \end{aligned} \quad (3.38)$$

is the vector of unknowns and  $[\mathbf{H}_X]$  and  $[\mathbf{H}_Y]$  are the  $(N + 3) \times (N + 3)$  matrices of coefficients for the knowns and unknowns respectively. The number of equations in the system can be immediately reduced by recognising that the last node on the portion  $C_{p-1}$  is at the same position as the first node on the portion  $C_p$  so that the corresponding equations will be identical for  $p = 1, 2, 3$ . Therefore, by removing the repeated equations a system of  $N$  linear equations with  $N + 3$  unknowns remains. Clearly the system is underdetermined and the solution of these equations requires three auxiliary equations. These are provided by imposing continuity of  $\phi$  at the intersection points. This continuity condition is first imposed at the intersection of the body boundary portion  $C_2$  with the free-surface portions  $C_1$  and  $C_3$ , respectively, by applying the equations

$$\phi_{1,M_1} = \phi_{2,1}, \quad \phi_{2,M_2} = \phi_{3,1}. \quad (3.39)$$

In the linear system of equations (3.37), these continuity conditions are imposed by subtracting the (column of) coefficients of the supposed unknowns  $\phi_{2,1}$  and  $\phi_{2,M_2}$  in the matrix  $[H_Y]$  from the relevant coefficients, i.e. those multiplying  $\phi_{1,M_1}$  and  $\phi_{3,1}$ , in the matrix  $[H_X]$ . Therefore, the number of unknowns will be reduced by 2 and  $[H_Y]$  will become and  $N \times (N + 1)$  matrix. The continuity of  $\phi$  condition at the final intersection point between the last node of the boundary portion  $C_3$  and the first node of the control surface  $C_4$

$$\phi_{3,M_3} = \phi_{4,1} \quad (3.40)$$

is satisfied by merging the two identical nodes. Both of these nodes are initially assumed to have prescribed  $\phi$  values. This merging procedure is implemented in the linear system (3.37) by adding the coefficients of the respective  $\phi_{M_3}^3$  and  $\phi_{M_4}^4$  values in each of the equations so that the two columns of the matrix  $[H_X]$  are combined in to one. Having satisfied the continuity of  $\phi$  conditions at these intersection points, the linear system comprises of  $N$  equations with  $N$  knowns and  $N + 1$  unknowns. To obtain a system of  $N$  equations and  $N$  unknowns the normal velocity  $u$  is assumed to be known on the control surface and so the vectors of knowns and unknowns become

$$\begin{aligned} \mathbf{x} &= (\phi_{1,1}, \dots, \phi_{1,M_1}, u_{2,1}, \dots, u_{2,M_2}, \phi_{3,1}, \dots, \phi_{3,M_3}, u_{4,1}, \dots, u_{4,M_4})^T \\ \mathbf{y} &= (u_{1,1}, \dots, u_{1,M_1}, \phi_{2,2}, \dots, \phi_{2,M_2-1}, u_{3,1}, \dots, u_{3,M_3}, \phi_{4,2}, \dots, \phi_{4,M_4})^T \end{aligned} \quad (3.41)$$

where  $\phi_{2,1}$ ,  $\phi_{2,2}$  and  $\phi_{4,1}$  are known by the continuity conditions (3.39) and (3.40). Therefore, a system of  $N$  equations with  $N + 1$  knowns and  $N$  unknowns has been obtained.

### 3.3.2 Evaluation of the influence coefficients

To populate the elements of the matrices in equation (3.32) and hence the total matrices  $[H_X]$  and  $[H_Y]$  for a given BIE of order  $n$  the integrals

$$\begin{aligned} \int_{C_j} t^k G_n(\mathbf{x}_i, \mathbf{x}') r' dl' &= \int_{C_j} t^k G_n(t) r'_j(t) \frac{dl'}{dt} dt, \\ \int_{C_j} t^k \frac{\partial G_n}{\partial n}(\mathbf{x}_i, \mathbf{x}') r dl' &= \int_{C_j} \frac{\partial G_n}{\partial n} r'_j(t) \frac{dl'}{dt} dt, \end{aligned} \quad (3.42)$$

known as the influence coefficients, must be evaluated for  $k = 0, \dots, 3$ . The accuracy of these computations will determine the overall accuracy of the solution because the cubic-spline matrices are simple functions of the spline parameter and the error introduced is minimal. Therefore, it is important to compute the influence coefficients and thus the Green's function as accurately as possible for all possible field point and source point positions. If the field point is the upper or lower node of the source element  $\Delta C_j$  then the Green's function will be singular at one point of the integral. Therefore,

an examination of the asymptotic properties of the Green's function and its normal derivative as the source point  $(r', z')$  approaches the field point  $(r, z)$  is necessary. It should be noted that the total term which must be evaluated is  $r'_j(t)G_n(t)$  and not the ring-source potential  $G_n$  and similarly the term  $r'_j(t)\partial G_n/\partial n$  and not  $\partial G_n/\partial n$  must be examined. In this manner, the computer implementation of the influence coefficient evaluations will be identical to the two-dimensional case with  $r'_j(t)G_n(t)$  replacing  $G(t)$  and so on.

The ring-source Green's function (3.18) is defined as

$$G_n(r, z; r', z') = \int_0^{2\pi} G(r, z; r', z'; \cos(\theta - \theta')) \cos n(\theta - \theta') d(\theta - \theta') \quad (3.43)$$

where the Green's function is the sum of a unit source and an image-source given by

$$G(\mathbf{r}, \mathbf{r}') = -\frac{1}{4\pi} \left( \frac{1}{r} + \frac{1}{r'} \right) \quad (3.44)$$

where  $r^2 \equiv R^2 + (z + z' + 2h)^2$ ,  $r'^2 \equiv R^2 + (z - z')^2$  and  $R^2 = r^2 + r'^2 - 2rr' \cos(\theta - \theta')$ . For the  $1/r$  Rankine part (neglecting the  $-1/4\pi$  factor), the integration with respect to  $\theta$  in (3.18) "can be obtained analytically for any  $n$  in terms of second-kind Legendre function of integral-minus-half-order/degree Abramowitz & Stegun (1964):

$$R_n \equiv \int_0^{2\pi} \frac{\cos n(\theta - \theta')}{r} d(\theta - \theta') = \frac{2}{(rr')}^{\frac{1}{2}} Q_{n-\frac{1}{2}}(a_0/b_0), \quad n = 0, 1, 2, \dots \quad (3.45)$$

where  $a_0 \equiv r^2 + r'^2 + (z - z')^2$  and  $b_0 = 2rr'$  as stated by Kim & Yue (1989). Using a similar analysis for  $1/r'$  integral it can be shown that the  $n^{\text{th}}$  order ring source is given by

$$G_n = -\frac{1}{4\pi} (R_n + R'_n) \quad n = 0, 1, 2, \dots, \quad (3.46)$$

where  $R'_n = 2/(rr')^{1/2} Q_{n-\frac{1}{2}}(a'_0/b_0)$ , for  $n = 0, 1, 2, \dots$  and  $a'_0 \equiv r^2 + r'^2 + (z + z' + 2h)^2$ . It is important to assess the accuracy with which  $Q_{n-1/2}(Z)$  can be computed for a range of  $Z$  and  $n$  values in order to ensure the numerical approximation of the ring-source integrations do not diverge from the true values. So a numerical investigation into the computational accuracy for the Legendre function was carried out and the results are shown here. The Fortran results were compared to those from *Mathematica* where the precision of the computations can be prespecified.

In the previous literature on ring-source/integral-equation methods, the nature of the singularity in the ring-source potentials was examined in order to devise accurate means of computing the integrals in the BIE. Black (1975) maintained that the ring-source potential was not singular; however, Fenton (1978) proved otherwise when investigating the asymptotics of the ring-source potential as the field point approached the source point. By consideration of the singular part (Rankine source) of the Green's function

in a series form, Fenton (1978) showed that the ring-source potentials corresponding to all Fourier modes possess a logarithmic singularity. Hulme (1983) noted this property and investigated the computational efficiency of various expressions for the ring-source potentials in the cases where the field point is close to and far from the source point. However, Kim & Yue (1989) presented the most comprehensive analysis of the evaluation methods of the ring source potential and its derivative at all orders of the Fourier cosine expansion. In § 3.2 of that paper, very useful expressions and evaluation methods for the ring source potentials were provided in both cases where the field point is close to the source and far from the source point. These expressions, involving the hypergeometric function, were utilised in the evaluation of the influence coefficients and are examined next.

The Legendre function of the second kind is related to the hypergeometric function due to the relation

$$Q_{n-\frac{1}{2}}(Z) = \frac{\pi^{\frac{1}{2}}}{(2Z)^{n+\frac{1}{2}}} \frac{\Gamma(n+\frac{1}{2})}{\Gamma(n+1)} F(\frac{1}{2}n + \frac{3}{4}, \frac{1}{2}n + \frac{1}{4}, n+1, \frac{1}{Z^2}). \quad (3.47)$$

It was decided that the Legendre function  $Q_{n-1/2}(Z)$  would be computed using the hypergeometric function because of the availability of numerical algorithms to evaluate it efficiently. However, there are two alternative expressions for the hypergeometric function which can be used depending on the value of

$$Z = \frac{r^2 + r'^2 + (z - z')^2}{2rr'} = 1 + \frac{(r - r')^2 + (z - z')^2}{2rr'}. \quad (3.48)$$

The general expression for the hypergeometric function

$$F(a, b; c; \frac{1}{Z^2}) = \frac{\Gamma(c)}{\Gamma(a)\Gamma(b)} \sum_{m=0}^{\infty} \frac{\Gamma(m+a)\Gamma(m+b)}{\Gamma(m+c)\Gamma(m+1)} \frac{1}{Z^{2m}}. \quad (3.49)$$

converges rapidly if the source point is not close to the field point, i.e. for  $Z$  not close to unity. If the source point approaches the field point ( $Z \rightarrow 1$ ), then the asymptotic series expression involving a logarithmic singularity

$$F = \frac{\Gamma(n+1)}{\Gamma(\frac{1}{2}n + \frac{3}{4})\Gamma(\frac{1}{2}n + \frac{1}{4})} \sum_{m=0}^{\infty} \frac{(\frac{1}{2}n + \frac{3}{4})_m (\frac{1}{2}n + \frac{1}{4})_m}{\Gamma(m+1)^2} [2\Psi(m+1) - \Psi(m + \frac{1}{2}n + \frac{3}{4}) - \Psi(m + \frac{1}{2}n + \frac{1}{4}) - \ln\left(1 - \frac{1}{Z^2}\right)] \left(1 - \frac{1}{Z^2}\right)^n, \quad (3.50)$$

should be used to evaluate the hypergeometric function. During the evaluation of the influence coefficients the value of  $Z$  may vary from values very close to unity, e.g. when the integral over an element includes a singularity, to values quite far from unity, e.g. when  $r$  and  $r'$  are close to zero. In fact, it may occur that the value of  $Z$  may change rapidly from the general regime to the asymptotic regime when integrating over a single

element. Therefore, it is necessary to investigate the most accurate and efficient way of computing the hypergeometric function (3.45) to ensure the accurate evaluation of the Green's function for all source and field points.

Accurate computations of the hypergeometric function  $F(\frac{1}{2}n + \frac{3}{4}, \frac{1}{2}n + \frac{3}{4}, n + 1, \frac{1}{Z^2})$  for any value of  $n$  in the whole domain  $Z > 1$  require the use of the two different series definitions, (3.49) and (3.50), respectively. A direct numerical evaluation of the asymptotic series is possible and yields accurate results for  $Z \rightarrow 1$ . Convergence is generally quite rapid due to the  $(1 - \frac{1}{Z^2})^m$  term in the series and results close to machine precision, in the regime of validity of the expression (e.g.  $Z < 1.1$  for  $n < 5$ ), can be obtained with relatively few terms. However, inaccuracies do occur in the evaluation of the  $\log(1 - \frac{1}{Z^2})$  terms for extremely small values of  $Z$ . The general expression for the hypergeometric function is not suitable for computational purposes and thus a Chebyshev polynomial expansion is used instead to evaluate the function for general values of  $Z$ . The algorithm to implement the Chebyshev expansion is described by Luke (1977). In the  $n = 0$  case, this Chebyshev expansion method, truncated after 200 terms, evaluates the hypergeometric function to at least 15 figures of precision for  $Z > 1.05$ . In some cases, convergence is much more rapid and 200 terms is quite a pessimistic estimate of the truncation level. Therefore, for  $n = 0$  it is possible to compute the hypergeometric function/Legendre function and hence the ring-source Greens function to a high degree of precision, by combining both computational algorithms.

The relative errors in the hypergeometric function for both of the computational algorithms in the critical interval  $1.001 < Z < 1.1$ , where the accuracy of the Chebyshev expansion method and asymptotic series method increases, were computed for values of the azimuthal mode  $n \leq 14$ . The computational results from both algorithms were compared with a high precision computation from *Mathematica*. The precision of the computed value was at least 20 figures in all cases — far in excess of the double-precision Fortran computations. Figures 3.4 and 3.5 illustrate the variation of the error in the computational algorithms for the  $n = 0$  and  $n = 10$  modes. The changes in the order of magnitude of the errors should be noted from the units of the graphs. This illustrates the progressive difficulty in maintaining a high degree of accuracy as  $n$  increases. Furthermore, the increase in the asymptotic error as  $Z$  decreases below the value 1.01 illustrates the difficulty in computing  $\log(1 - \frac{1}{Z^2})$  accurately using double-precision Fortran framework as was noted previously.

To maintain the accuracy of the computation of the ring-source Green's function for all source point and field point values it is necessary to combine the hypergeometric computational algorithms. This requires the use of an if construct in Fortran to select the most accurate method to compute the hypergeometric function depending on the value of  $Z$  and  $n$ . The if construct must then be incorporated in the ring-source

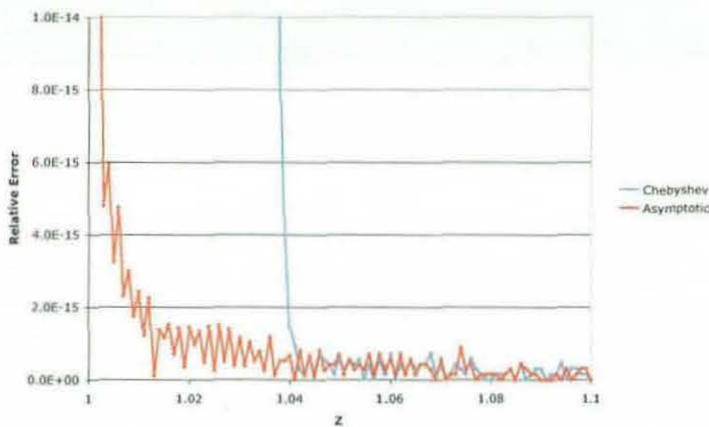


Figure 3.4: A graph of the relative error for the computation of the hypergeometric function  $F(\frac{1}{2}n + \frac{3}{4}, \frac{1}{2}n + \frac{3}{4}, n+1, \frac{1}{Z^2})$  for  $n = 0$  by the Chebyshev polynomial expansion method (blue) and the asymptotic series method (red).

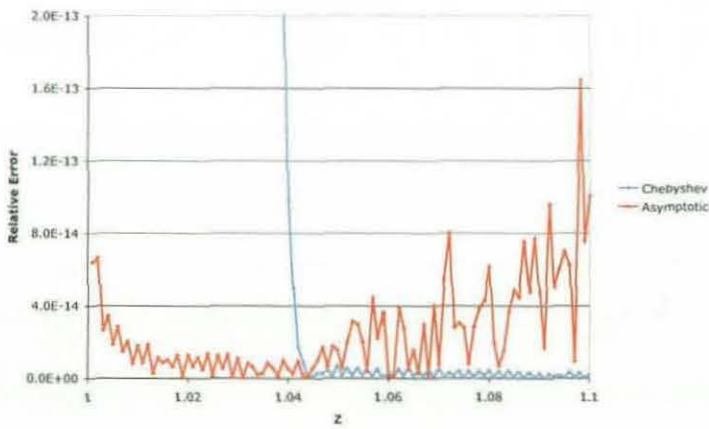


Figure 3.5: A graph of the relative error for the computation of the hypergeometric function  $F(\frac{1}{2}n + \frac{3}{4}, \frac{1}{2}n + \frac{3}{4}, n+1, \frac{1}{Z^2})$  for  $n = 10$  by the Chebyshev polynomial expansion method (blue) and the asymptotic series method (red).

Green's function Fortran implementation to ensure an accurate value will be returned on evaluation for any value of  $Z$ . Clearly, this will result in a significant increase in the computation time of the Green's function. The relative error in the Green's function computation will be very similar to that of the hypergeometric function because the two can be directly related via the Legendre function  $Q_{n-1/2}(Z)$  as follows:

$$G_n(r, z; r', z') = -\frac{1}{4\pi} \frac{2}{(rr')^{\frac{1}{2}}} \left( Q_{n-1/2}(Z) + Q_{n-\frac{1}{2}}(Z_1) \right) \quad (3.51)$$

where the Legendre function is defined in terms of the hypergeometric function in equation (A.2) and  $Z_1$  is the image source equivalent of  $Z$  so that  $z - z'$  is replaced by  $z + z' + 2h$  in equation (3.48). Thus, the accumulation of error will be minimal. Comparing the ring-source Green's function to the two-dimensional Green's function which is defined as

$$G(x, z; x', z') = \frac{1}{2\pi} (\ln r + \ln r_1), \quad (3.52)$$

where  $r^2 = (x - x')^2 + (z - z')^2$  and  $r_1^2 = (x - x')^2 + (z + z' + 2)^2$ , it is clear that the numerical evaluation of the two-dimensional Green's function is far more straightforward than for the ring-source case. The asymptotic forms of the Green's function in two-dimensions and the 'effective' ring-source Green's function  $r'G_n(r, z; r', z')$  are very similar as will be shown next. However, it should be noted that the normal derivative of the Green's function  $\frac{\partial G}{\partial n}$ , largely neglected until now, can be dealt in the same way as the actual ring-source function. The derivation (A.27) of the form of  $\frac{\partial R_n}{\partial n}$  in Appendix A illustrates this. However, the error in the hypergeometric function may accumulate in this case due to the relative complexity in the expression.

The singular terms from  $r'G_n(r, z; r', z')$  and  $r'\frac{\partial G_n}{\partial n}(r, z; r', z')$  have been derived in Appendix A, equations (A.18) and (A.30). By the definition of  $G_n$ , it is clear the singular term will have the logarithmic form

$$r'G_n(r, z; r', z') \sim \frac{1}{2\pi} \ln((r - r')^2 + (z - z')^2)^{\frac{1}{2}}. \quad (3.53)$$

as the source point approaches the field point. Similarly, the normal derivative ring-source Green's function has a singular term of the form

$$r'\frac{\partial G_n}{\partial n} \sim \frac{n_r}{2\pi r} \ln((r - r')^2 + (z - z')^2)^{\frac{1}{2}}. \quad (3.54)$$

Contrasting these singularities with those for the two-dimensional Green's function (3.52) and its normal derivative, as the source point approaches the field point yields some interesting results. The asymptotic form of the Green's function is identical to that of the axisymmetric ring-source case

$$G(x, z; x', z') = \frac{1}{2\pi} \ln((x - x')^2 + (z - z')^2) \quad (3.55)$$

whereas the normal derivative of the Green's function possesses no singularity, as remarked in Chapter 4 of Linton & McIver (2001). Therefore, the treatment of the reduced BIE relating to the 3D axisymmetric water-wave problem will differ from the BIE due to the 2D water-wave problem primarily in the computation of the influence coefficients involving the singular normal derivative term. As discussed previously, the actual computation of the Green's function will also differ significantly from the 2D case. However, in terms of the overall algorithm the integration of the  $\frac{\partial G_n}{\partial n}$  term on elements where the field point is present will differ the most.

The cubic spline definitions of  $r'$  and  $z'$  on an element  $\Delta C_j$  where the field point is the bottom node, i.e. the field point corresponds to the source point value when the spline parameter  $t = 0$ , are as follows

$$r' = \sum_{k=1}^3 a_{kj} t^k + r \quad z' = \sum_{k=1}^3 b_{kj} t^k + z \quad (3.56)$$

where  $a_{kj}$ ,  $b_{kj}$  can be computed from the geometry of the element and continuity conditions. Therefore, as the source point approaches the field point  $t \rightarrow 0$  the term  $\ln((r - r')^2 + (z - z')^2)$  from the asymptotic form of the Green's functions becomes simply  $\ln t$ . Similarly, if the field point is the upper node of the source element then the asymptotic form as the source point approaches the field point, in terms of the cubic spline parameter, is  $\ln(t_{j+1} - t)$  where  $t_{j+1}$  is the maximum value of the spline parameter on the element. A simple schematic of the element is shown in figure 3.3. Of course, this cubic spline representation of the singularity is identical for the 2D Green's function also and the log term in the normal derivative of the ring-source Green's function. To compute the influence coefficients (3.42) by numerical integration when the integrand possesses a logarithmic singularity, the following method must be used. Assuming the integral can effectively be written as

$$\int_0^{t_{j+1}} f(t) \frac{ds}{dt} dt \quad (3.57)$$

where  $f(t) \sim \frac{1}{2\pi} \ln t$  as  $t \rightarrow 0$  then:

- The integral  $\int_0^{t_{j+1}} (f(t) - \frac{1}{2\pi} \ln t) \frac{ds}{dt} dt$  with the non-singular integrand is computed by a numerical quadrature routine.
- The term  $\frac{ds}{dt} \ln t$  is computed by an adaptive integration routine which can handle integrands with algebraic-logarithmic singularities at the end-points.<sup>1</sup>
- By adding the integrals

$$\int_0^{t_{j+1}} \left( f(t) - \frac{1}{2\pi} \ln t \right) \frac{ds}{dt} dt + \frac{1}{2\pi} \int_0^{t_{j+1}} \ln t \frac{ds}{dt} dt \quad (3.58)$$

---

<sup>1</sup>See the NAG routine D01APF. Documentation can be found at [www.nag.co.uk](http://www.nag.co.uk).

which have been computed by the separate integration routines an approximation to the total integral can be obtained.

This procedure was implemented in the BEM used by McIver et al. (2003) to compute the two-dimensional wave-motion due to the forced motion of floating structures. It can be applied in a similar fashion to the BEM discretisation procedure that is applied to the reduced integral equation (3.17) involving the ring-source Green's function.

### 3.4 Time-stepping algorithm

To complete the numerical time-domain solver an algorithm to advance the flow in time must be implemented in conjunction with the system of linear BEM equations. The time-stepping of the free-surface and structure displacement is achieved using a fourth-order Runge-Kutta method, an outline of which will be given later. First, the treatment of the control surface  $P$  as a piston absorber must be explained in the context of the discretised BEM equations.

#### 3.4.1 Piston boundary condition

The introduction of the control surface  $P$  is necessary in order to obtain and numerically solve a BIE from the wave-structure interaction boundary value problem. However, this artificial boundary will generate unphysical reflections if a no-flow boundary condition is imposed on the surface, i.e. the surface is assumed to be a rigid wall. Minimisation of the artificial wave-reflections is best achieved by treating the control surface as a piston absorber and combining it with a damping zone on the adjacent free-surface. This approach was first suggested by Clément (1996) for two-dimensional problems and a numerical implementation in the BEM was proposed by McIver et al. (2003). By considering the two-dimensional equation it is straightforward to explain the extension to the different modes for the axisymmetric three-dimensional problem.

The non-dimensionalised piston boundary condition proposed by Clément (1996) for two-dimensional problems was

$$\frac{\partial \Phi}{\partial x}(\pm L, z, t) = \mp \int_{-1}^0 \frac{\partial \Phi}{\partial t}(\pm L, \zeta, t) d\zeta, -1 < z < 0 \quad (3.59)$$

so that the control surfaces moves uniformly in response to the average fluid pressure on the surface, i.e. the control surface moves as a rigid piston. In the long wavelength limit, the fluid motion is independent of depth and the piston boundary condition

reduces to the Sommerfeld conditions for waves with speed one

$$\frac{\partial \Phi}{\partial x} = \mp \frac{\partial \Phi}{\partial t} \quad \text{at} \quad x = \pm L \quad (3.60)$$

which is just the long-wave speed  $\sqrt{gh}$  in dimensional terms. The piston absorber is therefore most effective at absorbing longer waves. For three-dimensional problems involving structures with vertical axes of symmetry, it is desirable to obtain the Sommerfeld condition in the long wavelength limit for each Fourier mode  $\phi_n$  of the potential expansion. Therefore, at each mode  $n$  the boundary condition is identical:

$$\frac{\partial \phi_n}{\partial r}(L, z, t) = - \int_{-1}^0 \frac{\partial \phi_n}{\partial t}(r, \zeta, t) d\zeta \quad \text{at} \quad r = L. \quad (3.61)$$

The piston absorption condition is imposed as follows:

- introduce an extra variable  $q$  and equation to the linear system of equations through the definition

$$q = \int_{-1}^0 \phi_n(L, \zeta, t) d\zeta \quad (3.62)$$

- advance  $q$  in time using the time-evolution equation

$$\frac{dq}{dt} = -u_P \quad (3.63)$$

where  $u_P$  is the uniform piston velocity.

The initial value of  $q$  is assumed to be zero since the fluid is initially assumed to be at rest. The piston absorber is most effective at absorbing longer waves so that combining it with a damping zone, which is most effective at absorbing shorter waves, ensures most of the outgoing wave energy is absorbed and not reflected. The damping zone is implemented by introducing a dissipative term in the dynamic free-surface boundary condition as follows

$$\frac{\partial \Phi}{\partial t} = -\eta - \nu(r) \frac{\partial \Phi}{\partial z} \quad \text{on} \quad z = 0 \quad (3.64)$$

where the non-dimensional form of the condition has been used. The function  $\nu(r)$  is zero outside the damping zone and positive inside the damping zone. The details of the function are provided by Clément (1996).

The introduction of a new variable and equation related to the control surface requires a reconsideration of the number of knowns and unknowns in the linear system as there are  $N+1$  equations now. The new variable  $q$  is assumed to be known and so the vectors of knowns and unknowns will be

$$\begin{aligned} \mathbf{x} &= (\phi_{1,1}, \dots, \phi_{1,M_1}, u_{2,1}, \dots, u_{2,M_2}, \phi_{3,1}, \dots, \phi_{3,M_3}, u_{4,1}, \dots, u_{4,M_4}, q)^T \\ \mathbf{y} &= (u_{1,1}, \dots, u_{1,M_1}, \phi_{2,1}, \dots, \phi_{2,M_2}, u_{3,1}, \dots, u_{3,M_3}, \phi_{4,2}, \dots, \phi_{4,M_4})^T \end{aligned} \quad (3.65)$$

If the control surface is assumed to move as a piston then the velocity of each node can be represented by the single variable  $u_P$ . The coefficients of the known variables  $\{u_{4,1}, \dots, u_{4,M_4}\}$  are merged together also leaving a single term for the control surface velocity in each of the BEM equations. Therefore, there will be  $N + 1 - (M_4 - 1)$  elements in the vector of knowns  $\mathbf{x}$ . The nodal values of  $\phi$  on the control surface remain different and no simplifications can be made. To form a well-defined system the control surface velocity  $u_P$  and the potential values on the control surface are assumed to be unknown and the new variable  $q$  to be known – this requires a number of adjustments to the coefficient matrices. The last element of the vector  $\mathbf{x}$  ( $u_P$ ) must be appended to the vector  $\mathbf{y}$  and so the column of merged coefficients relating to the control surface velocity must also be transferred from  $[\mathbf{H}_X]$  to  $[\mathbf{H}_Y]$ . Thus there will be  $N + 1$  unknowns and  $N + 3 - M_4$  knowns while  $[\mathbf{H}_Y]$  and  $[\mathbf{H}_X]$  will be  $N \times (N + 1)$  and  $N \times (N + 3 - M_4)$  matrices, respectively. Using the cubic spline representation of  $\phi$  on the control surface, the integral equation in (3.61) can be expressed as an equation relating  $q$  to the unknown  $\phi$  values at the nodes and the unknown velocity  $u_P$  of the control surface. Without describing the details, the  $u$  term appears in the equation due to the presence of the tangential derivative of  $\phi$  in the cubic spline representation. The tangential derivative at the intersection (double) node with the free-surface is equal to the unknown velocity  $u$  by the continuity of velocity. Therefore, in vector notation the equation becomes

$$cu - \alpha_1^T \mathbf{a}_1 = q. \quad (3.66)$$

Here,  $c$  is just a multiplicative coefficient of  $u$  and  $\mathbf{a}_1$  is the column of known  $\phi$  values on the control surface nodes and  $\alpha_1$  a coefficient vector due to the integration over the boundary elements. Including this equation in the linear system of equations (3.37) transforms the unknown matrix  $[\mathbf{H}_Y]$  into a square  $(N + 1) \times (N + 1)$  matrix so the number of unknowns and equations is equal. The vector  $\mathbf{x}$  and its coefficient matrix  $[\mathbf{H}_X]$  transform into and  $N + 3 - (M_4 - 1)$  and  $(N + 1) \times (N + 3 - (M_4 - 1))$  vector and matrix respectively. It then remains to implement the time-stepping algorithm.

### 3.4.2 Runge-Kutta method

At the beginning of each time-step all the knowns are specified and the evolution equations for the problem in question must be used to advance the flow in time. For radiation and diffraction problem the evolution equations are the kinematic and dynamic free-surface boundary conditions and the piston boundary condition and are

written in the following non-dimensional form

$$\begin{aligned}\frac{\partial \eta}{\partial t} &= u \quad \text{on } z = 0 \\ \frac{\partial \Phi}{\partial t} &= -\eta - u\nu(r) \quad \text{on } z = 0 \\ \frac{dq}{dt} &= u_P \quad \text{on } P\end{aligned}\tag{3.67}$$

where  $u$  is the normal velocity on the free surface and  $u_P$  the normal velocity of the piston control surface. A fourth order Runge-Kutta method is used to time-step the equations and the linear system of equations, which does not change in time, is used to update the right hand sides of the equations for the subsequent time step.

The algorithm assumes that all relevant quantities are specified at some time  $t = t_0$  and the objective is to advance to time  $t = t_0 + \Delta t$ . Therefore,  $\Phi$ ,  $\eta$ ,  $q$ ,  $u$  and  $u_P$  are all assumed known to begin with. For simplicity it is assumed that the motion of the body is prescribed by the velocity function  $v(t)$ . The fourth order Runge-Kutta time-stepping algorithm then proceeds as follows.

**Runge-Kutta step 1 (RK1):**  $t = t_0$  Determine the changes in  $\eta$ ,  $\Phi$  and  $q$  using equation (3.67)

$$\begin{aligned}\Delta\eta_1 &= u\Delta t \\ \Delta\Phi_1 &= -(\eta\Delta t + u\nu(r))\Delta t \\ \Delta q_1 &= u_P dt\end{aligned}\tag{3.68}$$

**Runge-Kutta step 2 (RK2):**  $t = t_0 + \Delta t/2$  Update the free-surface knowns  $\eta$ ,  $\Phi$ , and  $q$  on the control surface and the normal velocity of the structure, i.e. the vector of knowns  $\mathbf{x}$

$$\begin{aligned}\eta' &= \eta + \Delta\eta_1/2, \\ \Phi' &= \Phi + \Delta\Phi_1/2, \\ q' &= q + \Delta q_1/2 \\ v' &= v(t + \Delta t/2)\end{aligned}\tag{3.69}$$

and then solve the linear system of equations using the new right-hand side  $[\mathbf{H}_X]\mathbf{x}$  to obtain updated values of the normal velocity of the free-surface and the piston control surface ( $u', u'_P$ ) as well as  $\phi$  on the solid boundaries. Then, determine the changes in  $\eta$ ,  $\Phi$  and  $q$  using the new values of the normal velocity, free-surface

elevation and  $q$ .

$$\begin{aligned}\Delta\eta_2 &= u'\Delta t \\ \Delta\Phi_2 &= -(\eta'\Delta t + u'\nu(r))\Delta t \\ \Delta q_2 &= u'_P dt\end{aligned}\tag{3.70}$$

**Runge-Kutta step 3 (RK3):**  $t = t_0 + \Delta t/2$  Identical to RK2 except the knowns are updated using the results of RK2, i.e. if  $f$  is the unknown then the new  $f$  is given by

$$f' = f + \Delta f_2/2.\tag{3.71}$$

The solution of the linear system of equations using the vector of knowns yields the updated vector of unknowns. Therefore the changes  $\Delta\eta_3$ ,  $\Delta\Phi_3$  and  $\Delta q_3$  can be computed using the new values of the normal velocity, free-surface elevation and  $q$

$$\begin{aligned}\Delta\eta_3 &= u'\Delta t, \\ \Delta\Phi_3 &= -(\eta'\Delta t + u'\nu(r))\Delta t, \\ \Delta q_3 &= u'_P dt.\end{aligned}\tag{3.72}$$

**Runge-Kutta step 4 (RK4):**  $t = t_0 + \Delta t$  The final step is identical to the previous steps except the updated known quantities are computed by

$$f' = f + \Delta f_3.\tag{3.73}$$

The procedure for updating the unknowns and computing  $\Delta\eta_4$ , etc. is the same as for RK2 and RK3.

**Complete the time-stepping:** The final part of the Runge-Kutta method is to update all quantities so they correspond to the new time  $t = t_0 + \Delta t$ . The formulae for updating the known quantities is

$$\begin{aligned}\eta &= \eta + \Delta\eta_1/6 + \Delta\eta_2/3 + \Delta\eta_3/3 + \Delta\eta_4/6, \\ \Phi &= \Phi + \Delta\Phi_1/6 + \Delta\Phi_2/3 + \Delta\Phi_3/3 + \Delta\Phi_4/6, \\ q &= q + \Delta q_1/6 + \Delta q_2/3 + \Delta q_3/3 + \Delta q_4/6.\end{aligned}\tag{3.74}$$

The unknowns are then updated so as to correspond to time  $t = t_0 + \Delta t$  by solving the linear system of BEM equations.

The Runge-Kutta method is essentially the same for coupled motion problems. However, the equation of motion must be incorporated into the algorithm. The equation of

motion can be written as

$$M\ddot{\xi}_i = F_i^H + F_i^B + F_i^E, \quad i = 1, 3, 5, \quad (3.75)$$

where  $F^H$ ,  $F^B$  and  $F^E$  are the hydrodynamic, hydrostatic (buoyancy) and external forces. The index  $i$  indicates the mode of motion with only surge, heave and pitch permitted. The non-dimensional hydrodynamic force is defined as

$$F_i^H = - \int_S \Phi_t n_i dS \quad (3.76)$$

and this requires the time derivative of the potential  $\partial\Phi/\partial t$  on the surface of the structure. In a similar approach to the decomposition of Cummins (1962), the hydrodynamic force can be written as

$$F_i^H = F_i^t + \ddot{\xi}_i F_i^0 \quad (3.77)$$

where  $F^t$  must be computed at each time step and  $F^0$  only once. If the velocity of the structure is defined as  $v_i = d\xi_i/dt$  then the equation of motion is

$$\dot{v}_i = \frac{F_i^t + F_i^B + F_i^E}{M - F_i^0}. \quad (3.78)$$

The equation of motion can then be written in a form suitable for the Runge-Kutta time-stepping

$$\begin{aligned} \dot{\xi}_i &= v_i, \\ \dot{v}_i &= \frac{F_i^t + F_i^B + F_i^E}{M - F_i^0}, \end{aligned} \quad (3.79)$$

which enables the computation of the displacement  $\xi$  and velocity  $v$  at the next time step. The Runge-Kutta method described previously must then be modified in the following way.

1. In RK1 compute  $\Delta\xi$  and  $\Delta v$  along with  $\Delta\Phi$ ,  $\Delta\eta$  etc. This requires the hydrodynamic force and structure velocity from the previous time step.
2. Update the velocity on the structure surface, in the same way as the other knowns, using  $v + \Delta v/2$  in RK2 and RK3 and  $v + \Delta v$  in RK4.
3. Solve the BEM equations for the unknown quantities.
4. After the computation of  $\Delta\eta$ ,  $\Delta\Phi$  and  $\Delta q$ , determine the force on the structure by numerical integration and then compute  $\Delta v$  and  $\Delta\xi$  using the new force and velocity.
5. Complete the Runge-Kutta method by including  $v$  and  $\xi$  in the final update (3.74) and recompute the force after updating all the variables.

### 3.4.3 Computing the hydrodynamic force

The computation of the hydrodynamic force in both the coupled motion and prescribed motion problems requires the computation of the hydrodynamic force integral (3.76). There are a number of different methods that can be used to compute this integral. An obvious choice is to use numerical differentiation to obtain  $\Phi_t = \partial\Phi/\partial t$ ; however, such a procedure may lead to numerical instability as it is not always accurate particularly in floating body cases. A suggestion by Wu & Eatock Taylor (2003) for nonlinear interactions between waves and bodies was to represent  $\Phi_t$  as another boundary value problem similar to that used to describe  $\Phi$ . However, this method was developed for the coupled motion of the structure and fluid and so is not necessary in the case of radiation or diffraction problems. The method described next is useful for those interactions where the motion is prescribed and it can be modified in a straightforward manner (based on an adaptation of the method by Wu & Eatock Taylor (2003) for linearised interactions) to return the force in the case of coupled motion problems. Koo & Kim (2004) describes a variety of methods to compute the force including the ‘indirect method’ implemented by Wu & Eatock Taylor (2003).

Considering the boundary-value problem for  $\Psi = \partial\Phi/\partial t$ : by differentiation of this boundary-value problem (2.47) for  $\Phi$ ,  $\Psi$  must satisfy

$$\begin{aligned} \nabla^2\Psi &= 0 && \text{in the fluid,} \\ \frac{\partial\Psi}{\partial n} &= 0 && \text{on } z = -h, \\ \Psi &= -\eta - \nu(r)\frac{\partial\Phi}{\partial z} && \text{on } z = 0, \\ \frac{\partial\Psi}{\partial n} &= \ddot{\xi}_i n_i && \text{on } \Gamma. \end{aligned} \tag{3.80}$$

where  $\Psi$  corresponds to the motion in the generalised mode  $i$ . The control surface equation requires the introduction of a new quantity  $Q$  defined by the equation

$$\int_{-1}^0 \Psi(L, \zeta, t) d\zeta = Q \tag{3.81}$$

and related to  $q$  by

$$Q = \frac{dq}{dt} = -u_P \tag{3.82}$$

and since  $u_P$  is updated during the Runge-Kutta method no evolution equation is necessary on the control surfaces. The derivative potential  $\Psi$  is assumed to be known on the free-surface and  $Q$  on the control surface. In the case of radiation and diffraction problems the normal derivative  $\partial\Psi/\partial n$  which equals the acceleration of the body will be known as the motion of the body is prescribed. (The coupled motion problem will be considered separately shortly.) The unknown quantities are  $\partial\Psi/\partial n$  on the free-surface,

$\Psi$  on the structure surface and control surface and the single value  $a = \partial\Psi/\partial n$  on the control surface. Therefore, the form of the boundary value problem for  $\Psi$  is identical to that for  $\Phi$ . The only changes necessary are made to the vector of known quantities. It should be noted that the unknown normal velocities  $u$  on the free-surface and control surface are required before specifying  $\Psi$  on the free-surface; thus, it is necessary to solve the boundary value problem for  $\Phi$  before computing the hydrodynamic force. Once  $\Psi$  has been computed on the surface of the body a simple numerical integration method for cubic splines gives the force.

In the coupled motion problem, the boundary value problem cannot be solved immediately because the acceleration  $\ddot{\xi}_i$ , which gives the term  $\partial\Psi/\partial n$  on the body, is determined by the equation of motion and this depends on  $\Psi$  through the definition of the hydrodynamic force. This difficulty is overcome by introducing the following definition for the derivative potential

$$\Psi = \Psi^0 + \ddot{\xi}_i \Psi^t \quad (3.83)$$

which corresponds directly to the force relation (3.76). The potential  $\Psi^0$  is chosen to be zero on the free-surface and to have a zero contribution to  $Q$  in the equation (3.81). Furthermore, the boundary condition on the structure is simply  $\partial\Psi^0/\partial n = n_i$  so it is independent of time. This potential  $\Psi_0$  is essentially identical to the ‘auxiliary potential’ described by Wu & Eatock Taylor (2003) (apart from the conditions on the control surface which are treated differently in that paper) and corresponds to the infinite frequency problem. On the other hand,  $\Psi^t$  is chosen to satisfy the free-surface condition in (3.80) and also the control surface condition (3.81). Therefore, it depends on time and must be computed at every time-step. After solving these boundary value problems which have an identical form that of  $\Psi$  and integrating  $\Psi_0$  and  $\Psi_t$  over the surface of the body the force components  $F_i^0$  and  $F_i^t$  and hence the total hydrodynamic force can be determined. The equation of motion for the body can then also be solved as described in the last section in order to obtain the dynamics of the structure.

### 3.5 Structure of Fortran code

The Fortran code that implements the numerical time-domain solver has a particular structure related to a key property of the BEM solver for linearised water-wave problems - namely that the solution domain does not change in time. Therefore, in the linear system of equations (3.37) representing the discretised boundary integral equation the only input which changes in time is the vector of knowns  $\mathbf{x}$ ; the system matrices remain the same throughout the time-stepping procedure. Therefore, the computations of the BEM coefficients and subsequent assembly of the system matrix arrays are performed once for a given structure and domain. The system matrices are different for each

Fourier mode  $n$  of the potential expansion and so a loop over the computational algorithm must be implemented with the required number of modes specified in an input file.

The files necessary for the compilation and execution of the BEM computations are listed, in addition to their primary function, next. An essentially hierarchical structure exists:

**nodes.f90** — constructs the nodal distribution for the domain specified by the input files **bem.in** and **geometry.in**,

**parameterise.f90** — computes the parameterisation of the domain boundary using cubic spline functions,

**assmat.f90** — assembles the system matrices by computation of the influence coefficients using the results of the previous files,

**bem.f90** — contains the commands to execute the subroutines specified in the previous files and a looping construct to compute the system matrix data for the number of Fourier modes specified in **bem.in**.

These files are compiled and executed independently from the time-evolution code. The execution of the compiled files generates the following output files:

**node.dat** — contains the  $(r, z)$  coordinate specifications of the nodes and the components of the boundary normal  $(n_r, n_z)$  at each node;

**sysmat1.dat** — contains the BEM coefficients, i.e. the elements of the system matrices  $[H_X]$  and  $[H_Y]$  for each required Fourier node  $n$ ;

**sysmat2.dat** — contains the coefficients describing the discretised control surface equation (3.66);

**sysmat3.dat**, **sysmat4.dat** — contains the force coefficients necessary for the computations of the hydrodynamic force in heave, surge and pitch at each time step.

This data is subsequently utilised in the time-stepping procedure. It is important to note that any simulation featuring the structure and domain geometry specified in **geometry.in** and **bem.in** can be run from this output data. In particular, simulations with different initial conditions, initial wave-profiles and different damping zone properties use the same data output from the BEM part of the code.

The implementation of the time-stepping procedure is contained in the files **march.f90** or **move.f90** for prescribed structure motion problems and for coupled motion problems, respectively, depending on the interaction problem considered. Related subroutines such as that which specifies the initial wave-profile are contained in the module

file **march\_module.f90** or **move\_module.f90**. The program structure in the files containing the time-stepping procedure is as follows:

1. Read the initial conditions and problem specification from **march.in** or **move.in** in addition to the system matrix data.
2. Assemble all the system matrix data (including that relating to the control surface) to represent the discretised time-dependent BIE problem.
3. Initialise the vector of knowns, i.e. specify the initial potential on the free-surface and the initial velocity and displacement of the structure.
4. Run the Runge-Kutta time-stepping procedure.
5. Output the flow and structural motion data.

This algorithm sequence was then placed within a looping construct thus enabling the simulation of the interaction in each successive Fourier mode. The output data files for the flow are **eta.dat**, containing all the free-surface elevation for all free-surface nodes, **elevation.dat**, containing the free-surface elevation for a single node, and for the motion of the structure **motion.dat**, containing the displacement, velocity and acceleration of the structure in the specified Fourier modes.

## Chapter 4

# Boundary element method – development

The central proposal for this project was to develop a time-domain solver to simulate a variety of wave-structure interaction problems. It was hoped that a general solver capable simulating a wide-range of complex interactions such as mode coupling in the structural motion, resonant fluid motion, power take-off by wave-energy devices etc. could be developed. However, prior to simulating these interactions it was necessary to verify the code by considering some standard water-wave problems. Therefore, rather than developing the most general form of the code immediately an incremental approach was taken so that each addition to the code was verified before generalising the code further. In this chapter, the results of the verifications are presented in a chronological order starting from the most basic form of the code.

### 4.1 Verification of BEM computations

The code developed to solve time-domain problems consists of two parts — the boundary element discretisation of the solution domain and the time-marching procedure to advance the solution in time. The time-marching procedure was dependent on the results of the boundary element discretisation, i.e. the linear system generated from the numerical integrations of the influence coefficients, so the BEM part of the code was considered for testing first.

The uniquely solvable linear system of algebraic equations obtained in § 3.3.1 was used for the purposes of verification. The underlying boundary value problem was the

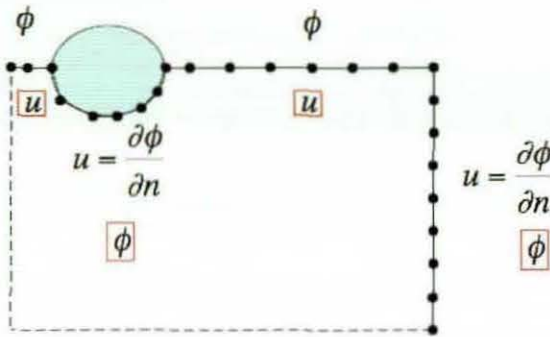


Figure 4.1: A schematic of the verification procedure where the unknown quantities on each boundary segment are surrounded by a red box.

modified three-dimensional problem

$$\begin{aligned} \frac{\partial \phi}{\partial r} (r \frac{\partial \phi_n}{\partial r}) + \frac{\partial^2 \phi_n}{\partial z^2} - \frac{n^2}{r^2} \phi_n(r, z) \cos n\theta &= 0 \quad \text{within the fluid} \\ \frac{\partial \phi_n}{\partial z} &= 0 \quad z = -h \end{aligned} \tag{4.1}$$

where the full three-dimensional potential is assumed to have the form  $\Phi = \phi_n(r, z) \cos n\theta$ . In the discretisation of the modified boundary value problem the normal velocity was assumed known on the structure and control surfaces and the velocity potential on the free-surface sections. The verification procedure was as follows:

- consider a test-potential  $\phi_n^T$  satisfying the boundary value problem (4.1);
- populate the vector of knowns  $\mathbf{x}$  in equation (3.41) by evaluating the specified test-potential and its normal derivative at the relevant nodes;
- numerically solve the linear system to obtain the vector of unknowns;
- compare the solution values to the actual test-potential values at all the relevant nodes.

A diagrammatical representation of the procedure is shown in figure 4.1. Once the relative error in the numerical solution was considered sufficiently small then the code implementing the BEM was assumed to be correct. A true verification of the BEM code required the development of the time-stepping procedure and subsequently a comparison with a solution to a standard water-wave problem.

A simple test-potential satisfying Laplace's equation and the bed condition is

$$\phi_T(r, z) = J_0(kr) \cosh(k(z + h)) \tag{4.2}$$

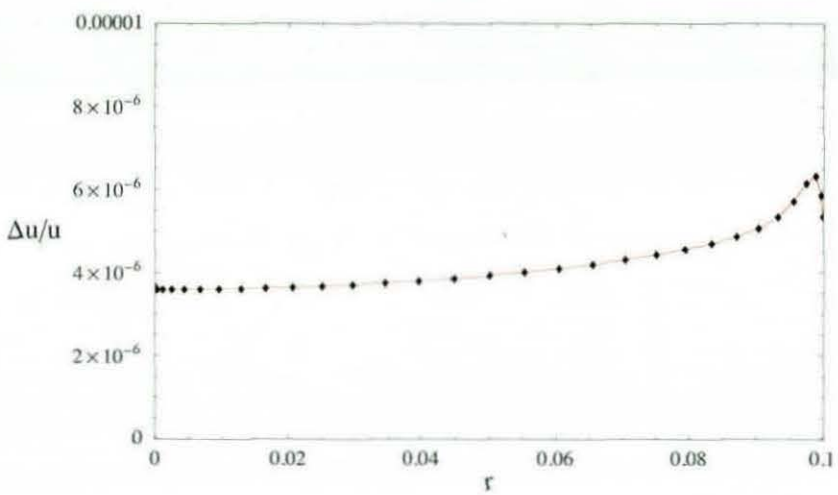


Figure 4.2: Relative error in the computational solution for the normal velocity on the internal free-surface using the test potential (4.2) with  $k = 4.0$ .

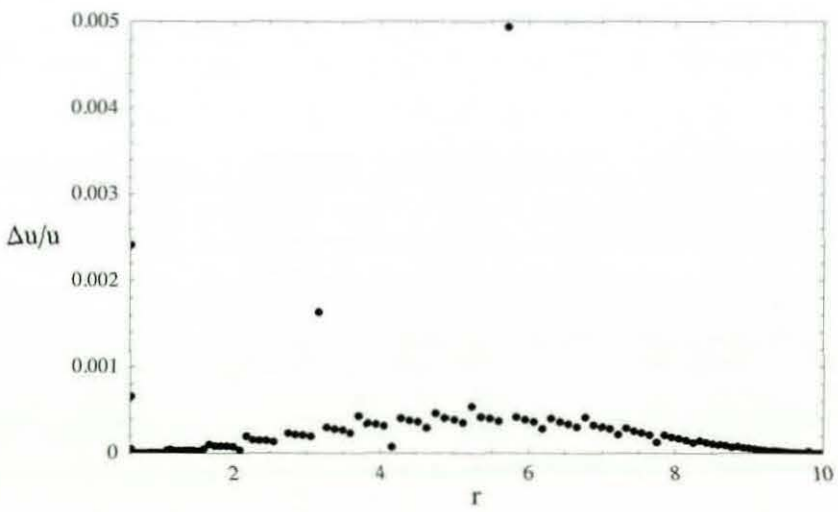


Figure 4.3: Relative error in the computational solution for normal velocity on the external free-surface for the test potential (4.2) with  $k = 4.0$ .

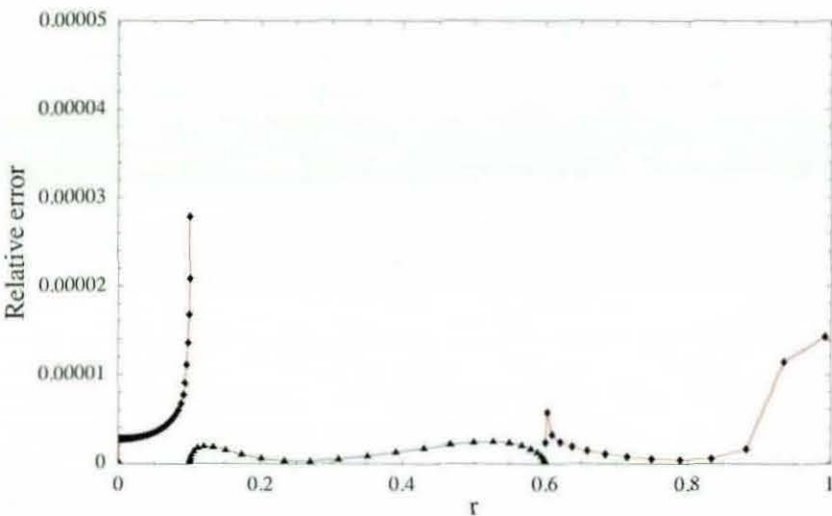


Figure 4.4: Relative error for the normal velocity  $u$  (red) on the free-surface and the potential  $\phi$  (black) on the structure surface for the mode  $n = 1$ .

where  $k$  is effectively the wavenumber of this frequency-domain potential and the depth is assumed to be unity. By specifying the value of  $k$ , it was possible to evaluate  $\phi_T(r, z)$  on the internal free-surface nodes ( $\{(r_{1,i}, z_{1,i}), i = 1, \dots, M_1\}$ ) and on  $(r_{3,i}, z_{3,i})$  for  $i = 1, \dots, M_3$  and similarly  $\partial\phi_T/\partial n$  on the boundaries  $C_2$  and  $C_4$  so as to populate the vector of knowns. In figure 4.2, the error in the numerical solution for  $u = \partial\phi/\partial n$  is shown on the external free-surface nodes for a domain 10 units long containing a torus of tube radius  $a = 0.25$  and axial radius  $c = 0.35$ . The absolute value of the normal velocity is of the order  $O(10^{-2})$  on this boundary section. It was observed that in general the error was largest near the intersection of the structure boundary and free-surface boundary. Thus, despite imposing the continuity of  $\phi$  at the intersections and clustering the nodal distributions around the intersections these discontinuities in the boundary remained problematic for the BEM solver. Nevertheless, the relative error remained quite small throughout the domain apart from the regions of the domain where the absolute value of  $\phi_n^T$  approached zero - this can be observed in figure 4.3 where the error values are significantly larger near the zeroes of  $J_0(4r) = 0$ . In the vicinity of these  $r$ -values the absolute error gives a better indicator of the solution accuracy. It should be noted that the error in  $\phi$  on the structure surface was generally quite small ( $O(10^{-5})$  at most) and that on the control surface the nodes near the sea bed had relative error approaching  $O(10^{-2})$  corresponding to absolute error of  $O(10^{-4})$ .

Further testing was carried out on the  $n = 0$  mode for different geometries and different values of  $k$ . The numerical solution was found to be quite accurate in all cases with less variation in the magnitude of the error for smaller values of  $k$ . Therefore, testing was extended to the modes  $n = 1, 2, \dots$  once the respective BEM routines had been

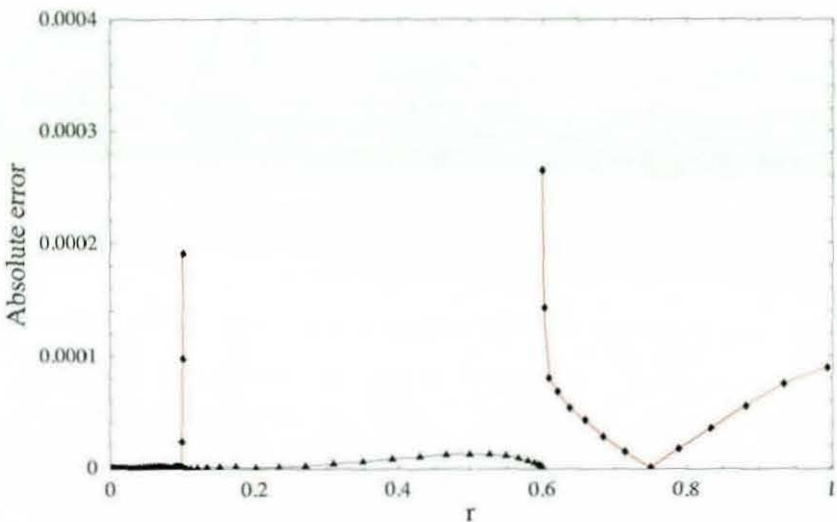


Figure 4.5: Absolute error for the normal velocity  $u$  (red) on the free-surface and the potential  $\phi$  (black) on the structure surface for the mode  $n = 2$ .

implemented. Slight differences in the BEM implementation exist at the axis of symmetry  $r = 0$  for  $n = 0$ , where  $u = \frac{\partial\phi}{\partial n}$  is unspecified, and  $n = 1$ , where  $u = 0$  and the tangential velocity is non-zero. For  $n \geq 2$  the BEM was identical in all cases because the fluid velocity is zero at the axis for all modes. These solution properties can be observed by considering an eigenfunction expansion of the potential in terms of the cylindrical coordinates and evaluating  $\frac{\partial\Phi}{\partial z}$  and  $\frac{\partial\Phi}{\partial r}$  at  $r = 0$  for each  $n$ . Therefore, only a sample of  $n$  values were investigated once  $n = 0, 1$  had been verified. In figure 4.4 the relative error for the unknowns on the inner free-surface, structure surface and outer free-surface, corresponding to the radial ranges  $0 \leq r < 0.6$ ,  $0.6 < r < 1.0$  and  $r \geq 1.0$  for the torus geometry described previously, are plotted for the  $n = 1$  azimuthal mode. Finally, the *absolute* error for the same geometry is shown in figure 4.5 for the mode  $n = 2$  and provides a good example of the increase in the error near the intersections of the structure and free-surface. The average error in both the potential and the normal velocity was  $O(10^{-4})$  for this computation.

## 4.2 Verification of time-stepping results

In this section, the numerical solutions of the time-domain equations are verified using the solutions of initial-value problems. Given that the BEM computations have been verified, the next step in the development of the time-domain solver was to implement and verify the time-stepping procedure. Initially, only very simple problems such as the harmonic forced heave motion of the structure were considered. Therefore, a variety of radiation, diffraction and wave propagation problems are first considered. Thereafter,

verifications of the coupled-motion code are provided.

#### 4.2.1 Radiation and diffraction problems

In a radiation problem, the fluid response to the forced motion of a structure is sought. The structure moves according to a prescribed velocity which may comprise a number of modes of motion. The response of the fluid is described by the hydrodynamic force on the structure and the free-surface elevation of the surrounding fluid. By prescribing the structure velocity to correspond to a standard radiation problem the hydrodynamic force and, if necessary, free-surface elevation can be compared to previous computations for confirmation of the validity of the time-marching code.

One of the simplest radiation problems is to determine the fluid response to the forced harmonic oscillations of a sphere in heave. Solutions for this problem date back to 1955 when Havelock developed a semi-analytical method to determine the hydrodynamic force on the structure and had produced some preliminary computational results. Many other authors have developed methods to determine the solution to this and other radiation problems and so finding previous results for comparison is not difficult. However, the commercial software WAMIT (see <http://www.wamit.com/>) is an efficient and accurate frequency-domain solver which can compute the forces and free-surface elevations in radiation, diffraction and coupled motion problems involving structures with arbitrary geometries. To use the frequency-domain results for the purposes of comparison, the prescribed oscillatory motion of the structure in the time-domain must be harmonic. The long-time or asymptotic time-domain response to the regular forcing should then agree with the WAMIT computational results. In the simulation results presented next, only structures which do not enclose a portion of the free-surface were considered. Toroidal structures which enclose a portion of the free-surface generally excite slowly decaying resonances and so the time taken for the motion to settle to a steady oscillation is much larger for torus-type structures. Therefore, analysing the validity of the code using the structures which do not enclose a portion free-surface is far less time-consuming and much more practical.

A comparison of the time-domain solver and WAMIT computations for the hydrodynamic force on a sphere of radius  $a = 0.3h$  due to the forced harmonic heave oscillations of the sphere is shown in figure 4.6. In both computations the frequency of oscillation is  $\omega = \sqrt{g/h}\sqrt{4.0 \tanh 4.0}$  (in non-dimensional terms this is  $\Omega = \sqrt{4.0 \tanh 4.0}$ ). The prescribed heave velocity in the time-marching algorithm is  $V(t) = \cos \omega t$ . The WAMIT computations return, among other data, the non-dimensional added mass  $\tilde{a}_{33}$  and damping coefficients  $\tilde{b}_{33}$ , at the specified frequencies. From Newman & Lee (1995)

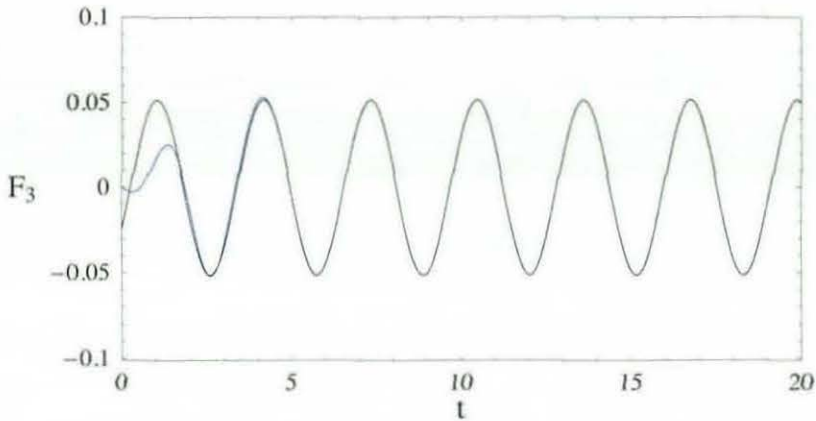


Figure 4.6: Comparison of the non-dimensional radiation force computations using the BEM time-stepping method (blue) to the WAMIT results (black) for a heaving hemisphere.

it can be shown that the time-harmonic frequency-domain heave force is

$$F_3^H(t) = \operatorname{Re}\{-i\omega(a_{33} - i\frac{b_{33}}{\omega})u_3 e^{i\omega t}\} \quad (4.3)$$

where  $a_{33}$ ,  $b_{33}$  and  $u_3$  are, respectively, the added mass, damping coefficient and heave velocity amplitude. The computational results are expressed in terms of dimensionless quantities and so it is necessary non-dimensionalise the time  $t$ , frequency  $\omega$ , added mass  $a_{33}$  etc. as follows:

$$\begin{aligned} t &= \tilde{t}T, & \omega &= \Omega/\sqrt{g/h}, & u_3 &= \tilde{u}_3 h, \\ a_{33} &= \tilde{a}_{33} \rho h^3, & b_{33} &= \tilde{b}_{33} \rho h^3 \omega, \end{aligned} \quad (4.4)$$

in terms of the density  $\rho$ , the finite depth  $h$  and the acceleration due to gravity  $g$ . Therefore, the time scale  $T$  is  $\sqrt{h/g}$ , the mass scale  $\rho h^3$  and the length scale  $h$ . The substitution of these definitions into the heave force expression (4.3) gives

$$F_3^H(t) = \rho h^3 \operatorname{Re}\{-i\frac{\Omega}{\sqrt{h/g}}(\tilde{a}_{33} - i\tilde{b}_{33})\tilde{u}_3 \frac{h}{\sqrt{h/g}} e^{i\Omega \tilde{t}}\} \quad (4.5)$$

and the subsequent division through the equation by  $\rho gh^3$  (the force scale) yields the following expression for the non-dimensionalised harmonic force denoted by  $\tilde{F}_3^H(\tilde{t})$ :

$$\tilde{F}_3^H(\tilde{t}) = \operatorname{Re}\{-i\Omega(\tilde{a}_{33} - i\tilde{b}_{33})\tilde{u}_3 e^{i\Omega \tilde{t}}\}. \quad (4.6)$$

This gives an expression for the non-dimensionalised force in terms of the non-dimensional added mass and damping coefficients computed by WAMIT at the non-dimensional frequency  $\Omega$  for a given velocity amplitude. In the time-domain computations, the

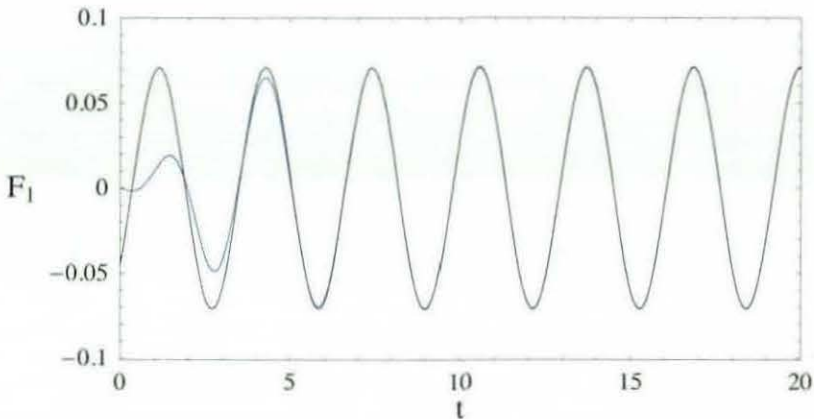


Figure 4.7: Comparison of the BEM time-stepping results (blue) to the WAMIT results (black) for the computation of the non-dimensional surge force on a surging hemisphere.

prescribed velocity is of unit amplitude, i.e.  $V_3(t) = \cos(\omega t)$ , so that the corresponding complex velocity amplitude is  $\tilde{u}_3 = 1$ . Therefore, if the time-marching algorithm is used to compute the non-dimensionalised time-dependent radiation force  $\tilde{F}_3^T(\tilde{t})$  for a harmonic unit forcing then after the initial transient it should agree closely with the results for  $\tilde{F}_3^H(\tilde{t})$  corresponding unit complex velocity amplitude provided the time-domain code is correct. In figure 4.6 and all the subsequent figures in this section, the *non-dimensional* radiation forces as computed by time-domain solver and WAMIT are compared although the dimensional notation  $F_3(t)$  is used. In the case of the heaving hemisphere the results coincide after a short transient thus verifying the time-marching algorithm as applied to the axisymmetric term in the potential expansion  $\Phi(r, \theta, z, t) = \sum_{n=0}^{\infty} \phi_n(r, z, t) \cos n\theta$ .

The time-stepping of the forced heave motion simulation utilises the BEM coefficients corresponding to the axisymmetric mode only. Therefore, it is necessary to extend the time-stepping procedure to include the  $\cos \theta$  term in the Fourier expansion of the total potential  $\Phi$  to verify any surge or pitch computations. In the surge result comparisons the structure geometry and the frequency of oscillation are identical to that in the heave analysis. The transient build-up of the surge radiation force on a hemisphere to a steady oscillation due to the prescribed surge motion

$$\frac{\partial \Phi}{\partial n} = n_1 \cos \omega t \quad \text{on } \Gamma, \quad (4.7)$$

where  $n_1$  is the normal in the (horizontal) surge direction, is shown in figure 4.7 with the time-harmonic result. Again the computations agree to high-degree of accuracy after a short transient. It should be noted that on a structure with a vertical axis of symmetry, the  $x$ -component of the normal is given by  $n_x = n_r \cos \theta$  and so the boundary condition is just  $\frac{\partial \phi_1}{\partial n} = n_r \cos \omega t$  once the  $\cos \theta$  term has been factored out. So, just



Figure 4.8: The wetted surface of a half-immersed prolate spheroid of waterplane radius  $a = 0.2h$  and draft  $0.5h$ .

as in the heave simulation, only the BEM coefficients corresponding to the  $n = 1$  term of the BIE (3.17) are utilised in this computation. No coupling will occur between the modes. Furthermore, to reduce numerical problems related to jump-discontinuities in the velocity and acceleration the prescribed velocity is smoothly ramped from 0 to  $\cos \omega t$  over the first period of motion.

The forced motion of a body in the pitch mode must also be analysed using the  $\phi_1(r, z, t) \cos \theta$  term. This can be seen by considering the boundary condition on the structure

$$\frac{\partial \Phi}{\partial n} = n_5 \cos \omega t \quad \text{on } \Gamma, \quad (4.8)$$

where  $n_5 = zn_1 - xn_3$  is the pitch component of the generalised normal with  $n_3$  being the heave or vertical component  $n_z$  of the normal. For a structure with a vertical axis of symmetry,  $n_5 = (zn_r - rn_z) \cos \theta$  and so the pitch computations will involve only the  $n = 1$  BEM coefficients. To verify the pitch motion simulations a half-immersed prolate spheroid with a circular horizontal cross section of radius  $a = 0.2h$  and vertical major axis  $0.5h$  was considered. A three-dimensional image of the structure is shown in figure 4.8. A hemisphere could not be used in the pitch simulations because waves cannot be generated by motion in any of the rotational modes due to the inviscid fluid assumption inherent in the linearised framework. The forcing frequency was the same as in the heave computations. Two sets of results are illustrated in figure 4.9. The first compares the time-dependent and time-harmonic hydrodynamic pitch forces due to the regular oscillatory pitch motion of the structure whereas the second compares the time-dependent and time-harmonic surge forces due to the pitch motion. In both cases the

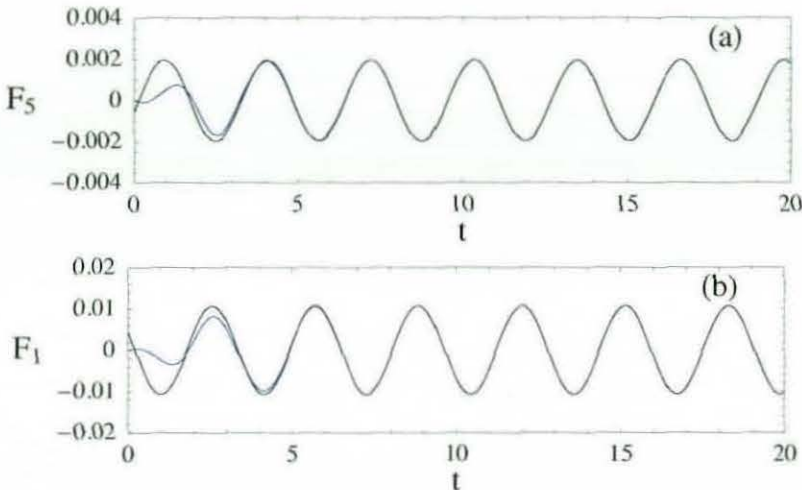


Figure 4.9: Comparison of the time-domain (blue) and frequency domain (black) computations of the non-dimensional radiation force in pitch (a) and surge (b) due to the pitching motion of a prolate spheroid.

agreement is very good between the time-stepping simulation and the WAMIT results. It should be noted that the pitch and surge modes are coupled and that motion in the surge mode will generate pitch forces on the structure and *vice versa*.

The final verification of the time-stepping procedure implementation in the time-domain code is obtained by the simulation of the combined motion of a structure in heave and pitch. The free-surface elevation at a specific position in the fluid, instead of the hydrodynamic forces, was measured and compared to the frequency domain results to ensure the combination of results from different Fourier modes could be achieved. The boundary condition on the structure for this simulation is

$$\frac{\partial \Phi}{\partial n} = (n_3 + n_5) \cos \omega t \quad \text{on } \Gamma \quad (4.9)$$

and it describes a combined oscillatory motion in heave and pitch with unit velocity amplitudes in both modes. Decomposing the equation using the Fourier expansion yields two separate boundary conditions: one concerning the axisymmetric motion

$$\frac{\partial \phi_0}{\partial n} = n_z \cos \omega t, \quad (4.10)$$

and the other concerning the motion associated with the  $\cos \theta$  dependence

$$\frac{\partial \phi_1}{\partial n} = (zn_r - xn_z) \cos \omega t. \quad (4.11)$$

The free-surface elevation  $\eta$  was then computed at a particular position  $(r_0, \theta_0)$  in the  $n = 0$  and  $n = 1$  BEM time-stepping procedures and the results combined using the

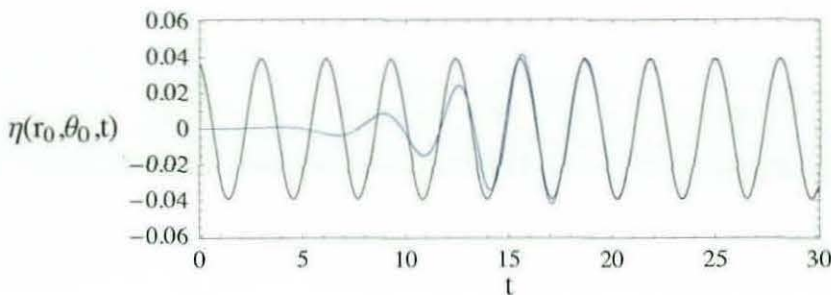


Figure 4.10: Free-surface elevation at  $(r_0, \theta_0) = (2.65, 0)$  due to the combined heave and pitch motion of a prolate spheroid as computed by the BEM solver (blue) and WAMIT (black).

Fourier series expansion

$$\eta(r_0, \theta_0, t) = \eta_0(r_0, \theta_0, t) + \cos n\theta_0 \eta_1(r_0, \theta_0, t). \quad (4.12)$$

The comparison with WAMIT results are shown in figure 4.10 and a good agreement is obtained.

Verifying the time-domain diffraction simulations proved somewhat problematic. In contrast to the radiation problem, it was practically impossible to generate an indefinite oscillatory motion. That is, it was not possible to introduce a semi-infinite regular wave train into the domain and so it was impossible to generate steady scattered wave motion. Two methods for wave-generation within the BEM formulation are: impose an initial wave-profile with a primary component consisting of a regular single-frequency incident wave; treat the piston control surface as a piston wave-maker and force it to oscillate so as to create regular waves. Each method has some inherent difficulties that cannot easily be overcome. In the case of the initial wave-profile generation method, the domain is of finite horizontal extent and thus so is the resultant wave-train. Furthermore, the non-regular wave-train components (necessary to ensure the continuity of the initial wave-profile) will interfere with the regular component as the wave propagates. Such problems can be observed in the heave exciting force plot in figure 4.11. In this interaction, a wave-train resultant from an initial wave-profile of finite extent and dominant frequency  $\omega = \sqrt{g/h} \sqrt{2.5 \tanh 2.5}$  is diffracted by a hemisphere of radius  $a = 0.3h$ . The agreement between the computational methods is good for a short period of time after the initial transient; however as the simulation proceeds the dispersion effects due to finite nature of the wave-train begin to show and the results diverge. This interaction involves the axisymmetric  $n = 0$  mode only and higher order modes are not considered. In the case of the wave-maker, the time taken for the motion to settle into steady oscillations is very long for a domain of radius  $10h$ . Reducing the size of the domain will not necessarily improve matters as treating the control-surface as

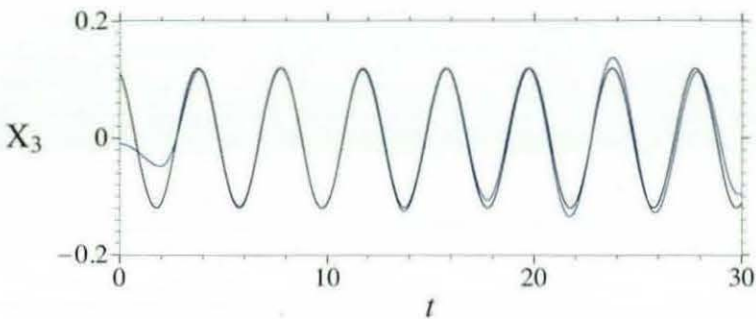


Figure 4.11: Heave exciting force on a hemisphere of radius  $a = 0.3h$  as computed by BEM solver (blue) and WAMIT (black) due to the diffraction of a finite wave train.

a piston wave-maker reduces its absorption capabilities and so artificial reflections will become problematic. For a small domain the appearance of artificial reflection effects will occur much sooner in the simulation than for a larger domain. A more detailed discussion of the wave generation methods for a time-domain BEM solver is given in the next chapter.

#### 4.2.2 Cauchy-Poisson problem

Thus far, the time-stepping procedure has been applied only to the azimuthal modes  $n = 0$  and  $n = 1$  which relate to the dynamics of the structure in expansion (3.9). Also, all the previous simulations have featured time-harmonic motions only. Therefore, the higher order modes of fluid motion  $n \geq 2$  must be investigated and if possible more general time-dependent motions verified. These higher order modes are important in diffraction problems involving plane waves as the accurate description of such interactions require all the modes in the Fourier azimuthal expansion of the motion.

To verify the time-stepping of the higher order modes the classical initial-value water-wave problem known as the *Cauchy-Poisson* problem is solved using numerical and semi-analytical methods. In this problem, the initial elevation and velocity of the free-surface is given and the subsequent motion of the fluid is sought. The initial disturbance is assumed to be of finite extent and to satisfy some continuity conditions. Furthermore, the fluid domain is assumed to be of infinite horizontal extent, free of obstacles and to have a finite depth  $h$  at rest. It is important to note the absence of the structures as hitherto only domains containing structures have been investigated. Nevertheless, the changes to the BEM are relatively straightforward; in fact the formulation of the linear system of equations is much simpler without the presence of a structure.

To solve the Cauchy-Poisson problem independently of the time-domain solver the following solution method is employed. The potential  $\Phi$  and free-surface elevation  $\eta$

are expanded as Fourier series in the azimuthal angle  $\theta$  and the contribution to the total motion at each mode  $n$  is then determined from the reduced water-wave equations

$$\begin{aligned} \frac{1}{r} \frac{\partial}{\partial r} \left( r \frac{\partial \phi_n}{\partial r} \right) + \frac{\partial^2 \phi_n}{\partial z^2} - \frac{n^2}{r^2} \phi_n &= 0 && \text{in } \Omega, \\ \frac{\partial \phi_n}{\partial z} &= 0 && z = -h, \\ \frac{\partial \phi_n}{\partial t} + g\eta_n &= 0 && z = 0, \\ \frac{\partial \phi_n}{\partial z} &= \frac{\partial \eta_n}{\partial t} && z = 0. \end{aligned} \quad (4.13)$$

The initial value problem is completed by the specification of the initial conditions

$$\begin{aligned} \eta_n(r, 0) &= \eta_{0n}(r) \\ \phi_n(r, 0, 0) &= \phi_{0n}(r) \end{aligned} \quad (4.14)$$

and requires that  $\phi_n$  and  $|\nabla \phi_n|$  vanish as  $r \rightarrow \infty$  for uniqueness. The Hankel transform

$$F(k) = \int_0^\infty r f(r) J_n(kr) dr \quad (4.15)$$

must then be applied to the equations and conditions describing the initial-value problem. The reduced Laplace's equation and the bed condition then become

$$\begin{aligned} \frac{\partial^2 \Phi_n^*}{\partial z^2} - k^2 \Phi_n^* &= 0, \\ \frac{\partial \Phi_n^*}{\partial z} &= 0 && z = -h, \end{aligned} \quad (4.16)$$

under the Hankel transformation, where  $\Phi_n^*(k, z, t)$  is the Hankel transform of  $\phi_n$ . The general solution of this boundary value problem is

$$\Phi_n^* = A(k, t) \cosh k(z + h). \quad (4.17)$$

The free-surface conditions and initial conditions are then used in order to obtain the time dependence of  $A(k, t)$ . The Hankel transform of the free-surface elevation is denoted as  $H_n^*(k, t)$  and the initial profile as  $H_{0n}^*(k)$ . Assuming the potential is initially zero, the transformed free-surface elevation is determined from the free-surface conditions to be

$$H_n^*(k, t) = H_{0n}^*(k) \cos(\omega t) \quad (4.18)$$

and so the physical free-surface elevation is given by the inverse Hankel transform

$$\eta_n(r, t) = \int_0^\infty k H_{0n}^*(k) \cos \omega t J_n(kr) dk. \quad (4.19)$$

Given the quantity  $H_{0n}^*$ , the free-surface elevation is determined by numerical integra-

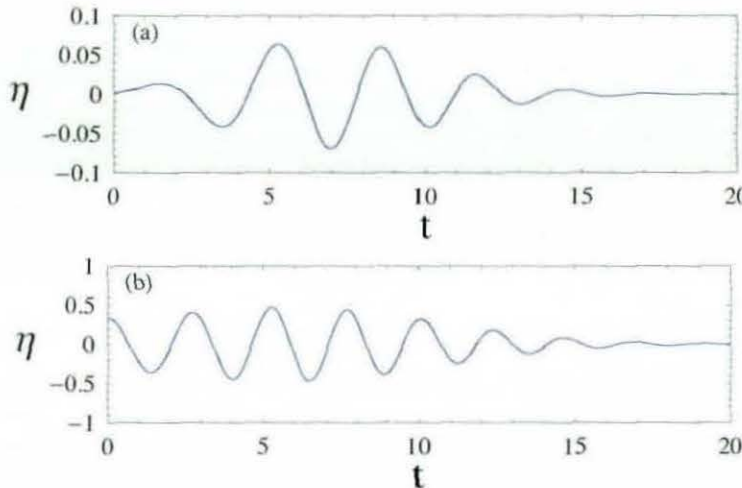


Figure 4.12: Comparison of the BEM (blue) and semi-analytic (black) computations of  $\eta(r, t)$  at  $r = 2.0$  given the initial condition (4.22) with  $\alpha = 2$  for (a)  $n = 2$  and (b)  $n = 10$ .

tion of (4.19) for a specific value  $r_0$  of the radial coordinate. In the BEM time-domain solver, the evolution of the total free-surface can then be found by time-stepping the solution from  $t = 0$ . The initial free-surface elevation is computed by numerical integration of the specified Hankel transform  $H_{0n}^*$

$$\eta_n(r, 0) = \int_0^\infty k H_{0n}^*(k) J_n(kr) dk. \quad (4.20)$$

Therefore, a comparison to the results determined using (4.19) can be obtained by outputting the free-surface evolution results at  $r = r_0$  from the BEM solver. The initial Hankel transform of  $H_{0n}^*(k)$  was chosen to be

$$H_{0n}^* = \frac{k^n e^{-k^2/4\alpha}}{(2\alpha)^{n+1}} \quad (4.21)$$

which corresponds to an initial free-surface elevation

$$\eta_n^*(r, 0) = r^n e^{-\alpha r^2}. \quad (4.22)$$

A comparison of results is shown for  $n = 2$  and  $n = 10$  in figure 4.12 and the agreement is generally excellent. It should be noted that other methods of solution exist for the Cauchy-Poisson problem, for example Wehausen & Laitone (1960) considered the problem in detail.

### 4.2.3 Coupled motion simulations

In the previous subsection, the time-stepping method was verified for radiation, diffraction and wave-propagation problems. However, the time-domain solver must also be capable of simulating coupled motion interactions wherein the structure is free to respond to incident waves. As described in chapter 3 the time-advancement algorithm for the coupled motion problem is more complex than for the prescribed motion problems. So, to further generalise the scope of the solver the equation of motion for the structure was incorporated into the time-advancement algorithm. Therefore, a separate verification procedure is employed to ensure the validity of this new time-stepping implementation.

It was mentioned in chapter 2 that very few time-domain solutions based on analytical methods exist for floating body problems. Ursell (1964) determined analytic functions to describe the vertical motion of a half-immersed horizontal circular cylinder and Beck & Liapis (1987) determined the free vertical motion of half-immersed sphere. The paucity of available results for the coupled motion of a floating body and the surrounding fluid meant that an alternate method of verifying the BEM solver results was needed.

Maskell & Ursell (1970) numerically investigated the functions determined by Ursell (1964) which relate to the problem of a horizontal circular cylinder given either an initial displacement or velocity. It was concluded that the motion is damped harmonic after an initial transient and before an asymptotically large time elapses. This dominant damped harmonic term  $e^{-i\omega_r t}$  is determined by the location, in the complex  $\omega$ -plane, of a pole in the frequency-domain velocity (2.68). As shown in § 2.2.2, for a structure constrained to move in one mode only the location of this pole is given by the solution for  $\omega$  of

$$c_{\mu\mu} - \omega^2 [M_{\mu\mu}\delta_{\mu\mu} + a_{\mu\mu}(\omega) + i(b_{\mu\mu}(\omega) + \gamma_{\mu\mu})/\omega] = 0, \quad (4.23)$$

i.e. the zero of the denominator of the frequency-domain velocity expression determined by consideration of the equation of motion of the body. The estimate is obtained using the following procedure outlined by Maskell & Ursell (1970):

- the first approximation  $\omega_1$  to the complex resonance location is taken as the zero of the equation (4.23);
- the so-called ‘tangent approximation’ or first order correction to this approximation is then

$$\omega_2 = \omega_1 - \frac{Q(\omega_1)}{Q'(\omega_1)} \quad (4.24)$$

where  $Q(\omega) = c_{\mu\mu} - \omega^2 [M_{\mu\mu}\delta_{\mu\mu} + a_{\mu\mu}(\omega) + i(b_{\mu\mu}(\omega) + \gamma_{\mu\mu})/\omega]$ .

- the resultant approximation will be a complex number with the real part giving

the estimate for the resonant frequency  $\omega_0$  and the imaginary part the estimate for the decay constant  $\epsilon$ .

A similar method will be employed in the next chapter when considering sloshing resonances, i.e. resonances arising in radiation and diffraction problems. The resonances occurring in water-wave problems involving freely-floating structures are referred to as motion resonances and a comprehensive discussion of the different properties possessed by the two types of complex resonances is given by McIver (2005). Since the added mass and damping coefficients of an arbitrary structure can easily be computed using WAMIT an estimate of the location of the motion resonance and hence of the properties of the time-dependent motion can be obtained independent of the time-domain BEM solver. Exact details of this method are provided for the case of a heaving hemisphere. A verification of the time-domain BEM solver can thus be obtained by comparing the frequency-domain predictions to the time-domain results.

The time-domain simulations for the coupled motion of floating structures which are to be validated are restricted in scope. Firstly, only motion in one mode is permitted so that heave, surge and pitch motions will be verified independently. Secondly, only simulations without an incident wave and a non-zero initial structural displacement or velocity are considered. However, simulations involving structures which do not enclose a portion of the free-surface and those which do (i.e. toroidal-type structures) will be investigated in heave, surge and pitch. A description of the verification procedure for a heaving sphere is given next. Thereafter, a table of results will be presented summarising the results of all the time-domain and frequency domain computations.

Consider a freely floating half-immersed sphere permitted to move in heave only. The sphere has a radius of  $a/h = 0.3$  and is given an initial displacement of  $X_0/h = 1$ . The initial velocity is assumed to be zero. Once released the sphere will oscillate with a damped harmonic motion after an initial transient. Although the motion will eventually become algebraic decay this will only occur when the amplitude of motion is extremely small. The fluid surrounding the structure will initially be at rest but as the energy radiates from the structure it will oscillate in a coupled manner with the structure. The time-domain BEM solver results for the variation in the vertical displacement of the structure and the free-surface elevation with time are shown in figure 4.13. The information desired is the frequency and decay time of the structure's oscillation. Therefore, the discrete Fourier transform of the signal  $X_3/h$  is taken and the results are shown in figure 4.14. To compute the decay constant of the structure motion a least-squares linear fit is applied to the data set consisting of the time at which each local maximum occurs and the log of the respective displacement amplitudes. In this case it was computed to be approximately 0.172.

The frequency-domain predictions for the resonant frequency and decay time of the

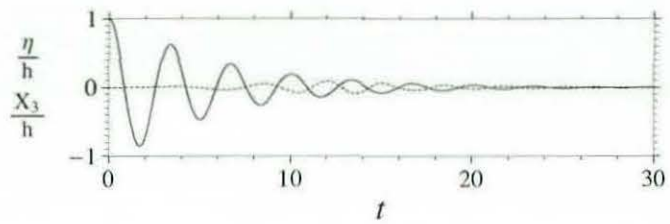


Figure 4.13: Release from rest of a freely floating sphere: free-surface elevation  $\eta$  at a distance  $r/h = 2.725$  from the axis of symmetry (---) and the displacement  $X_3/h$  of the structure (—)

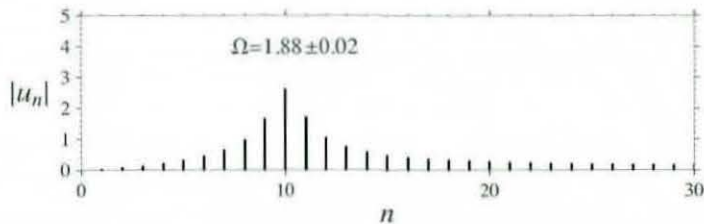


Figure 4.14: Discrete Fourier transform of the heave displacement given in figure 4.13.

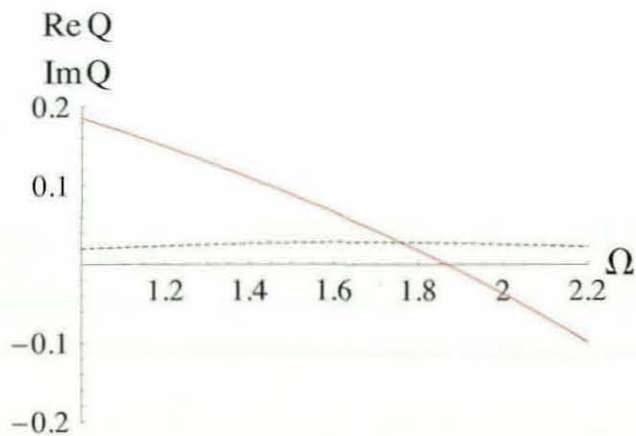


Figure 4.15: Variation of the  $\text{Re } Q$  (red) and  $\text{Im } Q$  (---) with non-dimensional frequency  $\Omega$  in the vicinity of the motion resonance.

			Complex Resonance Estimate	
Structure	Mode	Mooring	Time-domain	Frequency-domain
Hemisphere	Heave	$k_{33} = 0.00$	$1.89 \pm 0.02 - i0.172$	$1.87 - i0.173$
	Surge	$k_{11} = 0.25$	$1.59 \pm 0.02 - i0.117$	$1.59 - i0.122$
	Pitch	$k_{55} = 0.01$	$0.99 \pm 0.02 - i0.00435$	$0.99 - i0.00430$
Torus	Heave	$k_{33} = 0.00$	$2.43 \pm 0.02 - i0.00922$	$2.44 - i0.00924$
	Surge	$k_{11} = 1.25$	$2.20 \pm 0.02 - i0.255$	$2.19 - i0.259$
	Pitch	$k_{55} = 0.05$	$2.10 \pm 0.02 - i0.0870$	$2.10 - i0.087$

Table 4.1: Comparison of frequency- and time-domain results for the location of the motion resonance in the freely-floating body simulations.

heave oscillation require the computation of the non-dimensional velocity coefficient  $Q(\Omega)$  which in the heave mode is  $W - \Omega^2(M + \mu(\Omega) + i\nu(\Omega))$  where  $\Omega$ ,  $\mu$  and  $\nu$  are the non-dimensional frequency, added mass and damping, respectively and  $M$  and  $W$  are the mass and waterplane area of the structure. The waterplane area term arises from the coefficient  $c_{\mu\nu} = \rho g W b_\mu \delta_{\mu\nu} + k_{\mu\nu}$  in the dimensional equation of motion 2.51 where  $k_{\mu\nu}$  is the mooring spring coefficient matrix chosen to be zero here and  $b_3 = W$ . The behaviour of the real and imaginary parts are illustrated in figure 4.15. To obtain the frequency dependence of  $Q$ , the added mass and damping coefficients were computed at discrete frequencies using WAMIT and the resultant data was numerically interpolated using *Mathematica* to form essentially continuous functions. It was straightforward to then determine the function  $W - \Omega^2(M + \mu_{33}(\Omega) + i\nu_{33}(\Omega))$ . The zero  $\Omega_1$  of  $\text{Re } Q$  corresponds to a peak in the value of  $1/|Q(\Omega)|$  and this in turn indicates the presence of a pole in  $1/Q$  in the complex plane with a real part close to  $\Omega_1$ . Therefore, once  $\Omega_1$  was determined using a root-finding method the tangent approximation  $\Omega_1 - Q(\Omega_1)/Q'(\Omega_1)$  was computed and yielded the estimate  $\Omega - i\epsilon = 1.873 - i0.173$  for the pole location. Comparing these values to the time-domain results ( $\Omega = 1.885 \pm 0.02$ ,  $\epsilon = 0.172$ ) it is clear there is very good agreement. This consistency indicates that the generalisation of the time-domain solver is correct and that it should be possible to solve surge and pitch problems also.

The motion of a freely floating body in surge poses a problem not present in the heave mode. The existence of the hydrostatic restoring force term  $\rho g W X_3$  in the heave equation of motion ensures the structure returns to equilibrium when given an initial displacement or velocity. No such term exists in the surge equation of motion so that if a structure is given an initial surge velocity with the fluid initially at rest then in general it will move indefinitely away from the equilibrium. Some particular cases may exist where continuing translation of the structure does not occur and this will be discussed in more detail next. Nevertheless, in most surge problems for freely floating bodies it is necessary to impose a mooring constraint by introducing a positive spring coefficient  $k_{11}$  to ensure the motion of the structure is oscillatory. In the equation of

motion  $c_{11} = k_{11} > 0$  and the velocity coefficient in the frequency domain is  $k_{11} - \Omega^2(M + \mu_{11}(\Omega) + i\nu_{11}(\Omega))$ . The frequency-domain and time-domain computations for the location of the complex resonance were performed in an identical manner to the heave case. The results for a half-immersed sphere of radius  $a/h = 0.3$  and for a half-immersed torus of tube radius  $a/h = 0.25$  and axial radius  $c/h = 0.35$  are shown in table 4.1. The pitch equation of motion does contain a hydrostatic term  $c_{55} = k_{55} + (I_{11}^A + I_3^V)$ , however, it can be positive or negative depending on the  $z$ -component of the centre of buoyancy  $I_3^V$  and the moment of the waterplane area  $I_{11}^A$ . This contrasts with the heave mode where the coefficient is always positive for a surface-piercing structure. So, depending on the structure it may be necessary to choose a positive pitch mooring spring coefficient  $k_{55}$  to ensure the structure will oscillate with a decaying amplitude. In the case of the prolate spheroid shown in figure 4.8 and the torus described above the spring coefficient was chosen to be positive in both cases. The results for pitch are also given in table 4.1. The agreement between the time-domain and frequency domain estimates is seen to be excellent in all modes and for geometries that enclose and do not enclose part of the free-surface.

#### 4.2.4 Free surge motion of a torus

An interesting question arises when considering the horizontal motion of a freely floating body. If no mooring restoring force is imposed is it possible to obtain an oscillatory horizontal motion without continuing translation given a non-zero initial velocity? In general the horizontal displacement of the structure will become unbounded, however it may be possible to excite a motion that does not become unbounded without the presence of a restoring force. This question should be addressed both analytically and numerically and it is expected that a consistent answer will result from both investigations.

To address the question analytically the frequency domain velocity expression (2.68) is considered in the case of the surge mode with both  $c_{11} = k_{11} = 0$  and  $\gamma_{11} = 0$  and the possibility of an applied force. The non-dimensional form is then

$$v_1(\omega) = \frac{i\{(M + \mu_{11}(\infty))V_1(0) + f(\omega)\}}{\omega [M + \mu_{11}(\omega) + i\nu_{11}(\omega)]} \quad (4.25)$$

where the term  $f(\omega)$  is the Fourier transform of the applied force  $F(t)$ . The inverse Fourier transform of  $v_1(\omega)$  gives the time-domain velocity  $V_1(t)$ ; the asymptotic limit of this integral as  $t \rightarrow \infty$  is of most interest as it will indicate whether or not continuous displacement of the structure will occur. Also of interest is the displacement function  $X_1(t)$  whose Fourier transform is related to the velocity transform by

$$v(\omega) = -X(0) - i\omega x(\omega) \quad (4.26)$$

and  $X(0) = 0$  will generally be assumed. The Riemann-Lebesgue lemma states that if the velocity  $v_1(\omega)$  is absolutely integrable, i.e.  $\int_0^\infty |v_1(\omega)|d\omega < \infty$ , then the inverse Fourier transform for  $t \rightarrow \infty$  will be zero. For horizontal motion in finite depth the following results are known

$$\begin{aligned}\mu_{11}(\omega) + \nu_{11}(\omega) &\rightarrow \mu_{11}(0) \neq 0 \quad \text{as } \omega \rightarrow 0 \\ \mu_{11}(\omega) + \nu_{11}(\omega) &\rightarrow \mu_{11}(\infty) \neq 0 \quad \text{as } \omega \rightarrow \infty\end{aligned}\tag{4.27}$$

so that if  $V_1(0) \neq 0$  then in general  $v_1(\omega)$  will not be absolutely integrable because of the singular behaviour as  $\omega \rightarrow 0$ . However, it is possible that  $V_1(t) \rightarrow 0$  despite  $v_1(\omega)$  not being absolutely integrable. However, it is generally true that if a structure is given an initial horizontal velocity it will continue to move away from equilibrium as time increases although superposed oscillatory motion may occur along with the translational motion.

However, if  $V_1(0) = 0$  is assumed then the transform of the applied force function  $F(t)$  determines absolute integrability of the velocity function. If the forcing is chosen to be a finite oscillation such as

$$F(t) = \begin{cases} \cos(\Omega t), & 0 \leq t \leq 2\pi/\Omega \\ 0, & t > 2\pi/\Omega \end{cases}\tag{4.28}$$

then

$$f(\omega) = \frac{-i\omega(e^{i2\pi\omega/\Omega} - 1)}{\omega^2 - \Omega^2}.\tag{4.29}$$

Analysis of this Fourier transform shows that  $f(\omega) \sim O(\omega^{-1})$  as  $\omega \rightarrow \infty$  and that  $f(\omega) \sim O(\omega^2)$  as  $\omega \rightarrow 0$ . For  $V_1(0) = 0$ ,  $v(\omega) = if(\omega)/\omega(M + \mu_{11}(\omega) + i\nu_{11}(\omega))$  and so  $v(\omega)$  is absolutely integrable and hence  $V(t) \rightarrow 0$  as  $t \rightarrow \infty$ . A similar consideration of the displacement transform (4.26) in the limit of small and large  $\omega$  indicates that  $X_1(t) \rightarrow 0$  as  $t \rightarrow \infty$  because  $x(\omega)$  is absolutely integrable.

A Fourier transform of a sine forcing of a similar form as (4.28) yields

$$f(\omega) = \frac{\Omega(e^{i2\pi\omega/\Omega} - 1)}{\omega^2 - \Omega^2}.\tag{4.30}$$

This has the asymptotic form  $f(\omega) \sim -2\pi i\omega/\Omega^2$  as  $\omega \rightarrow 0$ . Thus,  $v(\omega) = if(\omega)/\omega$  is not singular in this limit; however,  $x(\omega) = iv(\omega)/\omega$  is singular as  $\omega \rightarrow 0$  and so the limiting value of  $X_1(t)$  for  $t \rightarrow \infty$  is non-zero and so there will be a net displacement of the structure. This is in contrast to the cosine forcing where no net displacement occurs. Numerical confirmation of these conclusions are illustrated in figure (4.16) for the case of an oscillating torus of tube radius  $a/h = 0.25$  and axial radius  $c/h = 0.35$ . This provides further confirmation of the validity of the time-domain solver for freely-floating body problems.

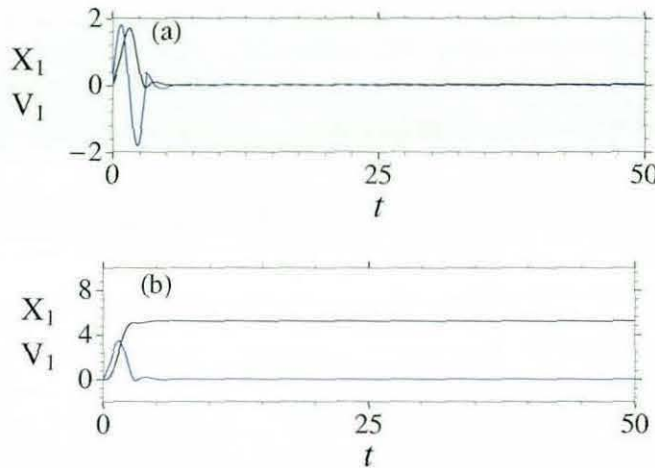


Figure 4.16: Displacement (black) and velocity (blue) of a torus in the surge mode starting from rest subject to (a) a finite cosine forcing and (b) a finite sine forcing .

### 4.3 Generalisation of time-domain solver

#### 4.3.1 Cross coupled modes of motion

Hitherto, the heave, surge and pitch modes have all been considered independently. However, it must be noted that the surge and pitch motions are intrinsically coupled because both are time-stepped in the  $n = 1$  Fourier mode. In a physical sense, this means that the motion of a body surge will excite a fluid motion which will in turn excite the motion of the body in pitch (and vice versa). Therefore, once the surge and pitch motions had been verified independently, the results of which were shown in the last section, the simulation code for floating body motion was then generalised to permit the coupled motion of the structure in surge and pitch. This generalisation was implemented by permitting the computation of the surge and pitch forces and the time-stepping of  $\{X_1, V_1\}$  and  $\{X_5, V_5\}$  simultaneously. The changes required in the Runge-Kutta method were relatively straightforward with the key amendment being to the body boundary condition

$$\frac{\partial \phi_1}{\partial n} = V_1 n_1 + V_5 n_5 \quad (4.31)$$

where either the surge normal velocity or the pitch normal velocity had been used.

The last generalisation necessary to the code is to include the possibility of coupling of the  $n = 0$  (heave) and  $n = 1$  (surge, pitch) modes. For a freely-floating body, such coupling will not occur; however, if general mooring constraints are imposed it is possible that the motion of the structure in heave may be coupled to the heave or pitch

mode. In modelling terms, the matrices  $\{k_{\mu\nu}\}$  and  $\{\gamma_{\mu\nu}\}$  describing such a mooring setup will have non-zero off diagonal elements and hence the equations of motion (2.51) may feature a mixture of displacement or velocity terms from each mode.

Simulating the motion of a structure whose modes of motion are coupled requires that the time-stepping of the concerned modes  $n = 0$  and  $n = 1$  be carried out simultaneously rather than successively as done for uncoupled floating body simulations. Therefore, a substantial change in the numerical solution algorithm was necessary in contrast to the coupling of the surge and pitch modes. The computation of the axisymmetric fluid motion and the  $\cos \theta$  fluid motion is now linked through the motion of the structure and so all computations must be conducted simultaneously to accurately model the motion. Thus, each step of the Runge-Kutta method is looped over the Fourier modes  $n = 0, 1$  and the BEM information regarding  $\phi_0$  and  $\phi_1$  is stored in different arrays to be accessed when required. In contrast, for uncoupled simulations the BEM information for  $\phi_0$  was required only when time-stepping the  $n = 0$  mode and so each mode could be solved successively. It should be noted that the higher order modes are not affected by this coupling and can be numerically solved as before. To confirm that all the changes were correct, the simulations were run with zero coupling and the results for the modes  $n = 0$  and  $n = 1$  compared to the previous simulations where the coupling of modes was not possible — essentially a self-consistency check. Although the agreement of the results does not absolutely confirm the validity of this generalisation of the floating body simulation code, it nevertheless gives a strong indication that the implementation is correct.

## Chapter 5

# Approximation of near-resonant wave motion using a damped harmonic oscillator model

### 5.1 Introduction

Near-resonant fluid motions may be observed when water waves interact with a surface-piercing structure that encloses a portion of the free-surface referred to sometimes as a moonpool. If the excitation is time-harmonic, then the resonant motions will be observed as local maxima in the amplitude of the fluid motion and the hydrodynamic forces on the structure when they are regarded as functions of frequency. In the time domain the onset of an oscillatory forcing will, in general, excite an initial transient but after sufficient time has elapsed the fluid motion in the vicinity of the structure will consist only of a steady oscillation at the forcing frequency. Nevertheless, the amplitude of the resonant response in the vicinity of the structure can be large relative to the exciting motion and, during the initial transient, can contribute significantly to the free-surface elevation and wave force. Therefore, predicting the effect of the transient resonant motion prior to the onset of steady harmonic oscillations is of considerable practical importance. Furthermore, the results of this investigation are relevant to the ‘moonpool problem’ (described by Molin (1999) among others) where the magnitude of the resonant fluid response, in radiation, scattering and coupled motion interactions involving the surrounding structure, is of interest.

Despite the mathematical inconsistency of analysing motions of large amplitude using the linearised theory of inviscid motion, important aspects of resonant wave-structure interactions can be described using this theory and it is extremely useful as a tool for preliminary analysis. In the present work, a fixed structure in incident waves is

considered and a straightforward procedure is used to gain insight into the solution of the time-domain equations from certain aspects of the solution to the corresponding frequency-domain problem.

In the frequency domain, considered in § 2.2.1, it is usual to think of the frequency as a real number (here a time dependence  $\exp(-i\omega t)$  is assumed, where  $\omega > 0$  is the radian frequency of the oscillations). However, all hydrodynamic quantities, and in particular the scattering and radiation potentials, may be regarded as functions of complex frequency and then a resonance is seen to be associated with a singularity (usually a simple pole) of the quantity at some complex frequency  $\omega = \omega_0 - i\epsilon$ , say (see, for example, McIver (2005)). These singularities are known as complex resonances or scattering frequencies. In the case of motion resonances which arise in coupled motion problems the singular behaviour occurs in the frequency domain structural velocity rather than in the radiation and scattering potentials. The real part  $\omega_0$  of the singularity location determines the frequency of the resonant motion, and the imaginary part  $\epsilon > 0$  determines the damping rate; the smaller the value of  $\epsilon$  the more persistent are the oscillations in the time domain. (Resonances with  $\epsilon = 0$ , so that the pole is on the real  $\omega$  axis, are called ‘trapped modes’ but these will not be considered until the next chapter where a discussion of trapped waves in the water-wave problem is contained.)

If the scattering interaction is highly resonant with a single pole dominating the resonant behaviour then the resultant motion will primarily consist of an incident wave component and a resonant mode component. The main idea in the present chapter is to estimate  $\omega_0$  and  $\epsilon$  from the location of the dominant pole, and then to use these values in a damped harmonic oscillator equation to predict the temporal behaviour of the transient resonant motion – an inhomogeneous term in the equation is used to account for the incident wave forcing while the homogeneous solution describes the resonant motion. The model cannot be used to obtain accurate information about the amplitude of the motion but it does yield very good approximations to the decay rate of transient motions. However, the decay in the vertical motion of a freely-floating structure (and hence the surrounding fluid also) in deep water in two and three dimensions is ultimately algebraic (Ursell (1964), Kotik & Lurye (1964)) and this cannot be described using a damped harmonic oscillator equation. Nevertheless, this algebraic decay is expected to occur only after a very long time when the amplitude of the motion is very small. Between the transient initial stages of the motion and this long-time limit the “motion of the body is closely approximated by damped harmonic oscillatory motion” as stated by Maskell & Ursell (1970) in reference to the two-dimensional problem – it is in this interval that the motion will be modelled. The singularity expansion method described by Meylan & Eatock Taylor (2008) can also be used to obtain approximations to the time-dependent solutions to scattering problems using the complex resonance locations for the system. This more comprehensive approach can predict the

amplitude of the wave-motion and typically uses a number of near-resonant modes to obtain the approximation. In contrast, it will be assumed here for simplicity that there is significant excitation of a single resonance only.

The estimates of  $\omega_0$  and  $\epsilon$  are obtained here from the behaviour of the added-mass and damping coefficients as was done for motion resonances in the last chapter. Resonances are associated with rapid changes with frequency of the hydrodynamic coefficients and, in particular, with the phenomenon of negative added mass (see Wang & Wahab (1971) and Newman (1977b)). These rapid changes are a manifestation of the singularity in the corresponding radiation potential at the complex frequency  $\omega_0 - i\epsilon$  and, as long as  $\epsilon$  is not too large, it is straightforward to obtain good approximations to  $\omega_0$  and  $\epsilon$  from the locations of the maxima and minima of the added-mass and damping coefficients near the resonance under consideration.

## 5.2 Oscillator model background

Consider the scattering of an incident wave by a structure, partially submerged in an inviscid, incompressible fluid with a still water depth  $h$ , which encloses a portion of the free surface. In the two-dimensional problems considered first, such a structure consists of two distinct surface-piercing elements. In general, the elements are taken to be identical although some problems featuring elements of different sizes are also investigated. The wetted surface of the structure is denoted by  $\Gamma$  and the normal coordinate to  $\Gamma$  directed out of the fluid is denoted  $n$ . A right-handed Cartesian coordinate system with the  $z$ -axis directed vertically upwards and the  $x$ -axis on the free surface is adopted and the origin of the coordinate system is chosen to lie at the midpoint of the internal free surface.

The fluid motion is, as usual, assumed to be irrotational so that the velocity potential satisfies the linearised water-wave equations for a diffraction problem. That is,  $\Phi$  satisfies Laplace's equation

$$\nabla^2 \Phi = 0 \quad (5.1)$$

within the fluid, the bed condition

$$\frac{\partial \Phi}{\partial n} = 0 \quad \text{on} \quad z = -h, \quad (5.2)$$

and the no-flow condition on the structure surface

$$\frac{\partial \Phi}{\partial n} = 0 \quad \text{on} \quad \Gamma. \quad (5.3)$$

Furthermore, the free-surface elevation  $\eta(x, t)$  is related to  $\Phi$  through the linearised

free-surface conditions

$$\frac{\partial \Phi}{\partial t} = -g\eta \quad \text{on } z = 0, \quad (5.4)$$

where  $g$  is the acceleration due to gravity, and

$$\frac{\partial \eta}{\partial t} = \frac{\partial \Phi}{\partial z} \quad \text{on } z = 0. \quad (5.5)$$

Finally, the motion is subject to the initial conditions

$$\Phi(x, 0, 0) = P_1(x), \quad \frac{\partial \Phi}{\partial t}(x, 0, 0) = P_2(x), \quad (5.6)$$

where  $P_1(x)$  and  $P_2(x)$  correspond to a prescribed incident wave and for all time

$$\nabla \Phi \rightarrow 0 \quad \text{as } |x| \rightarrow \infty. \quad (5.7)$$

It is assumed that the incident wave is initially localised within a region away from the structure so that at  $t = 0$  the fluid adjacent to the structure is at rest. The numerical solution of this time-domain scattering problem can then be obtained by the application of a two-dimensional boundary element method and time-stepping procedure, more details of which will be provided in § 5.3.

A simple approximation to the motion of the fluid between the structural elements can be found by modelling the internal wave motion as a damped harmonic oscillator (DHO) undergoing an oscillatory forcing. The introduction of the DHO model can be justified from a physical perspective as follows. Consider the diffraction of a regular incident wave, of frequency  $\omega$  and wavelength  $\lambda$ , by a two-element structure with a small spacing  $d$  relative to the wavelength. If a single resonant mode of frequency  $\omega_0$ , with  $\omega_0$  similar to  $\omega$ , and decay constant  $\epsilon$  is excited significantly by the incident wave, the fluid response between the structural elements will be dominated by these two wave modes — the damped, resonant wave mode and the forced mode. Both of these wave modes will cause approximately uniform vertical motion of the internal free-surface if the assumptions  $\frac{d}{\lambda} \ll 1$  and  $\omega \approx \omega_0$  are satisfied. (Interactions wherein the small-spacing restriction is violated will also be investigated in this chapter.) The free-surface motion is thus modelled using the simple one-dimensional oscillator equation

$$\ddot{\chi} + 2\epsilon\dot{\chi} + \omega_0^2\chi = F(t). \quad (5.8)$$

where  $\chi$  is the interior free-surface elevation and  $F(t)$  represents the incident wave forcing. Given that there is no initial disturbance in the vicinity of the structure, the initial conditions necessary to fully define the initial value problem are  $\chi(0) = \dot{\chi}(0) = 0$ . Although  $\chi$  can model other dynamic quantities associated with the fluid motion such as the exciting force on the structure, it is perhaps more intuitive to model the free-surface elevation. The solution of the homogeneous form of this equation which forms part of

the general solution is, for small  $\epsilon$ , a decaying oscillation with approximate frequency  $\omega_0$  and decay constant  $\epsilon$ . This matches the excited resonant motion of the fluid because a complex resonance at  $\omega_0 - i\epsilon$  in the frequency-domain potential corresponds to a time domain motion that is also a decaying oscillation with frequency  $\omega_0$  and decay constant  $\epsilon$ .

Utilisation of this model to compute well the time-dependence of the motion requires both a good estimate of the location of the complex resonance  $\omega = \omega_0 - i\epsilon$  and an accurate representation of the incident wave forcing which is assumed to be known. The determination of the former will be described in more detail in the next section. Prior to discussing these model inputs, it should be noted that in the solution to the damped harmonic oscillator equation (5.8) the forcing and resonant mode terms, corresponding to the particular and homogeneous solutions, contribute separately to the total solution. However, during the scattering interaction the diffraction of the incident wave by the left-hand element, which is related to the excitation of the resonant oscillation, changes the incident wave ‘forcing’ contribution to the internal free-surface motion. Thus, the resonant and forcing modes are coupled and, in a complete description, their contributions to the motion cannot be considered separately. Consequently, accurately predicting the amplitude of the fluid response is beyond the scope of the DHO model and an emphasis is placed on modelling the time-dependence of the incident wave excitation accurately.

### 5.2.1 Resonance location estimate

The method for obtaining an estimate for the resonant frequency  $\omega_0$  and the decay constant  $\epsilon$  (or the real and imaginary positions of the pole in the complex frequency plane) is a refinement of that used by McIver et al. (2003). A standard frequency domain code is used to compute the frequency dependence of the hydrodynamic coefficients in the neighbourhood of the resonant frequency corresponding to the significantly excited resonant mode. Thus, for example when the resonance is a vertical pumping motion, the heave-heave components of the added mass and damping coefficient matrices, denoted  $a_{33}$  and  $b_{33}$  respectively, must be computed. It is worthy of note that these coefficients require the solution of a canonical frequency-domain radiation problem and not the scattering problem. However, the only difference between the formulation of the two problems is the boundary data on the structure surface so that the problems are generally solved simultaneously. Furthermore, given that for all but the most pathological of structural geometries the radiation and scattering potentials (and hence the exciting and radiation forces which are defined as the integral of the corresponding potentials over the structure surface) have the same pole structure (McIver (2005)) then it is consistent to use the radiation force coefficients to locate the position of the resonances in the scattering problem.

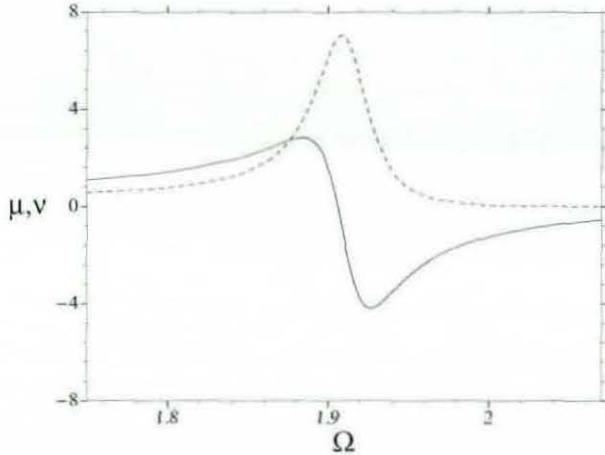


Figure 5.1: Variation of the added mass (—) and damping coefficient (--) with non-dimensional frequency  $\Omega = \omega\sqrt{h/g}$  near the resonant frequency for the first pair of half-immersed circular cylinders in table 1.

That the existence of a pole in the heave potential  $\phi_3$  implies the presence of a corresponding pole in the complex force coefficients can be seen from the definition of the heave-force coefficient

$$f_{33}(\omega) \equiv i\omega \left( a_{33} + \frac{ib_{33}}{\omega} \right) = i\omega \iint_{S_B} \phi_3 n_3 dS. \quad (5.9)$$

where  $n_3$  is the vertical component of the unit normal to the structure. With the non-dimensional forms of the added mass, damping and complex force coefficients denoted by  $\mu$ ,  $\nu$  and  $q$  respectively, the presence of a simple pole in the radiation potential at  $\omega = \omega_0 - i\epsilon$  implies that

$$q(\omega) \equiv \mu(\omega) + i\nu(\omega) \sim -\frac{\mathcal{A}}{\omega - (\omega_0 - i\epsilon)} \quad \text{as } \omega \rightarrow \omega_0 - i\epsilon \quad (5.10)$$

where the real number  $\mathcal{A}$ , referred to as the pole coefficient, must be greater than zero by the conservation of energy (see, for example, Newman (1999)). According to the asymptotic estimate (5.10) the damping coefficient will obtain a maximum value at  $\omega = \omega_0$  and the added mass coefficient will have a local maximum and minimum at  $\omega_{\pm} = \omega_0 \mp \epsilon$  respectively. This behaviour can be observed in figure 5.1 where  $\mu$  and  $\nu$  are plotted in the neighbourhood of the resonant frequency for a structure consisting of two half-immersed circular cylinders. The position of the complex resonance is thus estimated from the relations

$$\nu'(\omega_0) = 0, \quad \epsilon = \frac{\omega_+ - \omega_-}{2}. \quad (5.11)$$

This analysis also applies to the other modes of motion.

The previous asymptotic formulation only provides satisfactory estimates when the complex resonance is close to the real axis, i.e. when  $\epsilon$  is sufficiently small. In the cases where the complex resonance lies further from the axis, it is desirable to apply a correction to the asymptotic estimate that can be obtained from a Padé approximant (Bender & Orszag (1978)). In this method, which is very similar to the tangent approximation approach used in Chapter 4 for motion resonances, an initial estimate  $\omega_1$  for the position of the resonance forms the basis of a Taylor series for the force coefficient:

$$q(\omega) = q(\omega_1) + (\omega - \omega_1)q'(\omega_1) + \dots \quad (5.12)$$

The ‘first’ Padé approximant for the force coefficient is

$$q(\omega) = \frac{A_0}{1 + B_1(\omega - \omega_1)} \quad (5.13)$$

and when expanded and compared with the Taylor expansion (5.12) yields  $A_0 = q(\omega_1)$  and  $B_1 = -\frac{q'(\omega_1)}{q(\omega_1)}$  for the Padé coefficients. From equation (5.13) the pole of  $q$  is located at

$$\omega = \omega_1 - \frac{1}{B_1} = \omega_1 + \frac{q(\omega_1)}{q'(\omega_1)} \quad (5.14)$$

thus providing a corrected estimate for the resonance. The behaviour of the force coefficient is known in the vicinity of the resonance so that computation of the correction is straightforward. For simplicity  $\omega_0$  was chosen as the initial estimate. A standard frequency domain code can be used to compute the added mass and damping at discrete frequencies. Computing these force coefficients at small frequencies intervals near the resonance and interpolating the resultant data with cubic spline polynomials allows the maximum and minimum of the added mass and damping to be found to a high degree of accuracy. Table 5.1 shows the asymptotic and corrected results, for a variety of scattering structures, compared to computed time-domain results obtained by measuring the decay of oscillatory motion. In two-dimensions, results are given for circular cylinders of different radii  $r$  and centre positions  $c$  and also for a pair of thin barriers whose geometries are described in more detail in § 5.4. The three-dimensional scatters denoted  $A_1$  and  $A_2$  are both annular in shape with elliptical cross sections (the exact geometrical specifications are provided in 5.4.1). It should be noted that there is a possible unit error in the third (second) and fourth (third) decimal place respectively of the resonant frequency and decay constant in the 2D (3D) time-domain values.

Structure Geometry	Asymptotic		Padé Correction		Time	
2D Circular Cylinders ( $r, c$ )	$\Omega_0$	$\tilde{\epsilon}$	$\Omega_0$	$\tilde{\epsilon}$	$\Omega_0$	$\tilde{\epsilon}$
(0.30 $h$ , 0.35 $h$ )	1.909	0.0211	1.910	0.0208	1.910	0.0203
(0.30 $h$ , 0.37 $h$ )	1.754	0.0333	1.758	0.0323	1.760	0.0315
(0.30 $h$ , 0.40 $h$ )	1.599	0.0545	1.608	0.0511	1.616	0.0464
(0.478017 $h$ , 1.289123 $h$ )	1.449	0.0059	1.449	0.0054	1.448	0.0053
(0.27 $h$ , 0.31 $h$ )	2.167	0.0126	2.168	0.0125	2.167	0.0123
Thin barrier	1.872	0.0208	1.873	0.0198	1.870	0.0179
3D Annulus $A_1$	1.699	0.0458	1.704	0.0407	1.70	0.038
3D Annulus $A_2$	1.902	0.0281	1.905	0.0263	1.90	0.027

Table 5.1: Location of complex resonances for various two- and three-dimensional structures obtained from frequency- and time-domain calculations. The non-dimensional frequency and decay constant are both provided with  $\Omega_0 = \omega_0 \sqrt{\frac{h}{g}}$  and  $\tilde{\epsilon} = \epsilon \sqrt{\frac{h}{g}}$ .

## 5.3 Numerical implementation

### 5.3.1 Time-domain computations

The validity of the DHO model is established by comparison with numerical computations in the time domain. The numerical method used is a cubic-spline boundary element method formulated from the general water-wave equations by Maiti & Sen (2001) for the case of non-linear diffraction and adapted for linear radiation problems by McIver et al. (2003). The general solution procedure for linearised scattering and radiation has been described in detail in chapter 3 and is summarised as follows: express the velocity potential  $\phi$  representing the solution to the scattering problem in terms of a boundary integral by the application of Green's theorem to the velocity potential and an augmented Rankine Green function (an image source in the sea bed is added to the Rankine source in order to eliminate the integration over the sea bed); transform the integral equation into a system of linear equations by process of discretisation and collocation on a distribution of nodes; solve this system at time  $t = 0$  and use a time-marching algorithm to advance the solution in time. In this manner, a time-domain solution of the linearised scattering problem can be obtained. To reduce reflections of outgoing waves by the artificial control-surface boundaries, piston absorption conditions are applied on the control surfaces and the far-field free-surface conditions is augmented with an external ‘damping’ pressure term. These piston absorbers and damping zones combine effectively to minimise non-physical contributions to the numerical results.

To simulate near-resonant scattering interactions, an incident wave with a dominant regular time-harmonic component in the simulations was used. To ensure the consistency of the results, two different methods for the generation of a regular wave component with unit free-surface elevation amplitude were implemented. The first

method, referred to heretofore as the wave-maker method implements the left-hand control surface as both a piston absorber and piston wave-maker by the addition of an oscillatory term to the piston absorber condition on this surface. The left-hand damping zone must also be removed (by setting the external pressure to zero) to allow the wave to propagate without the loss of energy. A frequency domain analysis of this wave-generation problem shows that in order to generate a unit amplitude wave (after an initial transient wave front has passed) the boundary condition on the wave-maker piston must be

$$\frac{\partial \Phi}{\partial x} = \frac{(kh)^2}{\sqrt{kh} \tanh kh \sinh 2kh} \left( 1 + \frac{\sinh 2kh}{2kh} \right) \sin(\omega t) \quad \text{on} \quad x = -L, \quad (5.15)$$

where  $L$  is the distance of the control surfaces from the origin. A right propagating plane wave of unit amplitude can also be introduced into the fluid domain by assuming an isolated wave packet with a dominant harmonic component exists to the left of the structure at  $t = 0$ . Thus,  $\Phi$  and  $\frac{\partial \Phi}{\partial t}$  are initially non-zero on the free-surface, outside the vicinity of the structures so that the oscillator model's initial conditions are still valid. The initial profile of this wave-packet consists of two ramped intervals at the front and rear of a regular sinusoidal wave form so that the free-surface elevation is given by

$$\eta(x, 0) = \begin{cases} \frac{1}{2}(1 - \cos(\frac{k}{2}(x - x_1))) \cos kx & x_1 \leq x \leq x_1 + \lambda, \\ \cos kx & x_2 \leq x \leq x_1, \\ \frac{1}{2}(1 - \cos(\frac{k}{2}(x - x_2))) \cos kx & x_2 - \lambda \leq x \leq x_2, \end{cases} \quad (5.16)$$

where  $k = 2\pi/\lambda$  is the wavenumber of the regular wave component,  $\lambda$  is the wavelength and  $\eta(x, 0)$  is zero outside this range. These ramped intervals ensure the continuity of the elevation, potential and normal velocity at the free-surface which helps to minimise computational instabilities. In simulations involving such wave-packets, both control surfaces are implemented as piston absorbers with adjacent free-surface damping zones also present. This method for introducing a wave in the fluid domain will be referred to as the wave-packet method.

A brief comparison of the time-domain results (shown later in the chapter) for the interactions corresponding to different wave-forms reveals some advantages in generating the wave by the wave-packet method. First amongst these is the short time it takes for the regular component to reach the structure. In contrast, for the wave-maker case the transient wave front preceding the regular wave-train takes a significant length of time to reach the structure because of the large distance between the wave-maker and the structure. (The large distance between the wave-maker and structure was necessary to reduce problems due to reflections of scattered waves at the domain boundaries.) Therefore, the beat modulations of the internal fluid motion appear much later in the wave-maker simulation than for the wave-packet simulation. Furthermore, the scat-

tered waves are absorbed much more effectively in the wave-packet case because both damping zones are present whereas in the wave-maker simulations some interference attributable to non-physical reflections from the wave-maker control surface can be observed after the resonant mode has decayed. The advantages of implementing a wave-maker in the simulations is that an indefinitely propagating wave-train can be generated and that if the efficacy of the model is to be tested physically, experimental wave tanks use wave-makers to generate incident waves. It should be emphasised, however, that the steadily oscillating part of the resultant incident wave-train is identical in both cases.

### 5.3.2 Damped harmonic oscillator model computations

In order to compute an approximation to the internal free-surface motion for a particular scattering interaction the location of the complex resonance and a forcing function  $F(t)$  to model the effect of the incident wave must be input into the DHO equation (5.8).

The effect of the incident wave on the motion of the internal free-surface must be modelled using the forcing function  $F(t)$  in equation (5.8). To best describe the time dependence of the incident wave excitation the forcing was chosen to be the free-surface wave-elevation  $\eta$  in the case where the same incident wave propagates in the absence of the structure. That is, identical initial conditions to the interaction problem were imposed on the free-surface and  $\eta$  was measured at a distance from the initial wave-front equal to that from the centre of the left structural element to the initial wave-front in the original interaction problem. This distance was chosen based on a rather ad-hoc procedure; the corresponding forcing signal  $\eta_f(t)$  was found to yield the best results in most of the cases investigated. Such a forcing function can be computed using the time-domain solver to simulate the propagation of a wave in a domain free of obstacles. Other methods for obtaining this incident wave signal  $\eta_f$  exist (e.g. Eatock Taylor, Zang, Bai & Walker (2006) uses a semi-analytical method to compute a wave-maker generated wave) and the particular method used to obtain the incident wave forcing function is not of crucial importance; however, an *a priori* knowledge of the incident wave is required.

## 5.4 Application and results

The damped harmonic oscillator model is compared with full linear time-domain simulations in this section. In the latter simulations, the incident wave was usually generated by the imposition of a wave profile corresponding to a right-moving wave at  $t = 0$ . However, the piston-type wave-maker simulation was also considered in some cases to ensure the model results are not specific to a particular incident wave form. Regardless of the

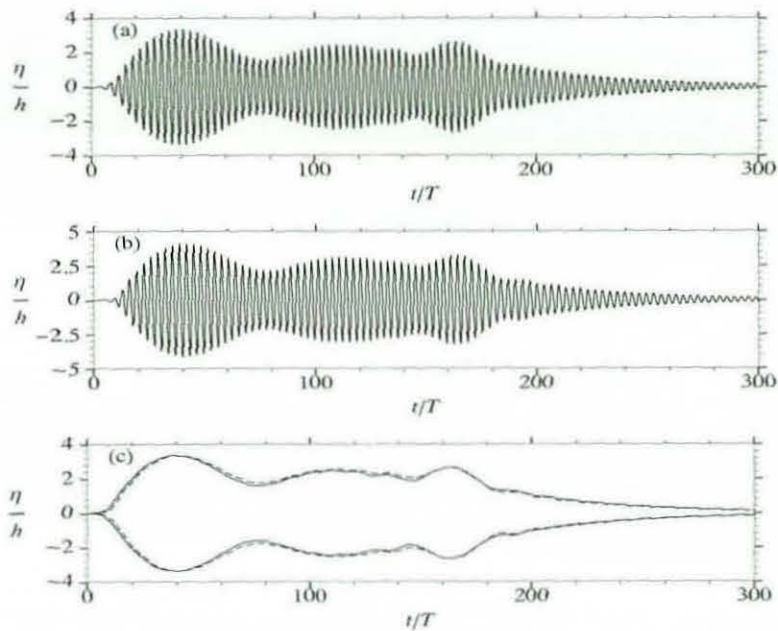


Figure 5.2: Free-surface elevation  $\eta$  at the mid-point between two half-immersed circular cylinders specified by  $(r, c) = (0.3h, 0.35h)$  as computed by (a) the linear time-domain solver; (b) the DHO model, for the wave-packet case. The response amplitude envelopes are compared in (c).

generation method, the incident waves had non-dimensional unit amplitude and in all except the wide-spacing structure case the frequency of the regular component of the incident wave was chosen as  $\omega = \sqrt{4 \tanh 4} \sqrt{g/h}$  corresponding to a non-dimensional wavenumber of  $kh = 4$  and non-dimensional frequency  $\omega\sqrt{h/g} \approx 1.999$ . The domain geometries, for a given structural configuration, were identical for both wave-generation methods with the left and right control-surfaces situated distances of  $50h$  and  $25h$ , respectively, from the midpoint of the internal free-surface. Thus it was possible to impose a long wave-train on the left free-surface initially and in the wave-maker case to ensure artificial reflections did not affect the wave-structure interaction until a significant time had elapsed. In particular, in all wave-packet interactions the initial wave-profile was specified to have a regular part of approximate length  $42h$  smoothly ramped to zero at either end over a distance of one wavelength  $2\pi/k$  with the wave-front initially positioned a distance  $h$  from the left structure element. Figures 5.2—5.6 illustrate the non-dimensionalised free-surface elevation  $\eta(x, t)/h$  as a function of non-dimensional time  $t/T$  where  $T = \sqrt{h/g}$ . Similarly, the non-dimensional incident wave and resonant frequencies are  $\Omega = \omega T$  and  $\Omega_0 = \omega_0 T$ , respectively.

The results of the linear time-domain solver and DHO model are shown together and compared for the incident wave generated by the ‘wave-packet’ method and by the wave-maker method in figures 5.2 and 5.3, respectively. The scattering structure consisted of

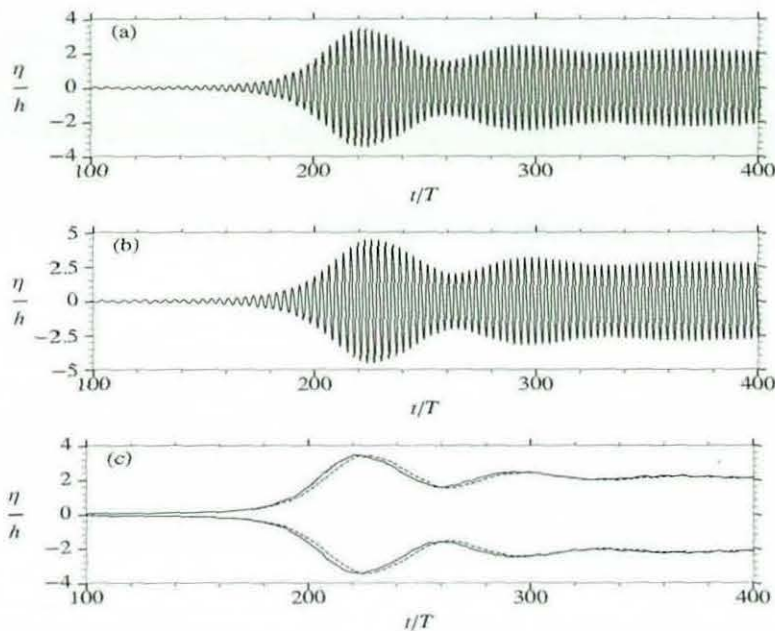


Figure 5.3: Free-surface elevation  $\eta$  at the mid-point between two half-immersed circular cylinders specified by  $(r, c) = (0.3h, 0.35h)$  as computed by: (a) the linear time-domain solver; (b) the DHO model, for the wave-maker case. The response amplitude envelopes are compared in (c).

two half-immersed circular cylinders of radii  $r = 0.3h$  with centres a distance  $c = 0.35h$  from the midpoint of the internal free-surface. The oscillator model results utilises the asymptotic estimate for the complex resonance location  $\omega_0 - i\epsilon$  (see table 5.1) and the free-surface elevation  $\eta_f(t)$  as the external forcing. This forcing describes the time-dependence of the incident wave forcing well, however, as stated earlier the amplitude of the response can not be predicted correctly and so the amplitudes for the oscillator results and the time-domain results are different. In figures 5.2 (c) and 5.3 (c), the envelope predicted by the DHO model was scaled so that the first maximum is of equal height to that of the time-domain envelope thus allowing the time-dependence to be compared in a straightforward manner. The amplitude scale factor, which is the ratio of the time-domain amplitude to the DHO amplitude (at the first envelope maximum), is approximately 0.7 meaning the oscillation amplitudes predicted by the model were approximately a factor 1.42 larger than in the time-domain simulations. It can be seen from a comparison of figures 5.2 (b) and 5.3 (b) to 5.2 (a) and 5.3 (a), respectively, that the ‘fast’ oscillations with frequencies  $\omega$  and  $\omega_0$  are described satisfactorily by the model. However, since the ‘slow’ beat modulations of the response amplitude with frequency  $|\omega - \omega_0|$  are of primary interest here, comparisons of the beat-envelopes, such as in figures 5.2 (c) and 5.3 (c), will henceforth be used to assess the success of the DHO model.

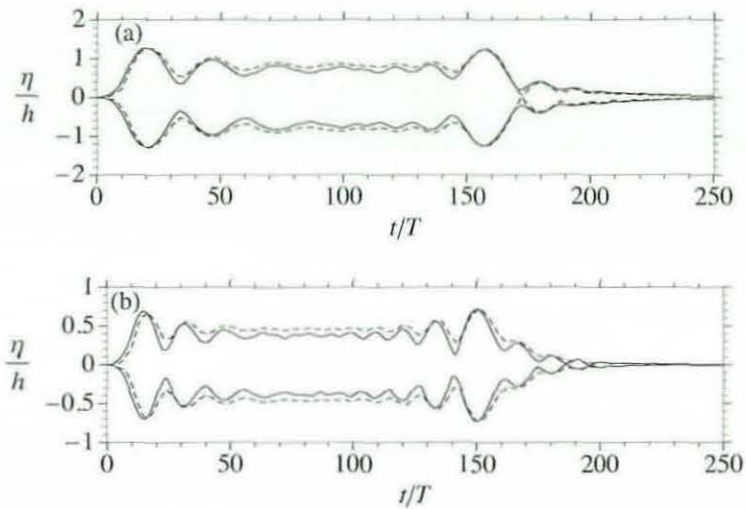


Figure 5.4: Free-surface wave elevation envelope for time domain (—) and DHO model results (---) at the midpoint of the internal free-surface for half-immersed circular cylinders of radius  $r = 0.3h$  with centres a distance  $c = 0.37h$  (a) and  $c = 0.4h$  (b) from the midpoint.

The development of beats after the transient wave front of the incident wave has passed are particularly apparent in the wave-maker plots and is a result of the superposition of the resonant and forced modes. A computation of the beat period  $2\pi/|\omega - \omega_0| \approx 70T$  confirms this deduction because it agrees well with the spacing of the local maxima in the time-domain response envelope in figure 5.3 (c) which occur at approximately  $t = 220T, 290T, 360T$ , although the last maximum is difficult to discern. Depending on the type of incident wave, the fluid motion either decays exponentially to zero or settles into steady oscillations at the incident wave frequency as  $t \rightarrow \infty$  as expected. However, in the wave-maker simulation noticeable interference due to artificial reflections exist for  $t > 400T$  and become increasingly prominent as  $t$  increases. Thus, more attention was focussed on the wave-packet propagation case for the other interactions investigated here even if the interference phenomenon between the resonant and the incident wave modes is somewhat easier to discern in the wave-maker results.

In the previous case, the resonant frequency of the structure  $\Omega_0 \approx 1.91$  is very close to the incident wave frequency and the inter-element spacing  $d$  is quite small ( $0.1h$ ). As a result, the modulation of the oscillations is quite slow and the beat period is quite large. However, it is important to analyse the performance of the model when the frequencies differ to a greater extent so that the beat period is shorter and also when the structures are more widely spaced. Therefore, the centre position  $c$  was increased from  $0.35h$  to  $0.4h$  incrementally in steps of  $0.01h$ , thus eventually doubling the inter-element spacing  $d$ , and the DHO model results assessed in each case. Frequency domain

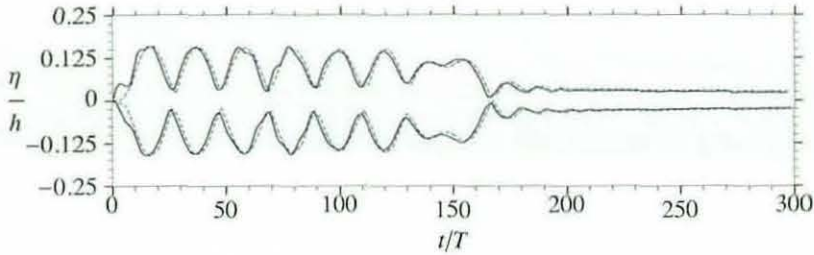


Figure 5.5: Time domain (—) and DHO model (---) results for free-surface elevation at the anti-nodal position of the surge resonant mode for two widely spaced half-immersed circular cylinders.

computations yielded an increase in the damping  $\epsilon$  of the resonance, whereas a decrease in the resonant frequency  $\Omega_0$  from 1.9 to 1.6 occurred as  $d$  increased. Illustrated in figure 5.4 are the response amplitude envelopes for the diffraction of the wave-packet of frequency  $\Omega = \sqrt{4 \tanh 4} \approx 1.999$  by circular cylinders of radii  $r = 0.3h$  and the centres a distance  $0.37h$  and  $0.4h$  respectively, from the midpoint. The envelope comparisons become less favourable as  $d$  and  $|\omega - \omega_0|$  increase. The oscillation beats are observed to decay in amplitude as before; however, the decay is more rapid for larger  $\epsilon$  and this, combined with the more rapid beat modulations of the response envelope resulting from larger  $|\omega - \omega_0|$  values, compromises the accuracy of the oscillator model results. An increase in the value of  $\epsilon$  also results in a decrease in the accuracy of the frequency and decay constant estimates (5.11) because the asymptotic approximation (5.10) is less accurate for real frequencies  $\omega_r$ , i.e.  $\omega_r$  becomes a worse approximation of  $\omega_r - i\epsilon$  as  $\epsilon$  increases. Nonetheless, the trends predicted by the DHO model are still very similar to the time-domain results despite the decrease in the accuracy of the asymptotic estimate for the resonance location as  $\epsilon$  increases that can be seen in table 5.1. Furthermore, the beat period estimates give a good agreement with the observed response maxima in the envelopes. In the case where  $c = 0.37h$  the beat period is calculated to be approximately  $26T$  and for  $c = 0.4h$  it is approximately  $16T$ , both of which are consistent with the response maxima observed in the initial stages of the simulation in figure 5.4.

The scattering structures considered so far all have similar geometries — they consist of two moderately sized ( $r = 0.3h$ ) circular cylinders with a small inter-element spacing with a maximum value of  $0.2h$  relative to the incident wavelength  $\lambda \simeq 1.57h$ . In these interactions, only the pumping resonance was significantly excited so that the free-surface motion was uniform in each case. Therefore, to investigate the limitations of the model the resonant fluid motion in a scattering interaction involving a widely-spaced pair of half-immersed circular cylinders was considered. The model was also used to predict the resonant fluid motion between a closely-spaced pair of vertically-aligned rectangular cylinders rounded by semi-circular bottoms to ensure the success

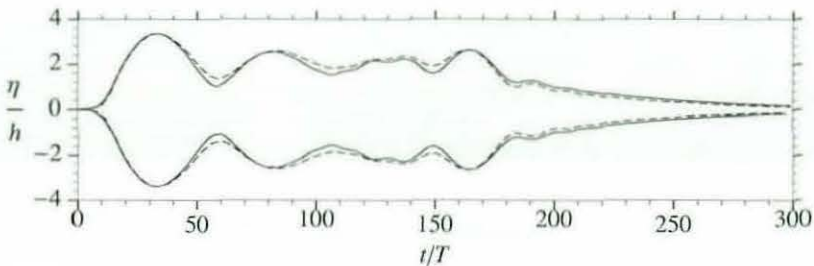


Figure 5.6: Time domain (—) and DHO model (---) results for free-surface elevation at the mid-point between two closely spaced thin vertical barriers.

of the model was not dependent on the shape of the structures involved. The results for a widely-spaced pair of half-immersed circular cylinders are shown in figure 5.5 and in figure 5.6 for a closely-spaced pair of vertical barriers. In the wide-spacing case, the cylinders' radii  $r$  and centre distance  $c$  from the midpoint of the internal surface are  $0.4h$  and  $1.0h$ , respectively. Thus, the internal free-surface is of sufficient extent  $d \simeq 1.2h$  to permit the existence of a surge resonant mode, that is a resonant mode with a free-surface node that involves a sloshing motion of the fluid, with a frequency close to that of the incident wave. In contrast, the frequency of the surge resonant modes for the closely spaced structural configuration were substantially greater than the incident frequency and thus these modes weren't significantly excited during the interactions. The motion of the internal free-surface is not uniform when the surge resonant mode and other higher-order resonant modes are excited. For this widely-spaced structural configuration, the frequency dependence of the heave added mass and damping revealed a weak pumping resonance at  $\Omega \simeq 0.8$  and a higher order heave resonance at  $\Omega \approx 2.3$ . A surge resonance was also observed to exist at the non-dimensional frequency  $\Omega \approx 1.7$ . Given that the pumping resonance is strongly damped, the surge resonant mode, being the lowest frequency resonance, dominates the motion of the internal free-surface. A Fourier transform of the motion of the midpoint also indicates the excitation of the higher-order heave resonance. It is not appropriate to use the DHO model to predict the motion of the mid-point of the internal free-surface as this corresponds to the nodal point of the surge resonance. However, an examination of the motion of the anti-node (half-way between the mid-point and the structure) reveals the familiar decaying beats in the modulation of the response. So, having assumed that the surge resonance is the significantly excited mode the DHO model describes the motion well as illustrated in figure 5.5 (a). In this case, the scale factor for the oscillator model results was 0.1. In summary, the damped harmonic oscillator model can predict the motion of the internal free-surface at positions where only one resonant mode dominates. So although the applicability of the model is not solely restricted to pumping resonances, it is more straightforward to use the one-dimensional oscillator equation (5.8) to describe the free-surface motion when the motion is approximately uniform because it is applicable

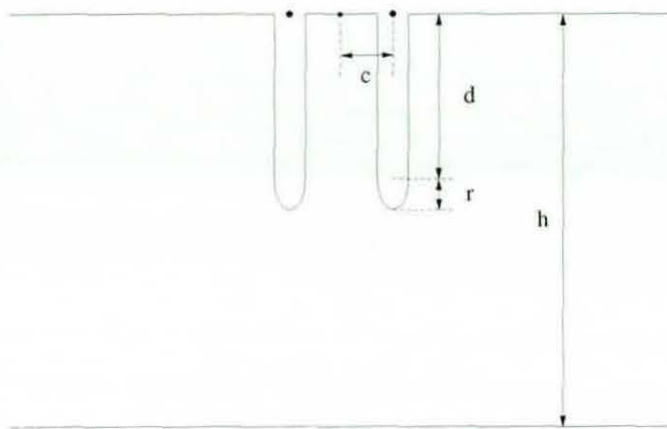


Figure 5.7: Closely spaced vertical scatterers.

across the full extent of the free-surface. In the wide-spacing cases where the resonance can have nodal points on the free-surface the same equation (5.8) with the same inputs ( $\omega_0, \epsilon$ ) will not be applicable everywhere on the free-surface because at the nodal points of the generally dominant resonance a higher order resonance may influence the motion of the free-surface to a greater extent.

The final scatterer investigated here is the pair of thin rounded vertical barriers illustrated in figure (5.7). The geometrical specifications of the particular pair of barriers considered here are as follows:  $d = 0.225h$ ,  $r = 0.025h$  and  $c = 0.05h$ . Therefore, the inner-free surface has a length  $0.1h$  so that the barriers are closely spaced relative to the incident wavelength  $2\pi/k = 2\pi h/4 \simeq 1.57h$ . These particular dimensions were chosen so that the structure had a pumping resonant frequency near the incident frequency  $\Omega = \sqrt{4 \tanh 4}$  just as for the first pair of half-immersed circular cylinders. This structural configuration was chosen to investigate the influence, if any, of the shape of the structure on the success of the DHO model. The model results can be seen to compare well to those of the numerical time-domain solver in figure 5.5 (b); in this case the scale factor for the DHO model is approximately 1.2. The structural configuration mainly affects the amplitude predicted by the model, but not the time-dependence of the envelope which is dominated by the excited resonance location  $\omega_0 - i\epsilon$  and the incident wave frequency.

#### 5.4.1 Three dimensional scattering interactions

Thus far, the validity of the damped harmonic oscillator model approximation of near-resonant motions has only been demonstrated in the case of two-dimensional scattering problems. However, the principles of the model do not preclude its usage for near-resonant motions in three dimensions. The one-dimensional oscillator theory will de-

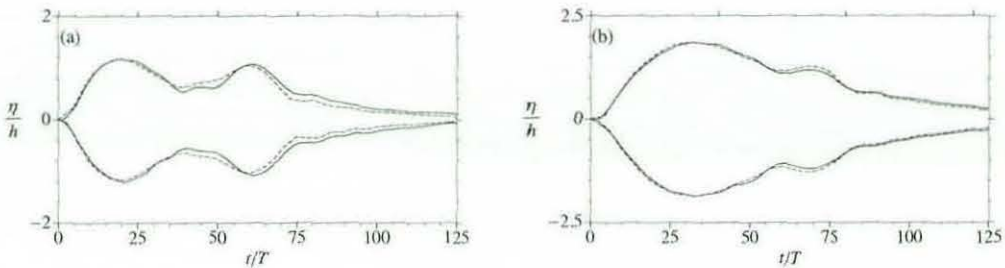


Figure 5.8: Free-surface wave elevation envelope for time domain (—) and DHO model results (---) at the midpoint of the internal free-surface for half-immersed annular structures.

scribe the fluid motion inside a three-dimensional structure particularly well if there is a vertical pumping motion in which the free-surface elevation is approximately uniform. Therefore, two three-dimensional simulations involving structures with vertical axes of symmetry and which possess heave resonances are considered here. Comparisons of the DHO model predictions to these simulation results are shown in figure 5.8. In both cases the structures possessed annular geometries and were constructed by rotating ellipses of different shapes around the axis of symmetry. The free-surface elevation was measured at the origin of the internal free-surface. The results in figure 5.8 (a) correspond to an annulus of an elliptical cross-section with a major and minor axis of length  $a = 1.2h$  and  $b = 0.1h$ , respectively. The centre of the ellipse is a distance  $c = 1.0h$  from the axis of symmetry. In table 5.1 this structure is denoted as  $A_1$ . The incident wave interacting with the structure was chosen to have a non-dimensional frequency of  $\Omega = \sqrt{3.5} \tanh 3.5$ . Results in figure 5.8 (b) correspond to the diffraction of a wave of frequency  $\Omega = \sqrt{4} \tanh 4$  by an annular structure (denoted  $A_2$  in the table) of elliptical cross-section with geometrical parameters given by  $(a, b, c) = (1.0h, 0.2h, 0.8h)$ . These structures were chosen because it was possible to significantly excite a single heave resonance only whereas for tori typically more than one resonance was significantly excited thus precluding the use of the mechanical oscillator model. The agreement between the model and time-domain results is again good. In both cases the amplitudes predicted by the DHO model were approximately twice those of the time-domain simulations corresponding to a scale factor of 0.5.

## 5.5 Conclusion

A damped harmonic oscillator model has been used to describe strongly resonant fluid motion in the vicinity of a structure which encloses a portion of the free-surface when subject to a predominantly regular incident wave. The results have been compared to the numerical solution of the linearised water-wave problem which was obtained by a cubic spline boundary element method. Different variations of the basic incident wave

were used in the simulations in addition to a number of different structure geometries. The primary goal of the model development was to obtain good predictions of the time-dependence of the motion of the free surface enclosed by the structure with relatively simple computations, although the simple nature of the model precludes a correct description of the response amplitude.

The damped harmonic oscillator model is found, in general, to describe the fluid response between the structures quite well given the free-surface elevation of the incident wave when propagating across the same domain in the absence of structures as the forcing term. In particular, the positions of maximum and minimum response amplitudes during the decay of the excited resonant modes coincide well with those computed by the linear theory. The beats in the response oscillations are also predicted extremely well in most cases with a good agreement between the estimated beat period and the successive maxima in the response envelope as the motion settles to a steady oscillation. The behaviour at the end of the simulation is attributed to the dispersion of the rear of the wave-packet – the short distance between the wave-front and the structure initially means that dispersion effects in the initial stages of the simulation will be small.

The success of the model must be qualified by some mildly restrictive conditions. Firstly, only one resonance may be significantly excited so that two wave motions, the incident and resonant mode, dominate the free-surface response both of which are accounted for in the DHO equation (5.8). Furthermore, it is preferable that the dominant resonance possess only a small number of internal free-surface nodes so that the motion is relatively simple because then equation (5.8) will be applicable across most of the free-surface for the dominant resonant inputs ( $\omega_0, \epsilon$ ). At the points on the free surface where the dominant resonance causes little or no disturbance the equation will not yield the correct results. If a pumping resonance is excited then the model predicts the motion of the entire internal free-surface. Nevertheless, as illustrated by the investigation of the structure with widely-spaced elements, the oscillator model can also account for the free-surface motion at particular locations between the structural elements when the surge resonances are excited.

The most important factors in describing the properties of the wave-motion using the DHO model are  $\omega - \omega_0$  and  $\epsilon$  where  $\omega_0$  and  $\epsilon$  are dependent on the structure geometry and  $\omega$  is the incident wave frequency. If the decay constant  $\epsilon$  of the resonant mode is sufficiently small and also the difference in the frequencies of the modes  $|\omega - \omega_0|$ , then the modulation of the near-resonant response consists of long slow beats which the model describes successfully. The exact nature of the geometry is unimportant in the predictions of the fluid response. However, the amplitude predictions of the model are affected by the geometry. In the comparisons made here, for all pairs of circular cylinders the amplitude scale factor was less than unity whereas for the pair of vertical scatterers the scale factor was greater than unity. It is interesting to note

that the amplitude predictions of the model for pumping resonances were generally reasonable with the scale factor in the range (0.5, 1.2). For resonances with nodes on the internal free-surface, however, the response amplitude predicted by the model was an order of magnitude *greater* than the time-domain result, corresponding to a scale factor of 0.1. A possible explanation for this disparity in the amplitudes, not witnessed in the other results, is that the structures were bigger than in the other scattering interactions considered so that more incident wave energy could be reflected at the left-hand element. The decrease in the incident wave energy would then have yielded a smaller net amplitude for the total oscillation in the linearised simulation whereas the oscillator model is incapable of accounting for such a decrease in amplitude.

A possible application of this method could be for investigations into scattering interactions in experimental wave tanks. In such experiments, it is typical to generate incident waves using a paddle wave-maker and to measure the response of the fluid enclosed in the structure. It is useful to be able to distinguish between transient effects and steady state effects in these experiments and from the damped harmonic oscillator model it is possible to estimate the time taken for the transient response to become negligible. For example, in the experiments conducted by Faltinsen, Rognebakke & Timokha (2007) on the analogous radiation problem of the vertical forcing of a barge enclosing a moonpool some initial beating was observed in the fluid oscillations prior to the onset of steady state. The steady state resonant motion was of interest and so the information provided by the model regarding the decay of the transient should be relevant in such experiments. The two inputs necessary for the application of the damped harmonic oscillator model are the complex resonance location and the incident wave forcing. The complex resonance location could be estimated using a standard frequency-domain code, given the geometry of the structure involved in the experiment, and the incident wave forcing function could be measured in the wave-tank. However, the damped harmonic oscillator model would only yield relevant results for scattering interactions where a single resonant mode is significantly excited. The primary benefit in using the model is the simplicity with which important properties of the time-domain response are obtained from basic frequency domain information and an *a priori* knowledge of the incident wave time signal.

# Chapter 6

## Passive trapped modes

### 6.1 Introduction

Investigations into the uniqueness of solutions to linearised inviscid water-wave problems have resulted in the discovery of trapped mode oscillations. A trapped mode is a free oscillation of an unbounded fluid with a free surface that has finite energy, does not radiate waves to infinity and persists for all time in the absence of viscosity. Trapped modes occur at isolated frequencies and can be supported only by special trapping structures. Two types of trapped mode have previously been identified: sloshing and motion trapped modes. Sloshing trapped modes are free oscillations of the fluid supported by particular fixed structures referred to as sloshing trapping structures. On the other hand, motion trapped modes are free oscillations involving coupled motions of floating structures and the fluid – the special floating structures are termed motion trapping structures. McIver (1996) proved the existence of sloshing trapped modes while investigating uniqueness in scattering and radiation problems problem while McIver & McIver (2006) demonstrated the existence of motion trapped modes in the coupled motion problem. If a trapping structure does not support a trapped mode at a particular frequency of oscillation then the solutions to the corresponding water-wave problems at that frequency are unique.

In the context of the boundary-value problem for wave-structure interactions, a trapped mode potential is a non-trivial solution of the homogeneous form of the water-wave problem. In the case of scattering and radiation problems this implies the potential satisfies a homogeneous Neumann condition on the structure surface whereas for a coupled wave-structure motion problem, there will be no external forcing causing the persistent motion of the fluid and structure. One consequence of the homogeneous Neumann condition for the particular class of sloshing trapped modes discovered by McIver (1996), demonstrated by McIver (1997), is that the modes are orthogonal to

any incident waves. Therefore, these trapped modes cannot be excited in a scattering problem in the time or frequency domains. However, the existence of such a sloshing trapped mode implies the non-existence of the solution to a radiation problem at the trapped mode frequency. This corresponds to a pole in the frequency-domain radiation potential at the trapped mode frequency and as a consequence the sloshing trapped modes of McIver (1996) can be excited in the time-domain by the forced oscillation of a trapping structure (McIver et al. (2003)). In contrast, McIver & McIver (2006) showed that the existence of a motion trapped mode in the freely floating water-wave problem results in both the scattering and radiation potentials being well-behaved at the trapped mode frequency. Thus, motion trapped modes cannot be excited in the time-domain by the forced motion of the structure nor can they be excited by wave incidence. Instead, excitation can be achieved by giving the structure a non-zero initial displacement or velocity. From a numerical perspective, the existence of the sloshing trapped modes discussed above has the consequence that it is difficult to accurately compute the added mass and damping coefficients near the trapped mode frequency where these hydrodynamic coefficients are singular. However, for motion trapped modes the hydrodynamic coefficients are all well behaved at the trapped-mode frequency.

It was previously thought that the trapped modes supported by a fixed structure could not be excited when the structure is allowed to float freely and respond to the hydrodynamic forces on it. In fact, this is true for the particular class of sloshing trapping structures discovered by McIver (1996) whose properties have just been discussed. However, Motygin & Kuznetsov (1998) constructed two-dimensional sloshing trapping structures whose corresponding trapped modes exert no net force on the structure. Such structures can still support the trapped modes when allowed to float freely as the fluid oscillation excites no motion of the structure. In the terminology employed by McIver (2005) these special structures can be considered to be both sloshing and motion trapping structures. Henceforth, these structures will be referred to as passive trapping structures and the corresponding persistent oscillations as passive trapped modes. It is useful to employ set notation to distinguish between the three classes of trapped modes. Let  $\mathcal{S}$  be the set of all possible sloshing trapped modes and let  $\mathcal{M}$  be the set of all possible motion trapped modes; the set of passive trapped modes  $\mathcal{P} = \mathcal{S} \cap \mathcal{M}$ . The original class of sloshing trapping modes investigated by McIver (1996) is in the set  $\mathcal{S} \setminus \mathcal{M}$ .

The purpose of the present work is to investigate the conditions required for the existence of passive trapped modes in two and three-dimensional water-wave problems involving structures constrained to move in the heave mode only and to confirm the existence of such modes in time-domain simulations. The properties of the trapping structures and the time-domain excitation methods for the passive modes will also be discussed. The two-dimensional passive trapping structures are constructed by the method of Motygin & Kuznetsov (1998) and this is extended to three-dimensions using

ring-source methods similar to those used by McIver & McIver (1997). Both methods have their origins in the inverse procedure used by Kyozuka & Yoshida (1981) to obtain wave-free oscillating structures. It is possible to obtain trapped modes that exert no net vertical hydrodynamic force on the corresponding structure by using a specific arrangement of wave-dipoles in the construction procedure. Therefore, accompanying the derivation of the zero-force condition is an explanation of how a trapped mode constructed from dipole potentials can yield a zero hydrodynamic force on the corresponding structure.

A structure that supports a passive trapped mode at a particular frequency in a single mode of oscillation will not experience a net force nor move as a result of the persistent trapped mode oscillations of the surrounding fluid. Due to these particular properties, the excitation methods used previously for sloshing trapped modes and motion trapped modes of the classes  $\mathcal{S} \setminus \mathcal{P}$  and  $\mathcal{M} \setminus \mathcal{P}$ , respectively, prove ineffective for passive trapped modes. Therefore, an excitation method analogous to that previously devised by McIver (1997) is utilised whereby the fluid surrounding the passive trapping structure is given an oscillatory pressure forcing on the free-surface in order to obtain excitation. The effectiveness of this method is demonstrated analytically using Green's theorem by showing that the frequency domain solution of the "pressure potential" (the potential satisfying the freely floating body equations while undergoing the free-surface pressure forcing) does not exist at the trapped mode frequency. Another method yielding trapped mode excitation is the imposition of an initial free-surface elevation on the fluid surrounding the structure; however, the frequency domain excitation analysis of the free-surface pressure forcing readily yields both an excitation condition and an analytic asymptotic result thus providing the opportunity for comparisons with the time-domain results.

In this chapter the motion of a structure in heave only is considered in both two- and three-dimensional fluid domains. The problem of a moored floating structure free to respond to incident waves is formulated in § 6.2. The zero-force condition for a passive trapped mode is introduced in the context of the conditions for a motion trapping structure in § 6.3. The construction of the passive trapping structures in two and three dimensions is demonstrated in § 6.4 and a description of the excitation method is given in § 6.5. Finally, in § 6.6 the results of time-domain simulations are presented to confirm the existence and illustrate the properties of passive trapped modes.

## 6.2 Formulation

Consider a moored surface-piercing structure, constrained to move in heave only, that is floating in an inviscid and incompressible fluid of infinite or finite depth. The fluid is also of infinite extent in all horizontal directions and Cartesian coordinates  $(x, y, z)$  are

chosen with the  $z$ -axis directed vertically upwards from the mean free surface. In the two-dimensional problems considered, the structure is assumed to extend indefinitely in the  $y$ -direction so that attention is restricted to the  $x$ - $z$  plane only. The vertical displacement and velocity of the structure are denoted by  $Z(t)$  and  $\dot{Z}(t)$  respectively. The wetted surface of the structure in both two and three dimensions will be denoted as  $\Gamma$ .

For a structure moored by an arrangement of linear springs and dampers then the equation describing the motion of the structure is

$$M\ddot{Z}(t) = -\rho \iint_{\Gamma} \frac{\partial \Phi}{\partial t} n_z dS - [(\rho g W + \kappa)Z(t) + \gamma \dot{Z}(t)] \quad (6.1)$$

where  $M$  is the mass of the structure,  $W$  the water-plane area,  $\rho$  the density of the water and  $g$  the acceleration due to gravity. The constants  $\kappa$  and  $\gamma$  describe respectively the properties of the springs and dampers in the mooring system. The  $z$ -component of the inward normal to the structure is denoted  $n_z$  and  $\Phi$  is the time-domain velocity potential describing the fluid motion. The motion is subject to the initial conditions

$$\Phi(x, 0, 0) = 0, \quad \frac{\partial \Phi}{\partial t}(x, 0, 0) = 0, \quad (6.2)$$

so that the fluid is initially at rest, and for all time

$$\nabla \Phi \rightarrow 0 \quad \text{as} \quad |x| \rightarrow \infty. \quad (6.3)$$

Furthermore, the initial displacement  $Z(0)$  and velocity  $\dot{Z}(0)$  of the structure must also be prescribed to yield a fully-specified initial value problem.

The frequency domain potential is obtained using the Fourier transform and is

$$\phi(\mathbf{x}, \omega) = \int_0^\infty \Phi(\mathbf{x}, t) e^{i\omega t} dt; \quad (6.4)$$

this satisfies the usual frequency domain equations governing the fluid motion, i.e. Laplace's equation, the infinite depth condition, the free-surface condition and the structure boundary condition. In the absence of an incident wave, the frequency domain potential must also satisfy a radiation condition stating that the waves described by this potential must propagate outwards from the structure. By applying the Fourier transform operator to the equation of motion (6.1) the corresponding frequency domain equation of motion

$$\begin{aligned} & [\rho g W + k - \omega^2 \{M + i\gamma/\omega\}]v(\omega) \\ &= \omega^2 \rho \iint_{\Gamma} \phi n_z dS - i\omega [(M + a(\infty))\dot{Z}(0)] - (\rho g W + k)Z(0) \end{aligned} \quad (6.5)$$

is obtained where the term  $v(\omega)$  is the Fourier transform of the velocity  $\dot{Z}(t)$  and  $a(\infty)$  is the added mass in the limit of infinite frequency. The inversion formula for the potential is

$$\Phi(\mathbf{x}, t) = \frac{1}{\pi} \operatorname{Re} \int_0^\infty \phi(\mathbf{x}, \omega) e^{-i\omega t} dt \quad (6.6)$$

and this is used later to obtain an asymptotic expression for the fluid motion in the long time limit.

### 6.3 Conditions for the existence of passive trapped modes

Trapped modes were first observed in uniqueness investigations into water-wave problems and it is in this context that the conditions for the existence of passive trapped modes are introduced. Consider two solutions  $\{\phi_1, v_1\}$ ,  $\{\phi_2, v_2\}$  to the frequency domain water-wave problem. The difference potential  $\phi = \phi_1 - \phi_2$  and velocity  $V = v_1 - v_2$  satisfy a homogeneous water-wave problem. That is, the potential must satisfy Laplace's equation

$$\nabla^2 \phi = 0 \quad (6.7)$$

within the fluid, the free-surface boundary condition

$$\frac{\partial \phi}{\partial n} = \frac{\omega^2}{g} \phi \quad \text{on } z = 0 \quad (6.8)$$

and the no-flow boundary condition on the surface of the structure

$$\frac{\partial \phi}{\partial n} = V n_z \quad \text{on } \Gamma, \quad (6.9)$$

where  $V$  is given by the homogeneous form of the equation of motion (the initial condition terms cancel as they are identical for both solutions)

$$[\rho g W + k - \omega^2 \{M + i\gamma/\omega\}]V(\omega) = \omega^2 \rho \iint_{\Gamma} \phi n_z dS. \quad (6.10)$$

It should be noted that the right-hand side of equation (6.10) is proportional to the hydrodynamic force on the structure due to the fluid oscillations. For a moored structure, the possibility of finite-energy motions that satisfy (6.9) and (6.10) with non-zero  $\phi$  and  $v$  has been known for some time and there have been a number of recent developments (Evans & Porter (2007), Newman (2008)). The non-trivial solutions of equations (6.7)-(6.9) for structures without moorings are referred to as motion trapped modes and their existence has been established by McIver & McIver (2006) and McIver & McIver (2007) in the case where  $V \neq 0$ . Unlike motion trapped modes, it is possible to retain the damping coefficient as the passive trapped modes excite no structural motion.

In addition to the motion-trapped modes for which both the potential  $\phi$  and the velocity

$V$  are non-zero, there is the possibility that finite-energy solutions to (6.9) and (6.10) exist with  $\phi \neq 0$  but with  $V = 0$  provided

$$\int_{\Gamma} \phi n_z dS = 0. \quad (6.11)$$

A solution of this type corresponds to a fluid motion that satisfies the homogeneous boundary condition for sloshing trapped modes

$$\frac{\partial \Phi}{\partial n} = 0 \quad \text{on } \Gamma, \quad (6.12)$$

but for which the structure is able to float freely as the net hydrodynamic force on the structure due to the fluid motion is zero. Structures that support modes of this type will be here referred to as passive trapping structures. Insight into how such structures might be found can be gained from examining the conditions under which (6.11) may be satisfied. For the particular case of two-dimensional motions in infinite depth, a trapped mode  $\phi_0$  does not radiate waves to infinity so that

$$\phi_0 \sim \frac{\mu \cos \theta}{R} \text{ as } R \rightarrow \infty \quad (6.13)$$

where  $R = \sqrt{x^2 + z^2}$  and  $\theta$  are polar coordinates and  $\theta$  is measured from the downward vertical. The constant  $\mu$  is referred to here as the dipole coefficient and to leading order the trapped mode is dipole-like at infinity. The trapped mode also satisfies the homogeneous Neumann condition (6.12) on the structure surface and condition (6.8) on the free-surface. Consider the fluid domain  $\Omega$  bounded by the free-surface, the structure surface and an enclosing semicircle  $S_\infty$  at infinity in  $z < 0$ . An application of Green's theorem to the trapped-mode potential  $\phi_0$  and  $u = z + g/\omega_0^2$ , where  $\omega_0$  is the trapped-mode frequency, on the fluid domain  $\Omega$  gives

$$\int_{\Gamma} \phi_0 n_z dS = \pi \mu \quad (6.14)$$

(note that this result requires  $\partial \phi / \partial n = 0$  on  $\Gamma$ ). Thus, equation (6.11) is satisfied if and only if  $\mu = 0$ , that is the coefficient of the dipole in the far-field expansion of  $\phi_0$  is zero. When the velocity  $V = 0$  the equations for  $\phi_0$  are the same as those for a sloshing trapped mode, and it so happens that such modes have been constructed with  $\mu = 0$  by Motygin & Kuznetsov (1998).

For two-dimensional motion in fluid of constant finite depth  $h$ , the Green's theorem analysis yields the equation

$$\int_{\Gamma} \phi_0 n_z dS = -\rho \omega_0^2 \int_{-\infty}^{\infty} \phi_0|_{z=-h} dx \quad (6.15)$$

so that a necessary condition for the existence of a passive trapped mode at the fre-

quency  $\omega_0$  is

$$\int_{-\infty}^{\infty} \phi_0|_{z=-h} dx = 0. \quad (6.16)$$

In three-dimensions, the derivation of the necessary condition for the existence of passive trapped modes in a fluid infinite or constant finite depth  $h$  is almost identical to that for two-dimensions. For a vertically axisymmetric three-dimensional structure in a fluid of infinite depth, any wave-free potential must satisfy

$$\phi_0 \sim \frac{\mu \cos \theta}{R^2} \text{ as } R \rightarrow \infty \quad (6.17)$$

where in this case  $R = \sqrt{x^2 + y^2 + z^2}$  and  $\theta$  is measured from the downward vertical. The application of Green's theorem to  $\phi_0$  and  $u = z + g/\omega_0^2$  on the three-dimensional fluid domain bounded by the free surface, the surface of the structure and an enclosing hemisphere in the lower half of the plane gives

$$\int_{\Gamma} \phi_0 n_z dS = 2\pi\mu. \quad (6.18)$$

Therefore, to obtain a passive trapped mode the dipole coefficient  $\mu$  of the potential must be zero. For a fluid of constant finite depth, the existence condition is the three-dimensional equivalent of the condition (6.16) for two dimensions, i.e.

$$\int_0^{\infty} \phi_0|_{z=-h} r dr = 0. \quad (6.19)$$

## 6.4 Construction of passive trapping structures

### 6.4.1 Two dimensional structures

Passive trapping structures are constructed using an inverse procedure similar to that employed by McIver (1996) to construct the original class of sloshing trapping structures  $\mathcal{SM}$ . In that paper a potential satisfying the wave-free condition at infinity is constructed from two free-surface sources and the streamlines isolating the singularities from infinity are interpreted as the body contours. Thus, the singularities of the potential are not on the boundary of the fluid domain because the source points are within the bodies. However, for passive trapping structures, the potential is constructed from a pair of wave dipoles rather than sources. It should be noted that McIver (1996) proved the existence of the dividing streamlines; here, the existence of dividing streamlines will be verified numerically for the sake of brevity. The dipoles are located symmetrically about the origin at  $(-\xi, 0)$  and  $(\xi, 0)$  where  $K\xi = \pi$  and  $K = \omega_0^2/g$  denotes the infinite depth wavenumber corresponding to a trapped-mode frequency  $\omega_0$ . Generally  $\xi$  can be chosen to satisfy  $K\xi = n\pi$  for  $n = 1, 2, \dots$  but here only the first solution is considered.

Thus, the dipole potential is given by

$$\phi_0(x, z) = -\frac{1}{K} [G_x(x, z; \xi, 0) - G_x(x, z; -\xi, 0)], \quad (6.20)$$

where  $G(x, z; \xi, 0)$  is an infinite-depth source potential with the source located on the free-surface at  $(\xi, 0)$ . The horizontal dipole is obtained by taking the derivative with respect to  $x$  so that  $\phi_0(x, z)$  is the sum of two dipole potentials. By positioning two dipoles of equal strength and opposite alignment on the free-surface at  $x = \pm\xi$  the wavefield will, at the trapped-mode frequency, be wave free with a vanishing far-field dipole coefficient. The latter property of the dipole potential can be shown by considering the asymptotic forms of the individual dipoles in the far-field and noting the cancellation of the dipole terms when combining them to form (6.20). The horizontal dipole term is obtained from differentiating the free-surface source term (see Linton & McIver (2001), equation B.13 albeit with the minus sign removed) and gives

$$\frac{\partial G}{\partial x}(x, z; \xi, 0) = - \int_0^\infty e^{kz} \sin(k(x - \xi)) dk - K \int_0^\infty e^{kz} \frac{\sin(k(x - \xi))}{k - K} dk. \quad (6.21)$$

An alternative expression for  $\phi_0$  without a singular integrand can be obtained by using the integral relation

$$\int_0^\infty e^{\mu z} \sin(\mu(x - \xi)) d\mu = \frac{x - \xi}{(x - \xi)^2 + z^2} \quad (6.22)$$

(see Gradshteyn & Ryzhik (1980), equations 3.943, 3.944(5) and (6)) so that the infinite-depth passive trapped mode potential can be expressed as

$$\begin{aligned} \phi_0(x, z) = & \frac{1}{K} \left[ \frac{x - \xi}{(x - \xi)^2 + z^2} - \frac{x + \xi}{(x + \xi)^2 + z^2} \right] + \\ & \int_0^\infty e^{kz} \frac{\sin(k(x - \xi)) - \sin(k(x + \xi))}{k - K} dk \end{aligned} \quad (6.23)$$

where the integrand has a removable singularity. The corresponding streamfunction, necessary for the location of the streamlines, is given by

$$\begin{aligned} \psi_0(x, z) = & -\frac{1}{K} \left[ \frac{z}{(x - \xi)^2 + z^2} - \frac{z}{(x + \xi)^2 + z^2} \right] + \\ & \int_0^\infty e^{kz} \frac{\cos(k(x - \xi)) - \cos(k(x + \xi))}{k - K} dk. \end{aligned} \quad (6.24)$$

where the arbitrary constant of integration in the relation

$$\psi = \int \frac{\partial \phi}{\partial x} dz \quad (6.25)$$

has been chosen to be zero.

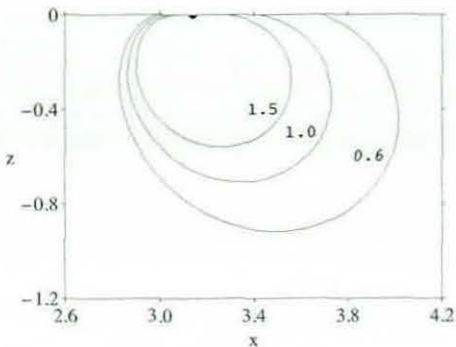


Figure 6.1: The right-hand element of passive trapping structures obtained from the streamfunction (6.24);  $K = 1$ . Each streamline is marked with the corresponding value of  $\delta$ .

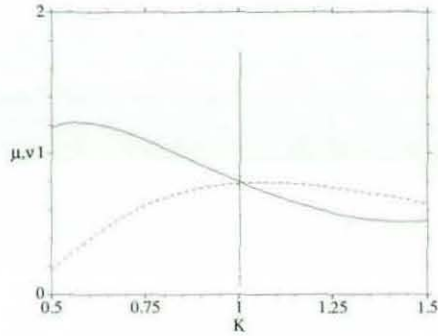


Figure 6.2: Non-dimensionalised added mass  $\mu$  (—) and damping  $\nu$  (---) as a function of frequency  $K$  for the structure  $\delta = 1.5$  with  $n_p = 402$  for  $K = 1$ .

In the inverse procedure, utilised by McIver (1996) among others, the streamfunction  $\psi$  associated with  $\phi$  is used to construct the trapping structures for a particular frequency  $\omega_0$  from the equation  $\psi(x, z; K) = \delta$ . A family of two-dimensional passive trapping structures in infinite depth fluid is shown in figure 6.1. The same approach can be adopted for a finite depth fluid domain; the only modifications necessary are in the form of the source potential  $G$  (and hence in the expressions for  $\phi$  and  $\psi$ ) and in the introduction of the finite depth wavenumber  $k$  which satisfies  $k\xi = \pi$  and is related to  $K$  through  $K = k \tanh kh$ . Therefore, the infinite depth source potential is replaced by the finite depth source

$$G(x, z; \xi, 0) = \int_0^\infty \frac{\cos(\mu(x - \xi)) e^{\mu z} (1 + e^{-2\mu(z+h)})}{\mu - K - (\mu + K)e^{-2\mu h}} d\mu. \quad (6.26)$$

in the equation (6.20) to give

$$\phi_0(x, z) = \int_0^\infty \frac{\mu(\sin(\mu(x - \xi)) - \sin(\mu(x + \xi))) e^{\mu z} (1 + e^{-2\mu(z+h)})}{\mu - K - (\mu + K)e^{-2\mu h}} d\mu \quad (6.27)$$

and this is substituted into equation (6.25) to obtain the finite-depth streamfunction expression

$$\psi_0(x, z) = \int_0^\infty \frac{\mu(\cos \mu(x - \xi) - \cos \mu(x + \xi)) e^{\mu z} (1 - e^{-2\mu(z+h)})}{\mu - K - (\mu + K)e^{-2\mu h}} d\mu. \quad (6.28)$$

The geometries of the resulting structures are very similar to those shown in figure 6.1. The excitation of passive trapped modes in a fluid of constant finite depth will be demonstrated later in the chapter and the geometry of the finite-depth passive trapping structures are used in these simulations. The condition (6.16) for a zero hydrodynamic force on the passive trapping structure in finite depth can be proven by considering the

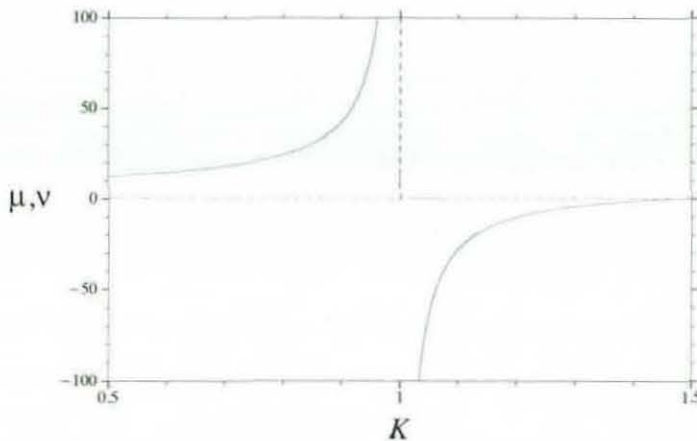


Figure 6.3: Variations in the non-dimensionalised added mass  $\mu$  (—) and damping  $\nu$  (--) near the trapped mode frequency  $K = 1$  for a sloshing trapping structure of the class  $\mathcal{S}\backslash\mathcal{P}$ .

contributions from each dipole to the total integral. Given that the dipoles are aligned in opposite directions and provided the dipoles are located at  $x = \pm\xi$  then the integral contributions from each dipole cancel exactly in the limit as the domain of integration becomes unbounded, although the integrals of the individual dipole potentials do not converge. Numerical confirmation of this property was obtained by integrating the potential over the range  $-10 < x/h < 10$  at  $z/h = -1$  for trapped mode potential of frequency  $k = 4$  – the computed value for the integral was  $O(10^{-6})$ .

Passive trapping structures support both sloshing and motion trapping modes because equations (6.12), (6.9) and (6.10) are all satisfied simultaneously by the (non-trivial) potential  $\phi_0$ . The behaviour of the hydrodynamic coefficients for passive trapping structures is similar to other motion trapping structures — both the radiation and scattering potentials exist at the trapped-mode frequency, despite the fact that structures also support sloshing trapped modes. Thus, the added mass and damping coefficient do not exhibit the singular behaviour of the trapping structures corresponding to the trapped modes in  $\mathcal{S}\backslash\mathcal{M}$  near that frequency. Seeking a numerical verification of these properties, a standard BEM frequency-domain code was used to compute the frequency dependence of the non-dimensionalised added mass  $\mu$  and damping  $\nu$  for a passive and sloshing trapping structure, i.e. trapping structures of the classes  $\mathcal{P}$  and  $\mathcal{S}\backslash\mathcal{M}$  respectively, near the trapped mode wavenumber  $K = 1$ . (The particular passive trapping structure used in these calculations corresponds to the streamline  $\delta = 1.5$  shown in figure 6.1.) For the passive trapping structure, the errors inherent in a numerical approximation is manifest in very localised variations in  $\mu$  and  $\nu$  near the trapped-mode frequency as may be seen in figure 6.2; these are present because the discretisation of the trapping structure is actually a near-trapping structure with the corresponding

radiation potential possessing a complex resonance located very close to the real- $\omega$  axis. As the number of panels  $n_p$  is increased the peaks reduce in width, increase in height, and converge on  $K = 1$ . On the other hand, the singular behaviour of the added mass and damping coefficients of the  $\mathcal{S}\backslash\mathcal{M}$  trapping structure shown in figure 6.3 is much more significant than for the passive trapping structure. The added mass tends to positive and negative infinity as  $K$  approaches the asymptote  $K = 1$  from the left and the right respectively with the asymptotic behaviour occurring over a much larger range of  $K$  values than in the passive trapping structure case. Furthermore, the damping coefficient is very close to zero for the range of  $K$  over which the added mass behaves in a singular manner; the passive trapping structure has finite non-zero values for  $\mu$  and  $\nu$  near  $K = 1$ . Therefore, although passive trapped modes obey the same equations as sloshing trapped modes the properties of the corresponding structures are significantly different.

#### 6.4.2 Three dimensional structures

The three-dimensional passive-trapping structures are assumed to have a vertical axis of symmetry and are constructed from ring-dipole potentials. The construction method is analogous to that used for two-dimensional structures because a dipole-like term must replace the source term in the expression for the sloshing trapped mode potential. Previously, McIver & McIver (1997) used an axisymmetric ring-source potential term of the following form

$$\begin{aligned} \phi_0(x, z) = & 4\pi^2 i K c e^{Kz} J_0(Kr_<) H_0(Kr_>) \\ & + 8c \int_0^\infty (\nu \cos \nu z + K \sin \nu z) I_0(\nu r_<) K_0(\nu r_>) \frac{\nu}{\nu^2 + K^2} d\nu, \end{aligned} \quad (6.29)$$

to generate a sloshing trapping structure in infinite depth where  $J_0$ ,  $I_0$ ,  $K_0$  and  $H_0$  denote standard Bessel, modified Bessel and Hankel functions of order zero and where  $r_< = \min\{r, c\}$  and  $r_> = \max\{r, c\}$ . To eliminate the first term in (6.29) corresponding to the outgoing radial waves the radius  $c$  of the ring source is chosen to satisfy

$$J_0(Kc) = 0, \quad (6.30)$$

where  $K = \omega_0^2/g$  and  $\omega_0$  is the trapped mode frequency.

To construct passive trapping structures, the potential due to a ring-dipole in the free-surface is used and the radius of the ring chosen so as to eliminate the far-field waves. The ring-dipole, is obtained in an analogous manner to the two-dimensional dipole potential, by taking the derivative of the ring-source potential with respect to the ring radius  $c$ . However, the multiplicative factor  $c$  is first removed from (6.29) so that no

source-like terms remain after differentiation. The resultant ring-dipole potential is

$$\begin{aligned}\phi_0(r, z) = & -4\pi^2 i K^2 e^{Kz} J_0(Kr) H_1(Kc) \\ & - 8 \int_0^\infty (\nu \cos \nu z + K \sin \nu z) I_0(\nu r) K_1(\nu c) \frac{\nu^2}{\nu^2 + K^2} d\nu, \quad 0 \leq r < c\end{aligned}\quad (6.31)$$

$$\begin{aligned}\phi_0(r, z) = & -4\pi^2 i K^2 e^{Kz} J_1(Kc) H_0(Kr) \\ & - 8 \int_0^\infty (\nu \cos \nu z + K \sin \nu z) I_1(\nu c) K_0(\nu r) \frac{\nu^2}{\nu^2 + K^2} d\nu, \quad r > c\end{aligned}\quad (6.32)$$

and to ensure it is wave-free at infinity, the coefficient of  $H_0(Kr)$  in (6.32) corresponding to the outgoing radial waves must be set to zero, i.e.

$$J_1(Kc) = 0 \quad (6.33)$$

so that  $c = j_{1,i}/K$  where  $j_{1,i}$ ,  $i = 1, 2, \dots$ , are the positive zeros of the Bessel function of order 1 arranged in ascending order. Thus, the dipole potential satisfies the zero radiated wave condition; however, to obtain a passive trapped mode the potential must also have a zero dipole coefficient at infinity. This necessitates an asymptotic analysis of the potential  $\phi_0(r, z)$  for large distances from the origin.

To demonstrate that the far-field dipole coefficient of the potential is zero, it must be shown that the maximum order of the potential in the far-field is  $O(r^{-3})$ . Therefore, an asymptotic analysis of the terms in the ring dipole potential  $\phi_0$  in the limit  $R = (r^2 + z^2)^{1/2} \rightarrow \infty$  is conducted. For simplicity of exposition, the far-field limit will be taken by setting  $r = 0$  and letting  $z \rightarrow -\infty$  so that the asymptotic analysis will concern the dipole potential representation for  $0 \leq r < c$ . When evaluated on  $r = 0$ , the ring-dipole potential contains the integral

$$I = \int_0^\infty (t \cos tz + K \sin tz) K_1(ct) \frac{t^2}{t^2 + K^2} dt \quad (6.34)$$

(and a smaller exponentially decaying term which is neglected). It is shown in appendix B that  $I = o(z^{-2})$  in the limit as  $z \rightarrow -\infty$  by expressing  $I$  as the sum of a sine and cosine integral and subsequently integrating by parts and applying the Riemann Lebesque lemma to these integrals. Thus the ring-dipole potential has a zero dipole coefficient at infinity.

It remains to derive the streamfunction  $\psi_0(r, z)$  corresponding to the ring dipole and to interpret a surface of a constant  $\psi_0$  as the surface structure. The Stokes stream function is related to the potential by the equations

$$\frac{\partial \phi}{\partial r} = -\frac{1}{r} \frac{\partial \psi}{\partial y} \quad \text{and} \quad \frac{\partial \phi}{\partial y} = \frac{1}{r} \frac{\partial \psi}{\partial r} \quad (6.35)$$

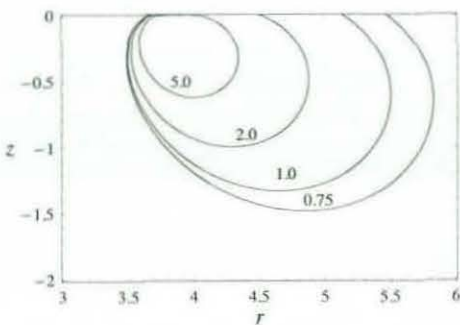


Figure 6.4: The trace of passive trapping structures in the  $r$ - $z$  plane obtained from the streamfunction  $\psi_d(r, z)$  for  $c = j_{1,1}/K$  and with  $K = 1$ . Each streamline is marked with the corresponding value of  $\delta$ .

the solutions of which give

$$\begin{aligned} \psi_0(r, z) = & -4\pi^2 r K^2 e^{-Ky} J_1(Kr) Y_1(Kc) \\ & - 8r \int_0^\infty (\nu \sin \nu z - K \cos \nu z) I_1(\nu r) K_1(\nu c) \frac{\nu^2}{\nu^2 + K^2} d\nu, \quad 0 \leq r < c \end{aligned} \quad (6.36)$$

$$\psi_0(r, z) = -8r \int_0^\infty (\nu \sin \nu z - K \cos \nu z) I_1(\nu c) K_1(\nu r) \frac{\nu^2}{\nu^2 + K^2} d\nu, \quad r > c \quad (6.37)$$

The constants of integration were chosen to be zero so that  $\psi \rightarrow 0$  as  $r \rightarrow \infty$ . A plot of a typical family of stream-surfaces for the deep water ring-dipole stream function is shown in figure 6.4 for the ring-dipole radius of  $c = j_{1,1}/K$  with the infinite depth wavenumber chosen to be  $K = 1$ . The corresponding structure is generated by the rotation of the contours about the  $z$ -axis and therefore the structures are torus-like and enclose a portion of the free-surface.

The finite-depth passive trapping structures are constructed by following the same derivation as in the infinite-depth case. Therefore, the dipole potential is obtained from  $\phi_0 = \partial/\partial c(R_0/c)$  where  $R_0$  is the integral representation of the finite-depth ring-source potential, quoted by Hulme (1983) to be

$$R_0(r, z; c, 0) = 4\pi c \int_0^\infty \frac{\mu \cosh \mu(h+z)}{\mu \sinh \mu h - K \cosh \mu h} J_0(\mu r) J_0(\mu c) d\mu, \quad (6.38)$$

where  $K = k \tanh kh$  and  $k$  is the finite-depth wavenumber. If the ring-dipole radius is chosen to be  $c = j_{1,i}/k$  for  $i = 1, 2, \dots$  then the singularity in the denominator of the integral is cancelled by the zero of the Bessel function  $J_1(\mu c)$  at  $\mu = k$  and the integral

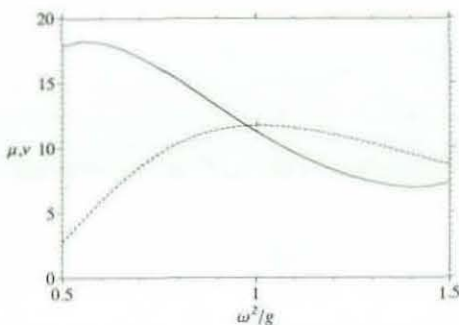


Figure 6.5: Non-dimensionalised added mass  $\mu$  (—) and damping  $\nu$  (---) as a function of frequency  $K$  for the structure corresponding to the streamline value  $\delta = 5.0$  with  $n_p = 2304$  for  $\omega_0^2/g = 1$ .

representation of the dipole potential becomes

$$\phi_0(r, z) = -4\pi \int_0^\infty \frac{\mu^2 \cosh \mu(h+z)}{\mu \sinh \mu h - K \cosh \mu h} J_0(\mu r) J_1(\mu c) d\mu \quad (6.39)$$

with no radiated wave term present. The streamfunction corresponding to this dipole potential is

$$\psi_0(r, z) = -4\pi r \int_0^\infty \frac{\mu^2 \sinh \mu(h+z)}{\mu \sinh \mu h - K \cosh \mu h} J_1(\mu r) J_1(\mu c) d\mu. \quad (6.40)$$

To evaluate the dipole potential and streamfunction numerically, the range of integration is first decomposed as

$$\int_0^\infty = \int_0^a + \int_a^\infty \quad (6.41)$$

where  $a$  is a finite constant. Provided  $a$  is sufficiently large (typical computational values were  $50 < a < 100$ ) an accurate approximation of the last integral can be obtained from the asymptotic form of the integrand and the integral over the range  $(0, a)$  can be computed using a standard numerical integration method. This method was also used in the computation of the finite-depth potential and streamfunction in two-dimensions. Nevertheless, difficulties with the convergence of the streamfunction integral (6.40) arise despite the application of this method. Thus, it is necessary to utilise the integral formula

$$\int_0^\infty f(\mu) d\mu = \int_0^\infty (f(\mu) - F(\mu)) d\mu + \int_0^\infty F(\mu) d\mu \quad (6.42)$$

for the computation of the streamfunction (6.40) where

$$f(\mu) = \frac{\mu^2 \sinh \mu(h+z)}{\mu \sinh \mu h - K \cosh \mu h} J_1(\mu r) J_1(\mu c) \quad (6.43)$$

and  $F(\mu)$  is the first order asymptotic approximation to  $f(\mu)$  given by

$$F(\mu) = -\frac{2}{\pi(r c)^{1/2}} e^{\mu z} \cos(\mu r - 3\pi/4) \cos(\mu c - 3\pi/4), \quad (6.44)$$

so that  $f(\mu) \sim F(\mu)$  as  $\mu \rightarrow \infty$ . This expression is considered more computationally robust because the integral of  $f(\mu) - F(\mu)$  converges faster than  $f(\mu)$  for  $z$  close to 0 and  $\int_0^\infty F(\mu) d\mu$  can be evaluated analytically. It should be noted that the integral range decomposition (6.41) must still be applied to the integral of  $f(\mu) - F(\mu)$ .

Thus, it is possible to obtain streamsurfaces of the passive trapping structures from the solution to the equation  $\psi_0(r, z) = \delta$  for various values of  $\delta$ . The resultant streamsurface traces in the  $r$ - $z$  plane are similar to those in the infinite depth case. The finite-depth passive trapping structures will be utilised in the numerical demonstration of the existence of passive trapped modes. To confirm that this streamfunction (6.40)

corresponds to a passive trapped mode, the potential (6.38) must satisfy the finite-depth condition (6.19). A numerical approximation to this infinite integral can be obtained by computing the integral over a sufficiently large radius. If the dipole potential  $\phi_0(r, z)$  is a trapped mode potential the integration is expected to yield a value close to zero – observed values were in the order of  $O(10^{-6})$  for a domain of radius  $20h$ . This was taken as tentative verification that the potential obeyed the zero-force condition.

## 6.5 Excitation of passive trapped modes

### 6.5.1 Excitation condition in the frequency-domain

If a frequency domain potential possesses a simple pole at a real frequency then the corresponding time-domain potential describes a persistent oscillation because the Fourier transform will yield a term of the form  $e^{-i\omega t}$  from the residue. In other words the non-existence of a frequency domain potential at a certain frequency implies that trapped mode excitation is possible in the corresponding time-domain problem. Thus, for example, the non-existence of the radiation potential at the trapped mode frequency in the forced motion problem involving a sloshing trapping structure of the class  $\mathcal{S}\backslash\mathcal{M}$  implies that certain forced motions of the structure will excite the trapped mode (see McIver et al. (2003) for details). However, neither forcing the motion of a passive trapping structure nor the imposition of an initial structural displacement or velocity will excite passive trapped modes. This is a consequence of the special properties possessed of the passive trapping structure, namely, the added mass and damping coefficients are well-behaved and also the velocity of the structure is non-singular at the trapped mode frequency. Excitation of motion trapped modes of the class  $\mathcal{M}\backslash\mathcal{S}$  is achieved by giving the structure an initial displacement or velocity because the resultant solution of the equation of motion (6.5) yields a singularity in  $v(\omega)$ . This is a consequence of the resonance condition for these motion trapped modes

$$[\rho g W - \omega^2(M + a(\omega) + ib(\omega)/\omega)] = 0 \quad (6.45)$$

which is the denominator term in the solution of the equation of motion (see McIver & McIver (2006)) for a floating trapping structure. However, this condition is not necessarily satisfied for passive trapped modes (the zero-force condition (6.11) must be satisfied instead) and so, in general, there is no pole in  $v$  for passive trapping structures. Therefore, no excitation can arise from the imposition of an initial displacement or velocity and an alternative excitation method must be used to obtain a persistent passive mode of oscillation in the fluid.

McIver (1997) explicitly demonstrates, using Green's theorem, how the violation of the existence condition for a frequency-domain potential due to a pressure forcing on the

free surface corresponds to an unbounded growth of a trapped mode oscillation in the time-domain. A similar approach can be taken for passive trapped modes by considering a potential due to an oscillatory forcing pressure in the presence of a freely-floating passive trapping structure. In this case, the pressure forcing potential  $\phi_p$  satisfies the usual freely floating conditions, i.e. the structure boundary condition (6.9) and the equation of motion (6.10), in addition to the modified free-surface boundary condition

$$\frac{\partial \phi_p}{\partial n} - K\phi_p = f \quad \text{on } z = 0 \quad (6.46)$$

where  $f$  is proportional to the pressure on the free-surface. The passive trapped mode potential  $\phi_0$  satisfies the homogeneous free-surface condition, the homogeneous Neumann condition on the structure surface (6.12) and the zero-force condition (6.11). Therefore, under the assumption that  $\phi_p$  exists, an application of Green's theorem to  $\phi_p$  and  $\phi_0$  at the trapped mode frequency  $\omega = \omega_0$  over the fluid domain yields the condition

$$\int_F \phi_0 f dS = 0, \quad (6.47)$$

because the integrals over the structure surface  $\Gamma$ , the far-field control surface  $S_\infty$  and the bottom boundary all vanish. If this condition is satisfied then the forcing pressure potential  $\phi_p$  exists and hence there will be no pole in  $\phi_p$  at  $\omega = \omega_0$  and excitation of the trapped mode in the time-domain problem will not be possible. On the other hand, if the condition is not satisfied then  $\phi_p$  will possess a pole at the trapped mode frequency and it will be possible to excite a persistent oscillation corresponding to the trapped mode in the time-domain by application of the corresponding time-dependent forcing pressure. Note that the analysis is valid in both two and three dimensions.

There are many different forcing pressure profiles  $f$  that can be used to excite passive trapped modes. An obvious choice is  $f(\mathbf{x}) = \phi_0(\mathbf{x}, 0)$  where  $\mathbf{x}$  denotes the coordinates in the horizontal plane. Otherwise, a forcing function which has the same sign as  $\phi_0(\mathbf{x}, 0)$  on the free-surface can be used. It is also possible to choose a pressure profile such that the existence condition is satisfied and so that no excitation occurs. This requires a particular choice of  $f(\mathbf{x})$ ; by choosing a polynomial form with free-coefficients it is possible to generate equations for the coefficients which when satisfied will yield a zero integral. For example, in two dimensions the forcing function is chosen to be

$$f(x; \omega_0) = \begin{cases} \sum_{k=0}^2 f_k x^k, & x \in F_- \\ 0, & x \in F_+ \end{cases} \quad (6.48)$$

where  $F_-$  ( $F_+$ ) is the internal (external) free-surface section. By setting  $f_1 = 0$ , the forcing function becomes even and to satisfy the existence condition the relation

$$f_0 = -f_2 \frac{\int_{F_-} \phi_0(x, 0) x^2 dx}{\int_{F_-} \phi_0(x, 0) dx} \quad (6.49)$$

must be obeyed. Letting  $f_2 = 1$  then yields a forcing profile  $f(x, \omega_0) = f_0 + x^2$  which does not excite the passive trapped mode. To demonstrate the excitation analysis, time-domain simulations are performed with the various free-surface forcing pressure described above. These forcing pressures do not need to exist indefinitely, it is also possible to use a transient forcing pressure to excite the passive trapped modes. Both indefinite and transient forcing pressures are considered; the former results in resonant growth of the passive trapped oscillation while the latter yields a persistent steady fluid oscillation. Finally, the oscillatory pressure forcing which satisfies the existence condition is shown not to excite the passive trapped mode. In all simulations it is assumed that the structure floats freely so that no mooring forces are present.

### 6.5.2 Resonant free-surface pressure forcing

The application of an oscillatory pressure forcing to the free-surface surrounding a passive trapping structure at the trapped mode frequency  $\omega_0$  will generally result in a fluid oscillation of indefinitely increasing amplitude near the structure. This can be demonstrated by an analysis of the time-domain problem in the long-time limit and this involves the asymptotics of the frequency domain solution as  $\omega \rightarrow \omega_0$ . Here, the analysis is conducted for a two-dimensional problem although it can easily be extended to axisymmetric three dimensional problems. The application of a pressure forcing on the free-surface means that the time-domain potential  $\Phi_p$  describing the response of the fluid to this forcing must satisfy the dynamic free-surface boundary condition

$$\frac{\partial \Phi_p}{\partial t} + g\eta = \frac{P(x, t)}{\rho} \quad (6.50)$$

where  $P$  is the forcing which is assumed to have the form

$$P(x, t) = \frac{\rho g f(x)}{\omega_0} \sin \omega_0 t. \quad (6.51)$$

Provided the fluid motion starts from rest then the frequency domain free-surface condition is

$$(K - \frac{\partial}{\partial z})\phi_p = \frac{i\omega}{\omega^2 - \omega_0^2} f(x), \quad (6.52)$$

for  $\omega \neq \omega_0$ , where  $\phi_p$  is related to  $\Phi_p$  by the Fourier transform relation (6.4). An estimate of the long-time response of the fluid can be made by an application of the inverse Fourier transform (6.6) to a Laurent expansion in  $\omega$  of the frequency-domain potential  $\phi_p$  about  $\omega_0$ . This expansion is determined using a similar derivation to that presented by McIver et al. (2003) (Appendix A) for a heaving sloshing trapping structure and the leading order term is

$$\phi_p(x, z, \omega) = \frac{i\omega A \phi_0(x, z)}{(\omega^2 - \omega_0^2)^2} + O(1) \quad \text{as } \omega \rightarrow \omega_0 \quad (6.53)$$

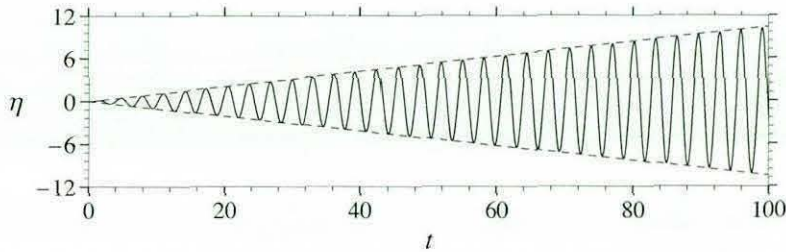


Figure 6.6: A comparison of the time-domain results (—) for the free-surface elevation  $\eta/h$  at the mid-point between the passive trapping structure elements to the asymptotic prediction of the oscillation amplitude (---).

for a two-dimensional passive trapping structure in finite depth. The amplitude  $A$  is determined by an application of Green's theorem to  $\phi_p$  and  $\phi_0$  for  $\omega \simeq \omega_0$  and the subsequent substitution of (6.53) for  $\phi_p$ . In contrast to the heave problem for a sloshing trapping structure, the inhomogeneous term in the Green's theorem is due to the forcing of the free-surface and it can be shown that the expression for the strength is

$$A = \frac{\int_F \phi_0(\xi, 0) f(\xi) d\xi}{\int_F [\phi_0(\xi, 0)]^2 d\xi}. \quad (6.54)$$

The calculation of  $A$  is thus straightforward as both the numerator and the denominator can be evaluated numerically given the trapped mode potential and the pressure profile  $f(x)$ . Note that if the condition (6.47) holds then  $A = 0$  and no trapped mode is excited.

Given that the pole structure of  $\phi_p$  is known the asymptotic form of  $\Phi_p$  for large time can be found by evaluating the inverse Fourier transform through moving the integration path across the poles and calculating the required residues. The free-surface elevation  $\eta$  is determined from the equation (6.50) and the dominant term in the long-time limit can be shown to be

$$\eta \sim -\frac{A\phi(x, 0)}{2\omega_0} t \cos \omega_0 t \quad \text{as } t \rightarrow \infty. \quad (6.55)$$

Thus, the asymptotic analysis accounts for the expected resonant growth in the amplitude. The time-domain BEM results were also observed to describe this resonant behaviour and a comparison between the results was made as illustrated in figure 6.6. In these computations the structure was specified to have a non-dimensional trapped mode frequency  $\Omega = \sqrt{4 \tanh 4}$  and the free-surface pressure profile takes the form

$$f(x) = \begin{cases} x_0^2 - x^2, & x \in F_I, \\ 0, & x \notin F_I, \end{cases} \quad (6.56)$$

where  $x_0$  is chosen to satisfy  $\phi_0(x_0, 0) = 0$  and  $\operatorname{sgn} f(x) = \operatorname{sgn} \phi_0(x, 0)$  on the internal free-surface  $F_I$  so that the existence condition (6.47) is violated. The free-surface

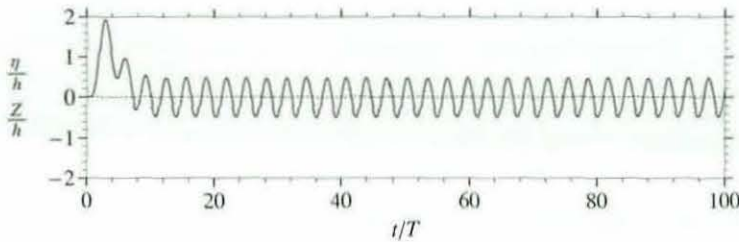


Figure 6.7: Displacement  $\eta/h$  of the mid-point of the free-surface (—) and the structure ((—)) due to a transient pressure forcing.

elevation was evaluated at the mid-point between the structures and compared to the asymptotic amplitude prediction  $A\phi(0,0)/2$  giving a good agreement. Note that the time-domain simulations involve non-dimensional times  $t/T$  and distances  $x/h$  where  $T = \sqrt{h/g}$  and the non-dimensional frequency is defined as  $\Omega = \omega/T$ .

## 6.6 Time-domain simulations of transient excitations

### 6.6.1 Two-dimensions

Passive trapped mode oscillations that persist with constant amplitudes can be excited by applying transient pressure oscillations to the free-surface. Therefore, instead of using the previous oscillatory pressure forcing (6.51) an exponentially decaying forcing with the dimensional form

$$P(x,t) = t^3 e^{-t} \frac{\phi_0(x,0)}{\phi_0(0,0)} \quad (6.57)$$

is applied on the internal free-surface. The factor  $\phi_0(0,0)$  is chosen to ensure the maximum magnitude of the forcing is of order unity. The time-domain results for the response of the fluid and the structure are shown in figure 6.7. This example illustrates how a persistent motion of the free-surface can occur without the excitation of a significant structural motion. In fact, the structure does move slightly due to the excitation of a motion resonance at the frequency  $\Omega \approx 1.28$  as can be seen from the discrete Fourier transform of the structure displacement shown in figure 6.8(b). A small peak at the trapped mode frequency (denoted by its non-dimensional value to two decimal places 2.00) is also apparent implying that a small force is exerted on the structure by the passive trapped mode. However, this is to be expected because the discretised structure is merely an approximation to the passive trapping structure and so the trapped mode will occur as a complex resonance of very small decay constant in the numerical computations. The amplitude of the fluid oscillation at the trapped mode frequency is much larger than that of the structure as is evident from the different

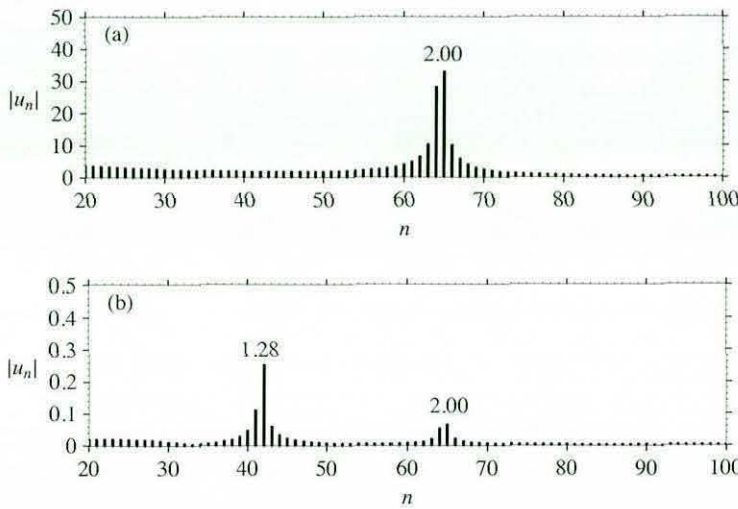


Figure 6.8: Discrete Fourier transforms of (a) the displacement  $\eta/h$  of the mid-point of the free-surface and (b) the displacement of the structure both of which are plotted in figure 6.7. Here  $|u_n|$  is  $N^{-1/2}$  times the amplitude of the Fourier component with index  $n$ , where  $N$  is the number of samples in the signal.

scales of the Fourier transform results shown in figure 6.8 and so it can be concluded that a passive trapped mode has been observed. The discrete Fourier transform of the free-surface elevation at the mid-point shown in figure 6.8(a) has a dominant peak at the trapped mode frequency. It should be noted that other methods can be used to excite passive trapped modes, for example if an initial free-surface elevation is specified on the internal free-surface that is non-zero and not orthogonal to the trapped mode then a persistent fluid oscillation will occur.

If the pressure profile  $f(x)$  in equation (6.51) is chosen using equations (6.48) and (6.49) so that the existence condition is satisfied then the passive trapped mode will not be excited. Therefore, even if an indefinite oscillatory pressure forcing is applied to the free surface at the trapped mode frequency the resonant growth of the fluid oscillations illustrated in figure 6.6 will not occur. This behaviour is demonstrated in the time-domain in a simulation involving the same passive trapping structure of the previous simulations and with a free-surface pressure forcing of the form

$$P(x, t) = \frac{x^2 + f_0}{\omega_0} \sin(\omega_0 t) \quad (6.58)$$

where  $f_0$  was computed numerically according to equation (6.49) for  $f_2 = 1$ . The results of this simulation are shown in figure 6.9 and it is clear that no resonant growth in free-surface oscillations occurs due to this pressure forcing. The free-surface does, however, oscillate at the frequency  $\omega_0$  due to the time-dependence of the oscillatory

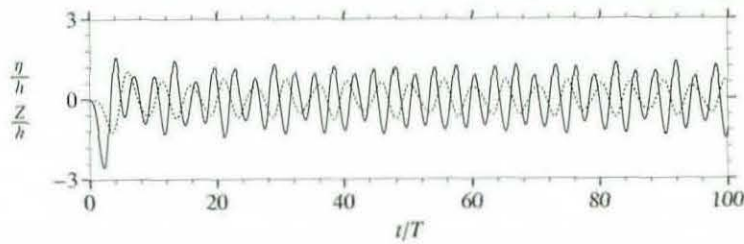


Figure 6.9: Displacement  $\eta/h$  of the mid-point of the free-surface (—) and the structure ((---)) due to the oscillatory pressure forcing (6.58).

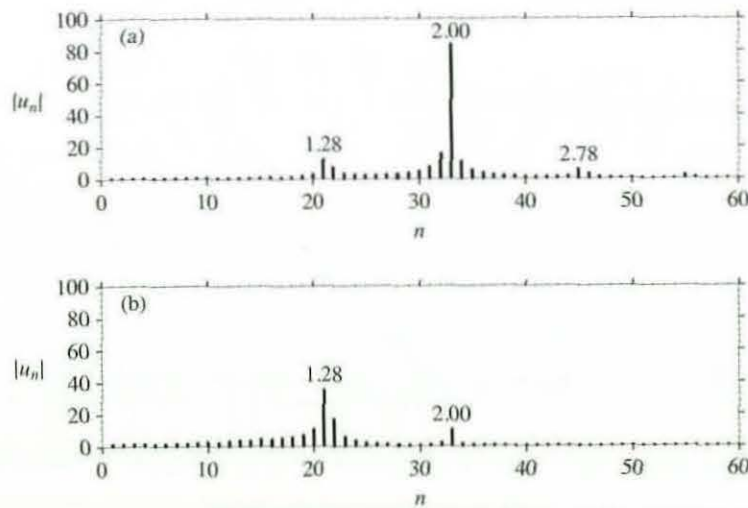


Figure 6.10: Discrete Fourier transforms of (a) the displacement  $\eta/h$  of the mid-point of the free-surface and (b) the structure shown in figure 6.9.

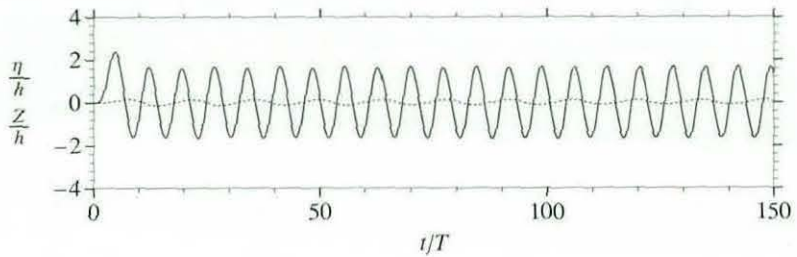


Figure 6.11: Displacement  $\eta/h$  of the mid-point  $r = 0$  of the free-surface (—) and the passive trapping structure (---) due to a transient pressure forcing in three dimensions.

forcing (6.58) but the structure also undergoes appreciable oscillations at this frequency. Although the structure oscillations of frequency  $\omega_0$  are smaller than those of the free-surface as can be seen from a comparison of the Fourier transforms in figure 6.10, the two oscillations are of the same order of magnitude. In contrast, when the passive trapped mode is excited the motion of the structure is negligible at the frequency  $\omega_0$  relative to the oscillations of the surrounding fluid. Thus, the frequency domain analysis of the excitation of the passive trapped modes in § 6.5 is validated numerically.

### 6.6.2 Three dimensions

To demonstrate excitation in three-dimensions, a passive trapping structure was constructed from the three-dimensional finite depth streamfunction (6.40) with the wavenumber  $k = 1.0$  and the stream-surface constant  $\delta = 2.0$ . Some difficulties occurred when determining the streamfunction from the representation (6.40) near the free-surface due to convergence difficulties for small values of  $z$ . Nevertheless, it was possible to overcome this problem, using the method related to equation (6.42), and hence to determine the stream-surface and subsequently to discretise this surface for use in the time-domain BEM simulations. A transient pressure forcing of the form  $(t/T)^3 e^{-t/T} \phi(r/h, 0)/\phi(0, 0)$  was applied to the internal free surface in order to excite the passive trapped mode. The resultant motion of the free-surface at the mid-point of the internal free-surface and of the structure itself are illustrated in figure 6.11. After the initial transient, caused by the free-surface pressure, has decayed a persistent oscillation of the free-surface accompanied by a small oscillatory motion of the structure can be observed. A discrete Fourier transform of the two signals reveals a motion resonance of frequency 0.46 has also been excited in addition to the passive trapped mode of non-dimensional frequency  $\Omega = \sqrt{1.0 \tanh 1.0} \approx 0.87$ . This resonance is observed as the only significant peak frequency in the Fourier transform of the structure motion (figure 6.12) and as a minor peak in the transform of the free-surface oscillation at a frequency lower than the passive trapped mode frequency. The persistent oscillation of

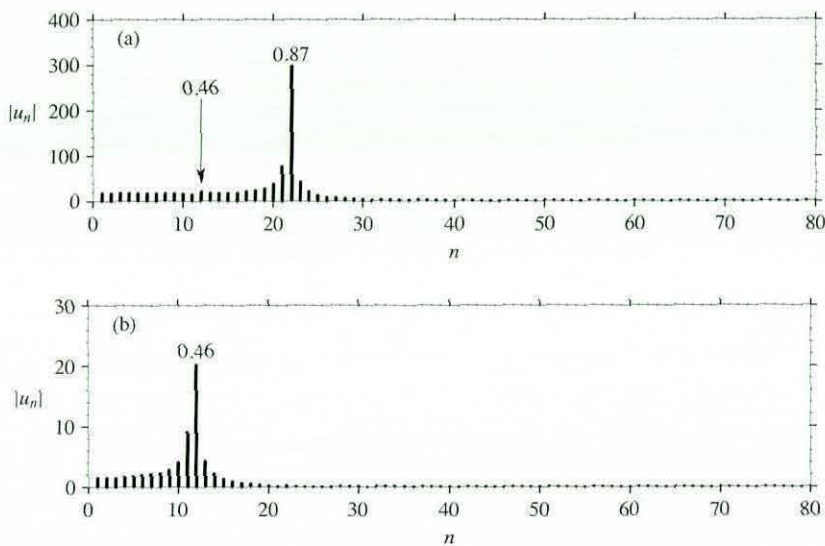


Figure 6.12: Discrete Fourier transforms of the displacement  $\eta/h$  of the mid-point of the free-surface (a) and the structure (b) depicted in figure 6.11.

the free-surface occurs at the trapped mode frequency. Thus, the existence of a passive trapped mode in an axisymmetric three-dimensional problem has been demonstrated using an equivalent/analogous BEM to that used in two-dimensions.

## 6.7 Conclusion

In this chapter special trapping structures have been constructed in both two and three dimensions which can support trapped modes both when fixed and when allowed to float freely. These passive trapping structures are such that the net force exerted by the corresponding trapped mode oscillation is zero and so in the absence of any forcing the structure does not move at the trapped mode frequency when allowed to float freely. In the frequency domain water-wave problem the passive trapped mode potential and the corresponding structure velocity satisfy the equation of motion non-trivially as required for motion trapping structures. However, in contrast to motion trapping structures the equation of motion is satisfied by assuming the velocity of the structure is zero which results in the requirement that the trapped mode exert a zero net hydrodynamic force on the structure at the trapped mode frequency. Thus, passive trapping structures possess properties of both sloshing and motion trapping structures. The zero-force condition is satisfied by any potential with a zero dipole coefficient at infinity in fluids of infinite depth. Previously, Motygin & Kuznetsov (1998) constructed such a structure in two-dimensions by the combination of two wave dipoles in the free-surface in order to

obtain symmetric sloshing trapped modes. This construction procedure is extended to three-dimensions by the introduction of a ring-dipole potential and the procedure is also modified for finite depth problems. Examples of passive trapping structures in infinite depth for both two and three dimensions have been provided. In all the investigations herein the motion of the structures are restricted to heave and the three-dimensional structures are assumed to possess a vertical axis of symmetry. A method for the excitation of the passive trapped modes has been investigated by the consideration of a potential due to an oscillatory pressure forcing on the free-surface surrounding a passive trapped mode. This frequency-domain analysis yielded an excitation condition and by extension an asymptotic prediction for the growth of the free-surface oscillations due to a resonant pressure forcing was obtained. This behaviour has been confirmed by a two-dimensional time-domain simulation thus providing a confirmation of the existence of passive trapped modes. Further time-domain simulations involving transient excitation mechanisms have been conducted to confirm the existence of the trapped modes and to demonstrate the properties of the passive trapped modes – large free-surface oscillations and negligible structural motion – in both two and three dimensions.

## Chapter 7

# Simulations of wave-structure interactions

A variety of water-wave problems and wave-structure interactions are investigated in this chapter. Thus far, the applications for the code have been the surge motion of toroidal structures (see § 4.2.4), the axisymmetric near-resonant motion of the fluid surrounding a structure and the heave motion of passive trapping structures. However, it is possible to utilise the code for more general problems involving a large number of the azimuthal Fourier modes. The problems of interest are: to simulate the propagation of wave-train with a planar regular component; to simulate the latching control mechanism in wave-energy interactions; to simulate the response of a structure and the surrounding fluid to an incident wave where the structure is free to move in heave, surge and pitch and where the modes of motion are dependent. In these simulations, the emphasis will be on the qualitative manner in which the time-domain code simulates the particular water-wave interactions considered rather than on quantitative power-absorption/body motion results. Therefore, the results of the simulations will generally not be compared to those in the literature. For example, it will be of more interest to see how the latching control improves the power-absorption capability of the wave-energy device compared to the uncontrolled case rather than verifying that the power absorption figures are consistent with previous simulations.

### 7.1 Plane-wave propagation

In this section propagation of a wave-packet with a dominant plane-wave component is modelled in a cylindrical domain free of structures using the time-domain BEM. A plane progressive wave travelling in a fluid of finite depth in the positive  $x$ -direction

with an amplitude  $A$  and wavenumber  $k$  is defined by the potential

$$\Phi_I(r, \theta, z, t) = \operatorname{Re} \left\{ -\frac{igA}{\omega \cosh kh} e^{ikx} \cosh k(z+h) e^{-i\omega t} \right\} \quad (7.1)$$

which corresponds to a free-surface elevation given by

$$\eta(r, \theta, t) = \operatorname{Re} \{ A e^{i(kx-\omega t)} \} \quad (7.2)$$

where  $\omega$  is defined by the dispersion relation  $\omega^2 = gk \tanh kh$ . It is most natural to describe a plane wave in terms of Cartesian coordinates  $(x, y, z)$  because of the wave-form's rectangular symmetry. However, it can also be expressed in terms of cylindrical coordinates using the relation  $x = r \cos \theta$  so that the spatial dependence becomes  $e^{ikr \cos \theta}$ . This expression must be expanded in a Fourier series in order to describe the wave using the BEM code based on the domain with an axis of symmetry. Obtaining an accurate description of the plane-wave motion provides a good test of the capability of the code to describe general fluid motions. Previous simulations of fluid and structure motions have involved straightforward angular dependencies such as  $\cos \theta$  for the surging and pitching of a structure. First of all, the Fourier expansion of the plane-wave potential at  $t = 0$  is considered and then the number of nodes necessary to describe the plane-wave accurately is determined. Finally, a particular wave-disturbance is considered and the results are shown.

A wave-disturbance of finite-extent with a dominant plane wave component can be generated in the time-domain BEM using a similar approach to that taken for the two-dimensional resonant motion problem in § 5.3. Thus, the potential  $\Phi$ , the normal velocity  $\partial\Phi/\partial z$  and the elevation  $\eta$  on the free-surface must be specified at the time  $t = 0$  so as to correspond to a planar wave-disturbance. Within the framework of the BEM developed here, the plane wave must be expanded as a Fourier series in  $\theta$  and the initial conditions for the potential, the normal velocity and the elevation on the free surface should then be computed for each Fourier mode  $m$ . Thereafter, the time-stepping procedure is used to obtain the solutions in each mode and finally the complete wave form is obtained by summing over the Fourier series. The Fourier series expansion in  $\theta$  of the  $e^{ikr \cos \theta}$  term in the plane-wave potential (7.1) is (see Abramowitz & Stegun (1964), 9.1.42-43)

$$e^{ikr \cos \theta} = \sum_{m=0}^{\infty} \epsilon_m i^m J_m(kr) \cos m\theta \quad (7.3)$$

where  $\epsilon_m$  is the Neumann symbol defined by  $\epsilon_0 = 1$ ,  $\epsilon_m = 2$ ,  $m \geq 1$ . Therefore, the initial potential on the free-surface  $z = 0$  can be represented by

$$\Phi_I(r, \theta, 0, 0) \simeq \operatorname{Re} \left\{ -i \frac{gA}{\omega} \sum_{m=0}^N \epsilon_m i^m J_m(kr) \cos m\theta \right\} \quad (7.4)$$

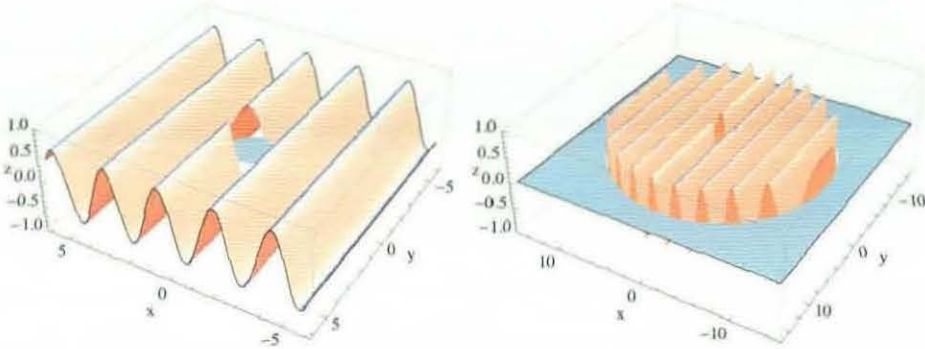


Figure 7.1: Surface plots of the plane wave disturbance at  $t = 0$ . The plot on the left illustrates the disturbance near the origin while the plot on the right shows the total disturbance.

with similar expressions for the normal velocity and elevation. The initial potential on the free-surface corresponding to the  $m^{\text{th}}$  Fourier mode of the plane-wave disturbance is thus given by

$$\phi_I^m(r, 0, 0) = \begin{cases} \frac{\epsilon_m A g}{\omega} (-1)^{(m-1)/2} J_m(kr) & \text{odd } m \\ 0, & \text{even } m \end{cases} \quad (7.5)$$

and the initial free-surface elevation by

$$\eta_m(r, 0) = \begin{cases} \epsilon_m J_m(kr) (-1)^{m/2}, & \text{odd } m \\ 0, & \text{even } m. \end{cases} \quad (7.6)$$

For the initial normal velocity on the free-surface, the  $m^{\text{th}}$  azimuthal mode is simply  $\phi_m(r, 0, 0) \tanh kh$  due to the  $\cosh(k(z+h))$  dependence in the plane-wave potential (7.1). Of course, only a finite number of modes can be considered in the time-domain BEM and so it is necessary to determine a suitable number of Fourier azimuthal modes to adequately describe the planar nature of the wave while ensuring the computational times are relatively modest. A simple but effective way of determining the truncation number for the series is to look at a sequence of Fourier series approximations of the potential (7.1) with increasing truncation numbers and then compare the convergence of these series with the desired plane wave form. The truncation number  $N$  can then be chosen based on the results of this investigation and the necessity to retain moderate computational times for the simulations.

A finite disturbance with a plane-wave form defined by

$$f(r, \theta) = \begin{cases} \Phi_I(r, \theta, 0, 0), & a \leq r \leq b \\ 0, & r < a, r > b \end{cases} \quad (7.7)$$

is approximated using a Fourier series

$$F_N(r, \theta) = \begin{cases} \sum_{m=0}^N \phi_I^m(r, 0, 0) \cos m\theta, & a \leq r \leq b \\ 0, & r < a, r > b \end{cases} \quad (7.8)$$

where  $\phi_I^m(r, 0, 0)$  is defined by (7.5) for odd values of  $m$  and is zero for even values. No smoothing at the edges of the wave-form is imposed here because it is sought only to determine the number of modes necessary to adequately describe the propagation of the plane wave component of the incident wave-packet. The initial profile in the BEM is smoothed to ensure numerical difficulties do not arise. The domain of the disturbance is specified as having an annular geometry because in the simulations involving floating structures that follow the initial disturbances will be zero in the immediate vicinity of the structure and for distances from the origin greater than that of the damping zone. This is to avoid any numerical difficulties due to discontinuities in the potential or normal velocity. An illustration of such a wave-packet in non-dimensional form is shown in figure 7.1 and in this particular example the non-dimensional inner and outer radii of the disturbance are specified by  $a/h = 0.5$  and  $b/h = 12$ . The non-dimensional wavenumber  $kh$  is chosen to be 2.5 which corresponds to a wave period of 8 seconds in fluid of depth  $h = 40m$ .

The absolute error  $\Delta F$  in the truncated Fourier series approximation  $F_N(r, \theta)$  to the planar wave-form  $f(r, \theta)$  is plotted in figure 7.2 over the domain  $\mathcal{D} = \{0 \leq r/h \leq b/h, 0 \leq \theta \leq 2\pi\}$  for the truncation numbers  $N = 15, 25, 35$ . All the lengths are non-dimensionalised by the depth  $h$  in these diagrams. It can be seen that the area of negligible error increases successively with increasing  $N$  and thus the Fourier series approximation is converging to the plane wave form over a progressively larger radius as the truncation number  $N$  increases. So, for  $N = 15$ , the agreement is good only within the radius  $r/h \lesssim 5.0$  but for  $N = 35$ , the error over the total domain  $\mathcal{D}$  is negligible and the Fourier series provides a good description of the wave disturbance. However, as more Fourier modes are considered the computational times will increase. For a domain with approximately 125 nodes and a truncation number  $N = 25$  the BEM computations take roughly four hours. In the case of the time-stepping, up to two hours is necessary to advance the solution over 100,000 time steps. Given that other simulations would require up to 200 nodes it was decided that  $N = 25$  is a sufficiently large number of Fourier modes for an accurate simulation of plane-wave propagation while also retaining modest computational times. From figure 7.2 it can be seen that the Fourier series representation of the initial planar wave profile is good for  $r/h < 10.0$  in this case and in most of the simulations the extent of the initial wave-disturbances will not have non-dimensional radii much bigger than 10.0 thus justifying the choice of this particular truncation number. It should be noted that the number of terms required in the Fourier series for an adequate description of the incident wave form decreases as the

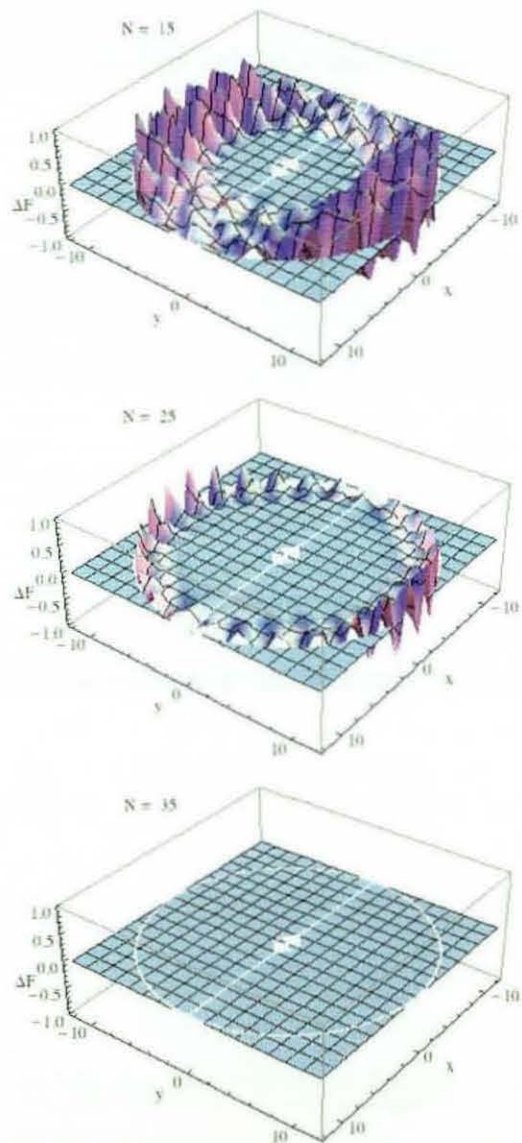


Figure 7.2: A surface plot of the error  $f(r, \theta) - F_N(r, \theta)$  in the truncated Fourier series description of the incident wave initial condition for truncation numbers  $N = 15, 25, 35$ .

wavenumber decreases (i.e. as the wavelength increases). Furthermore, disturbances without an oscillatory form such as a three-dimensional Gaussian form require as few as 10 modes for an accurate approximation. Essentially, a slowly varying wave-form will require less modes than a quickly varying form such as a plane wave with a large wavenumber.

In the time-domain BEM the inner and outer edges of the initial disturbance will be ramped to zero to ensure the profile in each mode is continuous at  $t = 0$  unlike in the Fourier series investigations above. Thus,  $\eta_m$ ,  $\phi_m$  and  $\partial\phi_m/\partial n$  will be defined analogously to the two-dimensional definition of the initial free-surface elevation from chapter 5 except the regular cosine term will be replaced by the Bessel function of order  $m$ ,  $J_m(kr)$ . Therefore, the non-zero initial free-surface elevation is defined as

$$\eta_m(r, 0) = \begin{cases} \frac{1}{2}(1 - \cos(\frac{\pi}{r_1 - r_0}(r - r_0)))J_m(kr), & r_0 \leq r \leq r_1 \\ J_m(kr), & r_1 \leq r \leq r_2 - \lambda/2, \\ \frac{1}{2}(1 - \cos(\frac{k}{2}(r - r_2)))J_m(kr), & r_2 - \lambda/2 \leq r \leq r_2, \end{cases} \quad (7.9)$$

with similar definitions for the initial potential and normal velocity. Thus, the outer smoothed section of the disturbance is half of a wavelength in radial extent and the inner smoothed section is  $r_1 - r_0$  in radial extent. In the simulation results presented here the initial conditions correspond to the non-dimensional radii  $r_0/h = 0.5$ ,  $r_1/h = 1.125$  and  $r_2/h = 12.0$  in each mode  $m = 0, 1, \dots, N$  and the time-stepping is conducted with 100,000 time steps for a non-dimensional step-size of  $\Delta/T = 0.01$  so that the total simulation time is  $100T$  where  $T = \sqrt{h/g}$ . Snapshots in time of the resultant propagating wave are shown in figure 7.3 within the non-dimensional radius  $r/h = 10.0$ . The area of zero disturbance around the origin perturbs the plane waves as they propagate to the right however this perturbation tends not to affect the incident waves from the left. The snapshots illustrate the success of the BEM in modelling a finite wave-train consisting of a small number of plane wave crests. The crests of longest extent remain perpendicular to the direction of propagation as the simulation advances however the crests to the farthest left tend to disperse and propagate with different speeds during the simulation. At the time  $t = 40T$ , the last of the significant wave crests have propagated past the origin and by time  $t = 50T$ , although not shown in figure 7.3, all that remains in the vicinity of the origin is a set of small high-frequency ripples – the planar wave crests have propagated to the right. The evolution of the free-surface at the origin is also shown in figure 7.4 (a) and (b) with comparisons to a fully harmonic plane wave and the oscillations can be seen to be regular for the initial phase of the simulation. Thereafter, the oscillations decay as the end of the wave-disturbance disperses and propagates past the origin. The main properties of a propagating plane wave are captured with the amplitude of the oscillations very close to  $A/h = 1.0$  and the primary (non-dimensional) frequency of oscillation at  $\Omega = \sqrt{2.5 \tanh 2.5}$  as

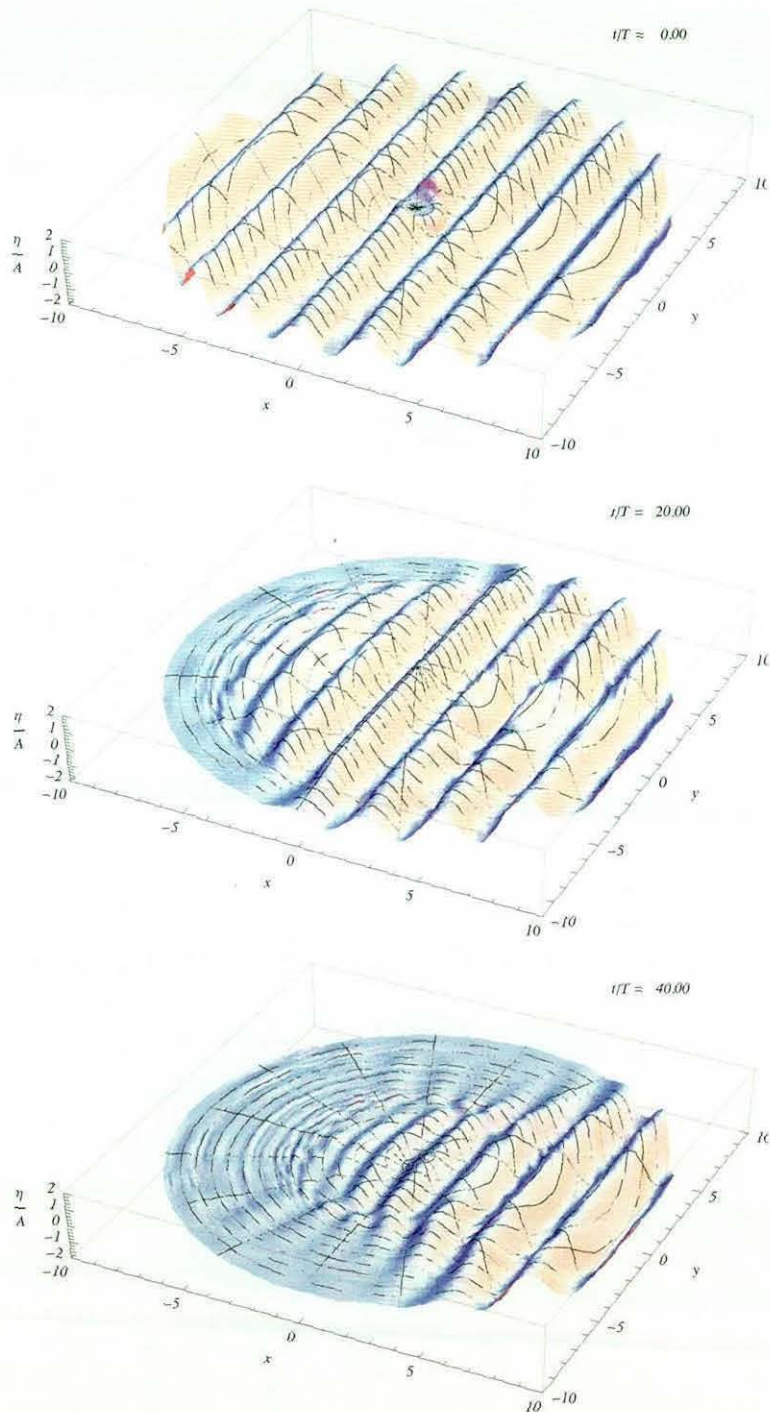


Figure 7.3: Plane wave propagation across part of the computational domain in a three-dimensional BEM simulation. Snapshots of the free-surface elevation  $\eta(r, \theta, t)$  are plotted at various times  $t$ .

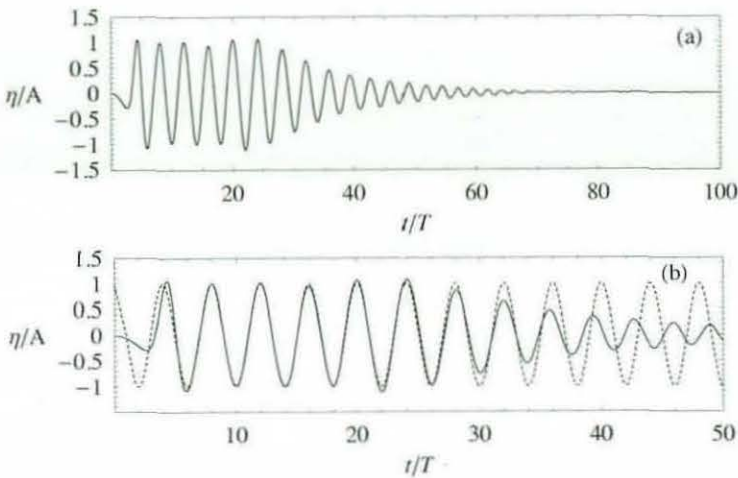


Figure 7.4: Non-dimensional free-surface elevation at the origin (a) over the total simulation and (b) compared to the free-surface elevation for the exact plane wave (--) over half the simulation time.

illustrated in figure 7.4 (b). The dispersion of the initial smoothing at the edge of the wave-disturbance causing the strongly irregular oscillations at the tail of the incident wave can also be observed in this figure. The heave exciting force results from the investigation into the diffraction problem in § 4.2.1 indicate that for a period of time this generation method for an incident wave will yield hydrodynamic forces like those of a plane wave; however, those results correspond to the  $n = 0$  mode only.

## 7.2 Latching control

In wave-energy interactions it is generally necessary to impose some motion control on the wave-energy devices in order to maximise the power-absorption capabilities of the device. Optimal power absorption conditions have been derived by Evans (1976) by means of a frequency domain analysis of the power-absorption problem in the linearised description of the motion of a heaving device with an axis of symmetry. However, the optimality condition requires the control of both the amplitude and phase of the device motion which is very difficult in practice. To obtain a gain in the power absorbed by the uncontrolled structure a more realistic method of control must be employed and one such method is latching control where the wave-energy device (WED) is held fixed for part of the motion cycle.

Budal & Falnes (1980) were among the first to propose latching as a method of control for wave-energy devices. If a wave energy converter is constrained to oscillate in a single mode of motion in regular seas the maximum power absorption is obtained

by satisfying two conditions; the first is an optimal phase condition and the second is an optimal amplitude condition. The former condition requires the phase of the body velocity to equal that of the exciting force due to the incident wave and once the phases are equal the amplitude of the oscillation must be adjusted to satisfy the optimal amplitude condition. This requires the power take-off damping equals the hydrodynamic damping coefficient at the incident wave frequency; however, optimal power absorption occurs only when both conditions are satisfied. A continuous control system, where the controller can act at any instant of time, may be used to satisfy both conditions for optimum absorption and Falnes (2002) provides a brief description of this method in addition to a mathematical expression of the optimal power absorption conditions. With this type of control, it may be necessary to return energy as well as to absorb it during the power take-off cycle to ensure the amplitude condition is met. Hence, this control method has been referred to as "reactive phase control". A practical implementation would require a combined generator-and-motor power take-off system. However, returning the correct amount of power at the correct moment would be extremely difficult. An alternative control system exists, referred to as discrete latching control, and consists of locking the oscillating body at the position of full extension (when the velocity is zero) and releasing it after a certain delay to be determined by some optimising criteria for the power-absorption. Only the phase of the body motion can be controlled and as the amplitude condition cannot be satisfied it is referred to as a sub-optimal control strategy.

Discrete latching control is also known as phase control as it directly controls only the phase of the body motion. In this case, the body is latched when its velocity is zero and released when the phase of wave-force is most favourable for power absorption. The body then moves from its latched position, subject to the hydrodynamic forces until its velocity is zero again and it is latched once more etc. The only control variable in this case is the latching duration. As discussed by Babarit & Clément (2006), previous latching simulations in irregular waves require the assumption that the excitation force is known sufficiently far in future to determine a favourable latching phase. In real-world conditions this may be difficult to implement although short-term forecasts for the incident wave-climate may be possible. Although discrete latching control is a sub-optimal control strategy it nevertheless is observed to yield significant gains in the absorption capabilities of the wave-energy device. That is, for the same configuration as an uncontrolled body, a latched body can absorb significantly more energy. A number of different latching control strategies exist, some of which were investigated by Babarit & Clément (2006) by application to a harmonic mechanical oscillator modelling the frequency-domain and to time-domain linear simulations. Here, only two variations on the basic latching strategy for regular seas will be investigated.

### 7.2.1 Equations of motion for latching

In the time-domain simulations, an incident wave packet with a dominant regular component will impinge on a floating structure with a vertical axis of symmetry. The structure is considered to be a wave-energy device and will be permitted to move in heave only and will be moored as usual by a system of linear springs and dampers with the assumption that the power take-off occurs through the dampers. Latching control will be implemented in order to optimise the power absorption and two slightly different latching methods will be considered – single-ended latching where the latching is only permitted at one extreme of motion and alternate-ended latching where the latching occurs at both extremes of motion. The latching duration will be chosen to obtain approximate coincidence of the phase of the body velocity and the exciting force. The vertical displacement  $Z(t)$  of the structure of mass  $M$  is determined from the single degree of freedom equation of motion

$$M\ddot{Z}(t) + \rho \iint_{\Gamma} \frac{\partial \Phi}{\partial t} n_z dS + [(\rho g W + \kappa)Z(t) + \gamma \dot{Z}(t)] = F(Z, \dot{Z}, t) \quad (7.10)$$

where  $\kappa$  and  $\gamma$  are the spring and damping coefficient of the mooring system. The instantaneous absorbed power is thus given by  $P(t) = \gamma \dot{Z}(t)^2$  and is easily computed using the time-domain code. The term  $F(Z, \dot{Z}, t)$  on the right hand side is any external forcing and is included for generality although in the following latching simulations no such term will be present.

The prescribed incident wave will be a finite wave-packet generated by imposing an initial free-surface wave-form as described in the last section. Therefore, a period of harmonic wave incidence will occur after a brief transient and during this period the maximum transport of wave-power will occur. The wave-disturbance and wave-energy transported will then decay to zero as the end of the wave-train propagates past the structure. Therefore, although not purely time harmonic the incident wave is predominantly harmonic with a frequency  $\omega$  and can be considered to be a plane wave for the purposes of computing the power absorption in heave. Given that the motion is in heave only, it is only necessary to consider the  $n = 0$  Fourier azimuthal mode in the time-domain and the regular part of the incident wave corresponds only to the axisymmetric component of a harmonic plane wave. The efficacy of latching is assessed by comparing the mean power absorbed by the uncontrolled and latched body over the same time interval during wave-incidence. The characteristics of the mooring configuration were chosen to yield a good performance for the uncontrolled body during the harmonic phase of the wave incidence; therefore  $\kappa$  and  $\gamma$  were chosen to satisfy the optimal power absorption conditions for the purely harmonic motion of an unconstrained axisymmetric body in heave. If the incident wave and structure motions are assumed to be harmonic and no external forcing is applied then the equation of

motion for the uncontrolled oscillation of a body is

$$(M + a(\omega))\ddot{Z} + (b(\omega) + \gamma)\dot{Z} + (\rho g W + \kappa)Z = F_d e^{i\omega t} \quad (7.11)$$

where  $a$ ,  $b$  and  $F_d$  are the added mass and damping coefficients and the diffraction or excitation force. It can be shown (see Falcão (2008) for a simple explanation) that the time-averaged absorbed power by the mooring is maximised by satisfying the conditions

$$\rho g W + \kappa = \omega^2(M + a(\omega)) \quad (7.12)$$

and

$$\gamma = b(\omega). \quad (7.13)$$

The former condition ensures the phase of the velocity of the structure equals that of the exciting force, i.e. it is the phase condition referred to earlier. To obtain the optimum amplitude an appropriate amount of power must be taken up through the power take-off (PTO) mechanism for each cycle and this is achieved by setting  $\gamma = b(\omega)$ .

The optimal phase condition requires the mooring spring coefficient to satisfy  $\kappa = \omega^2(M + a(\omega)) - \rho g W$  but for realistic ocean wave periods the right-hand side is negative for some device geometries such as the hemisphere. The optimal phase condition can thus be difficult to satisfy practically and in such cases the mooring spring coefficient is chosen to be small and positive to accurately model an actual mooring line. On the other hand, the mooring damping constant can be chosen to equal the damping coefficient for a given incident wave frequency as both are positive and in the subsequent simulations the PTO damping constant will be chosen to satisfy this condition. The power absorption performance of the uncontrolled body will then be measured with these mooring specifications. However, the phase of the exciting force and the body velocity will not coincide when condition (7.12) cannot be satisfied for  $\kappa > 0$ , so by implementing phase control by latching it should be possible to improve the power absorbed over the period of wave incidence. To realise this improvement a suitable latching duration must be estimated based on the harmonic approximation of the incident wave. Alternatively, instead of computing a constant latching duration for the whole simulation the times when the structure must be released to ensure the phases of the velocity and exciting force coincide were computed based on the fact that the incident wave form was known *a priori*. Since the structure is latched at the instant of zero velocity when the structure reaches a maximum or minimum displacement then the structure should be released when the exciting force is zero to achieve phase coincidence. In the latter case, the structure is released almost exactly at the times when the exciting force is zero given that the exciting force due to the incident wave-packet settles to the steady-state oscillatory form after a short transient as shown in figure 4.11. However, in the former case the time between the structure velocity

vanishing and the exciting force vanishing is not constant throughout the simulation because the structure velocity is slow to settle to the steady oscillatory state due to the excitation of a complex resonance. Therefore, a constant latching duration will not yield the best results – it is better to release the structure at the zeroes of the exciting force. Given that the exciting force is essentially harmonic for much of the simulation, its zeroes can be determined by consideration of  $|F_d|e^{i(\omega t+\sigma)}$  where  $|F_d|$  is the exciting force amplitude and  $\sigma$  the exciting force phase difference with the incident wave; both  $\sigma$  and  $|F_d|$  can be computed in WAMIT for a particular structure and frequency. The zeroes of the harmonic exciting force corresponding to the maximum and minimum displacement occur at

$$\begin{aligned} T_{max} &= \frac{(2n + 1/2)\pi + \sigma}{\omega} \quad \text{and} \\ T_{min} &= \frac{(2n + 3/2)\pi + \sigma}{\omega} \end{aligned} \quad (7.14)$$

for  $n = 0, 1, 2, \dots$ , respectively. These estimates are sufficiently accurate for the time-domain exciting force during most of the simulation until the wave-train begins to decay. This can be observed from the verification of diffraction simulations in Chapter 3 where the time-domain exciting force approximates the frequency domain result very well until the wave begins to decay as illustrated in figure 7.4 (a). Therefore, in the latching simulations to follow it is assumed that the incident wave is known prior to its propagation – this is consistent with most studies of discrete latching which is generally classified as a non-causal control method.

### 7.2.2 Time-domain latching simulations

The first set of latching simulations involve a semi-submerged spherical wave buoy of radius  $a = 12m$  floating in a fluid of depth  $h = 40m$  and moored such that the only significant motion is in heave. A finite incident wave-train of period 8s and wave amplitude 1m propagates in the positive  $x$  direction toward the wave buoy. The domain of computation has a radius of  $L/h = 15.0$  and a damping zone of width  $d/h = 2.5h$ . The regular component of the incident wave packet is specified to be of non-dimensional radius 10.0 and the resultant free-surface elevation at the axis of symmetry, in the absence of the structure, due to the propagation of the incident wave is illustrated in figure 7.4 (a). This incident wave packet is generated as described in § 7.1 and is used in all the subsequent latching simulations. The wave buoy will absorb some of the incident wave power *via* the power take-off implemented as a linear damper in the mooring. In non-dimensional terms, the wave-buoy has a radius  $a/h = 0.3$  and the frequency of the incident wave is  $\Omega \approx 1.57$ . The non-dimensional added mass and damping coefficients  $\tilde{a}$  and  $\tilde{b}$  at this frequency were computed using WAMIT and so the optimal non-dimensional mooring parameters for a harmonic motion were computed to

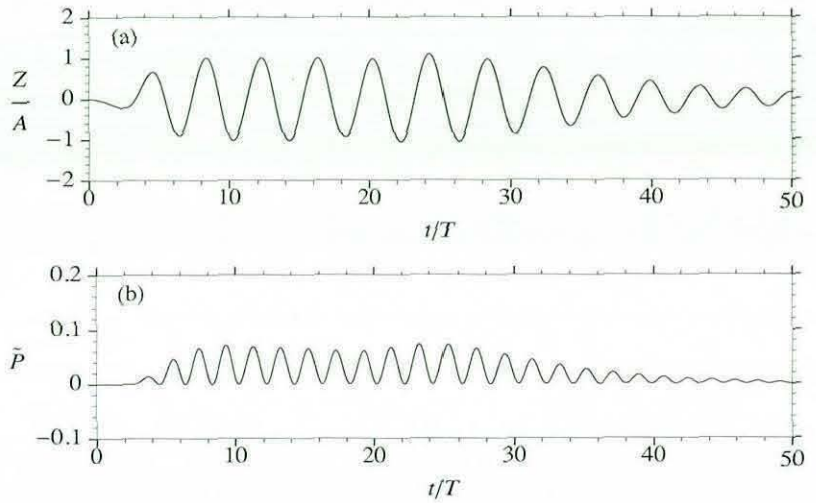


Figure 7.5: Variation with time of (a) the heave displacement  $Z/A$  and (b) absorbed power  $\tilde{P} = P/\rho g A^2 h^2$  for an uncontrolled moored spherical wave buoy subject to the incident wave of non-dimensional frequency  $\Omega = 2.5$  represented in figure 7.4 (a).

be

$$\begin{aligned}\tilde{\gamma}_{opt} &= \Omega \tilde{b}(\Omega) \approx 0.027 \\ \tilde{\kappa}_{opt} &= \Omega^2 (\tilde{M} + \tilde{a}(\Omega)) - \tilde{W} \approx -0.08\end{aligned}\quad (7.15)$$

where  $\tilde{M} = M/(\rho h^3)$  and  $\tilde{W} = W/h^2$  are the non-dimensional mass and water-plane area. The non-dimensional damping coefficient must be multiplied by the non-dimensional frequency as a result of the WAMIT non-dimensional definitions of the added mass and damping coefficients which use the frequency  $\omega$  rather than  $\sqrt{g/h}$  as the frequency-scale. In the simulations involving the wave buoy, the non-dimensional mooring damping coefficient  $\tilde{\gamma}$  was chosen to equal the optimal value for harmonic motions and the non-dimensional mooring spring coefficient  $\tilde{\kappa}$  was chosen to be 0.01, i.e. small and positive. Under the assumption of harmonic oscillations, the phase of the exciting force was computed using WAMIT to lead the phase of the incident wave by  $\sigma = 0.381$  radians.

The power absorption of the moored wave-buoy undergoing uncontrolled heave oscillations due the incidence of the wave-train is considered first. The device displacement and instantaneous power absorption due to the incidence of the wave-train described above are illustrated in figures 7.5(a) and 7.5(b) respectively. It can be observed that there is a simultaneous growth in the motion amplitude and power absorbed as the incident wave propagates past the structure. Similarly, as the tail of the incident wave train is reached the amplitude of the body oscillations decay and thus the power absorbed is also reduced in amplitude. It is likely that the incident wave train is not

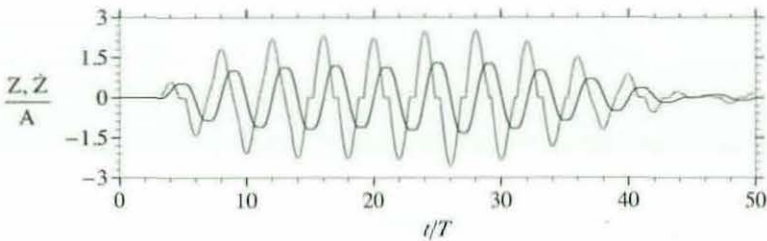


Figure 7.6: The heave displacement (—) and velocity (---) of a fully latched floating spherical wave buoy subject to the incident wave.

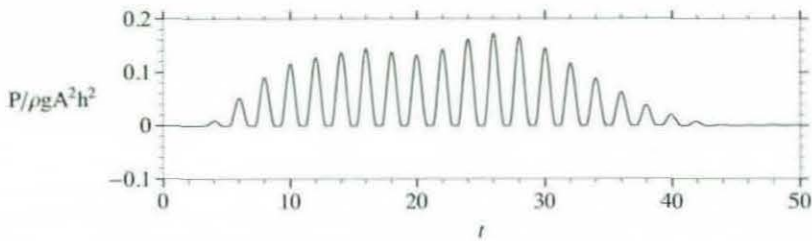


Figure 7.7: The variation in the instantaneous power absorption of the fully latched wave buoy subject to the incident wave.

sufficiently long for the body oscillations to reach a steady state oscillation and so the amplitude growth is a free-motion analogue to the diffraction resonant behaviour described in Chapter 4. The mean (non-dimensional) power absorbed over the course of the simulation which is of length  $T_S = 50T$  is  $P_M/(\rho gh^2 A^2) = 0.0206$  where

$$P_M = \frac{1}{T_S} \int_0^{T_S} \gamma \dot{Z}(t)^2 dt. \quad (7.16)$$

A phase difference exists between the body velocity and the excitation force when the body moves freely subject only to the mooring forces because of the transient incident wave start-up and furthermore because phase condition (7.12) is not satisfied. However, if latching occurs when the maximum (minimum) displacement is attained and release occurs when the exciting force goes from positive to negative (negative to positive) then this phase condition can be approximately be satisfied. Therefore, the imposition of latching control should improve the power absorption capabilities of the wave energy device. Initially the device is latched at the equilibrium position and the release time for the latching has been determined from the frequency domain. The variation of the device velocity and displacement for a double-ended latching strategy are illustrated in figure 7.6. A plot of the instantaneous power absorbed/taken up by the mooring PTO is shown in figure 7.7. A comparison between the latch controlled and uncontrolled body displacements reveals that by satisfying the optimal phase condition the displacement

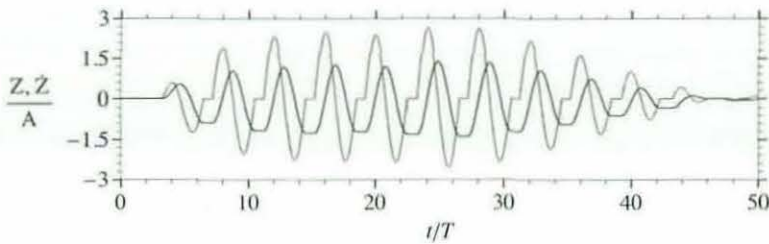


Figure 7.8: The heave displacement (—) and velocity (---) of a single-ended latched floating spherical wave buoy subject to the incident wave.

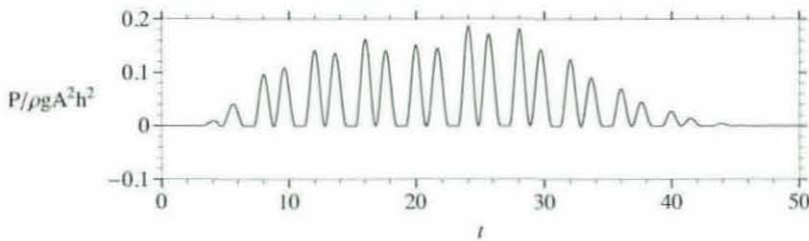


Figure 7.9: The variation in the instantaneous power absorption of the single-ended latched wave buoy subject to the incident wave.

(and hence velocity) amplitudes increase resulting in an increase in the power absorbed. The mean power absorbed over the total simulation time is  $P_M/\rho g A^2 h^2 = 0.0330$  – a 60% increase on the uncontrolled power absorbed. Therefore, it is clear the latching can significantly improve the power absorption capabilities of a wave-energy device.

A simulation of single-ended latching was also conducted. In this latching strategy, the device is only latched at the lowest point of the motion and is allowed to move subject to the mooring constraints through the highest point of the motion. Such a strategy should yield a similar improvement on the uncontrolled power absorption capabilities of the device as was obtained by the full latching control approach. Figures 7.8 and 7.9 illustrate the displacement/response of the buoy to the incident wave disturbance and the instantaneous power absorbed from the incident wave during the course of the interaction. The behaviour is as expected very similar to that of the full latching strategy. However, this latching strategy yields a mean power absorption value of 0.0361 which corresponds to an increase of 75% on the absorption capabilities of the uncontrolled device. Importantly, both latching strategies do not result in large increases in the amplitude of the device displacements although a small increase can be observed. The single-ended latching strategy yields a bigger improvement in the power absorption results of the device compared to the uncontrolled results than the double-ended latching strategy. However, it is not clear if this is always the case. In the paper Babarit,

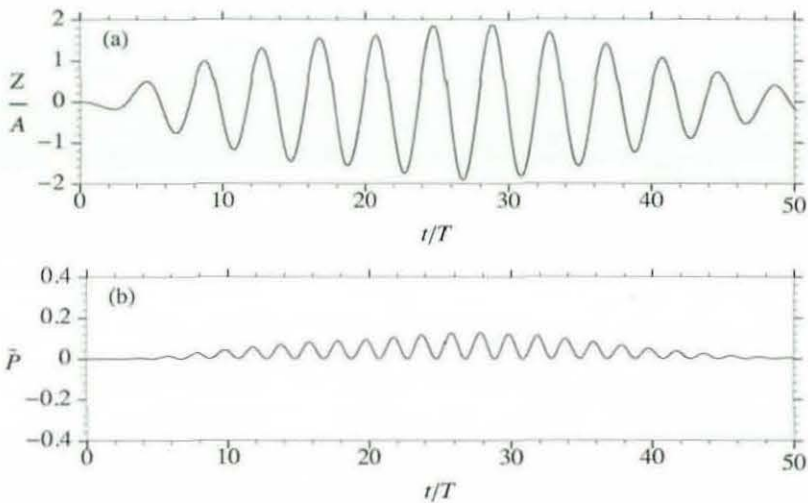


Figure 7.10: Variation with time of (a) the heave displacement  $Z/A$  and (b) absorbed power  $\bar{P} = P/\rho g A^2 h^2$  for a freely floating vertical circular cylinder subject to an incident wave of non-dimensional frequency  $\Omega = 2.5$ .

Duclos & Clément (2004), the single-ended latching strategy implemented in the mechanical oscillator model for the wave-energy device does yield a bigger improvement in the power absorption results in some instances where the incident wave frequency is greater than the natural resonant frequency of the device. It was later deduced in that paper that these results “seem to apply also to our hydrodynamic oscillator” in the frequency-domain.

The behaviour of a moored vertical circular cylinder of radius and draft 12m constrained to move in heave undergoing latching control was also investigated. An identical incident wave packet to that in the wave-buoy simulations was utilised and the computation of the added mass and damping coefficients for the cylinder at the incident frequency yield the following

$$\begin{aligned}\tilde{b}(\Omega) &\approx 0.0149 \\ \Omega^2(\tilde{M} + \tilde{a}(\Omega)) - \tilde{W} &\approx 0.0325\end{aligned}\tag{7.17}$$

so that it is possible to satisfy the optimal phase condition for harmonic motion. This significant change in the value of  $\Omega^2(\tilde{M} + \tilde{a}(\Omega)) - \tilde{W}$  results because of the change in the geometry of the structure; the mass and added mass increase while the waterplane area remains the same. It was expected that the gains from implementing the latching control would be smaller in this case as the absorption from the regular component of the incident wave will be close to the optimal. However, the transient effects may mean that latching could effect an improvement in the absorption capabilities as phase differences between the device velocity and the exciting force may arise during the

transient start-up of the device oscillations. The mean power absorbed over the duration of the interaction between the incident wave and the uncontrolled device was computed to be  $P_M/\rho g A^2 h^2 = 0.0317$  and this represents a 50% increase on the energy absorbed by the wave buoy. However, the uncontrolled device displacement amplitude for the cylinder, shown in figure 7.10, is also larger than that of the wave-buoy, so if an excursion bound is placed on the device then any theoretical gains may not be realised. The latching strategies were also applied to the floating cylinder interaction in order to see if any gains can be made due to transient effects. However, neither method improves on the uncontrolled setup where the mooring constants were chosen for optimal harmonic power absorption.

### 7.3 Multiple-mode motion of a moored freely floating body

In Chapter 4, the scope of the numerical time-domain solution code is expanded to include structure motions with three degrees of freedom and also to include coupling between these modes. Therefore, with the time-domain BEM it is possible to model the response of a structure to an incident wave in heave, surge and pitch and further to model the coupling effect mooring lines may have on the motions. In these ‘cross-coupling’ simulations, the motion of the structure is obtained from solutions of the first two Fourier azimuthal modes  $n = 0, 1$  while the diffraction field additionally requires the solution of the cosine modes  $n \geq 2$ . As shown in § 7.1, it is necessary to use a truncation number  $N$  for the Fourier cosine expansion of the potential that is greater than 20 to obtain a reasonably accurate description of a plane incident wave of non-dimensional wavenumber  $kh = 2.5$  with a radial extent of  $r/h = 10.0$ . It was expected that the same truncation number as was used for the incident wave propagation simulation would be sufficient to describe the diffracted and radiated wave-fields. This expectation was based on the assumption that the diffracted waves would have a similar frequency to the incident waves (a higher frequency would require more azimuthal modes) and would possess a sufficiently simple azimuthal form that could be adequately described using an azimuthal Fourier expansion of the velocity potential to a truncation number  $N = 25$ . The radiated wave-field involves oscillations in the first two azimuthal modes  $n = 0, 1$  only and so does not affect the choice of the truncation number. These modes corresponding to the structure motion are coupled in the time-stepping algorithm (as is the case in the previous cross-coupling simulations) and the other solution modes are time-stepped independently.

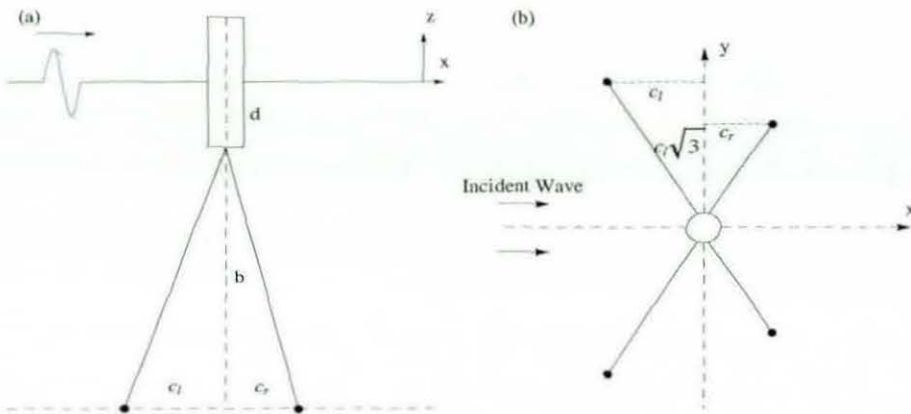


Figure 7.11: An elevation view (a) and plan view (b) of the mooring configuration. The bases of the mooring line in the plan of the mooring setup have the  $x - y$  coordinates  $(-c_l, \pm\sqrt{3}c_l)$  in the left half-plane and  $(-c_r, \pm\sqrt{3}c_r)$  in the right half-plane. In the elevation perspective,  $b = h - d$  denotes the distance from the mooring point to the sea-bed.

### 7.3.1 Cross coupling of modes of motion

Cross coupling of the structural modes of motion through mooring lines is first considered for a floating semi-submerged vertical cylinder of draft  $d$  and radius  $a$  in a fluid of depth  $h$ . The cylinder is moored by the combination of four separate mooring lines whose bases are placed symmetrically about the  $x$  and  $y$  axes. All mooring lines are assumed to be attached to the same point on the structure, i.e. the centre of the bottom face of the cylinder, and the pair of mooring lines to the left of the structure are assumed to be identical and symmetrically positioned relative to the  $y$ -axis and similarly for the pair to the right. However, each pair can have different mooring characteristics. An incident plane wave of the form described in § 7.1 propagates towards the structure from the left-half plane and the  $x$ -axis is defined by the direction of propagation of this wave. It is assumed that the propagation of the plane wave in the direction  $\theta = 0$  will not excite any motion in the  $y$ -direction, i.e. in the sway and roll modes. It is nonetheless considered more realistic to have two moorings to the left and to the right of the structure rather than just one on either side as in practice this will improve the control over the position of the structure. That is, if a perturbation of the structure in the  $y$ -direction were to occur then the combination of the symmetrically located mooring lines will help reduce this motion. So, this mooring configuration provides a physical justification for neglecting the motion in sway and roll in the simulations. Given that the motion of a body of revolution in yaw has no effect on an inviscid fluid then it is necessary to consider the motion in surge, heave and pitch only despite the complex mooring system. Thus, the effect of the mooring need only be considered in the  $x - z$  plane, i.e. on the surge, heave and pitch motions of the body. The mooring

lines to the left (right) of the structure are assumed to each exert a restoring force  $F_l$  ( $F_r$ ) along the direction of the lines. The mooring lines to the left and right of the structure are attached on the bed at positions  $(-c_l, \pm c_l\sqrt{3}, -h)$  and  $(c_r, \pm c_r\sqrt{3}, -h)$  as shown in figure 7.11(b) so that the net restoring force in the  $x - z$  plane for each pair is  $F_l$  and  $F_r$ , respectively, because the component of the force in the  $x - z$  plane is  $2F \sin \theta$  where  $\sin \theta = 1/2$  because the angle the mooring lines makes with the  $y$ -axis is  $\theta = \arctan 1/\sqrt{3}$ . Effectively, the pairs of identical mooring lines are represented as a single mooring line lying in the  $x - z$  plane. So, in the following derivation of the mooring forces only two mooring lines are considered, one lying to the left and one to the right of the body as illustrated in figure 7.11(a).

To be consistent with the linearised equation of motion for the structure (2.51) it must be assumed that the amplitude of the structure motions are small relative to the depth of the fluid when calculating the mooring forces. Furthermore, the action of the mooring lines are modelled as linear springs so that the restoring force acting along the direction of the mooring line due to an extension of  $\Delta l$  by Hooke's Law is

$$F = -\kappa \Delta l, \quad (7.18)$$

where  $\kappa$  is the spring constant describing the characteristic of the mooring line. To determine the components of the linearised forces in each mode due to the effective single mooring line in the  $x - z$  plane it is necessary to conduct a trigonometric analysis of the configuration when the structure has undergone a general translational and rotational displacement  $\mathbf{X} = (X_1, X_3, X_5)^T$  where  $X_5 = \beta$  is the angular displacement in pitch and  $X_1$  and  $X_3$  are the surge and heave displacements. In the case of a mooring line lying to the left of the structure the linearised extension is

$$\Delta l = \frac{c_l \Delta x + b \Delta z}{(b^2 + c_l^2)^{1/2}} \quad (7.19)$$

and for a mooring line lying to the right of the structure it is

$$\Delta l = \frac{-c_r \Delta x + b \Delta z}{(b^2 + c_r^2)^{1/2}} \quad (7.20)$$

where  $\Delta x = X_1 + d\beta$  and  $\Delta z = X_3$  are the net linearised horizontal and vertical displacements of the structure and hence mooring line.

The linearised restoring forces and moments exerted by the left mooring line in surge,

heave and the restoring moment pitch are then given by

$$\begin{aligned}(F_l)_1 &= -\kappa_l \frac{c_l(X_1 + dX_5) + bX_3}{(b^2 + c_l^2)^{1/2}} \cos \gamma_l \\(F_l)_3 &= -\kappa_l \frac{c_l(X_1 + dX_5) + bX_3}{(b^2 + c_l^2)^{1/2}} \sin \gamma_l \\(M_l)_5 &= -\kappa_l \frac{c_l^2(X_1 + dX_5) + bc_l X_3}{(b^2 + c_l^2)^{1/2}} d\end{aligned}\quad (7.21)$$

where  $\kappa_l$  is the spring constant of the left mooring lines,  $(M_l)_5$  denotes the restoring moment about the centre of rotation and  $\gamma_l = \arctan b/c_l$  is the angle the left mooring line makes with the sea-bed in the  $x - z$  plane when the structure is in equilibrium. Similarly, the restoring forces for the right mooring lines in the  $x - z$  plane are

$$\begin{aligned}(F_r)_1 &= \kappa_r \frac{-c_r(X_1 + dX_5) + bX_3}{(b^2 + c_r^2)^{1/2}} \cos \gamma_r \\(F_r)_3 &= -\kappa_r \frac{-c_r(X_1 + dX_5) + bX_3}{(b^2 + c_r^2)^{1/2}} \sin \gamma_r \\(M_r)_5 &= \kappa_r \frac{-c_r^2(X_1 + dX_5) + bc_r X_3}{(b^2 + c_r^2)^{1/2}} d\end{aligned}\quad (7.22)$$

with analogous definitions for  $\kappa_r$ ,  $\gamma_r$  and  $(M_r)_5$  as for the left mooring line. Therefore, the net mooring forces expressed in the generalised summation form are

$$F_\mu = - \sum_\nu \kappa_{\mu\nu} X_\nu \quad (7.23)$$

where the  $\kappa_{\mu\nu}$  is an element matrix of spring coefficients is

$$\kappa = \begin{pmatrix} \kappa_l \frac{c_l^2}{b^2 + c_l^2} + \kappa_r \frac{c_r^2}{b^2 + c_r^2} & \kappa_l \frac{bc_l}{b^2 + c_l^2} - \kappa_r \frac{bc_r}{b^2 + c_r^2} & \kappa_l \frac{c_l^2 d}{b^2 + c_l^2} + \kappa_r \frac{c_r^2 d}{b^2 + c_r^2} \\ \kappa_l \frac{bc_l}{b^2 + c_l^2} - \kappa_r \frac{bc_r}{b^2 + c_r^2} & \kappa_l \frac{b^2}{b^2 + c_l^2} + \kappa_r \frac{b^2}{b^2 + c_r^2} & \kappa_l \frac{bc_l d}{b^2 + c_l^2} - \kappa_r \frac{bc_r d}{b^2 + c_r^2} \\ \kappa_l \frac{c_l^2 d}{b^2 + c_l^2} + \kappa_r \frac{c_r^2 d}{b^2 + c_r^2} & \kappa_l \frac{bc_l d}{b^2 + c_l^2} - \kappa_r \frac{bc_r d}{b^2 + c_r^2} & \kappa_l \frac{c_l^2 d^2}{b^2 + c_l^2} + \kappa_r \frac{c_r^2 d^2}{b^2 + c_r^2} \end{pmatrix}. \quad (7.24)$$

The three sets of rows and columns are denoted 1, 3 and 5 respectively corresponding to the indices for the generalised modes of motion of a floating structure. Note that no damping is assumed to occur through the mooring mechanism so that all the elements of the damping coefficient matrix  $\gamma_{\mu\nu}$  in equation (2.51) are identically zero. Nevertheless, the floating body problem now features a fully cross-coupled structural motion. It must be emphasised that these equations are only valid for small structural motions relative to the depth of the fluid. In particular, if the mooring point on the structure moves beyond the mooring line base positions, that is if  $\Delta x > c_r$  or  $\Delta x < c_l$ , then one of the line extension expressions (7.19) or (7.20) will be incorrect. It is also clear that if  $|X_5| > \pi/2$  then the structure has effectively capsized and the results are no longer physically relevant. Therefore, it must be ensured that the simulation results

are consistent with the assumptions behind the linearised equations.

So far, the mooring equations have been developed under the assumption that the mooring lines are attached at the same point on the structure on the axis of rotation. In the case of a moored toroidal structure, it is more natural to attach the mooring lines at different points. Here, it will be assumed that the mooring lines are attached to the bottom of the torus (the point of lowest draft) on the  $x$ -axis. Some schematics of the configuration envisaged are shown in figure 7.12. The symmetry of the mooring line positions relative to the  $y$ -axis is again chosen to give a net force of  $F$  in the  $x - z$  plane where  $F$  is the force along one mooring line. The equations describing the mooring forces must therefore be altered in order to describe this new configuration. Once again it will be assumed that the mooring lines have different spring constants and are attached to the sea-bed at different distances from the axis of symmetry,  $c_l$  for the mooring line to the left of the structure and  $c_r$  for the mooring line to the right. The radius of the torus axis is denoted  $R$  and so the linearised extension of the left and right mooring lines due to a general displacement  $(X_1, X_3, X_5)$  of the structure are

$$\begin{aligned}\Delta L_l &= \frac{(c_l - R)\Delta x_l + b\Delta z_l}{((c_l - R)^2 + b^2)^{1/2}} \\ \Delta L_r &= \frac{(c_r - R)\Delta x_r + b\Delta z_r}{((c_r - R)^2 + b^2)^{1/2}}\end{aligned}\quad (7.25)$$

where  $\Delta x_l = \Delta x_r = X_1$  is the horizontal displacement of the mooring line and  $\Delta z_l = X_3 - RX_5$  and  $\Delta z_r = X_3 + RX_5$  are the vertical displacements of the left and right mooring lines. Therefore, the linearised mooring forces in each mode are given by (7.23) for the mooring matrix

$$\kappa = \begin{pmatrix} \frac{\kappa_l(\Delta c_l - R)^2}{b^2 + \Delta c_l^2} + \frac{\kappa_r \Delta c_r^2}{b^2 + \Delta c_r^2} & \kappa_l \frac{b\Delta c_l}{b^2 + \Delta c_l^2} - \kappa_r \frac{b\Delta c_r}{b^2 + \Delta c_r^2} & -\kappa_l \frac{b\Delta c_l R}{b^2 + \Delta c_l^2} - \kappa_r \frac{b\Delta c_r R}{b^2 + \Delta c_r^2} \\ \kappa_l \frac{b\Delta c_l}{b^2 + \Delta c_l^2} - \kappa_r \frac{b\Delta c_r}{b^2 + \Delta c_r^2} & \kappa_l \frac{b^2}{b^2 + \Delta c_l^2} + \kappa_r \frac{b^2}{b^2 + \Delta c_r^2} & \kappa_l \frac{b^2 R}{b^2 + \Delta c_l^2} - \kappa_r \frac{b^2 R}{b^2 + \Delta c_r^2} \\ -\kappa_l \frac{b\Delta c_l R}{b^2 + \Delta c_l^2} - \kappa_r \frac{b\Delta c_r R}{b^2 + \Delta c_r^2} & \kappa_l \frac{b^2 R}{b^2 + \Delta c_l^2} - \kappa_r \frac{b^2 R}{b^2 + \Delta c_r^2} & \kappa_l \frac{b^2 R^2}{b^2 + \Delta c_l^2} + \kappa_r \frac{b^2 R^2}{b^2 + \Delta c_r^2} \end{pmatrix} \quad (7.26)$$

where  $\Delta c_l = c_l - R$  and  $\Delta c_r = c_r - R$  and  $b = h - R$ . The assumption of small displacements is inherent in the derivation.

### 7.3.2 Stability of the cross-coupled motion

To understand the dynamics of the cross-coupling mooring system described by the mooring matrices (7.24) and (7.26) it is useful to consider the equation of motion of the structure subject to mooring and hydrostatic forces only. Hydrodynamic forces are neglected here as they are very difficult to describe without using the full description given by the linearised water-wave equations. Therefore, the dynamic system under

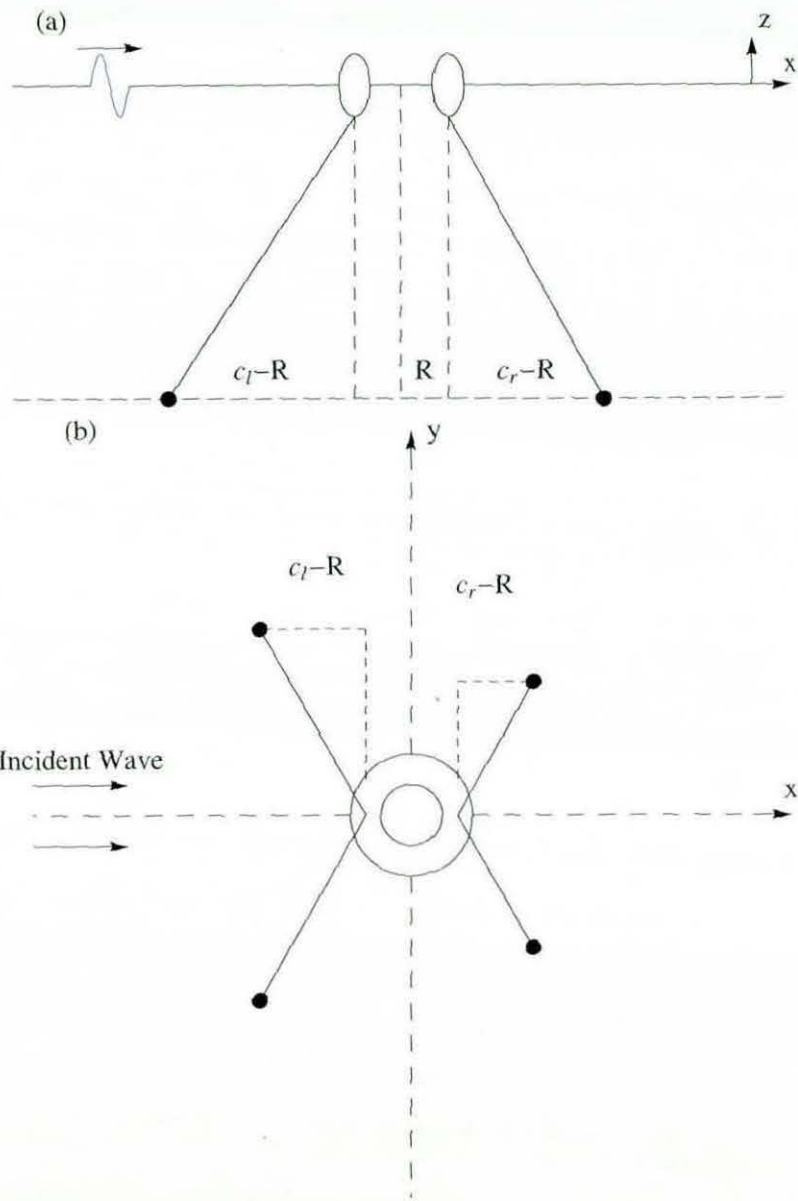


Figure 7.12: An elevation view (a) and plan view (b) of the mooring configuration for a floating torus. The bases of the mooring line in the plan of the mooring setup have the  $x - y$  coordinates  $(\pm c, \sqrt{3}c)$  while in the elevation perspective,  $b = h - d$  denotes the distance from the mooring point to the sea-bed.

consideration is

$$\mathbf{M}\ddot{\mathbf{X}} = -(\boldsymbol{\kappa} + \mathbf{H})\mathbf{X} \quad (7.27)$$

where  $\mathbf{X}^T = (X_1, X_3, X_5)$ ,  $\boldsymbol{\kappa}$  is the mooring matrix,  $\mathbf{M}$  is the mass matrix

$$\begin{pmatrix} M & 0 & 0 \\ 0 & M & 0 \\ 0 & 0 & I \end{pmatrix} \quad (7.28)$$

with  $M$  and  $I$  being the mass of the structure and the moment of inertia of the structure respectively. Finally,  $\mathbf{H}$  describes the hydrostatic restoring coefficients in heave and surge, i.e.

$$\mathbf{H} = \begin{pmatrix} 0 & 0 & 0 \\ 0 & \rho g W & 0 \\ 0 & 0 & \rho g(I_{11}^A + I_3^V) \end{pmatrix} \quad (7.29)$$

where  $W$  is the waterplane area and  $I_{11}^A$  is the moment of the waterplane area and  $I_3^V$  is the  $z$ -component of the centre of buoyancy. In chapter 2, the non-zero coefficients are denoted  $b_3$  and  $b_5$  for heave and pitch respectively. The initial-value problem is completed by the specification of the initial conditions  $(X_\mu(0), \dot{X}_\mu(0))$  for  $\mu = 1, 3, 5$  for the structure motion.

In a coupled oscillator problem such as this it is important to determine the stability of the system. In chapter 6 of Newman (1977a), the stability of a structure undergoing oscillatory motion involving no mooring forces is discussed. The signs of the coefficients of the buoyancy matrix (7.29) determine the stability of the structure. If the coefficient corresponding to a particular mode is positive then the structure is *statically stable* in this mode, that is the hydrostatic restoring force opposes the displacement and so ensures the structure will return to equilibrium. If the coefficient is zero then the structure is *neutrally stable* so that the structure will not experience a hydrostatic restoring force and so if given an initial displacement it will not return to equilibrium. Otherwise, the motion of the structure in that mode will be unstable as the hydrostatic restoring force will reinforce the displacements. For a floating body piercing the free-surface the waterplane area is always positive so the motion in heave is statically stable. The stability of the pitch mode depends on the geometry of the body through the centre of buoyancy  $I_3^V$  and the moment of the waterplane area  $I_{11}^A$ . In a problem without cross-coupling, an unstable pitch motion where the structure has a geometry such that  $b_5 < 0$  can be stabilised by choosing a mooring coefficient  $\kappa_{55} > b_5$  so that the net restoring coefficient  $c_5 = \rho g b_5 + \kappa_{55}$  is positive and hence opposes the pitch displacement. However, in a problem with cross-coupling where the mooring matrix has all non-zero elements the stability of each mode of motion will be inter-dependent and the total system will either be stable, unstable or neutral. The system is defined to be stable if given an initial structural disturbance the oscillatory amplitudes in each mode

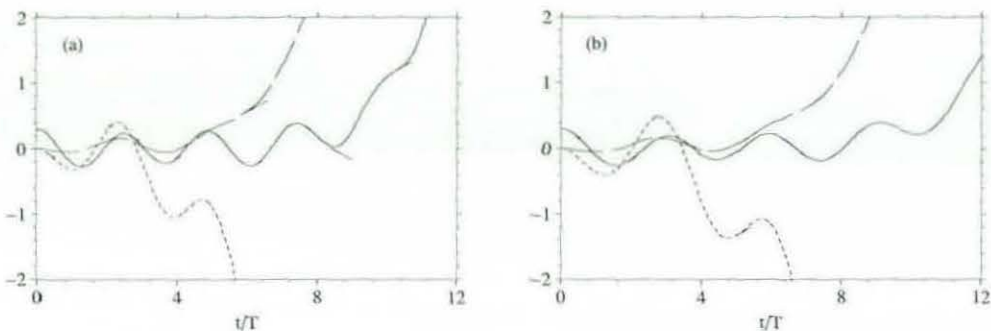


Figure 7.13: Variation of the cylinder displacements  $X_1/h$  (---),  $X_3/h$  (—) and  $X_5$  (---) after release from rest given a non-zero initial displacement  $X_3/h$  as modelled by (a) the coupled oscillator system (7.27) and (b) the linearised time-domain equations.

will all remain bounded, unstable if the oscillatory amplitudes all become unbounded and neutral if the structure does not move after being given an initial displacement. To determine the stability of the system the eigenvalues of the matrix  $\mathbf{M}^{-1}(\boldsymbol{\kappa} + \mathbf{H})$  must be computed. If one eigenvalue is negative then the system is unstable while if all the eigenvalues are positive then the system is stable. Other cases may also arise: if the matrix has all non-negative eigenvalues with one positive then the system will be stable and if all the eigenvalues are zero then the system can be classed as neutral.

Demonstrations of this dynamical theory can be obtained by considering the motion of a floating structure, moored in the manner illustrated in figure 7.11, after being released from an initial heave displacement. In the following, only cylindrical structures are considered and hence only the matrix (7.24) will be utilised in the computations. The first structure considered is a semi-submerged vertical cylinder with both a radius  $a$  and draft  $d$  of 12m floating in a sea of constant depth  $h = 40m$  (so  $b = h - d$  is 28m). The waterplane moment and centre of buoyancy were calculated using the BEM code (they can also be calculated analytically) and so it was found that the pitch buoyancy coefficient  $b_5$  is negative, i.e. the body is statically unstable in pitch. The bases of the mooring lines are positioned a distance  $c = 10m$  either side of the vertical axis of symmetry and the spring coefficient of the mooring line on the left (right) is approximately  $1.6 \times 10^7 \text{ kgs}^{-2}$  ( $6.4 \times 10^6 \text{ kgs}^{-2}$ ) corresponding to a non-dimensional value  $\bar{\kappa} = 0.25$  ( $\bar{\kappa} = 0.1$ ). The results of the coupled oscillator system (7.27) are to be compared with those of the time-domain BEM but first a list of all the non-dimensional system parameters is provided. As usual, all lengths, times and masses are expressed in terms of the depth  $h$ , the mass  $\rho h^3$  and the time  $\sqrt{h/g}$ , respectively, so the parameters

are:

$$\begin{aligned}
 \text{cylinder radius} & - a/h = 0.3, \\
 \text{cylinder height} & - 2d/h = 0.6, \\
 \text{cylinder mass} & - M/(\rho h^3) = 0.084823 \\
 \text{waterplane area} & - W = 0.282743, \\
 \text{moment of inertia} & - I = 0.004420, \\
 \text{hydrostatic pitch coefficient} & - b_5 = -0.006282, \\
 \text{mooring base distance} & - c_l = c_r = 0.25, \\
 \text{mooring line height} & - b = 0.7, \\
 \text{mooring spring coefficients} & - \kappa_l = 0.25, \kappa_r = 0.1
 \end{aligned} \tag{7.30}$$

where  $M = \rho \frac{\pi^2 d a^2}{2}$  and  $W = \pi a^2$ . The eigenvalues of the resultant system matrix  $\mathbf{M}^{-1}(\boldsymbol{\kappa} + \mathbf{H})$  were computed to be  $\lambda_1 = 2.5$ ,  $\lambda_3 = 2.5$ ,  $\lambda_5 = -0.7$  indicating that the system is unstable with the instability originating from the pitch mode. This is despite the fact that the net restoring force in pitch due to pitch motion is  $\kappa_{55} + b_5 > 0$ , that is if there were no cross-coupling, the pitch motion would be stable. Note that the eigenvalues are labelled according to the modes of motion. The results of the coupled oscillator system are shown in figure 7.13 (a) for the case where the cylinder is given an initial heave displacement  $X_3(0) = d/h$  and allowed to move in the absence of incident waves. It is clear that all the displacements become unbounded rapidly as expected by the eigenvalue stability analysis. The results of the linearised time-domain equations for a full mooring matrix (7.24) are shown in the adjacent figure 7.13 (b) and the agreement with the results of the coupled oscillator equations is clearly very good. Therefore, in the case of a structure undergoing oscillations due an initial displacement the system (7.27) is very useful in predicting the dynamic behaviour of the structure. However, the model is no longer physically realistic in the case where the displacement become very large relative to  $h$  because of the linearising assumptions necessary for the derivation of the equations describing the mooring.

The motion of a second vertical cylinder structure was also investigated to examine how the cross-coupling of the structural modes of motion due to mooring affect the dynamics of a structure that is statically stable in pitch. This cylinder of radius 8m and draft 4m is also semi-submerged in equilibrium and floats in a sea of constant depth  $h = 40m$ . The mooring line specifications remain the same apart from the height (36m) to which it must extend from the sea-bed. Therefore, the non-dimensional parameters

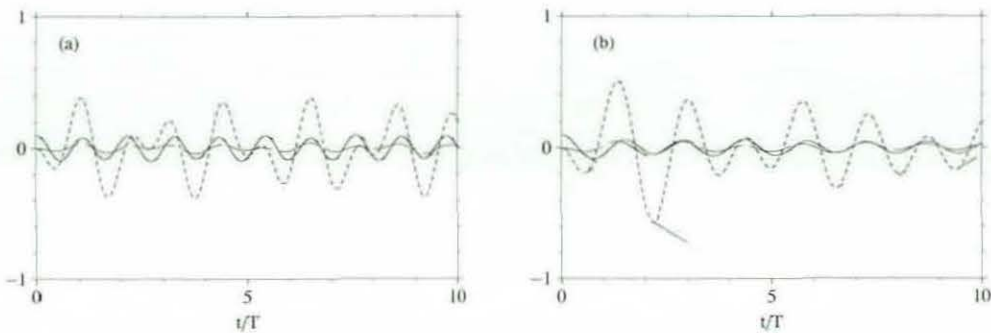


Figure 7.14: Variation of the cylinder displacements  $X_1/h$  (---),  $X_3/h$  (—) and  $X_5$  (---) after release from rest given a non-zero initial displacement  $X_3/h$  as modelled by (a) the coupled oscillator system (7.27) and (b) the linearised time-domain equations..

describing the problem are:

<i>cylinder radius</i>	—	$a/h = 0.2$ ,	
<i>cylinder height</i>	—	$2d/h = 0.2$ ,	
<i>cylinder mass</i>	—	$m/(\rho h^3) = 0.0125664$ ,	
<i>waterplane area</i>	—	$W = 0.125664$ ,	
<i>moment of inertia</i>	—	$I = 0.000163$ ,	(7.31)
<i>hydrostatic pitch coefficient</i>	—	$b_5 = 0.000644$ ,	
<i>mooring base distance</i>	—	$c_l/h = c_r/h = 0.25$ ,	
<i>mooring line height</i>	—	$b = 0.8$ ,	
<i>mooring spring coefficients</i>	—	$\kappa_l = 0.25, \kappa_r = 0.1$	

In this case, the eigenvalues of the system matrix  $M^{-1}(\kappa + H)$  are all positive and were computed to be  $\lambda_1 = 24$ ,  $\lambda_3 = 82$ ,  $\lambda_5 = 0.5$ . Therefore, when the structure is released from rest having been initially displaced the amplitude of the oscillations remain finite and do not become unbounded, i.e. the system is stable. This behaviour can be observed in the results for the coupled oscillator shown in figure 7.14(a) and similarly for the linearised time-domain results for the floating structure shown in figure 7.14(b). The behaviour of the solutions from both models are broadly similar once again, the most important aspect being that the solutions both consist of stable oscillations. In this case, the amplitudes of the surge motion lie well within the range of validity for the equations  $c_l < \Delta x < c_r$  because  $X_1/h \ll 1$  and  $X_5/h < 0.1$ . The pitch oscillations lie within the range  $-\pi/2 < X_5 < \pi/2$  so that at no point do the equations correspond to a physically unrealistic state. In the time-domain solution illustrated in figure 7.14(b), the displacements can be observed to decay as the simulation progresses due to wave radiation whereas in the coupled oscillator problem where no energy is dissipated the

amplitudes of the oscillations can remain the same as at the start of the simulation.

### 7.3.3 Floating body motion excited by an incident wave

In the final set of wave-structure interaction simulations an incident wave undergoes diffraction at the structure and excites motions in heave, pitch and surge modes which are all coupled by the mooring configuration described in § 7.3.1. Both the response of the moored floating body and the motion of the surrounding fluid due to the incident, radiated and diffracted waves are of interest in the simulations and so in addition to the displacement plots, snapshots of the free-surface in the vicinity of the structure are also presented. Only two simulations are considered, one involving a vertical cylindrical and the other a torus.

The cylindrical structure chosen for the simulations is the statically stable semi-submerged vertical cylinder of radius  $a = 8m$  and draft  $d = 4m$  whose response to an initial displacement was investigated in the last subsection. The cylinder is assumed to be floating in a fluid of constant depth  $h = 40m$  and the wave packet incident on this cylinder is specified to be the same as that investigated in § 7.1. Thus, it has a dominant plane wave-component of period  $8s$  and amplitude  $A = 1m$ . Furthermore, the initial conditions for the incident wave are based on the free-surface elevation (7.9) with  $r_0 = 0.5h$ ,  $r_1 = 1.25$  and  $r_2 = 12.0h$ . The mooring parameters are chosen to be the same as for the initial displacement simulation given in the list (7.31).

The structure is assumed to be floating in equilibrium initially and therefore its motion is excited by the wave incidence alone. The wave field surrounding the structure will have contributions from the incident, diffracted and radiated waves and so is expected to be quite complex. In the absence of damping by the mooring mechanism, the motion of the structure is damped only by the hydrodynamic interactions of the structure and surrounding fluid. In particular, the energy in the structural motion is lost through wave-radiation and so a good indication of how much damping occurs in a particular oscillatory mode is given by the amplitude of the corresponding radiated waves. In the frequency domain the damping coefficient of the structure in a given mode, defined through the relation (2.62), is related to the amplitude of the radiated waves in that mode and measures the rate of energy loss in some sense due to the structural oscillations in a given mode. Therefore, if the structure generates large waves then this corresponds to a large damping coefficient and hence a quicker decay in the motion and small waves indicate the motion will continue for longer. However, the radiated waves cannot be discerned properly until all wave-incidence has ceased because the diffracted wave-field will also contribute to the total wave-field during wave incidence and so the true extent of the energy radiation is difficult to ascertain.

In the free-surface plots, the floating cylinder is not illustrated for the sake of clarity

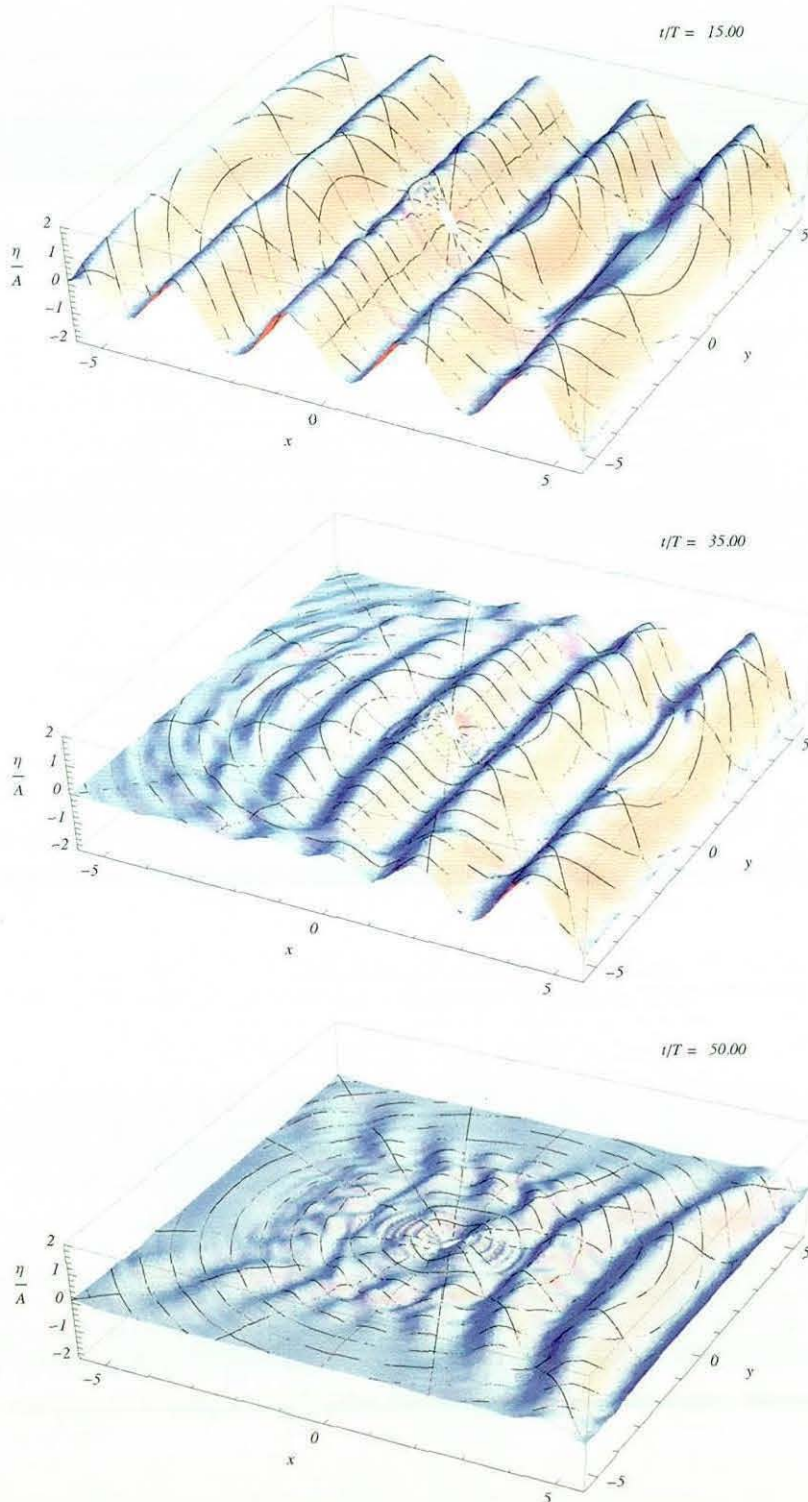


Figure 7.15: Excitation of diffracted and radiated waves due to wave-incidence on a moored floating cylinder in a three-dimensional BEM simulation. Snapshots of the free-surface elevation  $\eta(r, \theta, t)$  are plotted at non-dimensional times  $t/T = 15.0, 35.0, 50.0$ .

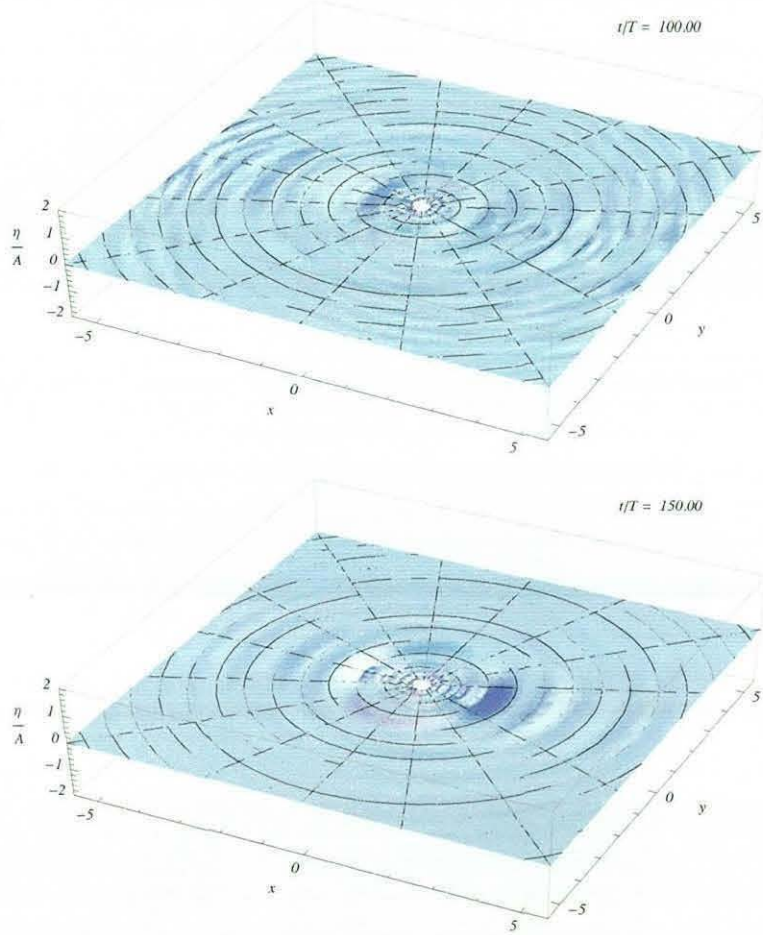


Figure 7.16: Excitation of diffracted and radiated waves due to wave-incidence on a moored floating cylinder in a three-dimensional BEM simulation. Snapshots of the free-surface elevation  $\eta(r, \theta, t)$  are plotted at non-dimensional times  $t/T = 100.0, 150.0$ .

and instead is represented by a hole in the domain. Furthermore, only a small section of the domain in the vicinity of the structure is illustrated in the figures because it is in this region that the most interesting behaviour occurs. Figure 7.15 shows the free-surface at different times during the initial period of the simulation  $t/T \leq 50$  when the plane wave component of the wave-packet is incident on the structure. It can be seen that the amplitude of the radiated and diffracted waves are significantly smaller than those of the wave-packet and the overall plane-wave form of the free-surface is maintained with the radiated and diffracted waves slightly perturbing this form. However, as the end of the wave-packet propagates past the structure for  $t/T \approx 50$  the incident and diffracted waves decay and the radiated waves become relatively more significant. At  $t/T = 35$  some small short wavelength 'ripples' are visible immediately to the left and right of the structure indicating wave-radiation due to the surge and pitch motions of the cylinder. Thereafter, the wave-field consists of the various radiated components in addition to the high-frequency dispersed components of the wave-packet and some outgoing diffracted waves. This phase of the simulation is illustrated in figure 7.16. After  $t/T = 100$  the free-surface waves due to the incident wave have essentially disappeared and the remaining disturbances are due to radiated waves with the possibility of some minor interference from artificial reflections of the plane waves reaching the domain boundary. Analysis of the free-surface plots between  $t/T = 100$  and  $t/T = 150$  shows the disturbance due to the radiated wave field to be very small but in a state of almost steady oscillation; the decay with time of the radiated waves is difficult to recognise. Thus, it can be expected that the structure will also settle into an almost periodic oscillation in the latter stages of the simulation.

The displacements of the structure in the heave, surge and pitch modes are shown in figure 7.17 over the whole simulation. The translational displacement amplitudes are plotted relative to the incident wave amplitude  $A$  and since  $A/h = 1/40$  it is clear the motions are small relative to the depth as assumed in the linearised mooring force derivation. Furthermore, the structure remains within the domain of validity required by the mooring equations namely,  $|\Delta x/h| < c$  where  $c = 0.25$  and  $|X_5| < \pi/2$ . However, the surge displacements are considerably larger than the heave displacements for most of the simulations. The strong coupling between the pitch and surge inherent in the mooring equations (the net horizontal displacement is  $\Delta x = X_1 + dX_5$  so the modes are clearly related) may account for this given that the motion of the structure in pitch is also significantly excited by the incident wave. It is also interesting to note that the motion of the structure in each mode is dominated by the mooring forces because a significant decay in the displacement amplitudes does not occur after the plane-wave incidence. Nevertheless, the effect of plane wave forcing of the structural motions can be discerned for  $t/T < 50$ . Thereafter, the motions in each mode tend to settle down into lightly damped oscillations dictated by the mooring forces. These oscillations are consistent with the free-surface plots in figure 7.16 where the magnitude of the radiated

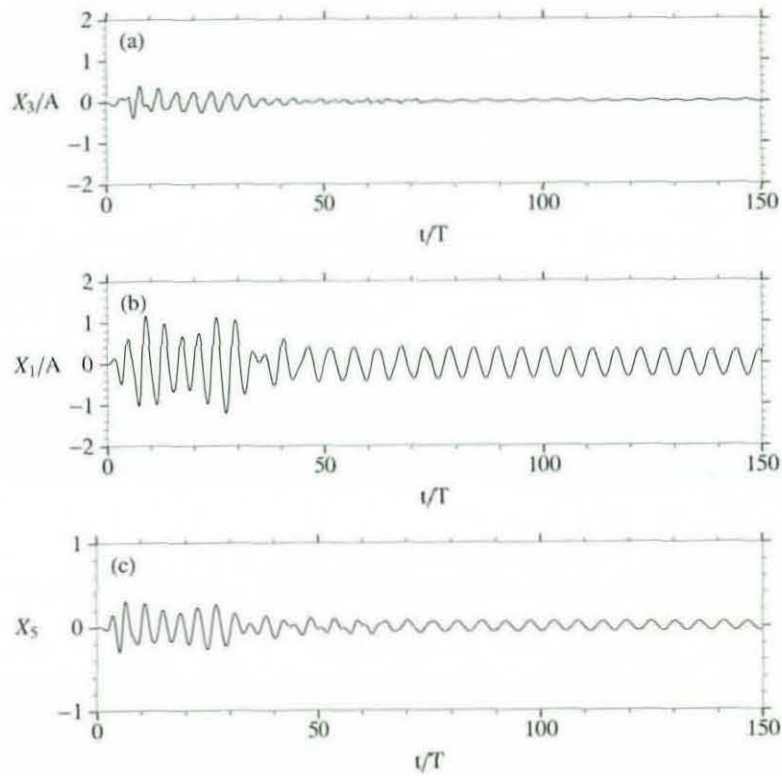


Figure 7.17: Response of the cylinder in (a) heave, (b) surge and (c) pitch after excitation by an incident wave packet with a dominant plane wave form.

waves, and hence the damping coefficient of each mode, is quite small. If waves of longer wavelength, i.e. waves transporting more energy, were generated then the decay in the motion would be more rapid as the loss of the kinetic energy of the structure through wave radiation would increase.

In the second cross-coupling simulation, the motion of a moored torus floating in a fluid of depth  $h = 40m$  is considered. The torus is specified to have an axial radius of  $R = 16m$  and a tube radius of  $a = 8m$  so that the structure is significantly larger in size than the vertical cylinder considered above. In particular, the radial extent of the structure ( $24m$ ) is much larger than that of the cylinder ( $8m$ ) and so the dynamics of the interaction are expected to be quite different. The non-dimensional parameters for the structural geometry and for the mooring configuration are

$$\begin{aligned}
 \text{torus axial radius} & - R/h = 0.4, \\
 \text{torus tube radius} & - a/h = 0.4, \\
 \text{torus mass} & - m/(\rho h^3) = 0.157914, \\
 \text{waterplane area} & - W = 1.00531, \\
 \text{moment of inertia} & - I = 0.016585, \\
 \text{hydrostatic pitch coefficient} & - b_5 = 0.087127, \\
 \text{mooring base distance} & - c_l/h = c_r/h = 0.75, \\
 \text{mooring line height} & - b = 0.8, \\
 \text{mooring spring coefficients} & - \kappa_l = 0.25, \kappa_r = 0.1
 \end{aligned} \tag{7.32}$$

where the mass and waterplane area of the semi-submerged torus are  $\rho\pi a^2(2\pi R)/2$  and  $\pi((R+a)^2 - (R-a)^2)$ , respectively. Although the geometry of the structure is very different to the vertical cylinder, the mooring configurations in both cases are quite similar. The corresponding system matrix  $\mathbf{M}^{-1}(\boldsymbol{\kappa} + \mathbf{H})$  for the oscillating body has three positive eigenvalues so that the system is stable. Finally, the incident wave-packet is chosen to have the same frequency and amplitude as in previous simulations but with the slightly different initial profile specifications of  $r_0/h = 0.75$ ,  $r_1/h = 1.375$  and  $r_2/h = 12.0$ .

The free-surface profiles for various times during the simulation are shown in figure 7.18. The diffracted and radiated wave disturbances are difficult to observe just as in the interaction involving the cylinder. However, the effects on the incident wave are larger than in the cylindrical case as is apparent from a comparison of the  $t/T = 15$  surface plots where in the torus interaction the crest approaching from the left is reduced in magnitude in the immediate vicinity of the structure due most likely to diffraction effects. In contrast, in the cylinder interaction the approaching crest is modulated by some short wavelength waves. The motion of the free-surface section interior to the torus is tracked during the simulation and has quite a large amplitude during the period

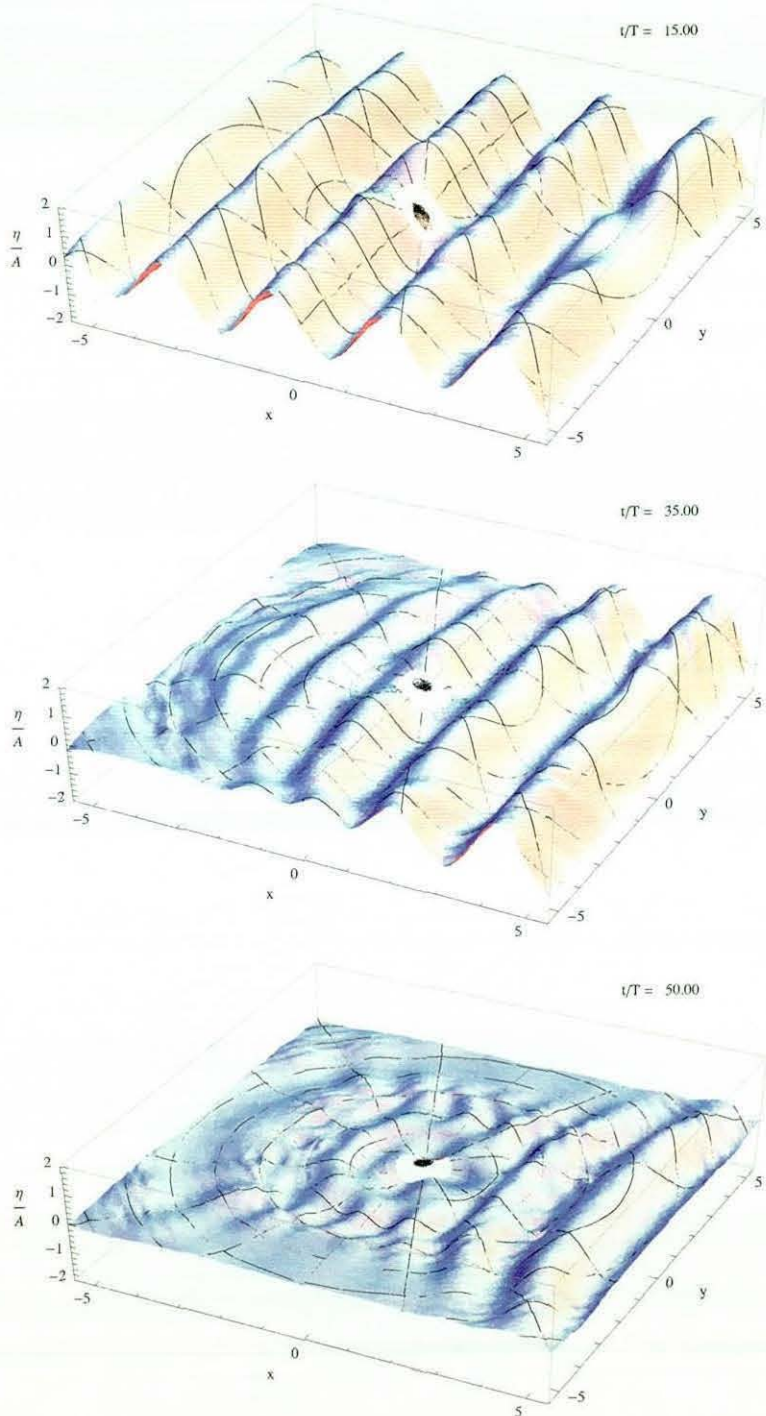


Figure 7.18: Excitation of diffracted and radiated waves due to wave-incidence on a moored floating torus in a three-dimensional BEM simulation. Snapshots of the free-surface elevation  $\eta(r, \theta, t)$  are plotted at non-dimensional times  $t/T = 15.0, 35.0, 50.0$ .

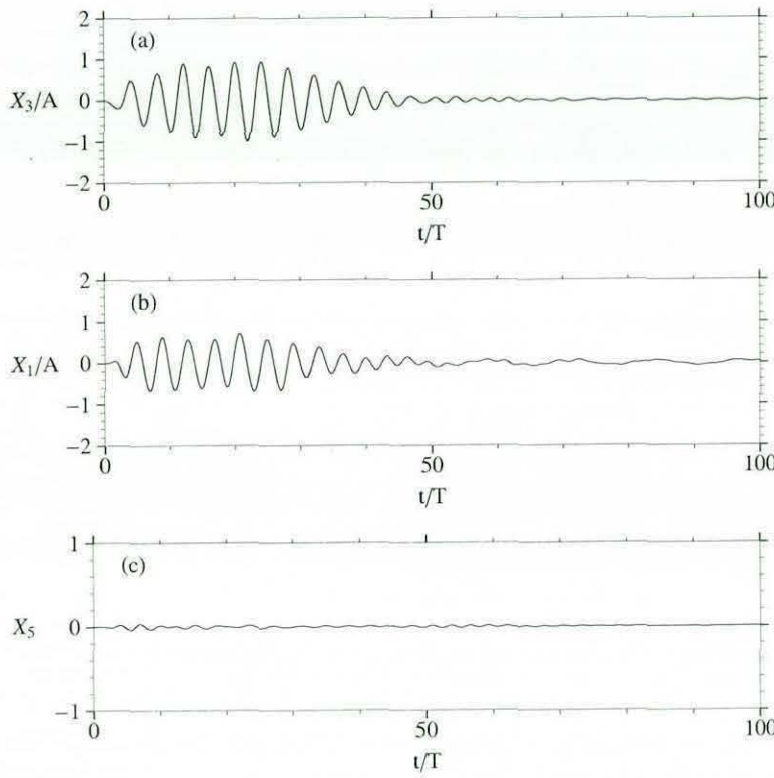


Figure 7.19: Response of the torus in (a) heave, (b) surge and (c) pitch to the excitation by an incident wave packet with a dominant plane wave form.

of wave incidence where the elevation is greater than twice the incident wave amplitude. At the time  $t/T = 35$  the radiated and diffracted wave fields are still not clearly visible; however again the absence of short wavelength waves is notable around the structure. By the simulation time  $t/T = 50$  the wave-packet has propagated almost completely to the right of the structure and the remaining radiated waves are relatively small. In this plot, the free surface section enclosed by the torus is visible and the elevation is essentially uniform over the extent of the internal section. Over the duration of the interaction the motion of the internal free-surface is a combination of motion in the vertical plane with some additional sloshing motion due to the surging of the structure and the incident wave motion. No high-frequency waves are visible in the interior section however and the free-surface moves like a planar disk with mainly vertical motion accompanied by some inclinations due to the surge component of the incident wave. In summary, it is the incident wave transmitted into the internal free-surface section that dominates the motion of the internal free-surface with the effects due to the motion of the structure superposed.

The displacement of the torus in heave, surge and pitch is shown in figure 7.19. In contrast to the cylinder motion, the amplitude of the heave motion of the torus is larger

than the surge motion while there is negligible pitch mode excitation. One reason for the presence of short-wavelength fluid oscillations in the coupled motion simulation for the cylinder was the dominance of the surge oscillations – the surge motion recreates the motion of a wave-maker which results in the generation of high-frequency oscillations (see Joo, Schultz & Messiter (1990)). In contrast to the vertical circular cylinder, the torus oscillates more uniformly with a lower frequency so that the generation of high frequency waves is substantially reduced. The low-frequency, long wavelength motion of the structure excited by the incident wave will have a corresponding free-surface oscillation and the wavelength is sufficiently long to preclude a non-uniform heave motion of the internal free-surface. The motion of the torus decays rapidly after the wave-packet propagates past the structure, this is also a consequence of the long-wavelength waves generated by the structure motion corresponding to a large damping coefficient. Furthermore, the coupling effects are significantly smaller in the motion of the torus because the diagonal elements of the mooring matrix are significantly larger than the off-diagonal elements. The pitch motion of the torus is also much smaller than in the case of the cylinder because the moment of inertia of the torus is an order of magnitude larger than for the cylinder so that a much larger amount of energy is required to excite a significant motion in pitch. Near the end of the simulation, the only slowly-decaying motion is in the surge mode and this results in the generation of small fluid motions along the  $x$ -axis which, although they are not visible in figure 7.18, can be observed for  $t/T > 80$ .

## 7.4 Conclusions

The motion of a floating structure excited by wave incidence has been simulated in two different cases. The cross-coupling effect of the mooring lines, modelled as a system of coupled linear springs, is also simulated. The coupled oscillator system described by the equations of motion for the structure due to the mooring and hydrostatic forces has also been investigated. In particular, the importance of the overall stability of the system has been shown to directly affect the wave-structure interaction simulations. For a stable structure-mooring setup the effects of cross-coupling can significantly affect the structure motion depending on the relative magnitude of the various mooring forces. In the case of the vertical cylinder, the structural motions were strongly coupled whereas for the torus the effects were much less visible. It has also been observed how the motion of the structure in pitch depends strongly on the moment of inertia of the structure.

An important aspect of the simulations yet to be discussed is the time-scales for the BEM computations and subsequent time-stepping. The simulations were run on a iMac with 2 Gb of RAM and a 2 Ghz processor. The typical computational time for the BEM computation for Fourier modes from  $n = 0$  to  $n = 25$  involving a domain

discretised by approximately 200 nodes is about 4 – 5 hours. A modest amount of storage, approximately 50 Mb , is also necessary to store this data for the time-stepping which in turn generates a maximum of 1Gb of data. The time taken for the time-stepping procedure for a simulation of duration 150 time units involving a structure free to respond to the incident wave is about two hours in the case where the heave and surge/pitch modes are independent. When the modes of motion for the structure are inter-dependent then the simulations take much longer, possibly as much as ten hours. This increase in computational time results from the increase in the amount of data which must be accessed during the simulation of the body motion and the increased complexity of the code itself.

# Chapter 8

## Conclusions

### 8.1 Summary

The primary aim of this project was to develop a linearised time-domain BEM capable of simulating general wave-structure interactions involving three-dimensional structures possessing a vertical axis of symmetry. The numerical method for obtaining the solution of the time-domain water wave equations requires the combination of a cubic spline BEM to solve the corresponding boundary integral equation and a fourth-order Runge-Kutta method to advance the solution in time. By assuming the structure possesses a vertical axis of symmetry located at the origin of the coordinate system it is possible to expand the quantities in the boundary integral equation, including the velocity potential, as Fourier cosine series in the cylindrical polar coordinate  $\theta$ . Thus it is possible to reduce the boundary integral equation to a series of integral equations in the  $r-z$  plane with each equation corresponding to a Fourier series mode. Each of these integral equations, up to truncation number  $N$ , can then be solved using a modified version of the two-dimensional BEM. The solution of each integral equation is then advanced from the specified initial conditions using the Runge-Kutta time-stepping algorithm.

Before using the time-domain BEM to solve water-wave problems it was necessary to validate it through a set of rigorous computational tests. These tests were conducted on the basic components of the code, that is the BEM discretisation results, the time-stepping algorithm for forced motion problems and the implementation of the equation for problems where the structure is free to respond to incident waves. As described in chapter 4, the simulations of time harmonic radiation problems in heave, surge and pitch were verified for various structures using the corresponding WAMIT results for comparison. Thereafter, the time-stepping algorithm for the higher order Fourier modes was confirmed by comparing the numerical time-domain solution of the classical

Cauchy-Poisson initial value problem to a semi-analytical solution. Once the code was modified to include the equation of motion of the structure in heave, surge and pitch a verification of the simulation of the motion of a floating structure was obtained using the theory of complex resonances. In this verification method the location of a complex motion resonance, excited in the time-domain by release of the structure from an initial displacement, was obtained from analysis of the time-domain results and compared to an estimate obtained from frequency domain computations. In all the time-domain simulation validations, the motions were constrained to a single mode – no coupling of modes was allowed as reliable results for such problems are not readily available. Therefore, the most general form of the code capable of simulating the cross-coupling of modes in floating body interactions was not tested. However, the extensive validation of the constituent components of the general code was considered sufficient evidence that the general implementation was reliable and correct.

After this comprehensive set of tests, the time-domain code was utilised as tool for assessing the success of the mechanical oscillator model in describing resonant scattering interactions. It was also used to confirm the excitation method for passive trapped modes and, as a consequence, the existence of passive trapped modes in the three-dimensional water-wave problem. The results of these investigations are summarised next. However, in addition to these particular applications the time-domain BEM code was also used to simulate various water-wave interaction problems, the results of which are presented in chapter 7. The water-wave problems considered include the propagation of a wave-packet with a dominant plane wave form, the latching control of a wave-buoy and the cross-coupling of structural modes of motion due to a general mooring configuration. The plane wave propagation simulation is a demanding computational problem for a method based on rotational symmetries; nevertheless, the results were observed to be reasonably good using a truncation number of  $N = 25$  for a wave of a period of approximately 8s. The latching control simulations yielded qualitatively similar results to those observed in previous literature and this was considered to be a useful demonstration of a possible future application of the code. Finally, the motion of a floating structure free to respond to the hydrodynamic forces on it subject to mooring forces which cause coupling of the modes of motion was simulated in order to illustrate the full capability of the code. An analysis of the effect of the cross-coupling mooring forces on the motion of the structure in the absence of hydrodynamic terms was also conducted and led to some interesting results regarding the motion stability.

As part of the time-domain simulation investigations a mechanical oscillator model was successfully developed to predict the time-dependence of the motion of the free-surface enclosed by a structure during a scattering interaction. The provisions for the model are as follows:

- the model can only be applied to scattering interactions where one resonance is

significantly excited only and where this resonance has a frequency similar to the plane wave frequency in the incident wave packet;

- the model requires as inputs, the location of the complex resonance excited through knowledge of the added mass and damping coefficients behaviour near the frequency of the excited resonance and *a priori* knowledge of the incident wave packet.

The applicability of the model is limited by the simplicity of the mechanical oscillator equation which can only account for the superposition of one resonant mode and the forcing motion. Furthermore, the magnitude of the fluid response cannot be predicted. Nevertheless, in the cases where it is applicable the mechanical oscillator model describes quite accurately the beats which occur in the free-surface oscillations due to the interference of the resonant mode and the incident wave mode during excitation and also the subsequent decay of this resonance. Therefore, the mechanical oscillator model is a simpler alternative to the full time-domain BEM for simulating the transient motion of the free-surface in a resonant scattering problem subject to the above provisos. For more complicated scattering interactions it is necessary to use the linearised time-domain equations to model the motion.

The discovery of passive trapped modes has yielded an important addition to the theory of trapped modes. A detailed investigation of the properties of passive trapped modes and the corresponding passive trapping structures was presented in chapter 6. The discussion of the conditions for the existence of passive trapped modes is particularly important because therein it was shown that these modes satisfy the existence conditions for both motion and sloshing trapped modes, that is passive trapped modes can be regarded as both sloshing and motion trapped modes. However, the defining characteristic of passive trapped modes – that they do not exert a net force on the corresponding trapping structure – means that these modes differ significantly from the sloshing and motion trapped modes discovered previously. This special property means that the frequency-domain equations for a floating body, considered from a uniqueness perspective, can be satisfied for a zero structural velocity in contrast to the original motion trapped modes which involve a non-zero motion of the structure and a non-zero hydrodynamic force. Examples of passive trapping structures in two and three dimensions were also provided in addition to an outline of the construction method. Thereafter, an excitation method was derived from a frequency-domain analysis and the existence of the passive trapped modes was demonstrated using time-domain simulations of the excitation in two and three dimensions. In these simulations significant free-surface oscillations at the trapped mode frequency were observed, accompanied by a negligible motions of the structure at same frequency, thus providing conclusive evidence of the existence of passive trapped modes.

## 8.2 Future work

The development and implementation of the time-domain BEM code for axisymmetric structures formed the largest part of this research project. Given the success of this implementation it is important to now utilise the code to simulate physical wave-structure interactions of relevance and interest. Obviously, the limitations of the linearised theory for inviscid fluids would compromise the relevance of simulation predictions to the physical problem. However, the linear theory yields results which generally give a good agreement with experimental work in the case where the ratio of the amplitude to the wavelength is quite small and is considered suitable for preliminary investigations of wave-structure interactions. One possible application would be to model the performance of various wave-energy converters which are often envisaged as cylindrical or spherical wave-buoys (see Falcão (2008) for example). Other wave-energy devices enclose a portion of the free-surface, such as floating oscillator water columns which are essentially hollow cylindrical structures. In both cases, the time-domain code developed here could be used to investigate the effect of transient phenomena on the absorption capabilities of the devices concerned. In particular, estimations of the time-taken for the motion to settle into steady-state oscillations and the effect of resonant fluid motions within the hollow structures are of practical importance in wave-energy investigations. If resonant fluid motions are significantly greater than the incident wave amplitude then the operation of the wave-energy device could be significantly compromised. Furthermore, the longer it takes for a wave-energy system to settle into a steady oscillatory state the less important the frequency-domain results are for predicting its absorption capabilities because it is expected that in real seas regular wave incidence will not occur for long periods of time.

A natural future developmental direction for the code would be to extend its scope in the manner of the Stokes wave expansion scheme to include the possibility of modelling second-order nonlinear effects. Such an extension would require an analytical review of second-order terms in all the time-dependent boundary conditions and in the equation of motion followed by a significant modification of the current code. Nevertheless, the basic structure of the underlying BEM algorithm would remain the same for the second order solution although the time-stepping of the second order boundary conditions would require the evaluation of first order quantities. Isaacson & Ng (1993), among others, has already described such a computational scheme for a time-domain BEM simulating radiation problems. If such a scheme were implemented then it would be possible to simulate weakly nonlinear wave-structure interactions thus further increasing the relevance of the simulation code to physical interactions. Furthermore, it would be interesting to determine the effects of second order nonlinear terms in resonant wave motions which in this thesis have only been modelled using linear theory.

## Appendix A

# Evaluations of the general-order ring-source potentials and its derivatives

In Chapter 3, the ring source Green's function was expressed in terms of the second-kind Legendre function of integral-minus-half-order as

$$G_n = -\frac{2^{1/2}}{4\pi(\rho\rho')^{1/2}} (Q_{n-1/2}(Z) + Q_{n-1/2}(Z')) \quad n = 0, 1, 2, \dots, \quad (\text{A.1})$$

where  $Z = 1 + ((\rho - \rho')^2 + (z - z')^2)/2\rho\rho'$  and  $Z' = 1 + ((\rho - \rho')^2 + (z + z' + 2h)^2)/2\rho\rho'$ . The different methods of evaluation of  $Q_{n-1/2}$  are of primary concern in this section because the integral involving the image source  $\frac{1}{r'}$  can be evaluated in an identical manner. For the first two modes corresponding to  $n = 0, 1$ , the quantity in equation (3.45) can be expressed and evaluated in terms of complete elliptical integrals of the first and second kind. Although a forward recurrence relation for  $Q_{n-\frac{1}{2}}$  does exist, it is computationally unstable for large  $n$ . Thus for  $n \geq 2$ , the hypergeometric function representation of the Legendre function,

$$Q_{n-\frac{1}{2}}(Z) = \frac{\pi^{\frac{1}{2}}}{(2Z)^{n+\frac{1}{2}}} \frac{\Gamma(n + \frac{1}{2})}{\Gamma(n + 1)} F(\tfrac{1}{2}n + \tfrac{3}{4}, \tfrac{1}{2}n + \tfrac{1}{4}, n + 1, \tfrac{1}{Z^2}) \quad (\text{A.2})$$

is utilised. In this equation  $\Gamma$  and  $F$  are the gamma and hypergeometric functions respectively and it is required that  $Z > 1$ . The hypergeometric function is usually expressed in series form for ease of computation (although it also has an integral representation); however there also exists an asymptotic series form for  $Z \rightarrow 1^+$  in addition

to the following general series form

$$F(a, b; c; \frac{1}{Z^2}) = \frac{\Gamma(c)}{\Gamma(a)\Gamma(b)} \sum_{m=0}^{\infty} \frac{\Gamma(m+a)\Gamma(m+b)}{\Gamma(m+c)\Gamma(m+1)} \frac{1}{Z^{2m}}. \quad (\text{A.3})$$

In the specific case of the evaluation of (A.2), the hypergeometric function will have the series form

$$\begin{aligned} F\left(\frac{1}{2}n + \frac{3}{4}, \frac{1}{2}n + \frac{1}{4}, n + 1, \frac{1}{Z^2}\right) &= \frac{\Gamma(n+1)}{\Gamma(\frac{1}{2}n + \frac{3}{4})\Gamma((\frac{1}{2}n + \frac{1}{4}))} \times \\ &\quad \sum_{m=0}^{\infty} \frac{\Gamma(m + \frac{1}{2}n + \frac{3}{4})\Gamma(m + \frac{1}{2}n + \frac{1}{4})}{\Gamma(m+n+1)\Gamma(m+1)} \frac{1}{Z^{2m}}. \end{aligned} \quad (\text{A.4})$$

This representation converges rapidly only *when the field point is not close to the ring source* and thus as the field point approaches the ring source a complementary asymptotic form (which excludes the singularity explicitly) must be used. Noting that  $Z = \frac{a_0}{b_0} = \frac{\rho^2 + \rho'^2 + (z - z')^2}{2\rho\rho'}$ , it is clear that as  $Z \rightarrow 1^+$  then  $a_0 - b_0 \rightarrow 0$ , i.e.  $(\rho - \rho')^2 + (z - z')^2 \rightarrow 0$ .<sup>1</sup> Hence, the limit  $Z \rightarrow 1^+$  implies that the field point approaches the ring source. When  $Z - 1 \ll 1$ , a more suitable expression for the hypergeometric series (A.4) is

$$\begin{aligned} F &= \frac{\Gamma(n+1)}{\Gamma(\frac{1}{2}n + \frac{3}{4})\Gamma(\frac{1}{2}n + \frac{1}{4})} \sum_{m=0}^{\infty} \frac{(\frac{1}{2}n + \frac{3}{4})_m (\frac{1}{2}n + \frac{1}{4})_m}{\Gamma(m+1)^2} [2\Psi(m+1) - \\ &\quad \Psi(m + \frac{1}{2}n + \frac{3}{4}) - \Psi(m + \frac{1}{2}n + \frac{1}{4}) - \ln\left(1 - \frac{1}{Z^2}\right)] \left(1 - \frac{1}{Z^2}\right)^n, \end{aligned} \quad (\text{A.5})$$

where  $\Psi = \Gamma'/\Gamma$  is Euler's psi function and  $(x_m) \equiv \Gamma(x+m)/\Gamma(x)$  and the logarithmic singularity has been separated from the other terms explicitly. The reason for this complementary expression is that it is much more efficient to compute the hypergeometric function with (A.5) than with (A.4) when  $Z \rightarrow 1^+$ . The efficiency of computation of the hypergeometric series is an important factor to consider when discussing the evaluation of the ring-source potentials.

## A.1 Asymptotic form of the Legendre function $Q_{n-\frac{1}{2}}(Z)$

"The singularity of the  $n^{th}$ -mode ring source  $R_n$  near the source ring is given by the asymptotic behaviour of  $Q_{n-\frac{1}{2}}(Z)$  as  $Z \rightarrow 1$ ". This asymptotic form can be derived from the  $m = 0$  term in (A.5), since the terms for  $m \geq 1$  are not singular they can be

---

<sup>1</sup>  $Z$  must approach 1 from above because the hypergeometric series formula is only valid for  $Z > 1$

neglected from the asymptotic considerations, using the following identity

$$\Psi(2z) = \frac{1}{2}\Psi(z) + \frac{1}{2}\Psi(z + \frac{1}{2}) + \ln 2. \quad (\text{A.6})$$

In the case where  $z = \frac{1}{2}n + \frac{1}{4}$ , it is straightforward to show that

$$\Psi(\frac{1}{2}n + \frac{1}{4}) + \Psi(\frac{1}{2}n + \frac{3}{4}) = 2\left(\Psi(n + \frac{1}{2}) - \ln 2\right) \quad (\text{A.7})$$

holds. Two further relations are required to simplify the asymptotic form of  $Q_{n-\frac{1}{2}}(Z)$  and these are

$$(x)_0 = \frac{\Gamma(x+0)}{\Gamma(x)} = 1 \quad (\text{A.8})$$

and

$$\begin{aligned} \Gamma(2z) &= (2\pi)^{-\frac{1}{2}} 2^{2z-\frac{1}{2}} \Gamma(z) \Gamma(z + \frac{1}{2}) \\ \Gamma(n + \frac{1}{2}) &= (2\pi)^{-\frac{1}{2}} 2^n \Gamma(\frac{1}{2}n + \frac{1}{4}) \Gamma(\frac{1}{2}n + \frac{3}{4}) \quad \text{for } z = \frac{1}{2}n + \frac{1}{4}. \end{aligned} \quad (\text{A.9})$$

Thus, the singular term in equation (A.5) corresponding to  $m = 0$  given by

$$F \sim \frac{\Gamma(n+1)}{\Gamma(\frac{1}{2}n + \frac{1}{4}) \Gamma(\frac{1}{2}n + \frac{3}{4})} \left[ 2\Psi(1) - \Psi(\frac{1}{2}n + \frac{1}{4}) - \Psi(\frac{1}{2}n + \frac{3}{4}) - \ln(1 - \frac{1}{Z^2}) \right] \quad (\text{A.10})$$

can be re-expressed as

$$F \sim \frac{2\Gamma(n+1)}{(2\pi)^{\frac{1}{2}} 2^{-n} \Gamma(n + \frac{1}{2})} \left[ \Psi(1) - \Psi(n + \frac{1}{2}) + \ln 2 - \frac{1}{2} \ln \left( 1 - \frac{1}{Z^2} \right) \right]. \quad (\text{A.11})$$

Using equation (A.2), simple cancellations of terms show that

$$Q_{n-\frac{1}{2}} \sim \left[ \Psi(1) - \Psi(n + \frac{1}{2}) + \ln 2 - \frac{1}{2} \ln \left( 1 - \frac{1}{Z^2} \right) \right] \quad (\text{A.12})$$

as  $Z \rightarrow 1$ .

## A.2 Asymptotic behaviour of $R_n$

Although the relationship between  $R_n$  and  $Q_{n-\frac{1}{2}}$ , given by equation (3.45), is quite simple, the derivation of the asymptotic form for  $R_n$  as  $Z \rightarrow 1^+$  requires the application of some important approximations and special function relations. Firstly, it is important to note that as  $Z \rightarrow 1^+$  then  $\rho \rightarrow \rho'$  and thus  $\rho + \rho' \simeq 2\rho'$  and  $\rho^2 + \rho'^2 \simeq 2\rho'^2$ . In the asymptotic approximations to follow, it isn't necessary to alter the quantity  $\rho\rho'$ . Nonetheless, the other approximations are necessary to acquire the asymptotic form of

the term  $(1 - \frac{1}{Z^2})$  in terms of  $a_0$  and  $b_0$ :

$$\begin{aligned} 1 - \frac{1}{Z^2} &= \frac{a_0^2 - b_0^2}{a_0^2} \\ &= \frac{(\rho^2 + \rho'^2 + (z - z')^2)^2 - (2\rho\rho')^2}{(2\rho\rho')^2} \\ &= \frac{(\rho^2 - \rho'^2)^2 + (z - z')^4 + 2(\rho^2 + \rho'^2)(z - z')^2}{(2\rho\rho')^2} \\ &= \frac{(\rho + \rho')^2(\rho - \rho')^2 + (z - z')^4 + 2(\rho^2 + \rho'^2)(z - z')^2}{(2\rho\rho')^2} \end{aligned} \quad (\text{A.13})$$

but  $\rho + \rho' \rightarrow 2\rho'$  and  $\rho^2 + \rho'^2 \rightarrow 2\rho'^2$  as  $Z \rightarrow 1^+$  so

$$\begin{aligned} 1 - \frac{1}{Z^2} &= \frac{4\rho^2(\rho - \rho')^2 + (z - z')^4 + 4\rho^2(z - z')^2}{4\rho'^2\rho^2} \\ &= \frac{4\rho'^2[(\rho - \rho')^2 + (z - z')^2] + (z - z')^4}{4\rho'^2\rho^2} \\ &= \frac{(\rho - \rho')^2 + (z - z')^2}{\rho^2} + O((z - z')^4) \quad \text{for } Z \rightarrow 1, \end{aligned} \quad (\text{A.14})$$

where  $\rho - \rho' \rightarrow 0$  and  $z - z' \rightarrow 0$  as  $Z \rightarrow 1^+$ . Furthermore, the  $\Psi$  terms in equation (A.12) can be simplified with the following relations<sup>2</sup>

$$\Psi(1) = -\gamma \quad (\text{A.15})$$

and

$$\Psi(n + \frac{1}{2}) = -\gamma - 2 \ln 2 + 2 \sum_{k=1}^n \frac{1}{2k-1}. \quad (\text{A.16})$$

Therefore, it is trivial to show that

$$\begin{aligned} Q_{n-\frac{1}{2}} &\sim -\frac{1}{2} \ln \left( \frac{(\rho - \rho')^2 + (z - z')^2}{\rho^2} \right) + 3 \ln 2 + 2 \sum_{k=1}^n \frac{1}{2k-1} \\ &\sim -\frac{1}{2} \ln[(\rho - \rho')^2 + (z - z')^2] + \ln \rho + 3 \ln 2 - c_n, \end{aligned} \quad (\text{A.17})$$

where  $c_n = 2 \sum_{k=1}^n \frac{1}{2k-1}$  for  $n \geq 1$  and  $c_0 = 0$ . Hence, the asymptotic form of the general order ring-source is given by

$$R_n \sim \frac{2}{\rho'} \left\{ -\frac{1}{2} \ln[(\rho - \rho')^2 + (z - z')^2] + \ln \rho + 3 \ln 2 - c_n \right\}, \quad (\text{A.18})$$

where  $(\rho\rho')^{\frac{1}{2}} \rightarrow \rho'$  in this case. As noted by Kim & Yue (1989), "It is of interest to note that the logarithmic singularity of  $R_n$  is the same for all  $n$ . For computations, the two complementary expressions (A.4) and (A.5) for the hypergeometric functions are

---

<sup>2</sup>See [www.mathworld.wolfram.com](http://www.mathworld.wolfram.com) or Abramowitz & Stegun (1964) Chapter 6

first converted to economised Chebyshev polynomials for a specific equal-ripple error in the whole domain  $Z > 1 \dots$ . In the case where the field point is far away from the source point the expression for the Legendre function involving the hypergeometric functions (A.2) converges rapidly when implemented numerically. However, as the field point approaches the source point, it is necessary to exclude the singularity explicitly so as to allow the efficient evaluation of the Legendre function. Hence, there are two complementary expressions for the  $n^{th}$ -mode ring-source.

### A.3 Asymptotic form of $\frac{\partial}{\partial n} R_n$

The “ $n^{th}$ -mode Rankine kernel”  $\frac{\partial R_n}{\partial n}$ , of the boundary integral equation can be obtained by directly differentiating the  $n^{th}$  mode ring source (3.45) and by the application of some derivative/recursion relations involving Legendre functions and their derivatives.<sup>3</sup> Further algebraic manipulations are necessary to modify the expression into the desired form given in equation (2.25) in the paper by Kim & Yue (1989). The derivation of this equation begins as follows:

$$\frac{\partial R_n}{\partial n} = \left( n_\rho \frac{\partial}{\partial \rho} + n_z \frac{\partial}{\partial z} \right) R_n. \quad (\text{A.19})$$

Therefore, two distinct derivatives must be obtained; to begin with the simpler derivative  $\frac{\partial}{\partial z}$  is determined:

$$\begin{aligned} \frac{\partial R_n}{\partial z} &= \frac{2}{(\rho \rho')^{\frac{1}{2}}} \frac{\partial Q_{n-\frac{1}{2}}(a_0/b_0)}{\partial \rho} \\ &= \frac{2}{(\rho \rho')^{\frac{1}{2}}} \frac{\partial a_0/b_0}{\partial z} Q'_{n-\frac{1}{2}} \\ &= \frac{2}{(\rho \rho')^{\frac{1}{2}}} \frac{2(z - z')}{b_0} Q'_{n-\frac{1}{2}}. \end{aligned} \quad (\text{A.20})$$

The derivative of the Legendre function  $Q_{n-\frac{1}{2}}$  can be expressed in terms of Legendre functions of different degrees by utilising relations (8.5.1, 8.6.7) given by Abramowitz & Stegun (1964) which together yield the following result:

$$\frac{dQ_{n-\frac{1}{2}}}{dx} = \frac{Q^1_{n-\frac{1}{2}}}{(x^2 - 1)^{\frac{1}{2}}} = (x^2 - 1)^{-1} \left( n - \frac{1}{2} \right) x Q_{n-\frac{1}{2}} - \left( n - \frac{1}{2} \right) Q_{n-\frac{3}{2}}. \quad (\text{A.21})$$

Hence, for this particular problem the derivative of the Legendre function satisfies

$$\frac{dQ_{n-\frac{1}{2}}}{dZ} = \frac{b_0}{2(a_0^2 - b_0^2)} (2n - 1) [a_0 Q_{n-\frac{1}{2}} - b_0 Q_{n-\frac{3}{2}}]. \quad (\text{A.22})$$

---

<sup>3</sup>In Abramowitz & Stegun (1964), the Legendre function  $Q_{n-\frac{1}{2}}$  is represented as  $Q^0_{n-\frac{1}{2}}$  where  $n - \frac{1}{2}$  denotes the *degree* of the function and 0 the *order*.

By substituting this result into the expression (A.20) the final desired form of  $\frac{\partial R_n}{\partial z}$  is

$$\frac{\partial R_n}{\partial z} = \frac{2}{(\rho\rho')^{\frac{1}{2}}} \frac{2n-1}{a_0^2 - b_0^2} \left\{ a_0 Q_{n-\frac{1}{2}} - b_0 Q_{n-\frac{3}{2}} \right\}. \quad (\text{A.23})$$

The calculation of  $\frac{\partial R_n}{\partial \rho}$  is more difficult because of the presence of the  $\rho^{-\frac{1}{2}}$  factor multiplying the Legendre function and also because  $b_0$  features a  $\rho$  term (but not a  $z$ -term). Nevertheless, the initial steps of the derivation are quite straightforward:

$$\begin{aligned} \frac{\partial R_n}{\partial \rho} &= \frac{\partial}{\partial \rho} \left\{ \frac{2}{(\rho\rho')^{\frac{1}{2}}} \right\} Q_{n-\frac{1}{2}} + \frac{2}{(\rho\rho')^{\frac{1}{2}}} \frac{\partial Z}{\partial \rho} Q'_{n-\frac{1}{2}} \\ &= -\frac{1}{\rho(\rho\rho')^{\frac{1}{2}}} Q_{n-\frac{1}{2}} + \frac{2}{(\rho\rho')^{\frac{1}{2}}} \frac{a_{0,\rho} b_0 - b_{0,\rho} a_0}{b_0^2} Q'_{n-\frac{1}{2}}. \end{aligned} \quad (\text{A.24})$$

However, to obtain the form given by Kim & Yue (1989) requires significantly more effort, particularly with regards the modification of the second term in the equation above. The most important part of this manipulation is given next:

$$\begin{aligned} \frac{\partial Z}{\partial \rho} &= \frac{2\rho'[(\rho^2 - \rho'^2) - (z - z')^2]}{b_0^2} \\ &= \frac{2\rho'[-((\rho - \rho')^2) + ((z - z')^2) + 2\rho(\rho - \rho')]}{b_0^2} \\ &= \frac{2\rho'(-(a_0 - b_0) + 2\rho(\rho - \rho'))}{b_0^2} \end{aligned} \quad (\text{A.25})$$

and by multiplying this term by  $Q'_{n-\frac{1}{2}} = \frac{b_0}{2(a_0^2 - b_0^2)}(2n-1)[a_0 Q_{n-\frac{1}{2}} - b_0 Q_{n-\frac{3}{2}}]$  and  $\frac{2}{(\rho\rho')^{\frac{1}{2}}}$  the second term in the last expression in equation (A.24) becomes

$$\left[ -\frac{1}{\rho(\rho\rho')^{\frac{1}{2}}} \left\{ \frac{2n-1}{a_0 + b_0} \right\} + \frac{2}{(\rho\rho')^{\frac{1}{2}}} \left\{ (\rho - \rho') \frac{2n-1}{a_0^2 - b_0^2} \right\} \right] (a_0 Q_{n-\frac{1}{2}} - b_0 Q_{n-\frac{3}{2}}). \quad (\text{A.26})$$

Substituting equations (A.23) and (A.26) into (A.19) yields the fully-formed expression for the normal derivative of the ring source:

$$\begin{aligned} \frac{\partial}{\partial n} R_n &= \left( n_\rho \frac{\partial}{\partial \rho} + n_z \frac{\partial}{\partial z} \right) R_n \\ &= -\frac{n_\rho}{\rho(\rho\rho')^{\frac{1}{2}}} \left\{ Q_{n-\frac{1}{2}}(Z) + \frac{2n-1}{a_0 + b_0} [a_0 Q_{n-\frac{1}{2}}(Z) - b_0 Q_{n-\frac{3}{2}}] \right\} \\ &\quad + \frac{2}{(\rho\rho')^{\frac{1}{2}}} \frac{2n-1}{a_0^2 - b_0^2} [(\rho - \rho') n_\rho + (z - z') n_z] [a_0 Q_{n-\frac{1}{2}}(Z) - b_0 Q_{n-\frac{3}{2}}]. \end{aligned} \quad (\text{A.27})$$

Just as the asymptotic behaviour of  $R_n$  was derived from the general expression (A.2), so must the asymptotic form of  $\frac{\partial R_n}{\partial n}$  be derived from (A.27). However, one important consideration stated by Kim & Yue (1989) is that:

The apparent singularity in the last term of (A.27) vanishes identically when the source point approaches the interior of piecewise linear segments approximating the body boundary  $\partial B \dots$

Consequently, only the first term in equation (A.27) will feature in the asymptotic analysis.

The asymptotic form of  $\frac{\partial}{\partial n} R_n$  is derived from the general form (A.27) using many of the relations used for the ring source potential  $R_n$  itself. Therefore, much of the analysis does not need to be explicitly reiterated. However, there are some simplifications which are important in the context of the derivation. Firstly, since the second term in A.27 does not possess a singularity as  $Z \rightarrow 1^+$ , then only the quantities associated with the  $n_\rho$  term need be considered. The asymptotic form of the Legendre functions have been stated already, nevertheless as a reminder they are given by:

$$\begin{aligned}\lim_{Z \rightarrow 1^+} Q_{n-\frac{1}{2}}(Z) &= -\frac{1}{2} \ln(1 - \frac{1}{Z^2}) + \Psi(1) - \Psi(n + \frac{1}{2}) + \ln 2 \\ &= -\frac{1}{2} \ln((\rho - \rho')^2 + (z - z')^2) + \ln \rho - 3 \ln 2 - c_n\end{aligned}\quad (\text{A.28})$$

and

$$\begin{aligned}\lim_{Z \rightarrow 1^+} Q_{n-\frac{3}{2}}(Z) &= -\frac{1}{2} \ln(1 - \frac{1}{Z^2}) + \Psi(1) - \Psi(n - \frac{1}{2}) + \ln 2 \\ &= -\frac{1}{2} \ln((\rho - \rho')^2 + (z - z')^2) + \ln \rho - 3 \ln 2 - c_{n-1}.\end{aligned}\quad (\text{A.29})$$

The terms  $a_0$  and  $b_0$  have asymptotic values of  $2\rho'^2$  from a simple analysis of the definitions of these quantities. Thus,  $\frac{a_0}{a_0+b_0} = \frac{b_0}{a_0+b_0} = \frac{1}{2}$  and so  $Q_{n-\frac{1}{2}}(Z) + \frac{2n-1}{a_0+b_0} Q_{n-\frac{1}{2}}(Z) = (n + \frac{1}{2})Q_{n-\frac{1}{2}}$ . Therefore, the asymptotic form of  $\frac{\partial}{\partial n} R_n$  is

$$\begin{aligned}\frac{\partial}{\partial n} R_n &\sim -\frac{n_\rho}{\rho \rho'} \left\{ n(Q_{n-\frac{1}{2}}(Z) - Q_{n-\frac{3}{2}}(Z)) + \frac{1}{2}(Q_{n-\frac{1}{2}}(Z) + Q_{n-\frac{3}{2}}(Z)) \right\} \\ &= -\frac{n_\rho}{\rho \rho'} \left\{ -\frac{1}{2} \ln((\rho - \rho')^2 + (z - z')^2) + \ln \rho - 3 \ln 2 \right. \\ &\quad \left. - ((n + \frac{1}{2})c_n - (n - \frac{1}{2})c_{n-1}) \right\},\end{aligned}\quad (\text{A.30})$$

## Appendix B

# Asymptotic analysis of far-field dipole potential

A infinite depth wave-free potential  $\phi_0$  in three-dimensions has a general asymptotic expansion of the form

$$\phi_0 \sim \sum_{m=2}^{\infty} e^{Kz} \frac{a_m}{R^m} \quad \text{as } R \rightarrow \infty \quad (\text{B.1})$$

for  $R = (r^2 + z^2)^{1/2}$  where  $r$  is the cylindrical radial coordinate. To demonstrate that the far-field dipole coefficient  $a_2$  of the axisymmetric passive trapped mode potential is zero, it must be shown that the maximum order of the potential in the far-field is  $O(R^{-3})$ . This requires an asymptotic analysis of the terms in the ring dipole potential  $\phi_0$  defined by equatons (6.31) and (6.31) in the limit  $R = (r^2 + z^2)^{1/2} \rightarrow \infty$ . As stated in chapter 6, the far-field limit will be taken by setting  $r = 0$  and letting  $z \rightarrow -\infty$  so that the integral term in (6.31) must be evaluated. The radiated wave is exponentially small in this limit and so can be neglected. It is useful to decompose this integral as

$$\begin{aligned} I &= \int_0^\infty (t \cos tz + K \sin tz) K_1(ct) \frac{t^2}{t^2 + K^2} dt \\ &= I_1 + KI_2 \end{aligned} \quad (\text{B.2})$$

where the integrals,  $I_1$  and  $I_2$ , respectively, are defined as follows

$$\begin{aligned} I_1 &= \int_0^\infty \cos(zt) f_c(t) dt, \\ I_2 &= \int_0^\infty \sin(zt) f_s(t) dt, \end{aligned} \quad (\text{B.3})$$

and the integrand functions are defined as

$$\begin{aligned} f_c(t) &= \frac{t^3}{t^2 + K^2} K_1(ct), \\ f_s(t) &= \frac{t^2}{t^2 + K^2} K_1(ct). \end{aligned} \quad (\text{B.4})$$

In order to obtain an expression for the far-field  $z$ -dependence of these integrals integration by parts must twice be applied.

Applying integration by parts to the cosine integral gives

$$\begin{aligned} I_1 &= \left[ \frac{\sin zt}{z} f_c(t) \right]_0^\infty - \int_0^\infty \frac{\sin zt}{z} f'_c(t) dt \\ &= -\frac{1}{z} \left( - \left[ \frac{\cos zt}{z} f'_c(t) \right]_0^\infty + \int_0^\infty \frac{\cos zt}{z} f''_c(t) dt \right) \end{aligned} \quad (\text{B.5})$$

where the first term after the first integration by parts is zero because  $f_c(t) \sin(zt) = 0$  at  $t = 0$  and  $f_c(t) \rightarrow 0$  as  $t \rightarrow \infty$  due to the exponential decay of the modified Bessel functions  $K_m$  for large arguments. The derivatives of the cosine integrand coefficient function  $f_c(t)$  are found to be, after some manipulation,

$$\begin{aligned} f'_c(t) &= \frac{(1+t^2)(6t^2K_1(ct) - ct^3(K_0(ct) - K_2(ct)) - 4t^4K_1(ct))}{2(1+t^2)^2}, \\ f''_c(t) &= \frac{t(-ct(t^4+6t^2+5)K_0(ct) + (2+t^2(c^2(1+t^2)^2) - 6)K_1(ct))}{(1+t^2)^3}. \end{aligned} \quad (\text{B.6})$$

Given that the asymptotic forms of the modified Bessel function of the second kind for large and small arguments are

$$\begin{aligned} K_m(x) &\sim \begin{cases} -\ln x, & x \rightarrow 0, m = 0, \\ \frac{1}{2}(m-1)!(x/2)^{-m}, & x \rightarrow 0, m = 1, 2, 3 \end{cases} \\ K_m(x) &\sim \sqrt{\frac{\pi}{2x}} e^{-x} \quad x \rightarrow \infty \end{aligned} \quad (\text{B.7})$$

then it is straightforward to obtain the following limits

$$\lim_{t \rightarrow \infty} f'_c(t) = 0, \quad \lim_{t \rightarrow \infty} f''_c(t) = 0. \quad (\text{B.8})$$

Furthermore, the second derivative of the function  $f_c$  is non-singular in the limit as  $t \rightarrow 0$  because the singularities in  $K_0(ct)$  and  $K_1(ct)$  are cancelled by the multiplicative factors  $t^2$  and  $t$  respectively. In the limit as  $t$  goes to infinity, the modified Bessel functions of order  $m = 0, 1, 2, \dots$  decay exponentially and so  $f''_c(t)$  must go to zero. Therefore,  $f''_c(t)$  is absolutely integrable as it can have no other real singularities and

by the Riemann-Lebegue lemma, the integral

$$\int_0^\infty \frac{\cos zt}{z} f_c''(t) dt \quad (\text{B.9})$$

is zero in the limit as  $z$  goes to negative infinity. Thus, the integral

$$I_1 = -\frac{1}{z^2} \int_0^\infty \cos zt f_c''(t) dt \quad (\text{B.10})$$

is  $o(z^{-2})$  in the limit as  $z \rightarrow -\infty$ .

In the case of the sine integral, applying integration by parts twice yields the following expression

$$I_2 = \left[ -\frac{\cos zt}{z} f_s(t) \right]_0^\infty + \int_0^\infty \frac{\cos zt}{z} f_s'(t) dt. \quad (\text{B.11})$$

However, the first derivative of  $f_s(t)$

$$f_s'(t) = \frac{(1+t^2)(4tK_1(ct) - ct^2(K_0(ct) + K_2(ct)) - 4t^3)}{2(1+t^2)^2} \quad (\text{B.12})$$

is non-zero at  $t = 0$  and so an alternative approach must be taken compared to the cosine integral. In this approach, the sine integral is rewritten as

$$I_2 = \int_0^\infty \frac{\sin zt}{ct} \frac{t^2}{t^2+1} dt + \int_0^\infty \sin zt f_{s2}(t) dt \quad (\text{B.13})$$

where the first integral is denoted  $I_{21}$  and the second  $I_{22}$  with the integrand function defined as

$$f_{s2}(t) = \frac{t^2(K_1(ct) - 1/ct)}{t^2+1}. \quad (\text{B.14})$$

To obtain a suitable form for  $I_{21}$  in order to take the limit as  $z \rightarrow -\infty$  it is best to first make the substitution  $y = -z$ . It is then straightforward to show by contour integration that  $I_{21} = o(y^{-2})$  in the limit as  $y \rightarrow \infty$  and hence  $I_{21} = o(z^{-2})$  as  $z \rightarrow -\infty$ . Next, the integral  $I_{22}$  must be evaluated and once again this is done by using integration by parts. So, it is necessary to evaluate the function  $f_{s2}(t)$  and its first and second-order derivatives for  $t = 0$  and in the limit as  $t \rightarrow 0$ . The derivatives are calculated to be

$$\begin{aligned} f_{s2}'(t) &= \frac{t^2 - 1 + ct(1-t^2)K_1(ct) - ct(1+t^2)K_0(ct)}{c(1+t^2)^2} \\ f_{s2}''(t) &= \frac{t(ct(2(t^2-3) + c^2(1+t^2)^2)K_1(ct) + c^2(t^2-3)(t^2+1)K_0(ct) + 6 - 2t^2)}{c(1+t^2)^3} \end{aligned} \quad (\text{B.15})$$

and both have vanishing limits as  $t \rightarrow 0$  and  $t \rightarrow \infty$ . Similarly,  $f_{s2}(t)$  is zero in both

limits and so applying integration by parts twice yields

$$I_{22} = -\frac{1}{z^2} \int_0^\infty \frac{\sin zt}{z} f''_{s2}(t) dt. \quad (\text{B.16})$$

because the anti-derivative terms both vanish. The term  $f''_{s2}$  is absolutely integrable because it possesses no singularities and decays exponentially to zero in the limit as  $t$  goes to infinity. Therefore, by invoking the Riemann-Lebesgue lemma  $I_{22} = o(z^{-2})$  as the remaining integral is zero. Thus,  $I_2 = o(z^{-2})$  also and combining this with the result for  $I_1$  it is clear that the total integral  $I$  has a vanishing dipole coefficient in the limit as  $z \rightarrow -\infty$ .

# Bibliography

- Abramowitz, M. A. & Stegun, I. A. (1964), *Handbook of Mathematical Functions*, 9th edn, Dover Publications, Inc., New York.
- Babarit, A. & Clément, A. H. (2006), 'Optimal latching control of a wave energy device in regular and irregular waves', *Applied Ocean Research* **28**, 77–91.
- Babarit, A., Duclos, G. & Clément, A. H. (2004), 'Comparison of latching control strategies for a heaving wave energy device in random sea', *Applied Ocean Research* **26**, 227–238.
- Beck, R. F. & Liapis, S. (1987), 'Transient motions of floating bodies at zero forward speed', *Journal of Ship Research* **31**, 164–176.
- Bender, C. M. & Orszag, S. A. (1978), *Advanced mathematical methods for scientists and engineers*, New York; London: McGraw-Hill.
- Black, J. L. (1975), 'Wave forces on vertical axisymmetric bodies', *Journal of Fluid Mechanics* **67**, 369–376.
- Budal, K. & Falnes, J. (1980), *Power from Sea Waves*, Academic Press, London, chapter Interacting point absorbers with controlled motion, pp. 381–399.
- Clément, A. H. (1996), 'Coupling of two absorbing boundary conditions for 2d time-domain simulations', *Journal of Computational Physics* **126**, 139–151.
- Cummins, W. E. (1962), 'The impulse response functions and ship motion', *Schiffstechnik* **9**, 101–109.
- Ducrozet, G., Bonnefoy, F., Le Touzé, D. & Ferrant, P. (2005), Development of a fully nonlinear water wave simulator based on higher order spectral theory, in '20<sup>th</sup> International Workshop on Water Waves and Floating Bodies, Longyearbyen, Norway', <http://www.iwwfb.org/Workshops/23.htm>.
- Eatoock Taylor, R. (2007), 'On modelling the diffraction of water waves', *Ship Technology Research* **54**, 54–80.

- Eatoock-Taylor, R. & Meylan, M. H. (2007), Theory of scattering frequencies applied to near-trapping by cylinders, in '22<sup>nd</sup> International Workshop on Water Waves and Floating Bodies, Plitvice, Croatia', <http://www.iwwfb.org/Workshops/22.htm>, pp. 73–76.
- Eatoock Taylor, R., Zang, J., Bai, W. & Walker, D. A. G. (2006), Transients in wave diffraction by cylinders and cylinder arrays, in 'Proceedings of 21<sup>st</sup> International Workshop on Water Waves and Floating Bodies'.
- Evans, D. V. (1976), 'A theory for wave-power absorption by oscillating bodies', *Journal of Fluid Mechanics* **77**, 1–25.
- Evans, D. V. & Porter, R. (2007), 'Wave-free motions of isolated bodies and the existence of motion-trapped modes', *Journal of Fluid Mechanics* **584**, 225–234.
- Falcão, A. F. d. O. (2008), 'Phase control through load control by oscillating-body wave energy converters with hydraulic pto system', *Ocean Engineering* **35**, 358–366.
- Falnes, J. (2002), *Ocean waves and oscillating systems : linear interactions including wave-energy extraction*, Cambridge University Press.
- Faltinsen, O. M., Rognebakke, O. F. & Timokha, A. N. (2007), 'Two-dimensional resonant piston-like sloshing in a moonpool', *Journal of Fluid Mechanics* **575**, 359–397.
- Fenton, J. D. (1978), 'Wave forces on vertical bodies of revolution', *Journal of Fluid Mechanics* **85**, 241–255.
- Gradshteyn, I. S. & Ryzhik, I. M. (1980), *Tables of integrals, series, and products*, 4th edn, New York : Academic Press. Translated from Russian by Scripta Technica, Inc ; translation edited by Alan Jeffrey.
- Havelock, T. (1955), 'Waves due to a floating sphere making periodic heaving oscillations', *Proc. Roy. Soc. Lond. A* **231**, 1–7.
- Hazard, C. (2000), The singularity expansion method: an application in hydrodynamics, in '5<sup>th</sup> International Conference on Mathematical and Numerical Aspects of Wave Propagation', Santiago de Compostela, Spain, pp. 494–498.
- Hulme, A. (1983), 'A ring-source/integral-equation method for the calculation of hydrodynamic forces exerted on floating bodies of revolution', *Journal of Fluid Mechanics* **128**, 387–412.
- Isaacson, M. & Ng, J. Y. T. (1993), 'Time-domain second order wave radiation in two dimensions', *Journal of Ship Research* **37**, 25–33.
- Joo, S. W., Schultz, W. W. & Messiter, A. F. (1990), 'An analysis of the initial-value wavemaker problem', *Journal of Fluid Mechanics* **214**, 161–183.

- Kennard, E. H. (1949), 'Generation of surface waves by a moving partition', *Quarterly of Applied Maths* **VII**(3), 303–312.
- Kim, M.-H. & Yue, D. K. P. (1989), 'The complete second-order diffraction solution for an axisymmetric body. part 1. monochromatic incident waves', *Journal of Fluid Mechanics* **200**, 235–264.
- Koo, W. & Kim, M.-H. (2004), 'Freely floating-body simulation by a 2d fully nonlinear numerical wave tank', *Ocean Engineering* **31**, 2011–2046.
- Kotik, J. & Lurye, J. (1964), Some topics in the theory of coupled ship motions, in 'Proceedings of the 5th Symposium on Naval Hydrodynamics', Office of Naval Research, Washington, Bergen Norway.
- Kyozuka, Y. & Yoshida, K. (1981), 'On wave-free floating body forms in heaving oscillation', *Applied Ocean Research* **3**, 183–194.
- Lamb, S. H. (1932), *Hydrodynamics*, 6th edn, Dover Publications.
- Linton, C. M. & McIver, P. (2001), *Handbook of mathematical techniques for wave/structure interactions*, Chapman & Hall/CRC, Boca Raton, Florida.
- Luke, Y. L. (1977), *Algorithms for the computation of mathematical functions*, Academic Press.
- Maiti, S. & Sen, D. (2001), 'Time-domain wave diffraction of two-dimensional single and twin hulls', *Ocean Engineering* **28**, 639–665.
- Maskell, S. J. & Ursell, F. (1970), 'The transient motion of a floating body', *Journal of Fluid Mechanics* **44**, 303–313.
- McIver, M. (1996), 'An example of non-uniqueness in the two-dimensional linear water wave problem', *Journal of Fluid Mechanics* **315**, 257–266.
- McIver, M. (1997), Resonance in the unbounded water wave problem, in 'Proceedings of 12<sup>th</sup> International Workshop on Water Waves and Floating Bodies'.
- McIver, P. (1994), 'Transient fluid motion due to the forced horizontal oscillations of a vertical cylinder', *Applied Ocean Research* **16**, 347–351.
- McIver, P. (2005), 'Complex resonances in the water-wave problem for a floating structure', *Journal of Fluid Mechanics* **536**, 423–443.
- McIver, P. & McIver, M. (1997), 'Trapped modes in an axisymmetric water-wave problem', *Quarterly Journal of Mechanics and Applied Mathematics* **50**, 165–178.
- McIver, P. & McIver, M. (2006), 'Trapped modes in the water-wave problem for a floating structure', *Journal of Fluid Mechanics* **558**, 53–67.

- McIver, P. & McIver, M. (2007), 'Motion trapping structures in the three-dimensional water-wave problem', *Journal of Engineering Mathematics* **58**, 67–75.
- McIver, P., McIver, M. & Zhang, J. (2003), 'Excitation of trapped water waves by the forced motion of structures', *Journal of Fluid Mechanics* **494**, 141–162.
- Mei, C. C. (1982), *The applied dynamics of ocean surface waves*, John Wiley and Sons. A Wiley-Interscience Publication not assigned an edition.
- Mei, C. C., Stiassnie, M. & Yue, D. K.-P. (2005), *Theory and Applications of Ocean Surface Waves. Part 1: Linear Aspects*, World Scientific Singaporee.
- Meylan, M. H. (2002), 'Spectral solution of time-dependent shallow water hydrodynamics', *Journal of Fluid Mechanics* **454**, 387–402.
- Meylan, M. H. & Eatock Taylor, R. (2008), Scattering by arrays of bottom mounted cylinders and the approximation of near trapping in the time domain, in '23<sup>rd</sup> International Workshop on Water Waves and Floating Bodies, Jeju Island, Korea', <http://www.iwwfb.org/Workshops/23.htm>, pp. 128–131.
- Molin, B. (1999), On the piston mode in moonpools, in '14<sup>th</sup> International Workshop on Water Waves and Floating Bodies', Port Huron, MI, USA, pp. 103–106.
- Motygin, O. & Kuznetsov, N. (1998), Non-uniqueness in the water-wave problem: an example violating the inside john condition, in '13<sup>th</sup> International Workshop on Water Waves and Floating Bodies'.
- Newman, J. N. (1977a), *Marine Hydrodynamics*, Cambridge, Massachussets.
- Newman, J. N. (1977b), 'The motions of a floating slender torus', *Journal of Fluid Mechanics* **83**, 721–735.
- Newman, J. N. (1999), 'Radiation and diffraction analysis of the mciver toroid', *Journal of Engineering Mathematics* **35**, 135–147.
- Newman, J. N. (2008), 'Trapping of water waves by moored bodies', *Journal of Engineering Mathematics* **62**, 303–314.
- Newman, J. N. & Lee, C. H. (1995), *WAMIT User's Manual*.
- Rogers, D. F. & Adams, J. A. (1989), *Mathematical Elements for Computer Graphics*, McGraw-Hill, London.
- Sen, D. (1995), 'A cubic-spline boundary integral method for two-dimensional free-surface flow problems', *International Journal for Numerical Methods in Engineering* **38**, 1809–1830.

- Ursell, F. (1964), 'The decay of the free motion of a floating body', *Journal of Fluid Mechanics* **19**(305-319).
- Wang, S. & Wahab, R. (1971), 'Heaving oscillations of twin cylinders in a free surface', *Journal of Ship Research* **15**, 33-48.
- Wehausen, J. V. (1971), 'The motion of floating bodies', *Annual Review of Fluid Mechanics* **3**, 237-268.
- Wehausen, J. V. & Laitone, E. (1960), 'Encyclopaedia of physics'.
- Wu, G. X. & Eatock Taylor, R. (2003), 'The coupled finite element and boundary element analysis of nonlinear interactions between waves and bodies', *Ocean Engineering* **30**, 387-400.

## **Thank You!**

In the acknowledgements I thanked everyone who helped me in completing my PhD. But I never thanked the great people (apart from family) who probably didn't help me complete my PhD!! That is, my friends from home in Ireland and especially the friends I have made in Loughborough. My PhD thesis is only a small part of the story of the last few years – the most important part won't be found in the preceding pages but here's a bit of it...

I had never heard of Loughborough/Loggoborro/Loogabarooga before I decided to come here but I have come to know it as an odd and colourful town full of strange and wonderful people. Fortune would have it that I have befriended a lot of amazing people here (and some strange ones too)! From the beginning there was Nick and Mariapia who made the year 2006 so memorable...if it hadn't been for Mariapia I wouldn't have met all the Italian immigrants momentarily stranded in Loughborough! During that one sunny summer I met so many people, some I am proud to still call great friends: that's you Laura, you Bruno, you Nik and you Fabio (Papini). With Nick sadly departing the scene, Fabio would then become my most trusted drinking comrade with Nik and Bruno too. From the spring of 2007 I would then go on to meet Davide (Ritardelli!), Carina (dude!), Vince (we're all amazing people!), Fausto (Santo Padre!), Fabio Di Martino (Toto!), Domenico, Enzo and lots of others. Only for them the last two years would have been much more academically productive...so way more boring. Instead it's been great, so many laughs, so many good times...who would have thought a place like Loughborough could be such fun!?

Other great people I've met along the path were Ismail (thanks for all the help Ish), Adrian and Ben from the office and Marc, Louis and Antonio in the department. Then there was Lenos (ela re!), Will and the rest of Barnett FC from football and Tom, Anny and Matt my (favourite) former housemates. There are plenty of others, sorry if I haven't mentioned you. And I still have to mention my friends from home especially Tom, MJ and Shane for the holidays we went on and Jamie, Joe and Ciaran too.

In the end I haven't even come close to capturing the story of the past few years but that doesn't matter...the story was made by all the good people I've mentioned and it will continue and remain with all of us. I can't wait to see you all again in the future when I return!

"All changes, even the most longed for, have their melancholy, for what we leave behind us is a part of ourselves..." — *Anatole France*

